Developing a model of acid-driven evolution for Pancreatic Ductal Adenocarcinoma (PDAC)



Wiktoria Z. Blaszczak

Linacre College

University of Oxford

A thesis submitted for the degree of

Doctor of Philosophy

Michaelmas 2022

Acknowledgements

It seems that this DPhil could not have come at a trickier time for myself. First, the global pandemic, then a war in a neighbouring country and last, difficult personal circumstances, altogether did not make it easy to focus on work and tackle all research-borne issues. Therefore, it was only thanks to the help and support of many different people that I managed to finish this project mentally intact and on time.

Firstly, I offer my gratitude to my supervisor, Prof. Paweł Świętach, for all his support and guidance I received throughout my time in his lab. Paweł, dziękuję. Oczywistym jest, że gdyby nie Ty i Twoja wiedza (szczególnie fizyczno-matematyczna) i doświadczenie, ten projekt nie zaszedłby zbyt daleko. Additionally, I would like to thank my secondary supervisor, Prof. Helen Christian for her kindness and support.

Secondly, I would like to thank Dr. Johanna Michl for her continuous support and advice. Johanna, you've been my mentor, my friend and often my ally, and I owe my mental stability mostly to you. Vielen dank!

Thirdly, I would like to thank Dr. Alzbeta Hulikova. Betka, I don't know who else I would have gone to with all my questions if you were not around. Ďakujem mnohokrát! I wish to thank Dr. KC Park, my motivation (coffee) supplier. KC, I think it's fair to say that I wouldn't have come this far without your input! And I wish to thank the remaining members of Swietach Lab, Dr. Eleanor Gill and Ms. Julija Rabcuka, we didn't share too much time, but, boy, was it eventful!

I also would like to thank Ms. Bobby White, Dr. Zhengchu Tan and Ms. Hannah Williams for their contribution to the work described in this Thesis.

I'm grateful to previous Swietach lab members, Dr. Stefania Monterisi, Dr. Mark Richards, Dr. Abigail Wilson, Dr. Aminah Loonat, Dr. Kate Curtis and Mrs. Mala Gunadasa-Rohling, I'm very fortunate to have met you. Thank you for all the advice, support, but also laughter and friendship. It was a blast working with you all!

Last, but not least I would like to thank all members of pHioniC consortium, especially students: Elena, Jiayi, Ganga, Julie, Renata, Roisin, Micol, Sofie, Xiaoyi, Madelaine, Jakub, Marco, Franco, and Tiago. The pandemic made it difficult for us to meet as planned, but I think we still managed to make the best of our time. Thank you for sharing the PhD troubles and all the memes and fun we had over the past three years. Special thanks are in order to Prof. Clemens Lowik, Prof. Laura Mezanotte and Ms. Roisin McMorrow, for their hospitality and help during my secondment at Erasmus Medical Centre in Rotterdam.

Finally, I would like to thank my husband, Dr. Wojciech Barczak for, well, everything really. Wojtek, w tym miejscu miało być tkliwe i osobiste podziękowanie za wszystko co dla mnie robisz, ale mój promotor rozumie polski, wiec niestety nie tym razem. Also, special thanks are in order to Dr. Joanna Wróblewska for our weekly moaning-science-drinking- sessions. I also would like to thank my family, who always bravely listened and attempted asking questions whenever I brought up my work, despite having literally no clue what I was talking about.

I wish to thank the European Commission for funding this project.

Abstract

Pancreatic ductal adenocarcinomas (PDAC) are characterised by poor prognosis and rising incidence. Their hallmarks include rapid progression, which suggests efficient metabolic reprogramming, and poor response to therapy, corresponding to accelerated somatic evolution. The elevated metabolic rate, necessary to sustain growth, creates an acidic microenvironment which may lead to more aggressive phenotypes. The high degree of heterogeneity in PDAC tumours sets up conditions for extensive feedbacks between metabolism, selection, and somatic evolution. The trajectory of the disease could be influenced by targeting these relationships, but, at present, understanding of these processes is incomplete. The aim of this doctoral project was to elucidate the role of acidity in PDAC with focus on the metabolic sources of acidity and feedback circuits that control metabolism. Furthermore, the role of low pH in selection and adaptation, and in maintaining population-level heterogeneity was explored.

A panel of PDAC cell lines was characterised for metabolic profiles using a specifically-designed fluorometric assay. Glycolytic metabolism, contrary to oxidative phosphorylation, was found to be highly sensitive to pH, which is a key negative feedback cue regulating the glycolytic output. Rapid or progressive acidification of media resulted in a reversible decrease in metabolic rate, arguing for an adaptive response rather than irreversible selection. Membrane permeability to lactic acid, the end-product of glycolysis, was assessed at single-cell resolution using fluorescence imaging. This readout revealed significant heterogeneity among cells of the same cell line. Surprisingly, the chemical inhibitors of lactic acid transport decreased the permeability of the transporters, but failed to reduce glycolytic flux, which may be due to autoregulation. Sorting according to lactic acid permeability showed that clones with high permeability manifested increased metabolic rates versus the low-permeability subgroup. However, the difference between these subpopulations was abolished with time, indicating a dynamic equilibrium. Transcriptomic analyses of the two populations identified a distinct pattern of expression, including elevated levels of IL6/STAT3 signalling in the high permeability cells. Pharmacological and genetic manipulations of this pathway revealed negative feedback loops between IL6 receptor-mediated activation of STAT3 and IL6R expression. This produced an oscillating system that periodically leads to STAT3 activation. This metabolic oscillation can explain the metabolic heterogeneity among PDAC cells, which is maintained even at uniform *in vitro* conditions. Evidence for the relevance of heterogeneity in PDAC was confirmed in xenografts *in vivo*.

Overall, these findings indicate that PDAC cell lines harbour a small population of cells characterised by increased metabolic rates due to elevated IL6R expression. This highly glycolytic phenotype, controlled by an IL6-mediated feedback circuit is transient. This has the advantage of favouring tumour progression at the cellular level in terms of growth and proliferation, without excessively acidifying their milieu.

Published works

- Blaszczak W, Tan Z, Swietach P. Cost-Effective Real-Time Metabolic Profiling of Cancer Cell Lines for Plate-Based Assays. Chemosensors. 2021;

- Blaszczak W, Williams H, Swietach P. Autoregulation of H^+/lactate efflux prevents monocarboxylate transport (MCT) inhibitors from reducing glycolytic lactic acid production. Br J Cancer. 2022;

- Blaszczak W, Swietach P. What do cellular responses to acidity tell us about cancer? Cancer Metastasis Rev. 2021;

- Michl J, Wang Y, Monterisi S, Blaszczak W, Beveridge R, Bridges EM, Koth J, Bodmer WF, Swietach P. CRISPR-Cas9 screen identifies oxidative phosphorylation as essential for cancer cell survival at low extracellular pH. Cell Rep. 2022

  The original articles *Cost-Effective Real-Time Metabolic Profiling of Cancer Cell Lines for Plate-Based Assays* and *Autoregulation of H^+/lactate efflux prevents monocarboxylate transport (MCT) inhibitors from reducing glycolytic lactic acid production* comprise the majority of data presented in Chapter 3 and Chapter 4, respectively and are an appendix to this Thesis. Some sections from the review article *What do cellular responses to acidity tell us about cancer?* were used in Chapter 1 and Chapter 6.

Statement of authorship

All the work presented in this Thesis was done by the author with some exceptions. These are indicated throughout the thesis, and include:

- All MATLAB codes used in data analysis were written by Prof. Pawel Swietach;
- The library preparation and next-generation sequencing were outsourced to Oxford Genomics Centre;
- The bioinformatic analysis of sequencing data was performed by Prof. Pawel Swietach;
- The Flow-Activated Cell Sorting was carried out with the support of Flow Cytometry facility staff: Dr. Robert Hedley and Ms. Vasiliki Tsiologa (Dunn School of Pathology);
- The automated scanning of tumour sections was done by Dr. Jana Koth (MRC Weatherall Institute for Molecular Medicine).

Some experiments have been conducted in collaboration with other researchers, including:

- postdoctoral scientist Dr. Zhengchu Tan: Chapter 3, Section 3.3.1 and 3.3.2;
- undergraduate student Ms. Hannah Williams: Chapter 4, Section 4.2.5;
- postgraduate student Ms. Bobby White: Chapter 5, Sections 5.2.10 and 5.2.11.

Table of contents

Acknowledgements i
Abstract ii
Published works iii
Statement of authorship iv
Table of contents v
List of figures ix
List of tables xi
List of abbreviations xii

Chapter 1. Introduction 1

1.1. The current state of knowledge about Pancreatic Ductal Adenocarcinoma 1
1.1.1. Characteristics 1
1.1.2. Epidemiology 1
1.1.3. Common mutations and cell lines 3
1.1.4. Carcinogenesis 8
1.1.5. Available therapies 9
1.1.6. Developing areas and future directions 10
1.2. Metabolic control and reprogramming in PDAC 11
1.2.1. Energy-supplying pathways 11
1.2.2. Metabolic regulation 12
1.2.3. Metabolic plasticity 14
1.2.4. The interleukin 6 signalling in cancer 15
1.2.5. IL6 as a modulator of cell metabolism 20
1.2.6. IL6 signalling-targeted therapies 21
1.3. Mechanisms and consequences of acidosis in PDAC 23
1.3.1. pH regulation at a systemic level 23
1.3.2. Regulation of intracellular pH 23
1.3.3. Acidosis in tumours 25
1.3.4. Effects of acidity 27
1.3.5. Acidosis as a driver of cancer evolution 28
1.3.6. Acidosis as a trigger of metastasis 29
1.3.7. Postprandial acidosis in pancreas 31
1.3.8. Prevention of metastasis 32
1.4. Rationale and aims 33

Chapter 2. Materials and methods 34

2.1. Maintaining in vitro cell culture 34
2.1.1. Cell lines 34

2.1.2. Cell culture 34
2.1.3. Media and solutions 35
2.1.4. Adjustment of medium pH 37
2.1.5. Medium buffering capacity 38
2.1.6. Intrinsic buffering capacity 38
2.1.7. Adaptation to acidity and selection by acid 39
2.2. Experimental procedures 41
2.2.1. Assessment of the glycolytic rate 41
2.2.2. H^+/lactate flux recordings 41
2.2.3. Glucose uptake measurements 43
2.2.4. Seahorse assay 43
2.2.5. The time-course measurements of metabolic acid production 44
2.2.6. Lactate production assay 45
2.2.7. High-throughput intracellular pH imaging 45
2.2.8. Cell proliferation assay 45
2.2.9. Metabolic phenotype assay 46
2.2.10. Flow cytometry and Fluorescence Activated Cell Sorting 47
2.2.11. Live cell imaging 50
2.2.12. Enzyme-linked immunosorbent assay 51
2.2.13. Immunofluorescence 52
2.2.14. In vivo xenograft experiments 53
2.2.15. Immunohistochemistry 53
2.2.16. RNA isolation 54
2.2.17. RNA Sequencing 54
2.2.18. RT-qPCR 55
2.2.19. Western blotting 56
2.3. Image processing and analysis 58
2.3.1. Image processing 58
2.3.2. MATLAB scripts 58
2.3.3. Statistical analysis 59

Chapter 3. Developing a cost-effective method for phenotyping the metabolic profile of PDAC cells 60
3.1. Introduction 61
3.2. Specific methods 63
3.2.1. Cells 63
3.2.2. Media 63
3.2.3. Fluorescent dyes and inhibitors 64
3.2.4. Equipment 64
3.3. Results 65

3.3.1. Selection of cost-effective pH and oxygen sensors to assay glycolytic and oxidative metabolism 65
3.3.2. Signal calibration to pH and O_2 units 69
3.3.3. Conversion of O_2 and pH time-courses into flux 71
3.3.4. Buffering 71
3.3.5. Description of the system 73
3.3.6. The efficiency of the assay to phenotype metabolism of cancer cells 75
3.3.7. Correcting for cell density 75
3.3.8. Real-time recordings of metabolic fluxes 78
3.3.9. The assessment of metabolic responses 80
3.4. Discussion 83
3.5. Key findings 84

Chapter 4. Description of the glycolytic metabolism and its control by pH in Pancreatic Ductal Adenocarcinoma 85
4.1. Introduction 86
4.2. Results 88
4.2.1. The negative feedback of pH on metabolic acid production 88
4.2.2. The interplay between glycolytic and oxidative metabolism depends on available nutrients 89
4.2.3. The effect of pH on glucose uptake 92
4.2.4. Glycolytic metabolism is inhibited by extracellular pH but not lactate 93
4.2.5. Negative feedback of extracellular pH can be disrupted by the increased buffering capacity 94
4.2.6. Membrane permeability 99
4.2.7. The pH dependence of MCT permeability 103
4.2.8. MCT inhibitors reduce permeability but fail to limit the glycolytic flux 106
4.2.9. The coupling between intra- and extracellular pH 111
4.2.10. The intracellular pH as a factor setting the glycolytic rate of cells 113
4.3. Discussion 115
4.4. Key findings 119

Chapter 5. Characterising cellular heterogeneity in terms of lactic acid efflux capacity and its metabolic consequences 120
5.1. Introduction 121
5.2. Results 124
5.2.1. Cells of any one cell line manifest heterogeneity of glycolytic phenotype 124
5.2.2. Cancer cells manifest heterogeneity in terms of their lactic acid removal capacity 125
5.2.3. The heterogeneity of lactic acid removal capacity is not related to the cell cycle phase 127

5.2.4. Cells sorted by their glycolytic phenotype manifest different metabolic profile ... 128
5.2.5. Cells of a high glycolytic profile have a proliferative advantage 130
5.2.6. Cells sorted according to the lactic acid venting capacity present distinctly different gene expression patterns 131
5.2.7. Differential gene expression is observed in subpopulations of MIA PaCa-2 cell line, but not PANC-1 133
5.2.8. Interleukin 6 production in vitro 136
5.2.9. Subpopulations sorted by IL6R expression present different transient glycolytic phenotypes 137
5.2.10. STAT3 inhibition causes metabolism collapse in MIA PaCa-2 but not PANC-1 cells 140
5.2.11. The heterogeneity of IL6 signalling among PDAC cell lines 142
5.2.12. The heterogeneity of IL6R expression in vivo 144
5.2.13. IL6R expression impacts the heterogeneity of lactic acid efflux 146
5.2.14. STAT3 inhibition increases IL6R-expressing population in MIA PaCa-2 but not PANC-1 cells 147
5.3. Discussion 150
5.4. Key findings 157

Chapter 6. Comparing and contrasting the effects of acid selection versus acid adaptation on pH-related cellular phenotypes 158
6.1. Introduction 159
6.2. Results 164
6.2.1. pH sensitivity of PDAC cell lines 164
6.2.2. Impact of acidosis on the heterogeneity of glycolytic phenotypes 165
6.2.3. Effects of acid treatment on metabolic profile 167
6.2.4. Effects of acid-selection and adaptation on intracellular pH 170
6.2.5. Anion Exchanger 2 undergoes degradation under acidic conditions 171
6.3. Discussion 173
6.4. Key findings 178

Chapter 7. Concluding remarks and future directions 179

References 184

Appendix 235

List of figures

Figure 1.1 Number of deaths caused by pancreatic and colorectal cancers in the United Kingdom between 1970 and 2019. 3
Figure 1.2 Distribution of most common mutations observed in PDAC cell lines. 5
Figure 2.1 Example of medium buffering capacity determination. 38
Figure 2.2 Intrinsic buffering capacity measurements. 39
Figure 2.3 Protocol created to sort cells according to their MCT permeability.. 48
Figure 3.1 Spectral analyses of HPTS and RuBPY. 68
Figure 3.2 Calibration curves for HPTS- and RuPBY-emitted fluorescence. 70
Figure 3.3 Measuring the pH buffering capacity. 72
Figure 3.4 Characterisation of the system with respect to O_2 dynamics. 75
Figure 3.5 Cell Tracker Orange (CTO)-based normalisation of the cell number. 77
Figure 3.6 Metabolic profiling of PDAC cell lines. 80
Figure 3.7 Assessment of cell response following a change in the metabolic substrate.. 81
Figure 3.8 Assessment of the effect of metabolic inhibitors. 82
Figure 4.1 pH-induced feedback loop on metabolic acid production. 89
Figure 4.2 Metabolic acid production is dependent on available nutrients. 91
Figure 4.3 pH sensitivity of glucose uptake. 92
Figure 4.4 Effect of glycolytic end products, extracellular lactate and protons, on metabolic acid production rate. 93
Figure 4.5 Increased medium buffering capacity removes negative feedback of extracellular pH and elevates glycolysis. 95
Figure 4.6 Increasing buffering capacity with volatile buffers elevates glycolysis. 97
Figure 4.7 Effect of pH on glycolytic and oxidative metabolism. 98
Figure 4.8 MCT permeability in PDAC cell lines. 100
Figure 4.9 Glycolytic rate of PDAC cells. 102
Figure 4.10 The correlation between MCT permeability and rate of cellular lactic acid production. 103
Figure 4.11 Treatment with DMOG activates hypoxic signalling in PDAC cells. 104
Figure 4.12 pH dependence of MCT permeability.. 105
Figure 4.13 Pharmacological inhibitors successfully reduce the permeability of the monocarboxylate transporters. 107
Figure 4.14 Pharmacological MCT inhibition does not impact the glycolytic flux.. 108
Figure 4.15 Pharmacological MCT inhibition does not affect cell metabolism. 109
Figure 4.16 Pharmacological MCT inhibition increases total protein lactylation. 110
Figure 4.17 Transfer of extracellular acidity into the cytoplasm.. 112
Figure 4.18 The effect of intracellular pH on glycolytic metabolism of PDAC cell lines. 114
Figure 5.1 Assessment of the heterogeneity of glycolytic rate in PDAC cell lines. 125

Figure 5.2 Variation of cell lactic acid efflux capabilities in PDAC cell lines. 126
Figure 5.3 Relating the MCT permeability to the cell cycle phase. 128
Figure 5.4 Cells of different MCT permeability status present different metabolic profiles. . 129
Figure 5.5 High MCT permeability status is associated with proliferative advantage. 130
Figure 5.6 MCT permeability status correlated with differential gene expression. 133
Figure 5.7 Stability of MCT-high and MCT-low populations during separation by FACS. 134
Figure 5.8 Validation of differentially expressed genes between high and low MCT subpopulations in MIA PaCa-2 and PANC-1 cells. 135
Figure 5.9 Interleukin 6 production *in vitro*. 137
Figure 5.10 Cell phenotype associated with IL6R expression. 139
Figure 5.11 Impact of STAT3 inhibition on metabolic profile. 141
Figure 5.12 Heterogeneity of IL6R expression and STAT3 activation among PDAC cell lines. 143
Figure 5.13 The heterogeneity of IL6R is maintained *in vivo*. 145
Figure 5.14 IL6R expression influences the heterogeneity of lactic acid efflux. 146
Figure 5.15 STAT3 inhibition increases surface expression of IL6R. 149
Figure 5.16 Proposed feedback circuit controlling the number of active surface receptors and heterogeneity of glycolytic metabolism in MIA PaCa-2 cell line. 149
Figure 6.1 pH sensitivity of PDAC cell lines. 165
Figure 6.2 Acid treatment induces a shift in MCT permeability in PDAC cells. 166
Figure 6.3 Acidic treatment alters the metabolic profile of PDAC cells. 169
Figure 6.4 Acid treatment alkalinizes intracellular pH of PDAC cells. 171
Figure 6.5 Anion Exchanger 2 degradation under acidic conditions. 172
Figure 7.1 The overview of main signalling pathways and transporters studied in this project with indicated feedback control between them 180

List of tables

Table 1.1. Extracellular pH reported in tumours. 26
Table 2.1. List of antibodies used for immunofluorescent staining 52
Table 2.2. Sequences of primer pairs used in RT-qPCR experiments 56
Table 2.3 List of antibodies used for western blotting 58
Table 3.1 Best fit calibration values for HPTS fluorescence 71
Table 4.1 Acid dissociation constants (pK_a) of selected buffering agents at room temperature (RT). 94
Table 6.1 Examples of acidity-triggered cellular responses 160

List of abbreviations

2-NBDG	2-(N-(7-Nitrobenz-2-oxa-1,3-diazol-4-yl)Amino)-2-Deoxyglucose
ADAM-10	A Disintegrin and metalloproteinase domain-containing protein 10
AE	Anion exchanger
ANOVA	Analysis of variance
A-RC	AR-C155858
ATCC	American Type Culture Collection
ATP	Adenosine triphosphate
BAG3	BAG Cochaperone 3
BSA	Bovine serum albumin
CA	Carbonic anhydrase
CDKN2A	Cyclin-dependent kinase inhibitor 2A
CEST	Chemical Exchange Saturation Transfer
CHC	α-cyano-4-OH-cinnamate
COX6B2	Cytochrome C Oxidase Subunit 6B2
cSNARF1	5-(and-6)-Carboxy SNARF-1
CFTR	Cystic fibrosis transmembrane conductance regulator
CTO	Cell tracker orange
DAPI	Diamidino-2-phenylindole
DEG	Differentially expressed gene
DMA	5-N,N-dimethylamiloride
DNMT-1	DNA methyltransferase 1
EFNB2	Ephrin B2
EGF	Epidermal growth factor
ELISA	Enzyme-linked immunosorbent assay
EPR	Electron Paramagnetic Resonance
ERK	Extracellular signal-regulated kinases
FACS	Fluorescence activated cell sorting
FBS	Foetal bovine serum

FOLFIRINOX	Combined treatment with leucovorin, fluorouracil, irinotecan and oxaliplatin
FOXJ1	Forkhead Box J1
GAPDH	Glyceraldehyde 3-phosphate dehydrogenase
HBEGF	Heparin Binding EGF-Like Growth Factor
HEPES	4-(2-hydroxyethyl)-1-piperazineethanesulfonic acid
HIF1α	Hypoxia Inducible Factor 1 Subunit α
HPTS	8-Hydroxypyrene-1,3,6-trisulfonic acid trisodium salt
IL6	Interleukin 6
IL6Rα	Interleukin 6 receptor α
IL6Rβ	Interleukin 6 receptor β
IPA	Ingenuity Pathway Analysis
JAK	Janus kinase
Jlac	Lactate flux
KEGG	Kyoto Encyclopaedia of Genes and Genomes
KRAS	KRAS proto-oncogene
MAPK	Mitogen-activated protein kinase
MARI	Marimastant
MCT	Monocarboxylate transporter
MDM2	E3 ubiquitin-protein ligase
MDSC	Myeloid-derived suppressor cells
MEK	MAPKK Mitogen-activated protein kinase kinase
MES	2-(N-morpholino)ethanesulfonic acid
MHC	Major histocompatibility complex
MRI	Magnetic resonance imaging
NAPA	Napabucasin
NBCn1	Sodium bicarbonate cotransporter
NFATC2	Nuclear Factor of Activated T Cells 2
NFκB	Nuclear factor kappa-light-chain-enhancer of activated B cells
NHE-1	Na^+/H^+ exchanger
OXPHOS	Oxidative phosphorylation
PanIN	Pancreatic intraepithelial neoplasia

PARACEST	Paramagnetic Chemical Exchange Saturation Transfer
PBS	Phosphate buffered saline
PCA	Principal component analysis
PDAC	Pancreatic ductal adenocarcinoma
PDP1	Pyruvate Dehydrogenase Phosphatase Catalytic Subunit 1
PE	Phycoerythrin
pHe	Extracellular pH
pHi	Intracellular pH
PIK3CA	Phosphatidylinositol-4,5-Bisphosphate 3-Kinase Catalytic Subunit Alpha
pKa	Acid dissociation constant
P_{MCT}	MCT permeability
PTEN	Phosphatase and tensin homolog
PVDF	Polyvinylidene fluoride
RB1	RB Transcriptional Corepressor 1
RIPA	Radioimmunoprecipitation assay buffer
RNA	Ribonucleic acid
RNASeq	RNA sequencing
RPMI	Roswell Park Memorial Institute medium
RT-qPCR	Quantitative reverse transcription polymerase chain reaction
RuBPY	Tris(2,2′-bipyridyl)dichlororuthenium(II) hexahydrate
Ryr	Ryanodine receptor
SEM	Standard Error of the Mean
SLC16A1	Solute Carrier Family 16 Member 1
SMAD4	SMAD family member 4
SNW1	SNW Domain Containing 1
SOCS3	Suppressor of Cytokine Signalling 3
SR	SR13800
SRB	Sulforhodamine B
STAT3	Signal transducer and activator of transcription 3
STR	Short tandem repeats
Syro	Syrosingopine

TAM	Tumour-associated macrophages
TBS	Tris-buffered saline
TGFβ	Transforming growth factor β
TNFα	Tumour necrosis factor α
TP53	Tumour protein 53
USP38	Ubiquitin Specific Peptidase 38
UV	Ultraviolet radiation

Chapter 1. Introduction

1.1. The current state of knowledge about Pancreatic Ductal Adenocarcinoma

1.1.1. Characteristics

Pancreatic Ductal Adenocarcinomas (PDAC) arise from the lining of the exocrine pancreatic ducts and account for the majority (95%) of all pancreatic cancers (1). Compared to other types of cancer, relatively little progress has been made in treating PDAC and its survival rates remain stubbornly low. Asymptomatic development (2), late stage at diagnosis, lack of reliable diagnostic and prognostic markers (3), high grading and pronounced desmoplasia (4), are all characteristic to PDAC and contribute to poor prognosis for most patients. Rising prevalence and poor outcomes warrant much-needed research to discover new mechanisms and targets for PDAC therapy and diagnostics.

1.1.2. Epidemiology

PDAC ranks as the 14th most common cancer in terms of incidence and 7th in cancer-related deaths worldwide, accounting for half a million deaths in 2020 alone (5). With dismal 1-year survival rates of only 24% and 5-year survival rates not exceeding 8%, PDAC continues to be one of the deadliest types of cancer (6). The incidence of PDAC is slightly higher in males than in females (5.7 vs 4.5 cases per 100,000), and it is more common in countries of higher socio-economic status including both Western and Eastern Europe, Australia, New Zealand and the United States of America,

with a mean incidence of 9.8 cases per 100,000 in males (5). On the contrary, a relatively low incidence is reported in Africa, and South-Central Asia, especially Guinea, India and Malawi with an incidence of 0.46 per 100,000 (5). Due to the link between the socioeconomic status and number of reported cases (7), the Western diet of highly processed food has been proposed as a risk factor (8). This hypothesis is strengthened by the sex-related difference in incidence (5, 8), as women are reported to follow a diet-regime of overall higher quality with lower red meat and alcohol intake in comparison to men (9). Other risk factors for PDAC development include family history, genetic disorders including hereditary pancreatitis (10), hereditary colorectal adenomatous polyposis (11), Lynch syndrome (12, 13), hereditary breast and ovarian cancer syndrome (14, 15), chronic pancreatitis (16-19), and diabetes (20, 21).

In the USA alone, the incidence of PDAC has been on the rise at 1.03% annually (22). If this trend continues, by 2030 PDAC will be the second leading cause of cancer-related death (23). A similar tendency is true for the United Kingdom. According to the World Health Organisation, the number of deaths caused by pancreatic cancer has doubled since 1970 accounting for almost 10,000 deaths in 2019 alone, while the number of deaths associated with cancers of the colon and rectum has remained stable over the last 50 years with a slight decreasing trend observed from 2000 (Fig 1, (24)).

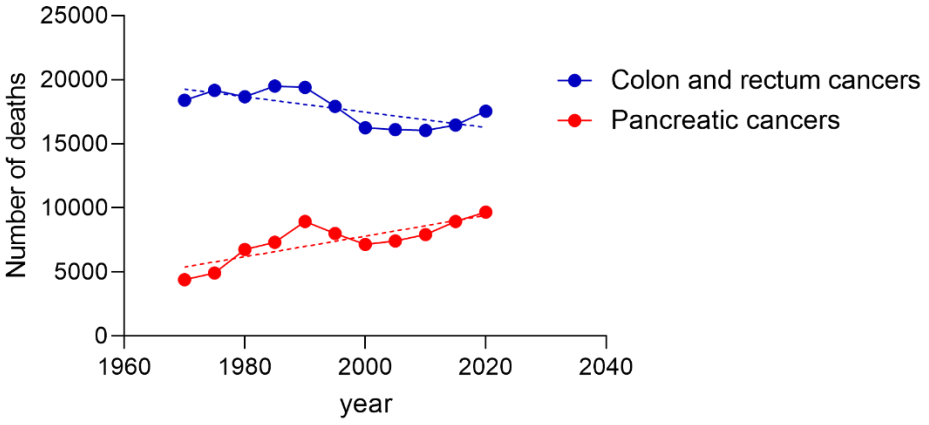


Figure 1.1 Number of deaths caused by pancreatic and colorectal cancers in the United Kingdom between 1970 and 2019. Plot created based on data collected by World Health Organisation (24), dashed lines depict best fit, for pancreatic cancers b=80.69 and for colorectal cancers b=-59.79; b-slope.

1.1.3. Common mutations and cell lines

Many studies of PDAC have relied on studies of transformed cells. Commonly used cell lines include AsPC-1, BxPC-3, Colo-357, HPAC, MIA PaCa-2 and PANC-1. AsPC-1 (CRL-1682) cell line was established from xenografts which were initiated using cells from the ascites of a 62-year-old, Caucasian female patient with cancer of the pancreas. BxPC-3 (CRL-1687) cell line was derived from a primary tumour of a 61-year old, female patient. These cells are characterized by epithelial morphology. Colo-357 cell line was derived in 1977 from a lymph node metastatic tumour of a 77-year old patient, and manifests unique features including enzyme production and allozyme profile (25). HPAC (CRL-2119) is another epithelial cell line derived in 1985 from a mouse xenograft of a primary tumour resected from the head of the pancreas. Similarly, MIA PaCa-2 (CRL-1420) is an epithelial cell line derived from a primary tumour of a 65-year old male patient (26). PANC-1 (CRL-1469) cell line was established from the pancreatic duct of a 56-year-old, Caucasian male suffering from epithelioid carcinoma (27). These lines

were chosen due to the manifested range of genotypes and phenotypes affecting cell behaviour and metabolism.

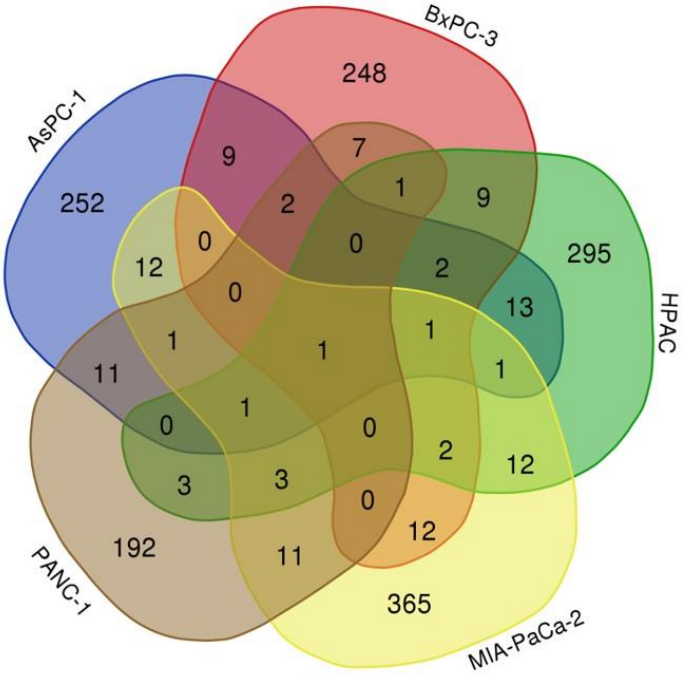
The chosen panel of cell lines presents a variety of mutations corresponding to cell phenotype and behaviour. The only mutation shared among the panel is in tumour-suppressing *TP53*. *KRAS* mutation has been reported in AsPC-1, HPAC, MIA PaCa-1 and PANC-1 cells (28). Most of the cell lines are characterised by poor to moderate differentiation and varied doubling time between 38 and 60 hours (29). The cell lines manifest different tumorigenicity, however, the reported ranking is often contradicting (30-32).

1.1.3.1. Tumor Protein P53 (TP53)

Loss of function mutations in *TP53* are a common feature of many types of cancer. In PDAC, it is reported that loss of functional activity happens during the pancreatic intraepithelial neoplasia (PanIN) development and is required for the progression to the developed malignancy. The reported *TP53* mutation rate in PDAC varies between 20-76% (33, 34). Functional p53, the product of *TP53* expression has a strong tumour-suppressing activity, which was confirmed by observed 100% spontaneous cancer incidence in Tp53 knockout mice (35, 36). Under physiological conditions in a healthy and unstressed cell, the protein level of p53 is low, as it is controlled by continuing proteasome degradation due to targeting by E3 ubiquitin-protein ligase (MDM2). Upon DNA damage, oncogene activation, nutrient deprivation or another stress stimulus, the E3 ligase is inhibited and activated p53 forms homotetramers which bind to promoter regions and regulate the expression of 500 genes (37), thus inducing cell cycle arrest, DNA repair pathways, metabolic adaptation, senescence and apoptosis (38).

This way, wild-type p53 prevents oncogenic transformation, which in case of loss of function becomes greatly facilitated (39).

A



B

	TP53	*KRAS*	*SMAD4*	*CDKN2A*
AsPC-1	+	+	+	+
BxPC-3	+			
HPAC	+	+	+	+
MIA PaCa-2	+	+		
PANC-1	+	+		

Figure 1.2 Distribution of most common mutations observed in PDAC cell lines. A: Venn diagram depicting the overlap in driver mutations observed in PDAC cell lines. The majority of harboured mutations are unique for each cell line with only one common for all lines. B: Driver mutations harboured by selected PDAC cell lines, the only shared driver mutation is the one in *TP53*. Mutatome data was retrieved from the Cancer Cell Line Encyclopaedia (28).

1.1.3.2. KRAS proto-oncogene (KRAS)

Gain of function mutations in *KRAS* are the most frequent genetic alterations observed in pancreatic cancers with a frequency of 70-95% of all tumours (40, 41). Product of *KRAS* expression is a GTPase and its activation is recognised as a driver of cancer as it mediates a vast number of oncogenic alterations that facilitate cancer initiation and progression. Activated KRAS signalling, through stimulation of MAPK and PI3K-mTOR pathways, contributes to uncontrolled proliferation and survival of cancer (42). Apart from its impact on tumour growth, *KRAS* mutation has been implicated in desmoplastic reaction (43) and promoting tumour survival via stimulation of pancreatic stellate cells to secrete autophagy-derived alanine (44). Additionally, *KRAS* contributes to tumour inflammation by stimulation of cytokine secretion, including interleukin 1, 6, 8 and 23, as well as several chemokine ligands (45), thus mediating the crosstalk with the microenvironment and contributing to the evasion of immune recognition (46).

1.1.3.3. Cyclin-dependent kinase inhibitor 2A (CDKN2A)

The *CDKN2A* has been identified as a tumour suppressor in 1994 when its frequent missense mutations were first associated with oesophagus cancer development (47). *CDKN2A* encodes two proteins, p16INK4a and p14ARF both of which contribute to differentiation, cell cycle regulation, senescence and apoptosis (48). While the function of p14ARF is the interaction with MDM2 to increase p53 levels, thus inhibiting the proliferation of transformed cells by causing arrest in the G1 phase or triggering apoptosis (49-51), p16INK4a regulates cell cycle progression at the point of G1/S transition (51, 52). The frequency of *CDKN2A* mutations in PDAC specimens falls within 49-98% (53, 54) and 27% of these are caused by hypermethylation of promoter

region (55). As the loss of CDKN2A activity is more common in advanced stages of the disease, it was suggested that it is a necessary event for cancer progression. Based on this notion, several nature-derived molecules of epigenetic regulatory function such as genistein (56, 57), sulforaphane (58), and epigallocatechin-3-gallate (59), have been proposed as potential therapeutics and the clinical trials designed to assess their efficacy are currently ongoing.

1.1.3.4. SMAD family member 4 (SMAD4)

Loss of function mutation in *SMAD4* is the fourth most frequent genetic alteration in PDAC with a mutation rate between 19-50% (60, 61). SMAD4 is a member of SMAD family of transcription factors and its expression is regulated by circadian control (62). SMAD4 is a key element of the Transforming Growth Factor-β (TGFβ) signalling pathway. Under physiological conditions, stimulation with TGFβ creates a downstream cascade of SMAD family and MAPK/ERK phosphorylation, leading to the translocation of SMAD2/3/4 complexes into the nucleus and transcription regulation of Snail, Sox4 and Klf5 (63). The effects of the TGFβ pathway are context dependent and may either promote or restrict tumour growth (64). In *SMAD4* wild-type cells activation of TGFβ signalling promotes the epithelial-to-mesenchymal transition (65), which is often considered a tumorigenic event. However, it was shown that once transformed, PDAC cells are susceptible to Sox4-triggered apoptosis (66). This mechanism controls the proliferation of pancreatic cancer cells, which is supported by the observation that *SMAD4* wild-type tumours form metastasis less frequently than the *SMAD4*-lacking group (67). Moreover, loss of SMAD4 activity has been recognised as a cause of resistance to oxidative phosphorylation inhibition due to simultaneous stimulation

of mitophagy (68). Expression of *SMAD4* is reported as inversely correlated with autophagy, which contributes to PDAC resistance to radiotherapy (69).

1.1.4. Carcinogenesis

The oncogenic transformation in pancreatic ducts is believed to be slow, with pre-malignant lesions typically remaining confined to the organ even for decades (70). Although PDAC development is understood to take several years, progression from stage T1 to T4 can be as rapid as 12 months (71). Tracking the tumour-load indirectly by serum CA 19-9 levels revealed advanced tumours to have the doubling time of 40 to 60 days, which makes the disease almost unstoppable (72). PDAC tumours are highly heterogenous with on average 63 mutations affecting 12 core cellular processes and signalling pathways including TGFβ, Hedgehog, KRAS, and Wnt/Notch (73). The oncogenic transformation has been associated with several somatic mutations including the activation of *KRAS*, and loss of tumour-suppressing *CDKN2A*, *TP53* and *SMAD4*, which have been reported to be acquired in this specific order (74, 75). Carcinogenesis begins with acinar-ductal metaplasia, usually triggered by the most frequently observed driver mutation in proto-oncogenic *KRAS* (76). Then, the pancreatic intraepithelial neoplasia (PanIN) is formed, which goes through three stages classed according to progressive remodelling of tissue architecture, before they progress into developed adenocarcinoma. All of these stages are associated with epigenetic dysregulation (77, 78) and increasing desmoplastic reaction (4), which eventually surrounds the formed tumour with a thick and difficult-to-penetrate fibrous layer contributing to evasion of immune recognition and affecting the penetration with chemotherapeutics (79, 80). Several types of classification systems of PDAC based

on the molecular signature have been proposed (76, 81-85). These class tumours according to the expression of a vast number of genes relating to (among others) enzyme secretion, extracellular matrix component production, and cytokine signalling. Although some subtypes correlate with prognosis, there is only limited overlap between all proposed classification systems, which limits their clinical value (86). This issue reflects the high heterogeneity of pancreatic tumours, which makes it difficult to create a uniform system of subtypes, as several features need to be included.

1.1.5. Available therapies

Treatment options include surgical resection, chemo- and less frequently, radiotherapy and are dependent on the disease stage and overall condition of the patient (87). The treatment of choice is based on the tumour resection in a Whipple or distal pancreatectomy followed by adjuvant chemotherapy with FOLFIRINOX or pyrimidine analogue, gemcitabine (87). While the latter has been used in PDAC treatment since 1996 (88), it is associated with milder adverse effects than multi-compound FOLFIRINOX, which combines 5-Fluorouracil, leucovorin, irinotecan, and oxaliplatin (87), and has shown improved overall survival when compared with gemcitabine-based monotherapy (89). Other chemotherapeutic options, including a variety of combination therapies, are administered in case of resistance and suboptimal health status of the patient. Trials of targeted therapies, designed to inhibit KRAS effector proteins were unsuccessful (90, 91), with insufficient tumour penetration, metabolic plasticity and high heterogeneity suggested as reasons for failure (92).
So far, no immunotherapeutic or targeted agent has been approved explicitly for the treatment of PDAC, but several promising clinical trials testing the efficacy of novel

approaches including neoantigen vaccines (93), anti-PD-1 antibodies (94), and adenosine receptor antagonists (95), are currently ongoing.

1.1.6. Developing areas and future directions

Whilst research on pancreatic cancer has been growing steadily, treatment outcomes have not improved proportionately. PDAC remains one of the most feared diagnoses with poor response to therapy. Despite the identification of a number of risk factors, these tend to be broad and inter-dependent with other, more prevalent disorders of lower overall morbidity. Consequently, population screening is not expected to be efficient. Recently, over 350 individuals with identified increased risk for developing PDAC either due to a genetic mutation or familial history have been included in a long-term surveillance project (96). Participants were followed for over 5 years and tested annually with endoscopic ultrasonography and magnetic resonance imaging cholangiopancreatography. Although, the screening improved the percentage of resectable tumours at diagnosis, it did not impact the overall survival. Perhaps the annual testing, given the rapid progression of the disease, was not frequent enough to significantly impact the prospects. As all cases have been diagnosed in a group of mutation carriers and no incidence was observed in the group of familial history without genetic burden, it was suggested that the latter should be excluded from surveillance in the future (96). It seems that stronger effort should be put into the development of more reliable diagnostic methods, as most pre-malignant lesions are invisible in MRI scans and the lack of a specific biomarker correlating with PDAC incidence excludes the possibility of cost-effective blood-based screening.

1.2. Metabolic control and reprogramming in PDAC

1.2.1. Energy-supplying pathways

As cancer cells proliferate at a significantly higher rate than the healthy tissue while remaining insensitive to the majority of controlling cues that under physiological circumstances limit the growth, hence deregulated metabolism has been recognised as an important hallmark of cancer (97). The two main energetic pathways used to meet the increased energetic demand in cancer cells are anaerobic glycolysis and oxidative phosphorylation (98). Cancer cells adapt to high metabolic demand and increase the number of mitochondria (99), along with the expression of glucose transporters (100), and glycolytic enzymes (101). Although glycolysis has a lower yield of adenosine triphosphate (ATP) per glucose, it is independent of oxygen and often upregulated in cancer, a finding known as the Warburg effect (102). In most cells, glycolytic fermentation of glucose occurs in response to hypoxia, when complete oxidation is not possible. In the absence of oxygen, pyruvate generated by the glycolytic pathway is converted to lactate by the enzymatic activity of lactate dehydrogenase and removed into the extracellular space, alongside an H^+ ion, largely via H^+-monocarboxylate transporters (MCTs) of the *SLC16* family (103).

Once removed from the cancer cells, lactic acid will tend to diffuse towards the nearest capillary for washout; however, this may be at a distance. To ensure there is a sufficient flux of lactic acid, a gradient is established, leading to the retention of lactic acid in tumours, as observed by Warburg in the 1920s. However, there are alternative fates for lactic acid. Cancer-associated fibroblasts can feed on extracellular lactate,

or it can diffuse into a more oxygenated niche for oxidation by cancer cells (104, 105). Since glycolysis and pentose phosphate pathway (PPP) are interconnected, the increased glycolytic rate contributes to the production of building blocks for biosynthesis, including nucleic and amino-acids and reducing agents (106, 107).

The common cancer mutations in *TP53* and *KRAS* also have been associated with increased metabolic rates. Loss of functional p53 has been reported to promote anabolism by increasing glycolytic flux (108). Activation of *KRAS* also impacts cell metabolism by increasing glucose uptake and promoting glycolysis (109), pentose phosphate pathway and hexosamine biosynthesis pathway (92). Additional effects of *KRAS* activation include stimulation of micropinocytosis and autophagy, providing transformed cells with building blocks for biosynthesis without putting additional strain on glucose oxidation (110). Additionally, overexpression of cytochrome c oxidase subunit 6B2 (COX6B2) was found to promote oxidative phosphorylation and was linked to increased metastatic potential in PDAC (111).

1.2.2. Metabolic regulation

Metabolic pathways are typically regulated at the level of substrate availability and by feedback from the end-products. Oxidative phosphorylation (OXPHOS) is, by design, regulated by oxygen availability. Glycolysis, in contrast, can be regulated through feedback by intermediates or end-products (112). A high concentration of intracellular pyruvate has been reported to regulate the expression of glycolytic enzymes and glucose transporters in an epigenetic feedback circuit via modulation of histone acetylases and deacetylases (113). The necessary condition for oxidative phosphorylation is sufficient oxygenation of the tissue around 3-7% O_2 (114).

Additionally, OXPHOS is dependent on substrate availability and increases in response to a rise in intermediate metabolites and substrates, not only glycolysis-derived pyruvate but also glutamine (115). The oxidative metabolism is also controlled by the changes to the levels of its end-product, ATP. OXPHOS is stimulated by increasing ADP concentration which directly signals the increasing energy demand (116, 117).

Microenvironment especially in under-perfused regions of the tumour, can put significant pressure on cancer cells in form of extracellular acidity, hypoxia and accumulation of lactate, all of which acutely limit the metabolic rate (118). On one hand, low extracellular pH is needed to drive lactic acid towards blood capillaries, along a diffusion distance across the interstitium. However, an environment of low pH will ultimately also impact cytoplasmic pH, triggering a number of intracellular effects. Among these effects is the inhibition of glycolytic enzymes (119). High extracellular lactate will also reduce lactate removal from the cytoplasm, which can lead to epigenetic changes in form of recently reported histone lactylation (120). This, however, can be partially offset by cell-to-cell coupling by connexins which allows lactate offloading in a more distant tumour niche, where microenvironment conditions might be permissive (121). Alternatively, extracellular lactate can become metabolic fuel to cancer and stroma cells and feed oxidative metabolism by entering the tricarboxylic acid cycle (122, 123). Hypoxic tumours are known to favour oxygen-independent ATP production via Hypoxia-Inducible Factor-mediated (HIF) metabolic reprogramming towards aerobic glycolysis (124). Although OXPHOS is reliant on oxygen tension, it has been shown that PDAC cells can efficiently oxidise glucose even under severe hypoxia (0.1% O_2) due to the assembly of mitochondrial super-complexes (125). Poor perfusion within the microenvironment combined with a high tumour load may

lead to aberrantly low nutrient concentrations. Under such conditions, extracellular lactic acidosis is protective as it provides cells with alternative fuel (lactate) when glycolytic efficiency is impaired (126).

1.2.3. Metabolic plasticity

Overall the growth success of tumours depends not only on a number of upregulated metabolic pathways which secure the energy demand for proliferation and biosynthesis but also on metabolic plasticity that allows a rapid adaptive response in case the microenvironment impacts negatively on metabolic rate. Rapid switching between pathways, stimulation of autophagy and micropinocytosis in order to recycle and scavenge extracellular intermediate substrates under limiting conditions all increase the survival of cancer cells (127, 128). This way, even when starved, cancer cells do not die immediately and can function and proliferate at a lower rate. Metabolic plasticity is a powerful tool of transformed cells that ensures their survival and is considered a main driver of immunosuppression and resistance to treatment, and needs to be addressed in order to design effective therapies. Several glycolysis and OXPHOS-targeted compounds have been proposed, which when administered simultaneously should significantly reduce the growth of cancer cells, though without targeted delivery the expected adverse effects would exceed the benefits. Such metabolic modelling of PDAC tumours on a genomic scale has been conducted in hope to help identify metabolic vulnerabilities and define efficient drug combinations, although the selected treatments have yet to be tested (129).

1.2.4. The interleukin 6 signalling in cancer

Interleukin 6 (IL6) is a pleiotropic cytokine exerting a wide range of actions. It is mostly secreted by immune cells including macrophages, monocytes and T-cells but secretion has also been shown for stromal and cancer cells (130, 131). The most recognised actions are on the immune system, as IL6 is crucial for innate and adaptive immunity and responses to pathogens (132). Although IL6 is synthesized by various cell types (132), its systemic levels physiologically are relatively low and rarely exceed the 1-5 pg/mL range (133). This can change rapidly in response to septic shock, leading to increase in IL6 measured in mg/mL (134). It is understood that IL6 manifests hormone-like properties with pleiotropic effects on insulin resistance (135), lipid metabolism (136), and even neuropsychological behaviours such as resilience to stress (137). Depending on the context, it can either promote or suppress inflammation, contributing to tissue regeneration, haematopoiesis, regulation of body weight and bone metabolism (138, 139). Apart from its physiological functions, IL6 has been implicated in the development of several auto-immune disorders including Crohn's disease, vasculitis, Castleman's and Still's disease (140, 141). Moreover, the knockout of IL6 provides the mice with complete protection against rheumatoid arthritis and multiple sclerosis (142).

The IL6 signalling cascade is activated by binding to the IL6R receptor (also referred to as IL6Rα or gp80). In the classical signalling mode, binding leads to the formation of a heterohexameric complex comprising two ligand molecules, two IL6R molecules, and two IL6 signal transducers (IL6Rβ, also called IL6ST or gp130). This, in turn, activates Janus kinases leading to phosphorylation and dimerization of signal transducer

and activator of transcription 3 (STAT3), which then translocates to the nucleus wherein it canonically binds to promoter regions regulating transcription (143). As the expression of IL6R is limited to leukocytes, hepatocytes, and some subsets of epithelial cells, the classical signalling is mostly restricted to these cell types. Unlike IL6Rα, its signal-transducing partner IL6Rβ is widely expressed (144). However, as signal transduction requires both components to interact, the classical signalling is not available in cells which lack expression of IL6R. In those, JAK/STAT3 pathway is activated via alternative trans-signalling. Here, soluble forms of IL6Rα (sIL6Rα) can be generated either by random cleavage mediated by the activity of disintegrin and metalloproteinase domain-containing protein 10 (ADAM-10, (145)) or via alternative splicing (146). sIL6Rα can associate with IL6Rβ and enable the cell to respond to IL6, even if it is not expressing the IL6Rα gene (147). While classical signalling mediates several physiological effects including anti-microbial defence, acute phase response and tissue regeneration (148), trans-signalling is considered pathological (149) with implications on inflammation (150). The overview of IL6-induced classical and trans-signalling is depicted in Figure 1.3.

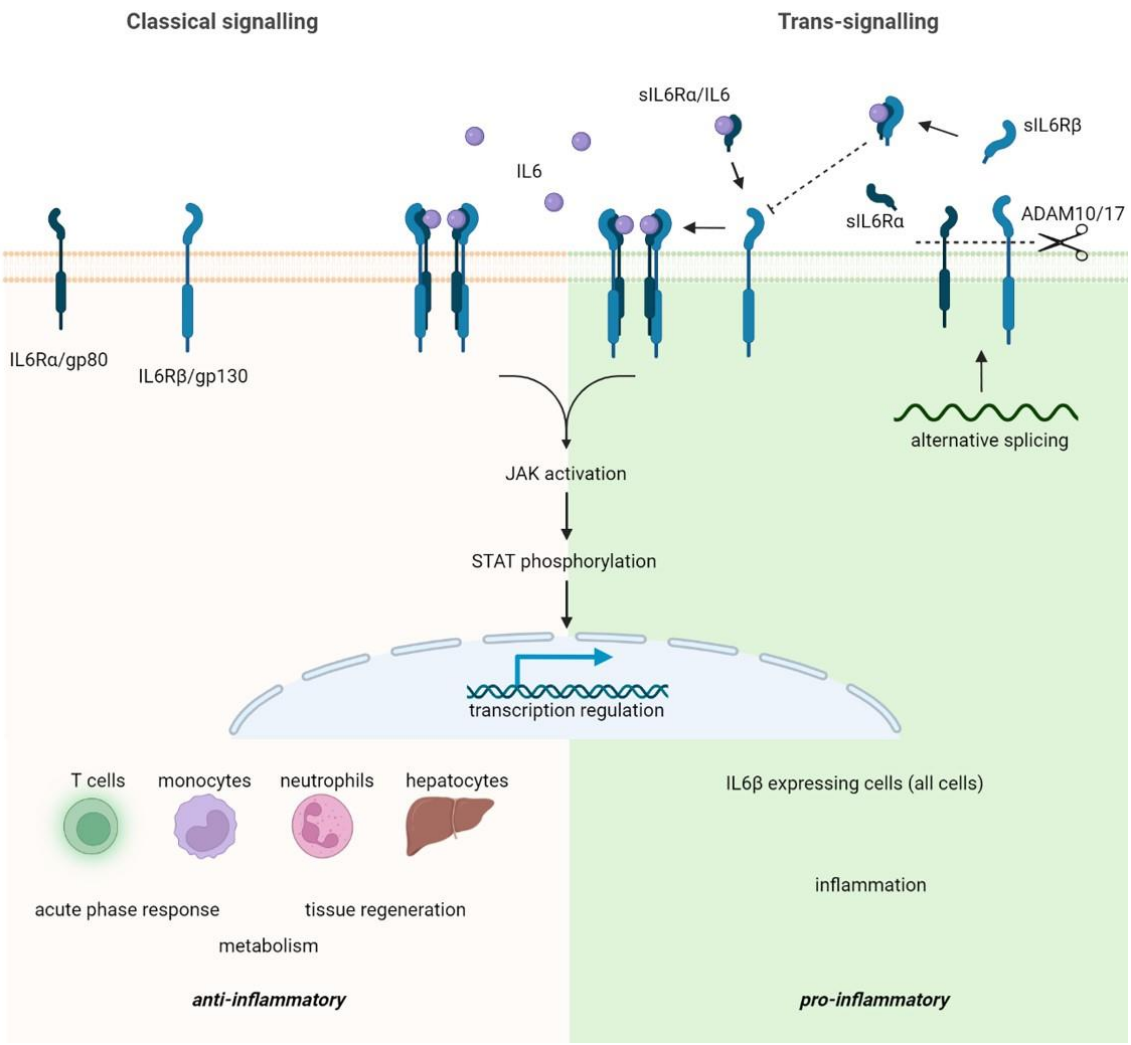


Figure 1.3 Overview of IL6-induced classical and trans-signalling. Classical signalling is limited to cell types expressing both IL6Rα and IL6Rβ, which include T-cells, monocytes, neutrophils and hepatocytes. In these cells, IL6 binds to IL6Rα, which then leads to the creation of heterohexameric complexes consisting of two molecules of ligand, IL6Rα and IL6Rβ. The dimerization activates JAK kinases, which phosphorylate STAT that in an activated state dimerizes and translocates to the nucleus where it acts as a transcriptional regulator. The classical signalling is considered anti-inflammatory and contributes to several physiological mechanisms including tissue regeneration, acute phase response and regulation of metabolism. In trans-signalling, IL6 cascade happens in cells that lack IL6Rα expression. Soluble IL6Rα (sIL6Rα) and IL6Rβ (sIL6Rβ) are generated by alternative splicing or ADAM-mediated cleavage. sIL6Rα binds IL6 and these complexes can interact with IL6Rβ expressed in all cell types activating downstream effectors. On the contrary, sIL6Rβ can scavenge IL6-sIL6Rα complexes preventing trans-signalling. Although the downstream effects of classical and trans-signalling are the same, the latter is considered pro-inflammatory and is implicated in a number of pathologies. Adapted based on (151).

Elevated serum levels of IL6 have been observed in patients with different types of cancer, including pancreatic (152), prostate (153), breast (154), ovarian (155), and head and neck (156). IL6 levels tend to increase in response to surgery or radiation (157), and often correlate with recurrence, and tumour size (158). Additionally,

the serum IL6 concentration is treated as a prognostic marker of survival (159, 160), and response to therapy (161, 162), which is probably related to its ability to induce cachexia (163, 164). IL6 signalling can trigger oncogenic transformation by initiating the hypermethylation of tumour suppressor genes (165). The main mechanism by which IL6 directly promotes tumour growth is the activation of STAT3, which increases the expression of genes implicated in survival such as Bcl-2, survivin, and Mcl-1 (166) and proliferation, by promoting cell cycle progression via c-Myc, Cyclin D1, and Cyclin B (167). In wild-type p53 cells, STAT3 phosphorylation can activate DNA (cytosine-5)-methyltransferase 1 (DNMT-1), which methylates the promoter of *TP53* leading to unrestricted growth (168). In established tumours, IL6 acts as a strong pro-angiogenic factor by increasing VEGF expression (169), and contributes to immunosuppression by decreasing the expression of major histocompatibility complex (MHC) class II on dendritic cells thus impairing antigen presentation (170, 171). Another way, in which IL6 contributes to immunosuppression, is the increased generation of myeloid-derived suppressor cells (MDSCs, (172)). Upregulated trans-signalling in metastatic ascites correlated with resistance to therapy-induced apoptosis and increased migration (173). Furthermore, IL6 was found to increase cancer stem cell population via hypomethylation of cell cycle regulators (174). IL6/STAT3 axis facilitates metastasis formation by stimulating epithelial-to-mesenchymal transition (175, 176), and priming of pre-metastatic niches (177). Although trans-signalling is considered derogatory by promoting chronic inflammation, driving immunosuppression and cancer progression, some conflicting reports describe its role in facilitating anti-tumour T cell responses (178, 179). Furthermore, IL6 was observed to promote T cell proliferation and seems to be protective against immunosuppressive actions of regulatory T cells (180).

Trans-signalling was also implicated in enhancing lymphocyte trafficking thus promoting rather than suppressing immune surveillance (181, 182). Taken together, it seems that the nature of IL6/STAT3 signalling, contrary to initial predictions, may be ambiguous and complex and cannot be oversimplified as either beneficial or damaging.

The main sources of IL6 within the tumour microenvironment are the immune cells, tumour-associated macrophages (TAMs, (183)), myeloid-derived suppressor cells (184), stroma cells and cancer cells themselves (185). Upon IL6/STAT3 activation, phosphorylated STAT3 dimers translocate to the nucleus to stimulate transcription of a number of genes, including suppressor of cytokine signalling 3 (SOCS3, (186)). SOCS3 proteins inhibit Janus kinases preventing prolonged activation of STAT3 (187), however, this effect may be abrogated by SOCS-insensitive EGF-dependent phosphorylation of STAT (188). The production and secretion of IL6 are directly stimulated by lipopolysaccharide (LPS (189)), pro-inflammatory tumour necrosis factor α (TNFα (190)), and interleukin 1α (IL-1α (191)), and can be modulated in several mechanisms, many of which comprise positive feedback (192, 193). For example, it was reported that IL6-triggered activation of STAT3 and NFκB pathways leads to the downregulation of SOCS3, thus releasing IL6/STAT3 axis from inhibition (194, 195). Additionally, activated STAT3 binds to the IL6 promoter and stimulates its expression in breast cancer model (196). Also, it was demonstrated that microRNAs suppress the IL6/STAT3 pathway on multiple levels (197-199), as they can inhibit all elements of the pathway including IL6, IL6R, JAK and STAT3 (200).

1.2.5. IL6 as a modulator of cell metabolism

Although IL6/JAK/STAT pathway has been identified as a metabolism modulator, and the IL6 is considered a 'metabolic hormone', the reported effects are often contradicting. STAT3 activation was found to promote both anabolic and catabolic branches of metabolism, depending on the context. At the systemic level, IL6 is a marker of energetic stress (201), and mobilizes energy stores by promoting lipolysis and glycogenolysis (202, 203), which can be stopped by inhibition of IL6R with tocilizumab (204). IL6 mediates the body's response to physical activity by stimulating glucose uptake due to an increase in membrane translocation of glucose transporters (205). At the cellular level, STAT3 has been reported to translocate into mitochondria and elevate oxidative metabolism in a transcription-independent mechanism (206, 207). Under oxidative stress, mitochondrial STAT3 has been shown to protect the cells from reactive oxygen species production and to desensitise them to stress-induced apoptosis (208). The IL6/STAT3 axis mediates the metabolic switch in cancer by favouring glycolysis over oxidative phosphorylation (209-211), which contributes to the evasion of apoptosis. Another way in which IL6 elevates glycolysis is by upregulating the expression of glycolytic enzymes (212, 213), and by activation of Akt downstream cascade (214). Furthermore, IL6 modulates tumour metabolism by promoting *de novo* fatty acid synthesis and stimulating β-oxidation, thus protecting the cell from nutrient-deprivation (215, 216). Although the effects of the IL6 signalling cascade on cell metabolism have been widely studied there seems to be a lack of universal understanding of the caused effects. Perhaps, it can be explained by the pleiotropic and context-dependent activity of IL6, or it might be modulated by coexisting mutations

affecting the activation of other signalling pathways, which may work either to enhance IL6-dependent effects or to suppress them. Furthermore, many systemic effects attributed to IL6 signalling might be correlative rather than causal, as in reality, the mechanisms mediated by potential STAT3 activation might be co-dependent on other pathways stimulated by IL6 such as MAPK (217), PI3K/Akt (218), or NFκB (219). For example, IL6 has been found to delay gastric emptying which is associated with a decrease in glycaemia and insulin secretion, as IL6 increases in response to exercise, it might explain how physical activity contributes to maintaining body weight (220). Another mechanism in which the IL6 axis regulates systemic glucose metabolism is the discovered increase in STAT3 activation in hepatocytes as a response to serum insulin, which decreases hepatic glucose production (203). This way, IL6 infusion in healthy individuals was found to improve insulin sensitivity mimicking the effects of exercise (205) although the results were not replicated in patients with type 2 diabetes (221). It was observed that rather than having a specific effect on glucose metabolism, IL6 regulates the secretion of several hormones including glucagon, prolactin, growth-hormone and cortisol (222, 223). Tumour-induced IL-6 impairs the ketogenic response to insufficient caloric intake, which triggers metabolic stress response that reduces the efficacy of anti-cancer immunotherapy (224). Overall, it seems that more research is needed to fully elucidate the role of IL6/STAT3 signalling *in vitro* and *in vivo*, to successfully entangle all of its effects and interactions.

1.2.6. IL6 signalling-targeted therapies

Due to the clear association between IL6 and cancer, therapies targeting this signalling axis have been designed. Several selective inhibitors of IL6/IL6R signalling have been

developed, although only one, IL6R-targeted tocilizumab, has been approved for the treatment of rheumatoid arthritis, adult-onset Still's disease, cytokine release syndrome and giant cell arteritis (225). More recently tocilizumab was approved for treatment of patients suffering from severe COVID-19 infection (226). Despite great interest in IL6 signalling effects on cancer development and progression, no IL6-based therapies have been approved in the treatment of malignancies, although several trials testing the efficiency of concomitant IL6/STAT3 inhibition and immunotherapeutic approaches are ongoing (227-234). Previously, inhibition of IL6 with siltuximab failed to improve treatment outcomes of patients with multiple myeloma (235). Other selective inhibitors affecting the downstream effectors of the IL6 pathway have also been developed. The anti-cancer effects of JAK-blocking pacritinib (236-239), itacitinib (240-242) and ruxolitinib (243-245), and STAT-targeting AZD5069 (246), IMX-110 (247), and OPB-111077 (248-250) were tested in the clinic, however, most of them failed to improve overall survival, and some were terminated due to high toxicity including the JAK2 inhibitor, AZD1480, which caused serious neurological adverse effects like ataxia and hallucinations (251). The most promising compound seems to be the JAK1/2 inhibitor, ruxolitinib, which anti-cancer efficacy is currently tested in over 80 clinical trials (252). More needs to be known about the exact interactions of the IL6/STAT pathway with the remaining cellular signalling machinery before specific treatment can be developed, as the wide range of effects mediated by IL6 creates a significant risk of serious adverse effects. Up to now the most frequently reported adverse effects of IL6/STAT3 inhibition include serious infections (253, 254), pancreatitis (225), and gastro-intestinal perforations (255), which corresponds to the signalling contributions to immunity and tissue regeneration.

1.3. Mechanisms and consequences of acidosis in PDAC

1.3.1. pH regulation at a systemic level

The pH of the blood and interstitial fluid is tightly regulated and maintained near pH 7.4 (256). This control is maintained via several mechanisms including CO_2 exchange in the lungs and tubular HCO_3^- transport in the kidney. There are several buffer systems in blood including CO_2/HCO_3^- and phosphate buffers, and proton-binding proteins like haemoglobin and albumins (257). Acid-base homeostasis is crucial in physiology and any disturbance to the balance exceeding the 7.38-7.42 range corresponds to acidosis and alkalosis respectively, and both pose a serious threat and require immediate medical attention (256).

1.3.2. Regulation of intracellular pH

At the cellular level, the intracellular pH is controlled by the activity of several transporters which can either take up or release H^+ ions, depending on concentration gradients and available substrates. As the balance of intracellular pH is affected by both cell metabolism and conditions of the microenvironment, the cell needs to be equipped with machinery to vent acid and prevent detrimental effects of over-acidified cytoplasm. Some protons can be bound by intrinsic buffers comprising phosphate groups and side chains of amino-acids (258). While the response of intrinsic buffering is rapid, it is also limited and does not have the capacity to serve as a single mechanism for maintaining pH homeostasis (259). Therefore, to maintain stable pH within the cytoplasm the activity of acid extruders and loaders is required. The primary acid-extruders include vacuolar-type electrogenic H^+-ATP hydrolases (V-type ATPases)

and H^+/K^+ ATPases, which catalyse the active export of H^+ ions, and their activity is supported by Na^+-coupled proton efflux carried out by Na^+/H^+ exchangers (NHEs (260)) and sodium-bicarbonate cotransporters (NBCs (261)). On the other hand, acid loading is mostly dependent on the activity of anion exchangers (AEs), which release HCO_3^- while importing chloride (262, 263).

1.3.2.1. Monocarboxylate transporters

Another group of transporters assisting in acid-removal are the H^+-monocarboxylate transporters, which catalyse the export of glycolytic end-product, lactic acid. MCTs co-export protons and monocarboxylates, such as lactate, pyruvate and ketone bodies, in a passive and gradient-dependent mechanism (264, 265). Although there are 14 members of the solute carrier family (SLC16) of proteins only four: MCT-1, 2, 3 and 4 were identified to catalyse the transport of monocarboxylic acids (103), while the function of the remaining ten members is not completely understood, though some have been implicated in the transport of thyroid hormone (266), and creatine (267). Although MCT-1, 2, 3 and 4 all carry the same substrates, they differ in terms of affinity to them and patterns of tissue expression. While MCT-1 expression is ubiquitous, the remaining three manifest more tissue-specific expression including the testis, ovaries and heart (268, 269). Expression of lactate-removing MCTs is upregulated in several types of cancer (270-273), probably to match the high glycolytic flux of cancer cells and protect them from metabolic inhibition. As the MCT-based transport is bidirectional, it can mediate both lactate efflux and uptake contributing to the Reverse Warburg Effect (274).

1.3.3. Acidosis in tumours

The ultimate source of chronic acidosis in tumours is cellular metabolism. Although the main source of extracellular acidity is the upregulated anaerobic glycolysis, oxidative phosphorylation can also contribute to it via the production of CO_2 and its hydration by exofacial carbonic anhydrases (CAs, (275). CAs catalyse the hydration of CO_2 forming HCO_3^- and H^+, which in case of high CO_2 production and impaired perfusion can generate significant proton levels able to influence both intra- and extracellular pH (276). As both main metabolic pathways have the capacity to create an acidic microenvironment, and in order to sustain growth cancer cells need to meet excessive energy demands, extracellular acidosis has been recognised as a hallmark of solid tumours and since then has been widely studied (277, 278). Over time several methods to measure intra-tumour pH have been exploited including pH microelectrode (279), electron paramagnetic resonance (EPR, (280)), and more recently, chemical exchange saturation transfer magnetic resonance imaging (CEST-MRI, (281, 282)). Overall the pHe within tumours manifested a wide range between 6.3–7.4, with a median value of 6.8. The specific pH values reported are listed in Table 1.1, and it seems they are greatly influenced not only by type of cancer, but also size and stage of malignancy. Although there is no single value of pH that describes the acidosis of a “typical” tumour, low pH is used in diagnostics, especially to monitor metastasis formation (283).

Table 1.1 Extracellular pH reported in tumours. Measurements methods are Chemical Exchange Saturation Transfer (CEST) Magnetic Resonance Imaging (MRI), Biosensor Imaging of Redundant Deviation in Shifts (BIRDS), Paramagnetic Chemical Exchange Saturation Transfer (PARACEST), 13C-labelled zymonic acid (ZA), Variable Radio Frequency Proton-Electron Double-Resonance Imaging (VRF PEDRI), Electron Paramagnetic Resonance (EPR), and pH microelectrode.

Model	*Method*	*pHe*	*Reference*
Breast cancer (MMTV-Erbb2 transgenic mice)	CEST-MRI	6.30-6.90	(284)
Hepatoma (McA-RH7777)	CEST-MRI	~6.80	(284)
Glioblastoma	BIRDS	6.90 ± 0.01	(285)
Bronchial tumours	pH-microelectrode	6.46 ± 0.35	(279)
Non-metastatic breast cancer (TUBO)	CEST-MRI	6.84 ± 0.03	(281)
Triple-negative breast cancer (4T1)	CEST-MRI	6.79 ± 0.02	(281)
Metastatic breast cancer (TS/A)	CEST-MRI	6.80 ± 0.03	(281)
Spontaneous lobular carcinoma (BALB-neuT)	CEST-MRI	6.96 ± 0.03	(281)
Hepatic carcinoma	CEST-MRI	6.66 ± 0.19	(282)
Hepatic hemangioma	CEST-MRI	7.34 ± 0.09	(282)
Glioma (U87)	CEST-MRI	7.00 ± 0.1	(286)
Glioma (U87)	CEST-MRI	6.60 ± 0.1	(286)
Breast cancer (MCF-7)	PARACEST-MRI	~6.50	(287)
MATB III adenocarcinoma	ZA-MRI	6.82-7.11	(288)
Breast cancer (C57Bl/6 Met-1)	VRF PEDRI	6.80 ± 0.10	(289)
Pancreatic cancer (MIA-PaCa-2)	EPR	~7.05	(290)
Pancreatic cancer (SU.86.86)	EPR	~6.90	(290)
Pancreatic cancer (Hs766t)	EPR	~6.91	(290)
Prostate cancer (LNCap)	CEST-MRI	6.78 ±0.29	(291)
Prostate cancer (PC-3)	CEST-MRI	7.23 ±0.10	(291)

1.3.4. Effects of acidity

Extracellular acidosis mediates a number of effects on cancer cells. Low pH in the microenvironment has been linked to metabolic deregulation, with stimulation of autophagy (292-294), enhanced glutaminolysis (295, 296), and lipid droplet accumulation (297). Acidity has immunosuppressive effects, mediated via prevention of T cell activation by blockade of glycolysis (298), and raising pH at the tumour site has been reported to improve response to immunotherapy (299). Additionally, the low pH of the environment was linked to decreased release of several cytokines (300) and was reported to stimulate pro-inflammatory phenotype in cancer-associated fibroblasts (301). Although many effects have been attributed to specific actions of high proton concentrations, *in vivo* low pH is most often coexistent with high lactate concentrations (lactic acidosis), and the impact of lactate on cell behaviours has gained the interest of researchers with the emerging role of lactate as a signalling molecule (302). Increased histone lactylation has been reported to contribute to cancer evasion of immune recognition by induction of M2-like gene expression in M1 macrophages (120). Extracellular lactate concentration exceeding 10 μM/g of tumour tissue has been correlated with distant metastasis (303-306). This might be at least partially explained by lactate-induced angiogenesis (307), which provides the tumour with access to the bloodstream. Additionally, extracellular lactate contributes to metabolic rewiring by stimulating glutaminolysis via HIF1α and HIF2α stabilisation (308, 309). Lactate itself is also associated with resistance to therapy by protecting cells from oxidative stress and mediating immunosuppressive actions on microenvironment (310).

1.3.5. Acidosis as a driver of cancer evolution

The concept of cancer evolution was first suggested by Nowell in 1976 (311). According to this model, cancers arise from a single, transformed cell, and the subsequent heterogeneity of tumour populations is driven by changing conditions within the microenvironment, including the administration of therapeutics. Nowell introduced the term 'selection' as a driver of aggressive behaviour, which is responsible for tumour progression (311). Cancers arise as a result of somatic evolution. As cancer incidence increases with age, some suggest that it is an inevitable 'price' the more complex organisms pay for their multicellularity and extended life-span (312). The number of somatic mutations accumulates with age and results from both random polymerase errors, and exposure to carcinogens, e.g. ultraviolet radiation (UV (313)), alcohol (314), and cigarette smoke (315). Furthermore, the mutation burden was found to correlate with disease progression (316, 317). This seems to be confirmed by a relatively low number of driver mutations in comparison to all genetic aberrations found in tumours (312). In a model of cancer evolution, the fate of cancer cells, similarly to the evolution of species, is dependent on their fitness to survive the perturbations to the microenvironment (oxygen tension, pH, nutrient availability, concentration of chemotherapeutics). Ultimately, the cells that survive are either adapted to these pressures (e.g. by altering their gene expression in response to a stressor) or have acquired resistance due to pre-existent mutation, which provides them with a proliferative advantage at limiting *testing* conditions. Ultimately what decides on selection or adaptation is the magnitude of the selection pressure. For successful adaptation, the pressure needs to be *just right*, not too strong, as it would create

a selection by eliminating the majority of unfit clones, and not too weak to have no effect. Although cells classed as unfit that do not carry advantageous mutations can be easily eliminated in the selection, if the selection pressure accumulates at a slower rate, or is lower in magnitude, the adaptive response would allow the cells to obtain resistance to the stressor, e.g. by altering their gene expression. This is a common situation, as it is the adaptation that leads to evolution of antibiotics-resistant bacteria in patients that omitted doses of medications or stopped taking them altogether, which decreases the strength of selection pressure (318, 319). This way, the high heterogeneity of tumours provides them with an advantage as irrespectively of a variety of potential pressures, it increases the chance of harbouring a clone with the capacity to survive the tests of the environment (320). Thus, extracellular acidosis is an excellent example of such a selection pressure with the capacity to cause both selection and adaptation in cancer cells, depending on the acidification rate.

1.3.6. Acidosis as a trigger of metastasis

One of the crucial factors resulting in poor prognosis in patients suffering from PDAC is the fact that most of them manifest an advanced stage of disease with distant metastasis at the moment of diagnosis (321). Metastatic spread is a hallmark of malignant cancers (322), and it is the primary reason for cancer-related mortality with over 90% of cancer-related deaths caused directly by metastasis (323). The typical metastatic sites for PDAC include the liver, peritoneum, lungs, bones and lymph nodes (1, 324) and in most cases, they are already established even if the primary tumour is still relatively small in size indicating an aggressive behaviour of pancreatic cancer.

The metastatic process is considered greatly inefficient with only 0.1% of tumour cells managing to spread (325). To successfully reach and colonize a new niche, cancer cells need to detach from the primary tumour, enter the bloodstream and escape immune surveillance in five steps including invasion, intravasation, circulation, extravasation and colonisation (326). Several studies attempted to characterize the genotype and phenotype of cells with the capacity to form metastasis in hope that targeted therapy might provide protection against the metastatic spread. Although reported results are conflicting, it was identified that cells in secondary sites manifest mutations common in PDAC such as those in *TP53* and *CDKN2A*, but also in phosphatase and tensin homolog (*PTEN*), phosphatidylinositol-4,5-bisphosphate 3-kinase catalytic subunit alpha (*PIK3CA*), and retinoblastoma (*RB1*, (327, 328)). However, there seems to be a lack of common understanding which mutations are necessary for metastasis to occur as cancers can arise from diverse cell clones (329). High expression of monocarboxylate transporter 1 was found at metastatic sites suggesting that cells with the ability to take up more lactate are more successful at colonizing new niches (330). It was proposed that extracellular lactate provides the colonising cells with protection against oxidative stress (330). Chronic extracellular acidosis is considered to be a factor that facilitates metastasis formation. Acidosis correlates with more aggressive phenotypes by modulating cell adhesion (331), increasing motility (332), and stimulating epithelial to mesenchymal transition (333, 334). Low pH is used to facilitate metastasis by migrating cells themselves, as these were found to express higher levels of acid extruders including sodium-hydrogen exchangers (NHE-1) or sodium-bicarbonate cotransporters (NBCn1), and carbonic anhydrase IX on the invadopodia (335, 336). This creates a more acidic niche directly in front of migrating cell and facilitates movement

by degradation of extracellular matrix (337, 338). Furthermore, tumour specific microbiome was recently recognised as an important driver of metastasis due to bacterial metabolism contributing to extracellular acidosis and mediating immunosuppression and resistance to therapy (339, 340). In addition to these direct effects of acidity, low pH in microenvironment acts as a selection pressure and impacts the trajectories of tumour progression (341). Although acidity has the capacity to eliminate non-adapted cells, e.g. by starving glycolysis-dependent clones, it will also select those fit to withstand harsh conditions and colonise new niches (341, 342).

1.3.7. Postprandial acidosis in pancreas

Unlike many other tumours, PDAC is unusual in the sense that its parent organ often experiences acid-shifts in the extracellular compartment during normal physiological function (343). This phenomenon may predispose the exocrine pancreas to an oncogenic transformation. The function of the exocrine pancreas is the production and secretion of digestive enzymes and large quantities of bicarbonate ions in response to the intake of food. The former are produced by acinar cells (344), and the latter by ductal cells due to the activity of carbonic anhydrases (345). The production and secretion of pancreatic juice is stimulated by the combined activity of gastrointestinal hormones (e.g. secretin, vasoactive intestinal peptide, bombesin), and cholinergic nerves (346, 347). While the enzymes are secreted by means of exocytosis, the bicarbonate ions need to be transported into the ductal lumen via several transporters including Cystic Fibrosis Transmembrane Conductance Regulator (CFTR) and SLC26A6 (348). As CFTR is crucial in this transport, any mutations harboured to its gene result in chronic pancreatitis and obstruction of the ducts, a common

situation in individuals suffering from cystic fibrosis (349). By mass-balance, apical bicarbonate secretion into the lumen must be coupled to an opposite process at the basolateral membrane, resulting in acidification of the interstitium (350). As [HCO_3^-] in pancreatic juice can reach 150 mM, the equivalent concentration of acid is released into extracellular space. In summary, ductal cells are exposed basolaterally to significant postprandial acidosis in a healthy organ, which may facilitate oncogenic transformation, or adapt cells to acidity, which would favour their survival once the tumour is formed.

1.3.8. Prevention of metastasis

A reasonable strategy to reduce the incidence of metastasis is to reduce the heterogeneity of cancer populations or eliminate factors that contribute to maintaining it. This is predicted mathematically by game theory, which states that greater phenotypic variation increases the rate of evolution, which culminates with metastasis (351). Reducing heterogeneity is a formidable challenge, as the only possible way to make tumours more homogenous would be to administer multi-targeted therapies, which in theory, should eliminate multiple populations at once. The alternative approach of removing the underlying selection pressures may be more plausible. In the case of acidosis, this could be achieved either by lessening the degree of acidity in the microenvironment, e.g. by administration of systemic buffers, or targeting the metabolism of cancers to reduce acid production. Increasing pH in tumours has been attempted before (352-354), and it shows promise as a tool for metastasis prevention, although the treatment protocols require improvement to decrease the adverse effects and improve adherence.

1.4. Rationale and aims

Despite continuing efforts to comprehensively characterize pancreatic cancer initiation and progression, relatively little improvement was made in the field of treatment outcomes. As a key end-product of upregulated metabolism, mediator of cancer progression, stimulator of metastasis, and an element of pancreatic physiology, acidity seems to be the recurring theme of PDAC development. Therefore, the primary aim of this project was to elucidate the roles of extracellular acidosis and its impact on cell behaviours. The specific aims were as follows:

i. To elucidate the metabolic sources of acidity and identify the feedback circuits controlling them;

ii. To investigate the metabolic heterogeneity and identify mechanisms maintaining it;

iii. To describe the impact of acidity on cell phenotypes and behaviours.

Taken together, these three points will contribute to the model of acid-driven evolution in Pancreatic Ductal Adenocarcinoma.

Chapter 2. Materials and methods

2.1. Maintaining in vitro cell culture

2.1.1. Cell lines

This thesis describes studies conducted on a panel of six genetically diverse Pancreatic Ductal Adenocarcinoma cell lines: AsPC-1(355), BxPC-3 (356), Colo-357, HPAC (357), MIA-PaCa-2(358) and PANC-1 (359). AsPC-1, BxPC-3, Colo-357 and PANC-1 cells were a kind gift from Prof. Anna Trauzold (University of Kiel, Germany). The MIA-PaCa-2 cell line was obtained from Prof. Alessandra Fiorio (University of Lille, France). HPAC cell line was purchased from American Type Culture Collection (ATCC). BxPC-3, HPAC, MIA-PaCa-2 and PANC-1 were derived from primary tumour, while AsPC-1 and Colo-357 cell lines were established from secondary sites, ascites and metastatic lymph node, respectively. Before commencing the experiments, the identity of all cell lines was confirmed by Short Tandem Repeat (STR) profiling.

2.1.2. Cell culture

The cells have been maintained in standard 22 mM $NaHCO_3$ containing Roswell Park Memorial Institute (RPMI) medium supplemented with 10% foetal bovine serum (FBS), 1% penicillin-streptomycin mixture (PS), 1% sodium pyruvate, 1% glutamine and 0.5% normocin. Cells were grown in monolayer, maintained in 5% CO_2 atmosphere and routinely tested for mycoplasma contamination. Cells for experiments were thawed at least a week prior and cultured for a maximum of 5 to 7 weeks.

2.1.3. Media and solutions

In this thesis, several versions of medium and solutions were used. The detailed recipes for them are listed below.

Lightly-buffered medium: D5030 medium, ddH_20, 2 mM 4-(2-hydroxyethyl)-1-piperazineethanesulfonic acid) (HEPES), 2 mM 2-(N-morpholino)ethanesulfonic acid (MES), 40 mM NaCl, 25 mM glucose, 10% FBS, 1% sodium pyruvate, 1% Glutamax, 0.5% normocin, titrated to test pH at 37°C and sterile filtered. The acid dissociation constant (pK_a) of HEPES and MES at room temperature (25°C) equals 7.55 (360) and 6.15 (361) respectively. The combination of the two within the same medium ensured low but constant buffering capacity over the physiological range of pH. When the medium was supplemented with sodium lactate (10 mM or 20 mM) the osmolality was maintained by reducing the NaCl concentration. For the experiments assessing the effects of additional exogenous buffering, the above medium formulation was adjusted by the addition of 5 mM sodium acetate, sodium propionate, sodium butyrate, sodium phosphate or imidazole and reduction in NaCl.

Highly-buffered medium: D5030 medium, ddH_20, 20 mM HEPES, 2 mM MES, 25 mM NaCl, 25 mM glucose, 10% FBS, 1% sodium pyruvate, 1% Glutamax, 0.5% normocin, titrated to pH 7.4, at 37°C and sterile filtered. For the experiments assessing the negative feedback of extracellular pH the HEPES concentration was increased to 32 mM and NaCl was reduced to 17 mM.

Mixed-buffering medium: For the experiments assessing the effects of volatile and non-volatile buffers on cell metabolism and proliferation the media were prepared as follows: D5030 powder medium was dissolved in ddH_20, 25 mM glucose,

1% glutamax, 1% sodium pyruvate, and 1% penicillin-streptomycin mixture was added and supplemented with either:

- 2.9 mM $NaHCO_3$, 41 mM NaCl;
- 2.9 mM $NaHCO_3$, 50 mM HEPES, 2 mM NaCl;
- 24 mM $NaHCO_3$, 20 mM NaCl;
- 24 mM $NaHCO_3$, 20 mM MES

The media containing 2.9 mM $NaHCO_3$ were maintained in decreased 0.5% CO_2 atmosphere, which equilibrated to pH 7.4. The media with 24 mM $NaHCO_3$ were kept under standard 5% CO_2 conditions. This step was necessary so that the buffering was manipulated (was either high or low), but medium pH was unchanged in all media variants. In the case of formulations containing both $NaHCO_3$ and HEPES/MES buffering, the non-volatile buffers were added first, and after all components were dissolved the medium was heated to 37°C and titrated to pH 7.4. Then, the respective amount of $NaHCO_3$ was added and dissolved in a closed bottle before filtering to prevent the loss of volatile buffering in form of CO_2.

Normal Tyrode's-based solutions: the main recipe for the solution was as follows: ddH_20, 135 mM NaCl, 1.5 mM KCl, 1 mM $MgCl_2$, 1 mM $CaCl_2$, 11 mM glucose, 10 mM HEPES, 10 mM MES, titrated to tested pH at 37°C

- Lactate loading solution (for permeability measurements) ddH_20, 105 mM NaCl, 30 mM NaLac, 1.5 mM KCl, 1 mM $MgCl_2$, 1 mM $CaCl_2$, 11 mM glucose, 10 mM HEPES, 10 mM MES, titrated to pH 7.4, at 37°C

Ca^{2+}-free medium for Fluorescence Activated Cell Sorting

- Lactate loading medium: 0.5L ddH_2O, 20 ml 1x RPMI amino acid mixture, 10 ml 1x RPMI vitamin solution, 0.4 g/L KCL, 0.05 g/L $MgSO_4$, 0.8 g/L Na_2HPO_4, 11 mM glucose, 20 mM HEPES, 53 mM NaCl, 60 mM sodium lactate, 0.5 mM EGTA, 1% Glutamax, 1% sodium pyruvate, 1% penicillin-streptomycin mixture, titrated to pH 7.4 at 37°C, and sterile filtered.
- Lactate free medium: 0.5L ddH_2O, 20 ml 1x RPMI amino acid mixture, 10 ml 1x RPMI vitamin solution, 0.4 g/L KCL, 0.05 g/L $MgSO_4$, 0.8 g/L Na_2HPO_4, 11 mM glucose, 20 mM HEPES, 113 mM NaCl, 0.5 mM EGTA, 1% Glutamax, 1% sodium pyruvate, 1% penicillin-streptomycin mixture, titrated to pH 7.4 at 37°C sterile filtered.

2.1.4. Adjustment of medium pH

Media and solutions containing non-volatile buffering agents (such as HEPES and MES) were titrated to test pH with NaOH and HCl and maintained in an atmosphere without CO_2. In media, in which buffering was provided by CO_2/HCO_3, the pH was manipulated by altering either the molar concentration of $NaHCO_3$ or the concentration of CO_2 in the atmosphere according to the Hendersson-Hasselbalch equation. The actual pH attained by manipulation of either element of carbonic buffer HCO_3/CO_2 was confirmed by measurements of 5-(and-6)-CarboxySNARF1-dextran (cSNARF1-dextran) fluorescence prior to commencing experiments. The osmolarity of the solutions was adjusted with NaCl and was kept at ~300 mOsm throughout.

2.1.5. *Medium buffering capacity*

To measure the buffering capacity of the lightly buffered (2 mM HEPES, 2 mM MES-containing) medium, 100 mL was heated up to 37°C and titrated to pH 5 and 8. Then, the pH change inflicted by consecutive additions of 0.5 mM acid or base (HCl or NaOH solutions) was recorded. The medium pH was plotted as a function of cumulative acid and base added to the solution and the buffering capacity was estimated as the inverse of the slope. The exemplar plot of medium buffering capacity determination is shown in Figure 2.1.

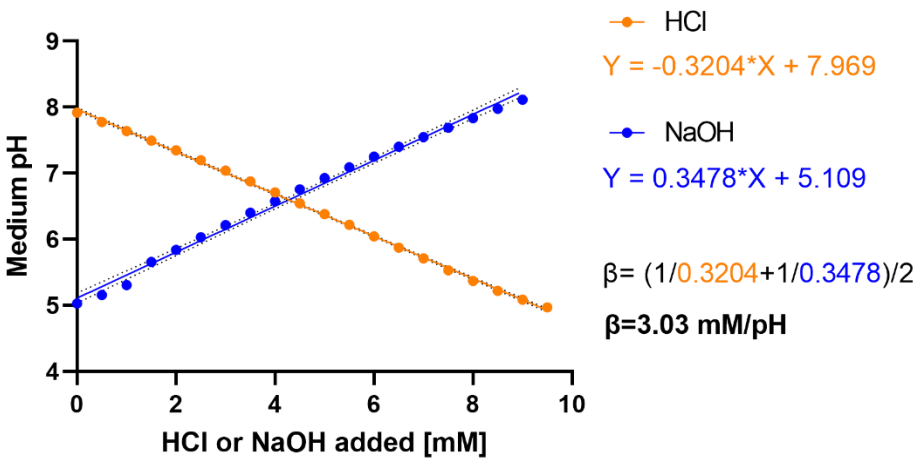


Figure 2.1 Example of medium buffering capacity determination. 100 ml of D3050-based medium containing 10% FBS, 1% PS, 1% Glutamax, 1% sodium pyruvate, 20 mM lactate, 2 mM HEPES, 2 mM MES, 25 mM glucose and 20 mM NaCl was warmed up to 37°C and the pH was recorded following the consecutive additions of 0.5 mM NaOH or HCl. The buffering capacity was calculated as 1/slope.

2.1.6. *Intrinsic buffering capacity*

The intrinsic buffering capacity was determined for a panel of PDAC cell lines using the ammonia removal method, as previously described (362). cSNARF1-loaded cells seeded in chamber slides were superfused by a sequence of HEPES-buffered solutions containing 0 mM, 20 mM, 10 mM, 5 mM and again 0 mM NH_4Cl. Increasing NH_4Cl concentration was osmotically compensated with a reduction in NaCl. Each solution

change evoked an injection of acid due to NH_4^+ deprotonation driven by NH_3 efflux. The intrinsic buffering capacity was calculated by dividing the acid concentration by measured change in pHi. The experimental protocol and data fitted to a line are depicted in Fig.2.2.

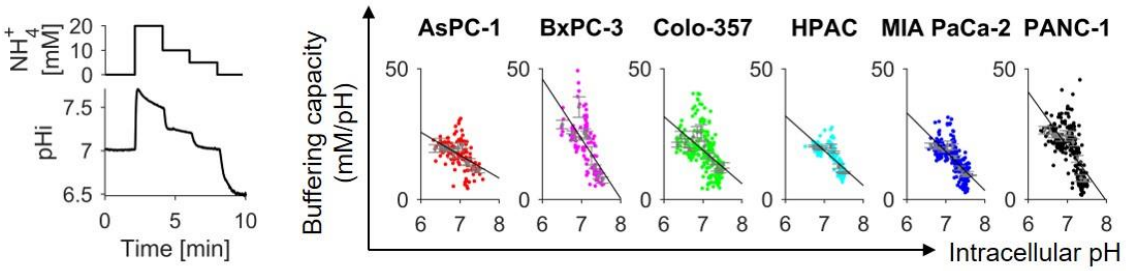


Figure 2.2 Intrinsic buffering capacity measurements. The representative plot shows the change in intracellular pH corresponding to the respective concentration of ammonium in the solution. The best fit depicting the intrinsic buffering capacity of PDAC cell lines.

2.1.7. Adaptation to acidity and selection by acid

The difference between selection by and adaptation to acidity in this Thesis is defined by the rate of pH change. To select cells by low pH, the medium was rapidly exchanged from neutral to acidic, in case of MIA PaCa-2 the pH of the acidic medium was 6.3 and for PANC-1 6.5. This level of acidity was expected to select for the fit minority of the total population ~5%, while eliminating the remaining majority. The selected cells were then maintained in cell culture for two weeks, and the medium was regularly changed every 2-3 days to prevent potential further acidification. To adapt cells to acidity, MIA PaCa-2 and PANC-1 cells were seeded at high density of 70-80% confluency and left to adhere overnight. Next day, the seeding medium was exchanged for a fresh culture medium of neutral pH 7.4. These cells were maintained in culture and allowed to acidify until a sufficiently low pH was reached. The level of acidity was judged by eye based on the colour of dissolved phenol red,

and once it resembled the colour of acidic media (pH either 6.3 or 6.5) the old medium was discarded and replaced with fresh, this time acidic, medium. Then, the cells were maintained for the remainder of two weeks with regular medium changes. This approach allows for the cells to experience acidity that is physiologically relevant and resembles *in vivo* setting, as the rate of pH change instead of being an arbitrary protocol chosen by the researcher, is dependent on the cells' own metabolism. The treatments were matched in terms of both treatment time and final pH, hence only the potential effects of the rate of pH change are being studied. The acidic medium for these experiments have been prepared by adjusting the concentration of sodium bicarbonate from 22 mM, which equilibrates to pH 7.4 in 5% CO_2-containing atmosphere, to 1.7 mM (pH 6.3) and 2.75 mM (pH 6.5). The formulation supplemented with additional non-volatile buffering, 10 mM MES were dissolved first and titrated to desired pH, then the medium was poured into the bottle, $NaHCO_3$ was added and the bottle closed until all the powder was dissolved. This step ensured that the loss of volatile buffer was minimal. The osmolality was maintained by a reduction of NaCl.

2.2. Experimental procedures

2.2.1. Assessment of the glycolytic rate

The glycolytic rate of PDAC cells was inferred from the rate of intracellular acidification following complete inhibition of all monocarboxylate transporters with α-cyano-4-hydroxycinnamate (CHC). The cells were seeded in 70% confluence in 4-chambered Lab-Tek slides and left to adhere overnight. On the day of the experiment the medium was replaced with HEPES-buffered RPMI and the cells were loaded with 8.5 µM cSNARF1 for 10 minutes. Next, the cells were superfused with normal Tyrode solution of pH 7.4 at 37°C for 1 minute to wash off cSNARF1 and culture medium residue. After the initial superfusion, the microstream was exchanged to 2mM CHC containing normal Tyrode and the time course of intracellular acidification (resulting from ongoing glycolytic activity) was recorded. The activity of Na^+/H^+ exchanger-1 (NHE-1) was inhibited by the addition of 30 µM 5-N,N-dimethylamiloride (DMA) to both solutions. The remaining, bicarbonate-dependent pH regulators were inactivated by media lacking their substrate (HCO_3^-) To ensure high accuracy and eliminate potential mixing artefact the rapid solution exchange device was used in the setup. The obtained data were analysed using ImageJ and plotted using MATLAB R2019b software.

2.2.2. H^+/lactate flux recordings

The monocarboxylate transporters carry one molecule of monocarboxylates (such as pyruvate, lactate or ketone bodies) with one H^+ in a passive, bidirectional transport across the cell membrane. As the transport involves the protons, the activity of the protein can be inferred from the change in intracellular pH. Most often

the experimental assessment of MCT permeability is based on fluorescent-lactate uptake (363), or cumulative lactate efflux into the extracellular compartment (364). The disadvantage of both these approaches is the limited information on the dynamics of the process as the time-courses are impossible to obtain. Here, time-courses of intracellular pH change resulting from lactate efflux observed in pre-loaded cells have been recorded in real-time. Additionally, the experimental setup based on a rapid solution switching device, which allows for solution exchange within 25 ms, eliminated the possible mixing artefact improving the accuracy of the recordings. First, the cells were seeded in Lab-Tek 4 chamber slides to reach optimal 70% confluence the next day. On the day of the experiments, the standard culture medium was removed for HEPES-buffered RPMI and the cells were loaded with 8.5 µM cSNARF1 for 10 minutes at room temperature. Next, the cells were superfused with 30 mM lactate-containing normal Tyrode- based solution of pH 7.4 for 5 minutes at 37°C to allow the cells to equilibrate and take up lactate. Next, using the rapid solution switching device, the lactate-free solution of tested pH (5.7- 7.8) was administered for 2 minutes and the time-course of intracellular alkalinisation was recorded until it reached the steady-state. Then, the lactate-containing solution was reintroduced until the intracellular pH acidified to initial levels. To assess the effect of MCT inhibition on the permeability the MCT-1 inhibitor SR13800, the MCT-1/2 inhibitor AR-C155858 (1 µM; 4960, Tocris) and MCT4/1 inhibitor syrosingopine (1 µM and 10 µM; SML1908, Merck) were added to both microstreams to maintain stable inhibition throughout the experiment. The obtained recordings were analysed in ImageJ and the data analysed using MATLAB R2019b software.

2.2.3. Glucose uptake measurements

To assess the pH sensitivity of glucose uptake, cells were seeded onto µ-Slide 4 well slides and left to adhere overnight. Before the experiments, the $NaHCO_3$-buffered medium was removed and replaced with HEPES-buffered RPMI. The slides were placed on the stage of the Leica LCS confocal microscope and the superfusion system was attached. Then, the cells were superfused with HEPES-buffered normal Tyrode solution until all medium was removed and loaded with 50 µM fluorescent glucose analogue, 2-(N-(7-Nitrobenz-2-oxa-1,3-diazol-4-yl)Amino)-2-Deoxyglucose (2-NBDG) and 1 µM Cell Tracker Deep Red for 15 minutes over the range of pH from 7.8 to 5.7. After the incubation period, the excess dye was washed off by perfusion, and the fluorescence was imaged in several fields of view within 2 minutes. The fluorescence was excited at 488 nm (2-NBDG) and 633 nm (Cell Tracker Deep Red) and collected at 520 nm and >650 nm for each of the dyes, respectively. The uptake of 2-NBDG in Cell Tracker-positive cells was quantified using ImageJ and the graphs were plotted in MATLAB R2019b software.

2.2.4. Seahorse assay

The pH sensitivity of extracellular acidification rate (ECAR) and oxygen consumption rate (OCR) was assessed in a panel of six PDAC cell lines using the Seahorse Analyzer. The experiments using Seahorse Analyzer were conducted thanks to the courtesy of Prof. Adrian Harris and Dr. Christos Zoiss (Weatherall Institute of Molecular Medicine, University of Oxford) and Prof Richard Wade-Martins and Dr. Brent Ryan (Department of Physiology, Anatomy and Genetics, University of Oxford). The cells were seeded on Seahorse 96-well plates at 25,000 per well and left to adhere overnight. The Seahorse

cartridge was hydrated with 200 µL hydration solution and incubated at 37°C in a CO_2-free atmosphere overnight. On the next day, the medium was changed to lightly buffered (2 mM HEPES, 2 mM MES), phenol red, FBS and antibiotics-free formulation and the acidic and alkaline media were added to the injection ports. The baseline levels of ECAR and OCR were measured for initial 30 minutes and then the acidic medium was injected creating stepwise acidification, followed by alkaline injection which restored the original, neutral pH. The measurements were taken for 30 minutes at each step of the assay including baseline, post-acidic and post-alkaline injection at 5-minute intervals. The control wells were injected with the neutral pH medium twice. The pH-sensitivity curves were plotted in MATLAB R2019b software.

2.2.5. The time-course measurements of metabolic acid production

The time-course of extracellular acidification has been assessed by seeding cells at high density (50,000/well) on a black 96-well plate and left to adhere overnight. Next, the culture medium was discarded and the residue removed by washing twice with a lightly buffered medium formulation (2 mM HEPES, 2 mM MES). The combination of high cell density, low medium buffering and low volume facilitated extracellular acidification. Next, the cSNARF1-dextran was dissolved in phenol red-free lightly buffered medium to a final concentration of 12.5 µg/mL and 100 µL was added to each well. The plate was then put in a pre-heated Cytation reader and fluorescence was excited at 555 nm and collected at 590 and 640 nm every 30 minutes for 17 h. The ratio of cSNARF1-dextran fluorescence was recalculated into pH units based on previously obtained calibration values and the graphs were plotted in MATLAB R2019b software.

2.2.6. *Lactate production assay*

After 17 h incubation, the medium was collected and frozen at -80°C to deactivate L-lactate dehydrogenase prior to lactate measurements on a YSI 2500 Biochemistry Analyzer (525000, Xylem) or ABX Pentra C400 Analyzer (Horiba). The experiments using ABX Pentra C4000 were conducted thanks to the courtesy of Prof. Samira Lakhal-Littleton and the assistance of Dr. Goran Mohammad.

2.2.7. *High-throughput intracellular pH imaging*

The intracellular pH of PDAC cell lines was measured according to a previously published high-throughput assay (365), the cells were seeded onto Ibidi 96-well µ-plates at 50% confluency. On the next day, the culture medium was removed and the cells were loaded with cSNARF1 at 8.5 µM and Hoechst 33342 at 16.5 µM for 15 minutes at 37°C. Then, the medium was discarded and the plates washed twice with pre-equilibrated $NaHCO_3$-buffered medium of varying $NaHCO_3$ concentration (0 mM - 44 mM). Then, the cells were imaged using Cytation Biotek at 37°C and 5 % CO_2 the images were analysed using MATLAB R2019b software.

2.2.8. *Cell proliferation assay*

Cell proliferation was assessed using sulforhodamine B colourimetric assay (366). The cells were seeded onto transparent 96-well plates at optimal density and left to adhere overnight. Next, the standard culture medium was replaced with 200 µL of experimental medium containing 44, 22, 11, 5.5, 2.75 or 0 mM $NaHCO_3$, which at 5% CO_2 conditions equilibrates to the pH of 7.71, 7.45, 7.21, 6.90, 6.72 and 6.32 within 30 minutes. The cells were treated with media of decreasing pH for one week, after

which, they were fixed using 100 µL of 10% trichloroacetic acid and incubated for 1h at 4°C. Next, the cells were washed four times with water and the residual liquid was removed by tapping the plates on the tissue paper. Then, the cells were stained with 100 µL sulforhodamine B solution (0.057% in 1% acetic acid) at room temperature for 30 minutes. The residue of the stain was removed by washing four times with 200 µL of 1% acetic acid and the plate was left to air dry. Finally, the sulforhodamine B crystals were dissolved in 200 µL tris(hydroxymethyl)aminomethane and the absorbance was measured at 520 nm on Cytation 5 (Biotek, Agilent). For the analysis background absorbance was subtracted and the pH-sensitivity curves of cell growth were plotted using MATLAB R2019b or GraphPad Prism software.

2.2.9. Metabolic phenotype assay

The developed method of metabolic phenotyping of adherent cancer cells is described in detail in Chapter 3 of this thesis. The assay uses two fluorescent dyes 8-Hydroxypyrene-1,3,6-trisulfonic acid trisodium salt (HPTS) and Tris(2,2'-bipyridyl)dichlororuthenium(II) hexahydrate (RuBPY), which report extracellular pH and dissolved oxygen in a 96-well plate covered with a layer of mineral oil. The addition of the oil on top of the culture medium creates a semi-closed compartment and forms a diffusive barrier for oxygen, which is essential for the functionality of the assay, as unrestricted access of oxygen would quench the fluorescence of RuBPY. Briefly, the cells were seeded onto black 96-well plates at high density (30,000 - 100,000 per well) to facilitate acidification and left to adhere overnight. On the day of the experiment, the culture medium was removed and for assessment of cells which adherence might vary (e.g. cells adapted to or selected by acidity)

the plates were pre-coated with poly-lysine prior to seeding, and once attached, stained with Cell Tracker Orange at 25 µM at room temperature for 10 minutes. Then, the medium was removed and the residue was washed off twice with PBS. Finally, 100 µL of lightly buffered medium (2 mM HEPES +2 mM MES) with the dyes at a final concentration of 2 mM and 50 mM for HPTS and RuBPY respectively was added to the wells, which were then covered with a 150 µL layer of mineral oil. The fluorescence of the dyes and cell tracker orange was excited at 400 and 460 nm (HPTS), 416 and 450 nm (RuBPY), 560 nm (Cell Tracker Orange), and collected at 510 nm (HPTS), 620 nm (RuBPY) and 580 nm (Cell Tracker Orange) every 10 minutes for 17 hours. The obtained data were analysed using MATLAB R2019b software and the detailed description of the analysis can be found in Chapter 3.

2.2.10. Flow cytometry and Fluorescence Activated Cell Sorting

Fluorescence Activated Cell Sorting (FACS) was used to collect cell populations depending on their MCT permeability. The experiments were conducted in Flow Cytometry Facility at Sir William Dunn School of Pathology (University of Oxford) with the help of Dr. Robert Hedley and Ms. Vasiliki Tsiologa. Cells were seeded on 15 cm dishes and cultured for 1 week prior to sorting, next the cells were trypsinised, counted and resuspended in standard culture medium at 10 mln/ml concentration and aliquoted into several tubes. The cells were loaded with cSNARF1 at 8.8 µM at room temperature for 10 minutes, then centrifuged at 1000 *g* for 1 minute after which the medium was replaced with 60 mM lactate solution. The cells were allowed to take up lactate for 5 minutes then they were centrifuged again, and the lactate-containing solution was replaced for lactate-free, the cells were then filtered through a cell strainer

snap cap and sorted immediately based on their intracellular pH for 5 to 10 minutes maximum. The dead population stained with DAPI (4',6-diamidino-2-phenylindole) and cell doublets were excluded in the gating. cSNARF1 fluorescence was excited at 561 nm and collected at 582 and 670 nm. As expected from previous experiments, the high-permeability MCT fraction did not exceed 5% of the total population of MIA PaCa-2 cell line and its presence was transient and disappeared within first 10 minutes from the beginning of the sorting. The cells were sorted based on their MCT permeability into two extreme populations of low and high activity of the transporter and either seeded for metabolic phenotype assessment after 24 h, 1 and 2 weeks after sorting or used for RNA extraction. The overview of sorting protocol is shown in Figure 2.3.

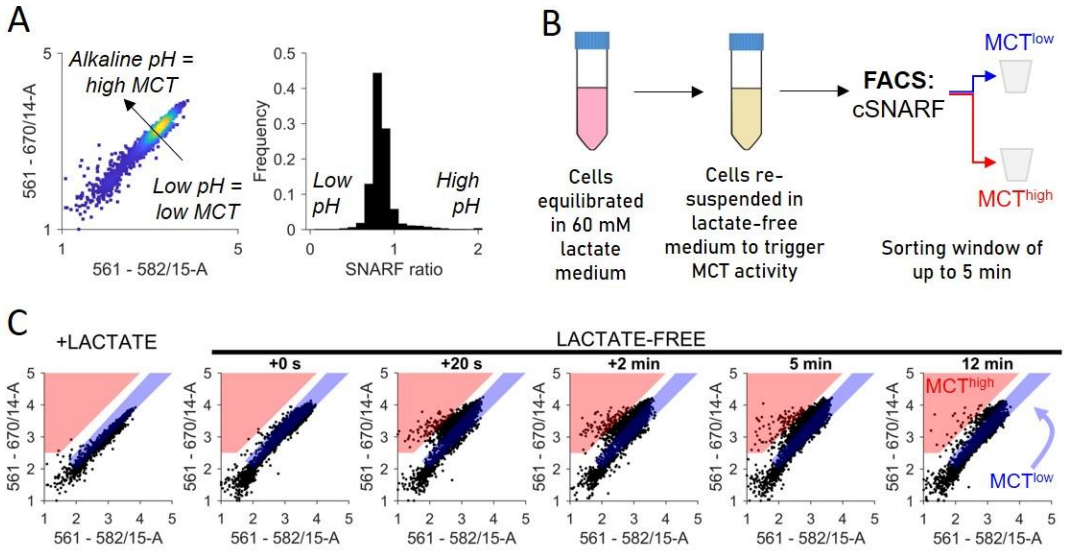


Figure 2.3 Protocol created to sort cells according to their MCT permeability. A: Exemplar dot plot of cells analysed by their intracellular pH (cSNARF1), showing narrow distribution under resting conditions (CO_2/HCO_3^- free buffer ensures stable extracellular pH). B: Protocol for sorting cells according to P_{MCT}. Cells were first equilibrated in high lactate medium (60 mM) to induce lactate uptake and then medium was promptly replaced with a lactate-free solution for sorting. C: Exemplar recordings of cSNARF1 fluorescence before and during lactate-efflux, depicting transient alkaline MCT-high population (pink-shaded).

For extracellular antigen (IL6R) staining the cells were trypsinised, counted and aliquoted into several tubes of 5 mln/ml concentration. Then, the cells were centrifuged at 300 g for 5 minutes and washed twice in an ice-cold Staining Solution. The non-specific binding was blocked by incubation with Human TruStain FcX™ for 5 minutes at room temperature. Next, the supernatant was removed and cells were incubated with 5 µL of PE-conjugated anti-human CD126 (IL6Rα) antibody, or PE-conjugated mouse IgG1 isotype control suspended in 100 µL of 3% FBS in PBS at 4°C, in the dark for 45 minutes. After staining, the cells were washed twice with ice-cold 3% FBS in PBS, the supernatant was removed and the cells were resuspended in 1 ml of 10% FBS in PBS and sorted immediately. The dead, DAPI-stained cells and cell doublets were not included in the gating. The cells were sorted based on the IL6R fluorescence into positive and negative populations and maintained in culture for metabolic phenotype assessment after 24 h, 1 and 2 weeks after sorting. For simultaneous staining of intra- and extracellular antigens (IL6R and STAT3 respectively) cells treated with 1 µM marimastat (Cayman Chemical Company, #14869), 0.5 µM napabucasin (Cayman Chemical Company, #22255) and untreated controls were collected and washed twice with the staining solution. First, the viable cells were stained for surface-bound IL6R. To avoid staining any intracellular proteins, the permeabilization step was omitted and the cells were blocked by adding 5 µL of Human TruStain FcX™ and incubating for 10 minutes at room temperature. Next, the cells were incubated with primary antibody against IL6R (1:100, Proteintech, #23457-1-AP) suspended in 3% BSA in PBS for 30 minutes at room temperature. Then, the remaining antibody was washed off twice with a staining solution prior to 30 minutes incubation with a secondary antibody

(anti-rabbit Alexa Fluor 488-cojugated, 1:1000, Invitrogen, #A32731). Next, the cells were washed with the staining solution and fixed by adding 4% cold paraformaldehyde for 15 minutes at room temperature, washed twice with PBS and permeabilised with 0.5% Triton-X in PBS for 15 minutes at room temperature. The non-specific binding was blocked by 30-minute-long incubation with 3% BSA dissolved in PBS, followed by incubation with a primary antibody raised against STAT3 (1:200, Cell Signalling, #124H6). Next, the samples were washed twice with PBS and incubated in the dark with a secondary antibody for 30 minutes at room temperature (1:1000, anti-mouse Alexa Fluor 594-conjugated, Invitrogen, #A21201). If the samples were measured immediately, the cells were washed twice and resuspended in PBS. For short-term storage of up to 3 days, the samples were washed, resuspended in the staining solution and kept at 4°C protected from the light with tin foil. The expression of IL6R and STAT3 was measured using a BD Fortessa flow cytometer (Dunn School of Pathology), the fluorescence of the fluorochromes was excited at 488 and 561 nm and the emission was measured at 530 and 610 nm. The obtained data were analysed with FlowJo software.

2.2.11. Live cell imaging

To confirm the viability of collected subpopulations, cells sorted by FACS according to their IL6R expression were seeded onto Ibidi 8-well µ-slides. The cells were left to adhere overnight, and loaded with calcein (4 µM, C3100MP, Invitrogen), Hoechst 33342 (1 mg/mL, H3570, Invitrogen) and MitoTracker Red (1 µM, 1 min, M7512, Invitrogen) the next day. The fluorescence of calcein, Hoechst and MitoTracker

was excited at 488 nm, 405 nm and 555 nm, respectively and imaged sequentially at 525 nm, 490 nm and 640 nm using Zeiss LSM 700 confocal microscope.

2.2.12. Enzyme-linked immunosorbent assay

The production of interleukin-6 in PDAC cell lines was measured by enzyme-linked immunosorbent assay (ELISA). First, the cells were seeded into the 10 cm dishes and left to adhere overnight. The next day, the medium was changed and the cells washed with PBS to remove cell debris. The cells were allowed to grow for 3 days prior to collection. Then, the cells were detached, washed in PBS and the cell pellets were suspended in radioimmunoprecipitation assay (RIPA) buffer containing protease and phosphatase inhibitors (Roche 62 cOmplete ULTRA protease inhibitor cocktail, #5892953001; Roche PhosSTOP phosphatase inhibitor cocktail, #4906845001) and lysed for at least 30 minutes on ice. Then, the samples were centrifuged at maximum speed (13,000 *g*) for 15 minutes and the prepared lysates were transferred into clean tubes. The protein concentration in prepared samples was measured using the Pierce BCA Protein Assay Kit (Thermo Scientific, #23227) according to the manufacturer's protocol. 40 µg of protein was added per well of high absorption 96-well plate and dried at 37°C overnight. The next day, the plate was washed twice with 100 µL PBS with 0.05% Tween and blocked with 3% BSA in TBST for 2 hours at room temperature. The primary antibody against IL-6 (#21865-1-AP, Proteintech) was diluted 1:400 in 1% BSA in PBST and added to the plate for 1 hour at room temperature. Then, the plate was washed three times with PBST and incubated with HRP-conjugated secondary antibody (anti-rabbit, #G21234 Invitrogen) at 1:7000 dilution for 1 hr at room temperature. After the incubation period, the plate was washed four times and the remaining fluid

was removed by tapping against tissue paper. For detection of IL6, 100 µL of development agent was added per well. After 90 seconds the reaction was stopped by 100 µL stop solution and the colour intensity was measured at 590 nm on Cytation 5 plate reader.

2.2.13. Immunofluorescence

For immunofluorescent staining, 100,000 cells were seeded onto 12-well Ibidi chamber slides and left to adhere overnight. The next day, the medium was removed and the cells were fixed by the addition of 100 µL 4% cold paraformaldehyde solution for 15 minutes at room temperature. The fixative was removed and the cells washed off three times with PBS. The non-specific binding was blocked by 1-hour incubation with 3% bovine serum albumin (BSA) in PBS at room temperature. Next, the cells were incubated with a primary antibody dissolved in 3% BSA for 1.5 h at room temperature. The list of primary and secondary antibodies is shown in Table 2.1. Before incubation with fluorophore-conjugated secondary antibodies, the sample was washed three times with PBS. Next, the cells were loaded with Hoechst for 1 minute at room temperature and the slide was sealed with a mounting medium and left to dry off before imaging. The permeabilization step was omitted on purpose to make sure only the surface-expressed proteins are stained.

Table 2.1 List of antibodies used for immunofluorescent staining

Target	Dilution	Host	Max Excitation/Emission	Supplier	Catalogue number
IL6R	1:200	rabbit	NA	Proteintech	23457-1-AP
STAT3	1:1000	mouse	NA	Cell Signalling	124H6
Alexa Fluor 488 anti-rabbit	1:7000	goat	490 nm/525 nm	Invitrogen	A32731
Alexa Fluor 555 anti-mouse	1:7000	goat	555 nm/580 nm	Invitrogen	A32727

2.2.14. *In vivo xenograft experiments*

All animal procedures conducted in this project followed The Animals (Scientific Procedures) Act 1986 and were authorised by Project License no. PPL P01A04016. To assess the levels of cell heterogeneity *in vivo*, six female athymic Nude Crl:NU(NCr)-Foxn1nu mice received a subcutaneous injection of MIA PaCa-2 cell suspension. The cells were resuspended in 100 µL of a 1:1 mixture of Matrigel and serum-free DMEM medium before injection. Each mouse was injected with 2 million MIA PaCa-2 cells on the left flank by Dr. Stefania Monterisi. Mice were weighed and tumours were measured 3 times a week. The animals were sacrificed when the tumour size reached the humane endpoint, and the tumour samples were collected into PBS and processed for immunohistochemical analysis. First, the samples were washed twice in PBS and fixed by incubation in 4% formalin solution at 4°C for 24 h. Next, the tumours were embedded in paraffin and cut into 4 µM sections by Ms. Roisin McMorrow at Erasmus Medical Centre (Rotterdam).

2.2.15. *Immunohistochemistry*

First, the sections were deparaffinised by incubation in xylene (two 5-minute incubations) and rehydrated by immersing the samples in the range of ethanol solutions of decreasing alcohol concentrations (100%, 100%, 95%, 70%, 50%) and then briefly washed in deionised water. Next, the sections were subjected to heat-induced epitope retrieval by boiling in sodium citrate solution titrated to pH 6 for 20 minutes. After the solution cooled down the samples were removed and rinsed in deionised water for 5 minutes. Then, the cells were permeabilised by 10-minute incubation with 0.2% Triton-X in PBST and washed in dH_2O. The tissue was circled with hydrophobic

pen and the sections were washed twice with PBST. The non-specific binding was blocked by incubation with a mixture of 2% bovine serum albumin and 0.3 M glycine dissolved in PBST for 1 hour at room temperature. After blocking, the tissue was incubated with a combination of primary antibodies against IL6R (Proteintech, #23457-1-AP, rabbit 1:100) and STAT3 (Cell Signalling, 1:500) suspended in 1% BSA/PBST solution for 1 hour at room temperature. After that, the samples were washed three times in PBST (5 minutes each) and incubated with fluorophore-conjugated secondary antibodies (1:1000) for 1h at room temperature (Alexa Fluor 488 anti-rabbit, Alexa Fluor 555 anti-mouse, Invitrogen, #A32731 and #A32727, respectively). Finally, the sections were washed in PBST, and then in PBS and the nuclei were stained by 10-minute incubation with Hoechst 33342 (1:1000). The samples were rinsed in deionised water, gently dried and mounted with coverslips using Prolong Diamond antifade mounting solution. The mounted sections were allowed to dry overnight and were kept in the dark, in an opaque box prior to imaging.

2.2.16. RNA isolation

The RNA for sequencing and RT-qPCR was extracted using a column-based RNeasy Micro Kit (Qiagen) according to the manufacturer's protocol. Once eluted, the RNA samples were stored at -80°C for future experiments. Freeze-thaw cycles were avoided. Nucleic acid quality control (by A260/A280 ratio) was performed using spectrophotometry.

2.2.17. RNA Sequencing

To identify the underlying causes for a differential metabolic profile of MIA PaCa-2 subpopulations, these were sorted according to their MCT activity, as described

in Section 2.2.16 *Flow cytometry and Fluorescence Activated Cell Sorting* and the RNA of each subpopulation was extracted. The purity and concentration of RNA was confirmed by NanoDrop™. The 500 µg of each sample was submitted to Oxford Genomic Centre for library preparation and RNA sequencing. Briefly, the mRNA fraction was selected from the total RNA and then converted to cDNA. Second strand cDNA synthesis incorporated dUTP. The cDNA was end-repaired, A-tailed and adapter-ligated. Prior to amplification, samples were digested with uridine. The prepared libraries were size selected, multiplexed and their quality was checked before paired-end sequencing. Data were aligned to the reference human genome. The obtained data were analysed in MATLAB using the DESeq2 package (367).

2.2.18. RT-qPCR

cDNA was prepared using iScript cDNA Synthesis Kit (Bio-Rad) according to the manufacturer's protocol. Quantitative reverse transcription PCR was conducted in technical triplicates using specific primer pairs and the Brilliant III Ultra-Fast SYBR® Green qPCR Master Mix (Agilent) on an AriaMX Real-Time qPCR Instrument (Agilent, Department of Oncology). Results were expressed as mean fold change compared with control using the $\Delta\Delta C_t$ method (368), from four biological repeat experiments. The expression of glyceraldehyde-3-phosphate dehydrogenase (GAPDH) and SNW Domain Containing 1 (SNW1) were used for internal calibration. The full list and sequences of primers used is presented in Table 2.2.

Table 2.2 Sequences of primer pairs used in RT-qPCR experiments

	Forward	*Reverse*
EFNB2	ATGCAGAACTGCGATTTCCA	GTCCTTGTCCAGGTAGAAATTTGG
IL6R	CCCCACTCCTGGAACTCATC	GGAGGTCCTTGACCATCCAT
FOXJ1	GTGGGAGCAACTTCTTCCAGA	ATAAGTATGTGGTGCCTGGCT
NFATC2	AGACGAGCTTGACTTCTCCA	TGCATTCGGCTCTTCTTCGT
USP38	CCAGAGGCGTTCCATTTGATTG	GCTGTACTTGAAGGCAGACCA
BAG3	AAACAGTGTGGACAGGTGGC	GGAGACTGGGACCGCTCA
PDP1	TGGAAAGAGCGCCGAGC	CTTCTGACTGGGATTCCGGG
HBEGF	AGGAGAGGAGGTTATGATGTGGA	CCAGCCGATTCCTTGAGCA
IL6ST	GTGAGTGGGATGGTGGAAGG	ACTTGTGTGTTGCCCATTCAG
SLC16A1	CCACCACTTTTAGGTCGGCT	ATTAGGACGACGCCACATGC
GAPDH	TCGGAGTCAACGGATTTGGT	TGAAGGGGTCATTGATGGCA
SNW1	GTATCACAGAAGGTCGCCGC	GCCACTCCTTGCTGAGATGG

2.2.19. Western blotting

Cells were grown in 10 cm dishes for 3 days, trypsinised and washed twice in PBS. For the assessment of monocarboxylate transporters' expression, the cell pellets were lysed with RIPA buffer containing protease and phosphatase inhibitors for 30 minutes on ice. Then, the samples were sonicated 3 times for 10 seconds each. The cell debris was removed by centrifugation at 12,000 *g* for 20 minutes at 4°C. The protein concentration in prepared samples was measured using the Pierce BCA Protein Assay Kit (Thermo Scientific, #23227) according to the manufacturer's protocol. Briefly, the samples were diluted 10x and the serial dilution of albumin standard was added to 96-well plate. The BCA reagents were mixed in a 50:1 ratio and the mixture was added to the wells, after which the plate was incubated for 30 minutes at 37°C. Absorbance was read at 562 nm. Protein concentration was assessed using a standard curve

generated by plotting albumin concentration against absorbance at 562 nm. The samples for the SDS page were prepared by the addition of 2x or 4x concentrated Laemmli buffer containing β-mercaptoethanol and loaded into 12.5% or 15% polyacrylamide resolving gel. The proteins were separated by size via electrophoresis at 120 V for 60-90 minutes. The proteins were transferred into the methanol-activated polyvinylidene fluoride (PVDF) membranes during electrophoretic wet-transfer at 70 V for 90 minutes. Next, the non-specific binding was blocked by incubating the membranes in 5% milk diluted in TBST (20 mM Tris-base, 137 mM NaCl, 0.1% Tween) at room temperature for 60 minutes. The primary antibodies we dissolved in 3% milk in TBST with 0.03% sodium azide and kept at 4°C for short-term use, or frozen at -20°C. The membranes were incubated with the primary antibodies at 4°C overnight unless stated otherwise. Before adding secondary antibodies, the membranes were washed three times with TBST for 5 minutes at room temperature. The incubation with HRP-conjugated secondary antibodies lasted 60 minutes, after that, the membranes were washed with TBST three times for 20 minutes. The protein bands were imaged using an imaging system (ChemiDoc, Bio-Rad) using enhanced chemiluminescence substrate (ECL, Bio-Rad). The detailed list of used antibodies is presented in Table 2.3.

Table 2.3 List of antibodies used for western blotting.

Target	Dilution	Host	Supplier	Catalogue number
MCT-1	1:500	rabbit	Millipore	#AB3538P
MCT-2	1:4000	rabbit	Proteintech	#20355-1-AP
MCT-4	1:1000	rabbit	Millipore	#AB3316P
HIF-1α	1:1000	mouse	BD Biosciences	#610958
IL6R	1:1000	mouse	Santa-Cruz Biotechnology	#sc-373708
STAT3	1:1000	mouse	Cell Signalling	#124H6
GAPDH	1:6000	mouse	Proteintech	#HRP-60004
β-actin	1:5000	mouse	Proteintech	#HRP-60008
anti-mouse HRP-conjugated antibody	1:10000	goat	Invitrogen	#G21040
anti-rabbit HRP-conjugated antibody	1:10000	goat	Invitrogen	#G21234

2.3. Image processing and analysis

2.3.1. Image processing

Prior to the analysis images collected during the flux and glucose uptake recordings were processed using Fiji software (369). To analyse data at a single cell resolution regions of interest (ROI) marking separate cells were drawn and the mean grey values for selected ROIs were measured. The numerical data were then analysed in MATLAB.

2.3.2. MATLAB scripts

All MATLAB scripts used in this thesis were written by Prof. Pawel Swietach.

2.3.3. Statistical analysis

The number of observations in this Thesis is reported as “n/N”, indicating the number of cells or wells and the number of biological repeats. Statistical significance between the two groups was determined with an unpaired t-test. A one-way analysis of variance (ANOVA) was used to assess the significance between three groups with post-hoc multiple comparisons analysis. At least three biological repeats were performed (i.e. from an independent cell passage), with at least three technical repeats each (i.e. concurrent measurements from the same yield of cells, but treated separately with drugs, e.g. in a separate well. Summary statistics are shown as mean ± SEM unless stated otherwise. The threshold level of significance for all tests was 5%. The significance was marked on figures with asterisks as follows: * $p < 0.05$, ** $p < 0.01$, *** $p < 0.001$, **** $p < 0.0001$. Detailed information about the statistical tests used is described in the legend for each corresponding figure.

Chapter 3. Developing a cost-effective method for phenotyping the metabolic profile of PDAC cells

Cellular processes are fuelled by two main energetic pathways, the glycolytic and oxidative metabolism. Both play a crucial role in cancer, as they are essential for tumour formation and growth, thus favouring the progression of the disease. However, these two energetic pipelines differ in terms of the ATP yield (with glycolysis being 17-fold less efficient than oxidative phosphorylation) and the optimal conditions (like oxygen tension and extracellular pH) which influence the metabolic trajectory. Due to these continuous changes in the microenvironment cancer cells will fluctuate their dependencies on glycolytic and respiratory metabolism, which will be influenced by both their immediate microenvironment (localisation within the tumour) and the metabolic history of adjacent cells. However, these processes take time. Longer periods of time might be required for the gas gradients to form and for protons to accumulate in the extracellular space, therefore short-term experiments, which describe cell metabolism over minutes or even hours might be insufficient. Hence, is it of vital importance to assess these two pathways simultaneously in order to adequately study the dynamics of metabolic profiles in cancer cells, which are influenced by changes within the microenvironment. In this Chapter, a novel, high-throughput and cost-effective method for reporting the balance between glycolytic and oxidative metabolism in adherent cells is described.

3.1. Introduction

Deregulated metabolism has been recognised as an important hallmark of cancer as tumours evade physiological control mechanisms which enables their unrestricted growth (322). Currently, there is a range of methods available to assess cell metabolism. Unfortunately, the recordings they offer are often limited and tend not to adequately represent the culture conditions due to required alterations to routinely used culture media and solutions. One of the most frequently used pieces of equipment designed to assay cellular metabolism is the Seahorse Analyzer, which reports the Extracellular Acidification Rate and Oxygen Consumption Rate as a readout of glycolytic and oxidative metabolism, respectively (370-373). However, in order to assay the metabolism using this device, all protein-bearing medium ingredients need to be omitted, to avoid the risk of clogging the instrument (374). This alone significantly reduces the utility of Seahorse as a measure of cell metabolism under culture conditions. The lack of foetal bovine serum, even only for the duration of the assay, may have a serious impact on cell biology and limit the meaning of the obtained data (375, 376). Other approaches include commercially available culture plates embedded with fluorescent probes, which react with protons and oxygen dissolved in the medium to report extracellular acidification and oxygen consumption (377-382). However, these assays report only a single factor in a specific plate, therefore it is not possible to measure the dynamics between glycolytic and oxidative metabolism in cells simultaneously. An additional issue that arises while using these methods is the lack of control in terms of cell density. The only point of control is the moment of seeding, which in case of different cell lines or treatment conditions might not correspond to the actual number of cells whose

metabolism is being probed during the experiment. However, this is crucial for drawing appropriate conclusions (383, 384).

The assay described in this Chapter provides a complete characterization of the interplay between glycolytic and oxidative metabolism as a mean of each well. The author shows that the method can be adjusted to include an internal control for cell density, and report long-term time courses of medium acidification and oxygen consumption which can be used in screening, high-throughput experiments.

3.2. Specific methods

3.2.1. Cells

Pancreatic Ductal Adenocarcinoma cell lines, AsPC-1, MIA PaCa-2 and PANC-1 were a kind gift from Professor Anna Trauzold (Christian-Albrecht University, Kiel, Germany), and were cultured in RPMI medium (Sigma-Aldrich, R0883), supplemented with 10% FBS (Sigma-Aldrich, F9665), 1% penicillin-streptomycin mixture (Sigma-Aldrich, P0781), 1% sodium pyruvate (Gibco, 11360-039) and 1% GlutaMAX (Gibco, 35050-038). Cells were plated at 30,000 50,000 and 70,000 density and left to adhere overnight. Next, the culture medium was removed, the cells were washed with PBS and 100 µL of lightly- or highly buffered medium was added. The cell compartment was sealed with 150 µL mineral oil added on top of the culture medium and the plate was transferred immediately for recordings.

3.2.2. Media

Powdered phenol-red free DMEM (Sigma-Aldrich, D5030) medium was used as a basis for the preparation of media of variable buffering. The remaining ingredients included either glucose (G7021) or galactose (G5388), NaCl (S7653), HEPES (H3375), and MES (M3671), all of which were obtained from Sigma-Aldrich. To prepare a lightly-buffered formulation DMEM powder was dissolved in deionised water and supplemented with 2 mM HEPES, 2 mM MES, 25 mM glucose, 40 mM NaCl, 10% FBS, 1% penicillin-streptomycin mixture, 1% GlutaMAX and 1% sodium pyruvate. Next, the medium was heated to 37°C and titrated to pH 7.4 using 0.4 N NaOH (VWR, 191373M) and sterilized by filtration. The highly-buffered medium was prepared accordingly but was

supplemented with increased HEPES concentration (20 mM) and reduced NaCl (25 mM) to maintain stable osmolality.

3.2.3. Fluorescent dyes and inhibitors

pH-reporter 8-Hydroxypyrene-1,3,6-trisulfonic acid trisodium salt (HPTS) and oxygen-sensor Tris(2,2'-bipyridyl)dichlororuthenium(II) hexahydrate (RuBPY) were obtained from Merck (H1529, 224758). The dyes were dissolved in deionised water to 4 mM and 100 mM, respectively and mixed in a 1:1 volume ratio to limit pipetting error. The stocks were aliquoted and stored at -20°C. Cell Tracker Orange CMRA (CTO) was purchased from Invitrogen (C34551) dissolved with DMSO and stored at -20°C. Electron Transport Chain inhibitor, rotenone (R8875, Sigma-Aldrich) was dissolved in DMSO and the aliquots kept at -20°C.

3.2.4. Equipment

Black, transparent bottom 96-well plates (655090, Greiner) were used for measurements as they are suitable for fluorescence-based assays. The plate reader used to record time courses of fluorescence was Bio-Tek Cytation 5 (Agilent). Excitation was provided by a monochromator, and fluorescence emission was detected sequentially at five wavelengths of visible light, which were optimized for the dye combination used. The optimal excitation wavelengths were 400, 416, 450, 460, and 540 nm, and the respective emissions were 510, 510, 620, 510, and 580 nm. To improve the signal-to-noise ratio, fluorescence was acquired using time-resolved mode with a delay of 0 µs and acquisition time of 500 µs.

3.3. Results

3.3.1. Selection of cost-effective pH and oxygen sensors to assay glycolytic and oxidative metabolism

There are several conditions that a sensor must fulfil in order to be successfully implemented into a cell-based assay. In this setting, to ensure appropriate reporting on cell metabolism selected dyes must be either oxygen or pH-sensitive to provide a read-out of oxidative phosphorylation and glycolysis, respectively. To avoid interference with cell metabolism, the dyes must be non-toxic and impermeable to the cell membrane to ensure reporting of only extracellular conditions. Additionally, the sensors need to be stable, easy to calibrate and enable simultaneous recording of both extracellular oxygen levels and pH so their fluorescence spectra cannot overlap. Ideally, an additional dye should be used to provide correction for cell density, which might fluctuate during prolonged experiments. For this purpose, CellTracker Orange CMRA has been chosen. There are several options available to provide a stable reading of extracellular pH including SNARF (385, 386), BCECF (387, 388), and HPTS (389-391). Out of this selection, HPTS is an appropriate choice, as it meets all aforementioned criteria and has the advantage of being cost-effective. Moreover, HPTS is a ratiometric dye with an emission and excitation spectrum between 400 and 500 nm, which facilitates the choice of an optimal oxygen sensor that emits fluorescence within the red range (392). Most oxygen-sensing dyes use the mechanism of oxygen-driven fluorescence quenching (393-395). RuBPY, which works according to the same principle, with emission and excitation spectrum outside the range of that of HPTS' has been selected as an oxygen sensor.

The HPTS' and RuBPY's spectra were characterized using the fluorescence plate reader BioTek Cytation 5. For the measurements, the dyes were dissolved at 2 µM and 50 µM concentrations (HPTS and RuBPY, respectively) in HEPES- and MES- buffered DMEM-based medium with pH adjusted to 6.0, 7.0 and 8.0. The fluorescence of HPTS was excited in dual mode at 400 and 460 nm, while for RuBPY the single-excitation mode was used at 450 nm. As shown in Figure 3.1A, the peaks of fluorescence emitted by HPTS and RuBPY show a clear distinction and do not overlap. Additionally, the fluorescence of HPTS is pH-sensitive, while RuBPY's is not. This proves that both dyes can be used simultaneously without interference.

Next, the HPTS emission spectrum was recorded within the optimal range of excitation between 400 and 460 nm (Fig.3.1B). The spectrum was recorded using 2 µM HPTS dissolved in a DMEM-based medium titrated to pH of 6.0, 7.0, or 8.0. The point at which pH-specific spectra intersect, the isosbestic point, was observed at 416 nm, and corresponds to the pH-insensitive wavelength. As opposed to RuBPY, HPTS is a ratiometric dye, which comes with the advantage of being much less prone to measurement errors that might arise as a result of varying dye concentration or photobleaching. The aforementioned HPTS' pH-insensitive wavelength, at 416 nm can be used as a reference point for RuBPY to provide another emission value to enable ratio calculation and thus correct for a possible variation in dye concentration. However, for this point to be reliable, the concentration ratio between the dyes must be kept consistent, which can be controlled by the preparation of pre-mixed stocks of the dyes, which decreases the chance of error by pipetting only a single stock rather than two. The spectrum of RuBPY emission has been recorded over an excitation range between 400 nm and 600 nm using a 50 µM concentration of the dye dissolved

in a medium titrated to pH or 6.0; 7.0 and 8.0. The peak of RuBPY excitation was found to be at 450 nm (Fig.1C). To optimize the concentrations of the dyes, HPTS and RuBPY have been mixed in various molar ratios and the fluorescence has been recorded. As optimal the combination of 2 µM HPTS and 50 µM RuBPY were selected, as these produced comparable emission peaks following the excitation at 450 nm without the risk of spectrum overlap (Fig.3.1D). To assess the fluorescence bleed-through into recording channels, a medium containing either 2 µM HPTS or 50 µM RuBPY was used, and the fluorescence was measured sequentially across four channels as shown in Figure 3.1E. Channels 1 to 3 are predominantly HPTS sensitive and RuBPY-emitted fluorescence accounted for less than 5% of the total signal recorded. Channel 4, which records RuBPY signal recorded bleed-through of HPTS-generated fluorescence below 7% of the total measured signal. As bleed-through values in neither case exceeded 10%, they were deemed minimal and did not require further corrections.

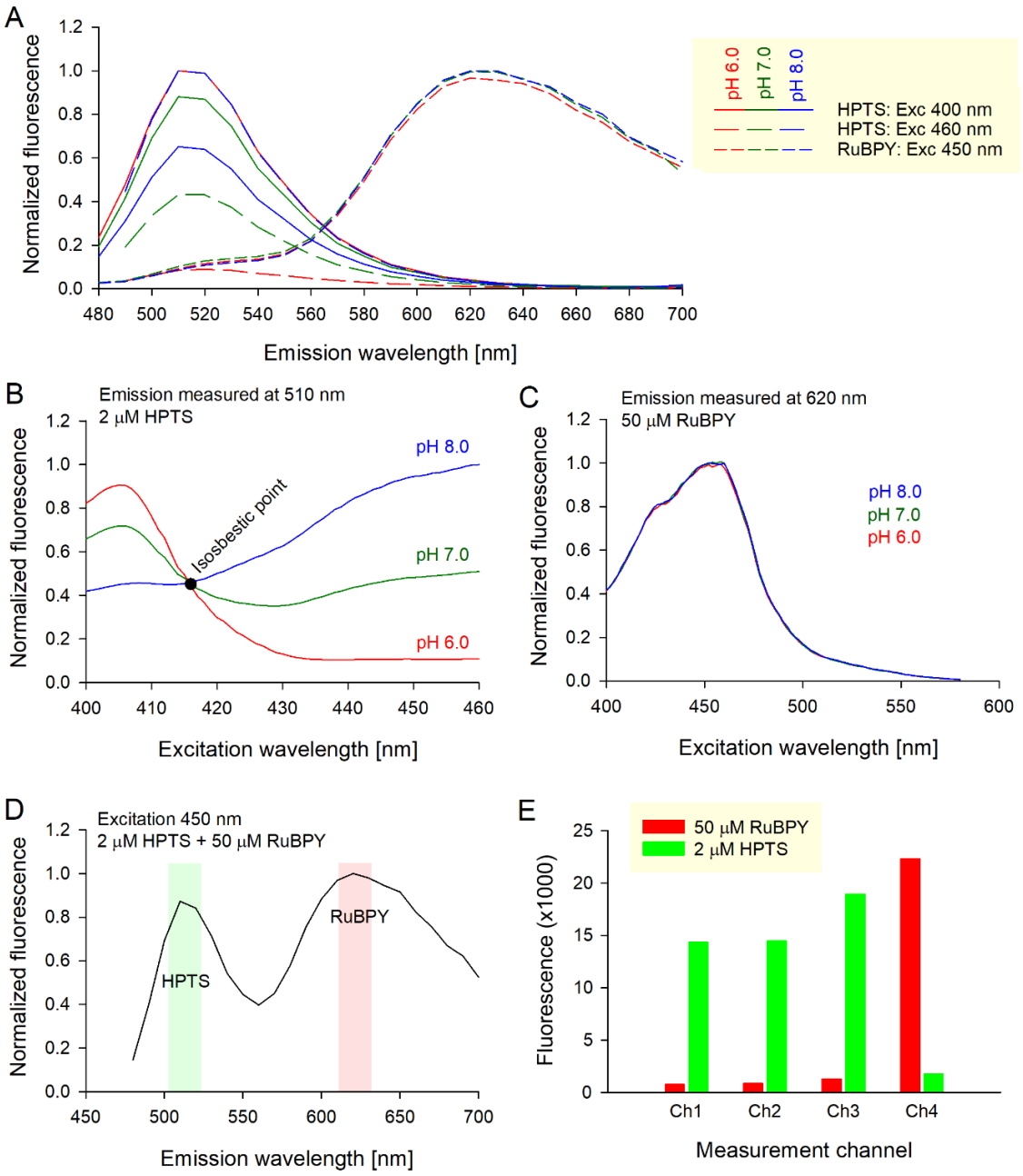


Figure 3.1 Spectral analyses of HPTS and RuBPY. A: Emission spectra for HPTS and RuBPY measured separately in medium buffered with a combination of 10 mM HEPES and 10 mM MES and adjusted to either pH 6.0, 7.0, or 8.0. B: The excitation spectrum for HPTS fluorescence recorded at optimal emission (510 nm). The isosbestic point is the wavelength at which fluorescence is pH-insensitive. C: The excitation spectrum for RuBPY fluorescence recorded at its optimal emission (620 nm). D: Concentrations of HPTS (2 µM) and RuBPY (50 µM) determined empirically in DMEM-based media to create similar in height emission peaks when excited at 450 nm. E: Assessment of the fluorescence bleed-through between recording channels. Media contained either HPTS (2 µM) or RuBPY (50 µM) at pH 7.4, and measurement protocols were performed to obtain signals across all four channels sequentially (Ch1–Ch4). Ch1–Ch3 are nominally HPTS channels and were found to detect a predominantly HPTS-emitted signal. Ch4 is nominally a RuBPY channel and detects a predominantly RuBPY-emitted signal. The experiments in this figure were conducted in collaboration with Dr. Zhengchu Tan.

3.3.2. Signal calibration to pH and O_2 units

In order for the assay to provide the user with quantifiable information on extracellular pH and dissolved oxygen, the fluorescent signals need to be calibrated using reference conditions. The calibration curves were produced by plotting obtained fluorescence values against those known of pH and oxygen. First, HEPES and MES-buffered medium (10 mM and 10 mM concentration respectively) was carefully adjusted to several pH points ranging from 5 to 8. The medium did not contain any sodium bicarbonate, as the measurements were performed in a CO_2-free atmosphere. The prepared media were mixed with an optimal concentration of both dyes and added in equal volume onto a 96-well plate. Next, to create a diffusion barrier for oxygen, each well was sealed by the addition of 150 µL of mineral oil on top of the medium. Each plate was prepared in duplicate, and one was measured instantly, which ensured atmospheric oxygen tensions, while the other was transferred into a hypoxic chamber pre-set to 0.1% O_2 and left to degas for 6h. After the incubation period the plate was immediately transferred into the plate reader and the recordings corresponding to complete anoxia (below 1% oxygen) were collected. The calibration curves are presented in Figure 3.2.

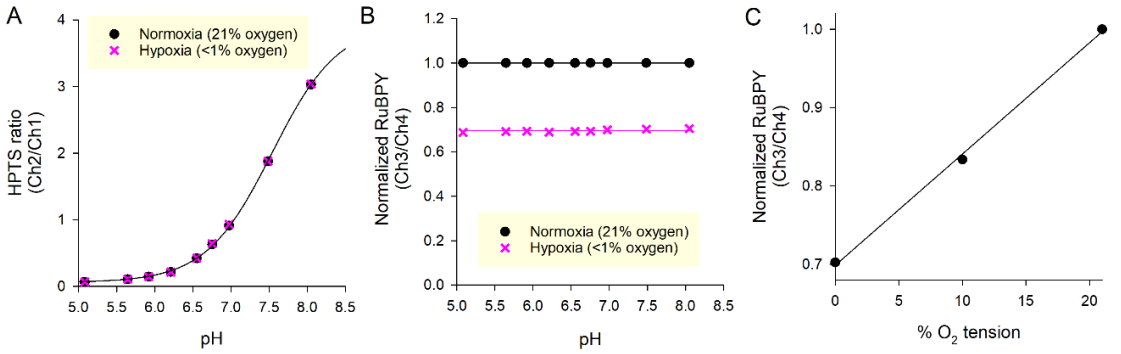


Figure 3.2 Calibration curves for HPTS- and RuPBY-emitted fluorescence. A: The calibration curve for the HPTS ratio (Ch2/Ch1) under normoxic and hypoxic conditions. Best fit to Equation (1) with constants listed in Table 3.1. B: Hypoxia-sensitive ratio of isosbestic HPTS to normalized and inverted RuBPY signal (as Ch3/Ch4). Hypoxia (<1% O2) reduces the Ch3/Ch4 ratio but is pH-insensitive. C: Three-point calibration for varied oxygen tension at 0.1%, 10%, and 21% O_2.

The HPTS (Ch2/Ch1) ratio was found to be highly pH-sensitive within the physiological range of pH (6 to 8), and was unaffected by the change in oxygen tension. On the contrary, HPTS isosbestic to RuBPY fluorescence ratio (Ch3/Ch4) was distinctly altered depending on O_2 concentration, with a significant decrease in fluorescence observed under hypoxic conditions, but did not respond to changes in extracellular pH. The ratio of RuBPY fluorescence is inversely correlated with oxygen tension due to the mechanism of oxygen-quenching implemented in this chemical sensor.

The best-fit equation for HPTS calibration curve was one of the Grynkiewicz type (396):

$$\mathrm{pH} = \mathrm{pK_a} - \log_{10}\frac{\mathrm{r_{max}} - \mathrm{R_{pH}}}{\mathrm{R_{pH}} - \mathrm{r_{min}}} \quad (1)$$

The oxygen-sensitive calibration curve was characterised using a modified Stern-Volmer equation (397):

$$\mathrm{O_2} = 21 \times \left(1 - \frac{1 - \mathrm{R_{O2}}/\mathrm{R_{normoxia}}}{1 - \mathrm{r_{anoxia}}}\right) \quad (2)$$

In this system, the best-fit calibration values are listed in Table 3.1.

Table 3.1 Best fit calibration values for HPTS fluorescence

Calibration Variable	Best-Fit
pKa	7.5383
rmax	3.9503
rmin	0.0603
ranoxia	0.6945

3.3.3. Conversion of O_2 and pH time-courses into flux

In order to appropriately convert the time-course data of oxygen and pH into molecular flux, several aspects need to be considered, including chemical buffering in the medium used, as well as the state of the system, i.e. as being open or closed. The former, open system, allows for free gas (oxygen) exchange between the compartment and atmosphere whereas in a closed one that exchange is limited, e.g. due to implemented diffusion barrier.

3.3.4. Buffering

Fluorescent sensors, as used here HPTS and RuBPY respond to levels of free ligands available within the probed system, H^+ and O_2, respectively. However, especially in terms of H^+ ions, the free levels might not correspond directly to the levels that were metabolically produced. Every medium, or solution that is used for cell culture, even for short-term experiments should be buffered to resemble physiological conditions. The total buffering capacity depends on the amount of protein or FBS added, type of buffering agent and its concentration, and is subject to changes relative to temperature. In order to recalculate experimentally obtained time-course of acid production into flux (J_{H+}), it must be corrected by the empirically measured buffering capacity (β) of the medium used. This ensures that the total amount of acid produced

can be obtained, rather than a free subset. Thus, the buffering capacity of the medium formulation used in experiments was determined by the addition of known amounts of acid and base (HCl and NaOH) and by monitoring the pH change. To reflect the experimental conditions, the medium was heated to 37°C and the temperature was maintained throughout the experiment. The curves depicting the change in pH followed by the stepwise addition of 0.5 M NaOH and HCl are shown in Figure 3.3A. For this experiment, a lightly-buffered medium formulation, containing 2 mM HEPES and 2 mM MES was used. The calculated buffering capacity showing a stable buffering over a physiological range of pH is plotted in Figure 3.3B.

$$J_{H+} = \frac{d[H^+]^{total}}{dt} = -\frac{dpH}{dt} \times \beta \quad (3)$$

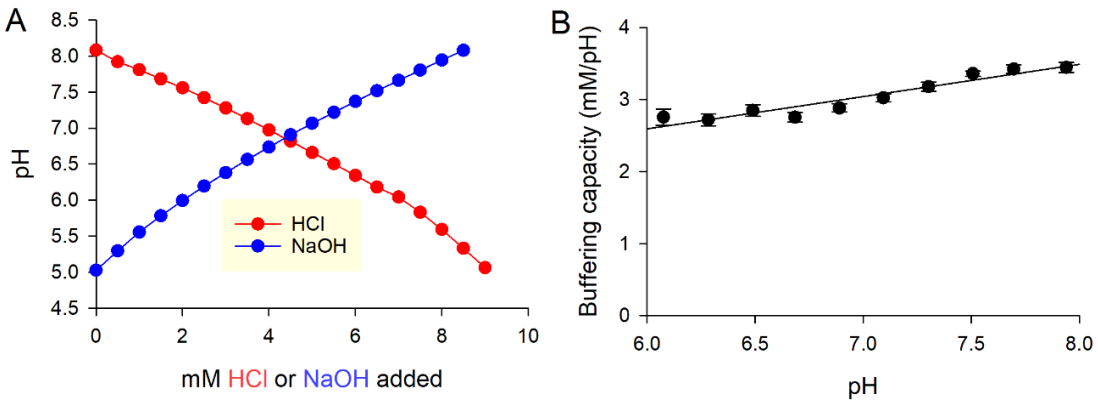


Figure 3.3 Measuring the pH buffering capacity. A: Cumulative addition of 0.5 mM HCl or NaOH to media of undetermined buffering capacity. The inverted slope provides buffering capacity for the entire tested pH range. B: Buffering capacity expressed as the ratio of HCl (or NaOH) added, plotted against pH. The best-fit line describes the pH-sensitivity of the buffering capacity of that specific medium formulation.

On the other hand, chelating agents are responsible for oxygen buffering, which *in vivo* (e.g. haemoglobin) bind and thus limit oxygen fugacity. Buffering can be quantified as a buffer ratio (B), which corresponds to the number of molecules bound to buffer vs free molecules. Usually, culture media contain minimal oxygen buffering, therefore

the rate of change of measured O_2 gives an adequate estimate of flux (J_{O2}), which can be described as follows:

$$J_{O2} = \frac{d[O_2]^{total}}{dt} = \frac{d[O_2]^{free}}{dt} \times (1 + B) \approx \frac{d[O_2]^{free}}{dt} \quad (4)$$

3.3.5. Description of the system

Experimental systems can be characterised as either open or closed. The benefit of a closed system is the lack of external variables that impact the readings and might be problematic to correct for. Lactic acid as non-volatile compound provides a good read-out of the glycolytic metabolism of cells that remains stable throughout the experiment and cannot be interfered with. On the contrary, dissolved oxygen is gaseous and highly volatile. It is therefore much more difficult to appropriately correct for given that it will always strive to reach equilibrium with the surrounding atmosphere. Even though the system can be considered closed in terms of one variable (pH) it can be open in terms of the other. The exchange of oxygen between the well and the atmosphere accounts for an additional flux that can be characterised by a permeability constant (P_{O2}) and gradient as follows:

$$J_{O2}{}^{exchange} = P_{O2} \times ([O_2]_{atm} - [O_2]_{well}) \quad (5)$$

Therefore, the overall oxygen dynamics in a well that contains respiring cells (Equation 5) and is open to the atmosphere must be described as follows:

$$J_{O2}{}^{measured} = J_{O2}{}^{respiration} + J_{O2}{}^{exchange} \quad (6)$$

Using Equation 6, it is possible to calculate the respiratory flux from O_2 recordings once passive oxygen exchange is taken into account. In order to calculate the latter, oxygen

permeability needs to be estimated first. This depends on a number of parameters including oxygen diffusivity in the medium and the height of the column of the fluid. A column of the medium allows for relatively fast gas diffusion, which comes with a risk that any change in levels of dissolved oxygen could be difficult to assess. To implement a controlled restriction barrier on gas diffusion, the medium in wells was covered with a layer of mineral oil. The total oxygen permeability across the column of medium and oil can be assessed in cell-free wells that had been previously equilibrated in hypoxic conditions. Once the plate is removed from the hypoxic chamber (and transferred into a fluorescent plate reader), the gradient of oxygen drives its ingress into the medium, which was tracked using RuBPY (Figure 3.4A). The time course of re-oxygenation provides a measure of time constant, that is inversely correlated to P_{O2} (Figure 3.4B). This experiment was performed using a range of oil volumes to provide a variety of diffusive barriers (Figure 3.4C). These data provide an estimate of the time constant of O_2 diffusion in the media and the efficiency of oil in restricting gas diffusion. For 150 µL of mineral oil, P_{O2} is 0.029 min^{-1}. This volume was selected for future experiments. Thus, the P_{O2} can be applied to equation (6) which enables the calculation of the respiratory fluxes.

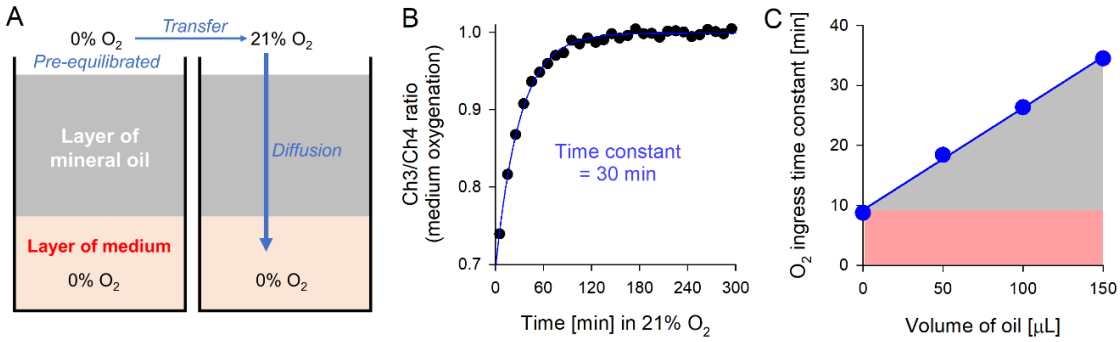


Figure 3.4 Characterisation of the system with respect to O_2 dynamics. A: The protocol for measuring oxygen permeability across a layer of medium (typically 100 µL) and oil (varied between 0 and 150 µL). B: Representative example of time course from well covered with 150 µL oil. Transferring a plate to an atmosphere of normal oxygen in the reader triggers re-oxygenation, which was monitored every 10 minutes for the isosbestic HTPS-to-RuBPY ratio. The best fit gives a time constant, which is inversely related to O_2 permeability. C: Relationship between the time constant of oxygen ingress time constant and the volume of oil added to wells. Red shading denotes the time constant attributable to the medium, and grey denotes that due to diffusion through oil. These experiments have been conducted in collaboration with Dr. Zhengchu Tan.

3.3.6. The efficiency of the assay to phenotype metabolism of cancer cells

Proof-of-principle experiments of glycolytic and respiratory metabolism were performed on three diverse pancreatic adenocarcinoma cell lines AsPC-1, MIA PaCa-2 and PANC-1. Obtained fluxes depend on not only the metabolic activity of the cells but also on the density, which in case of highly proliferating cell lines might fluctuate during the experiment. Thus, it was deemed necessary to obtain an independent measure of cell number for normalization.

3.3.7. Correcting for cell density

The number of cells potentially changing during the experiment can be monitored in real-time by loading cells with a fluorescent dye. Then, the increasing signal would relate to an increase in cell density and vice versa. However, for a dye to work effectively in this experimental setup, it must be stable (not undergoing chemical changes within the time frame of the assessment), membrane-impermeable post loading and its

spectrum cannot overlap with those of pH and oxygen-reporting sensors. The appropriate group of dyes for this purpose are CellTracker dyes, and the optimal choice considering the spectral requirements is CellTracker Orange (CTO). The CTO emission spectrum is shown in Figure 3.5A. There is no risk of interference with the fluorescence of HPTS and RuBPY, as it is excited at a considerably higher wavelength than either of those (540 nm vs <460 nm) (Figure 3.5B). Moreover, the CTO fluorescent signal is linear to cell number, which was confirmed by serial dilutions of red blood cells (Figure 3.5C). A similar calibration curve was obtained for adherent pancreatic ductal adenocarcinoma cells, regardless of cell line (Figure 3.5D). Note that the fluorescence of a cancer cell (0.455 F.U.) was higher than that of a red blood cell (0.19 F.U.). This results from differences in size and haemoglobin content, as the latter absorbs fluorescence. The degree of CTO's pH- and O_2-sensitivity was determined experimentally by loading MIA PaCa-2 cells with the dye at 12.5 µM for 15 minutes, followed by superfusion with solutions of varied pH or oxygen levels. The solutions contained 125 mM NaCl, 4.5 mM KCl, 11 mM glucose, 1 mM $CaCl_2$, 1 mM $MgCl_2$, and 20 mM HEPES and the pH was adjusted to either 6.4 or 7.4. For anoxic superfusates, solutions were bubbled in 100% N_2, and anoxia was stabilized chemically by the addition of 1 mM oxygen scavenger (sodium dithionite). The solutions were heated to 37°C and delivered to the cells by a peristaltic pump. CTO-loaded cells were imaged on a Leica confocal microscope using settings optimized previously for CTO. Fluorescence was first imaged at normoxic conditions (21% O_2 and pH 7.4), and then after a change in pH to 6.4 (Figure 3.5E), allowing 10 min for equilibration. Alternatively, a change in O_2 tension to anoxic levels was measured (Figure 3.5F), allowing 2 minutes for equilibration. Finally, baseline neutral and normoxic conditions were reintroduced.

No effect of hypoxia or acidity on CTO fluorescence intensity was observed, indicating that CTO provides a stable fluorescence signal.

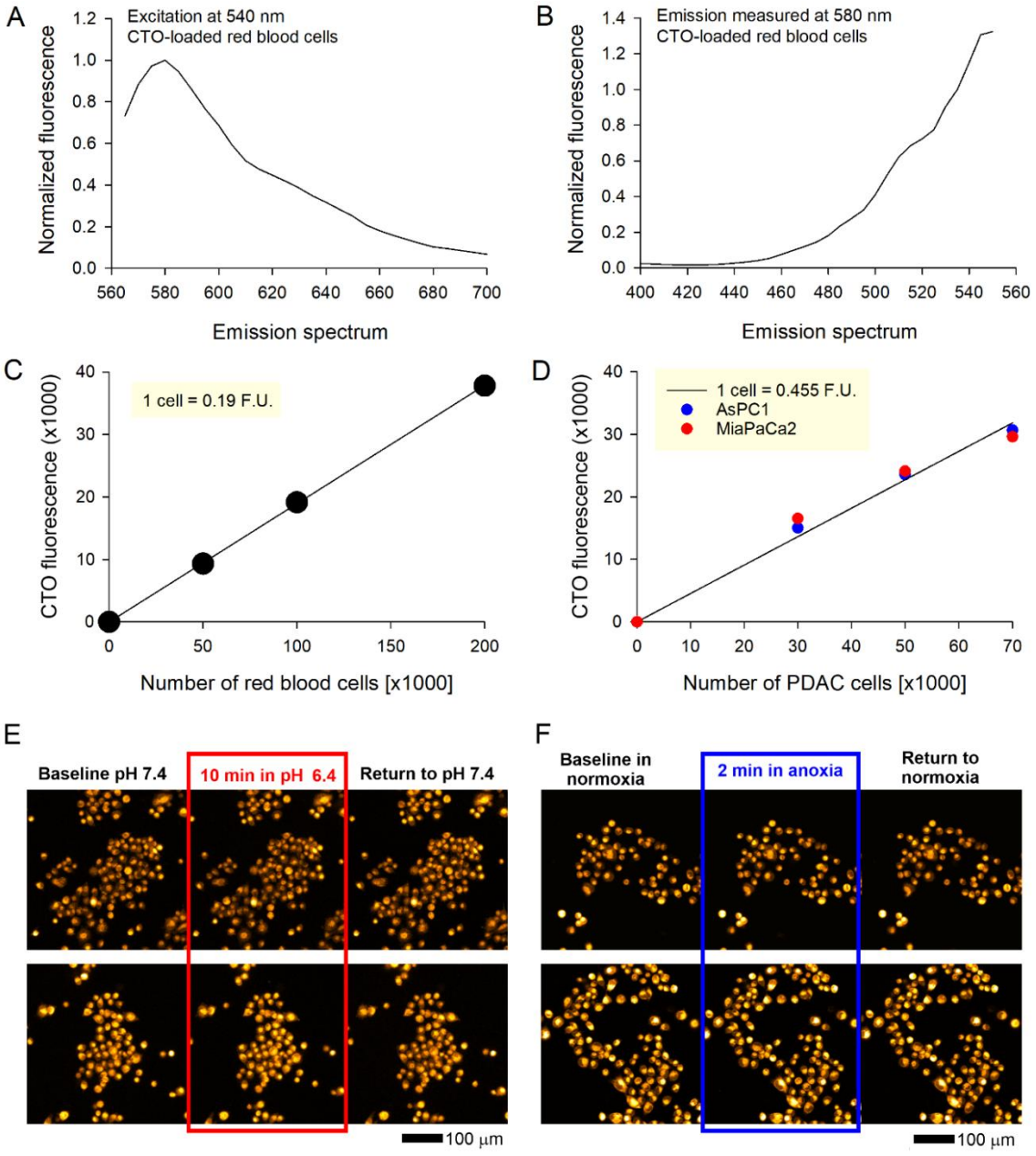


Figure 3.5 Cell Tracker Orange (CTO)-based normalisation of the cell number. A: The emission spectrum of CTO, excited at 540 nm. B: The optimal CTO excitation is 540 nm, which ensures that the signal is resolvable from HPTS and RuBPY. C: The correlation between CTO fluorescence and count of human red blood cells. D: The correlating CTO signal with the number of plated AsPC1 and MIA-PaCa2 cells in wells of a 96-well plate. E: Superfused MIA-PaCa2 cells imaged confocally. Fluorescence images were taken during superfusion at pH 7.4 (baseline; 20 mM HEPES-buffered solution), after 10 minutes of superfusion at pH 6.4, and 10 minutes after returning to normal pH. Two exemplar experiments are shown. F: Fluorescence images taken during superfusion with oxygenated solution (baseline), after 2 minutes of superfusion under anoxic conditions (superfusate contained 1 mM dithionite, 100% N_2), and 2 minutes after returning to normoxia. Two representative experiments are shown.

3.3.8. Real-time recordings of metabolic fluxes

To monitor glycolytic and respiratory fluxes in real time, AsPC-1, MIA PaCa-2, and PANC-1 cells were seeded in 96-well plates at various cell densities (30,000; 50,000 and 70,000) and left to attach overnight. Next, the cells were loaded with 25 µM CTO for 15 minutes, after which media were replaced with 100 µL of a lightly buffered medium formulation containing optimised previously concentration of the dyes (2 µM HPTS and 50 µM RuBPY). Wells were immediately covered with 150 µL of mineral oil and the plate was transferred into the plate reader for time-course measurements. In order to correct the measurements for the fluorescent background several wells have been kept cell-free to provide a baseline measure. The time courses of cumulative acid production (C_{H+}) and cumulative oxygen consumption (C_{O2}) have been calculated according to the following formulas:

$$C_{H+} = V \times \left(\sum_{t=0}^{T} J_{H+}{}^{cell} - \sum_{t=0}^{T} J_{H+}{}^{cell-free}\right) = V \times \left(-\sum_{t=0}^{T}\left(\frac{dpH}{dt}^{cell} \times \beta\right) + \sum_{t=0}^{T}\left(\frac{dpH}{dt}^{cell-free} \times \beta\right)\right) \quad (7)$$

$$C_{O2} = V \times \sum_{t=0}^{T}\left(J_{O2}{}^{cell} - P_{O2} \times \left([O_2]_{atm} - [O_2]_{well}^{cell}\right)\right) = V \times \sum_{t=0}^{T}\left(\frac{d[O_2]}{dt}^{cell} - P_{O2} \times \left([O_2]_{atm} - [O_2]_{well}^{cell}\right)\right) \quad (8)$$

The metabolic profile of three PDAC cell lines, AsPC-1, MIA PaCa-2 and PANC-1 differed significantly between the cell lines (Figure 3.6), with AsPC-1 being the least active, showing only marginal acid-production and oxygen consumption. The phenotype of MIA PaCa-2 and PANC-1 was more glycolytic with MIA-PaCa-2 attaining the lowest extracellular pH of around 6. The most respiring cell line was PANC-1. In all tested cell lines acid-production and oxygen consumption increased with cell density.

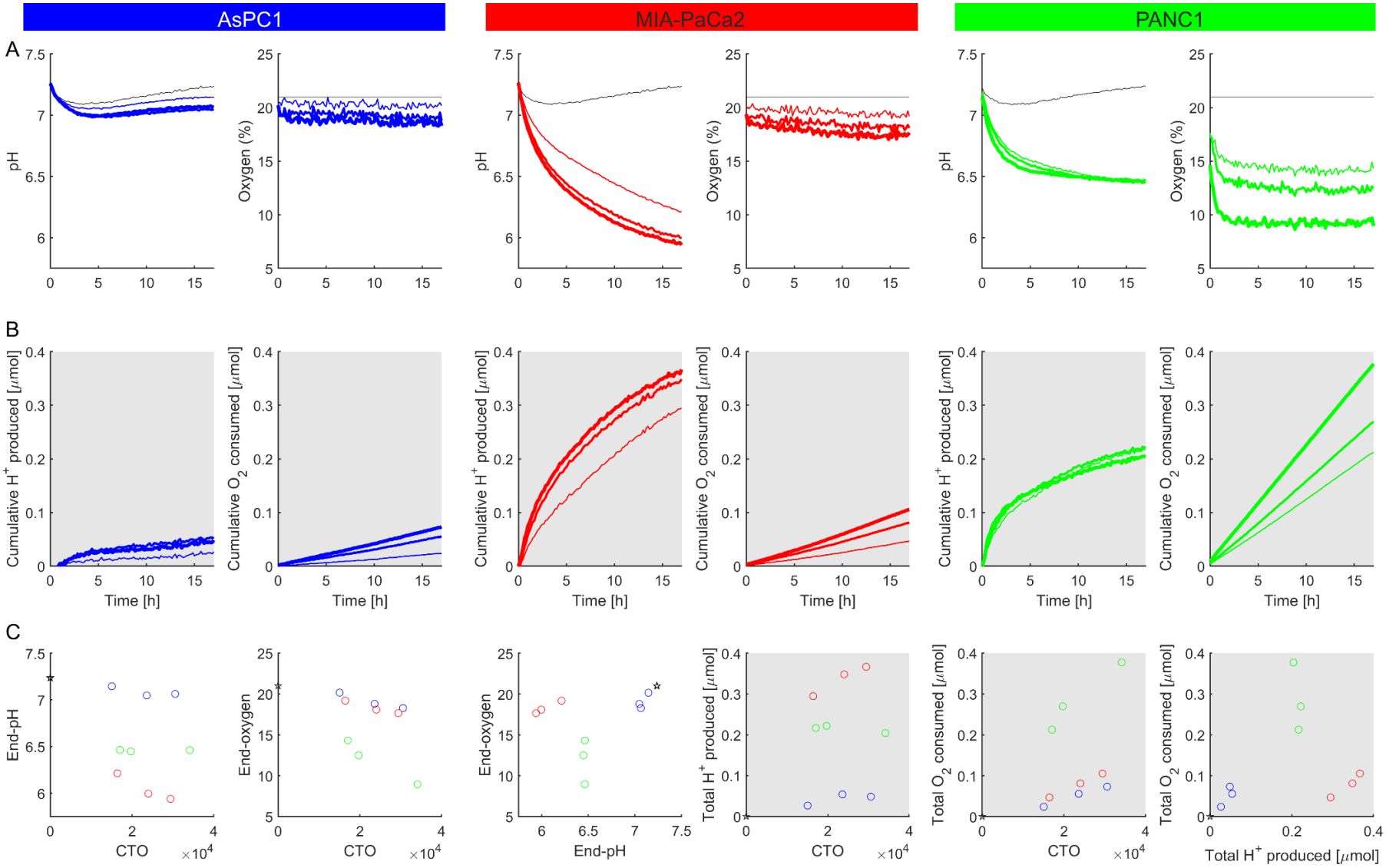

AsPC1
MIA-PaCa2
PANC1
A
pH
Oxygen (%)
B
Cumulative H+ produced [μmol]
Cumulative O2 consumed [μmol]
Time [h]
C
End-pH
End-oxygen
CTO
×10^4
Total H+ produced [μmol]
Total O2 consumed [μmol]

Figure 3.6 Metabolic profiling of PDAC cell lines. A: Time courses of pH and O_2 for AsPC-1 (blue), MIA PaCa-2 (red), and PANC-1 (green) plated at 30, 50, or 70 k cells per well. Thicker lines denote higher cell density. Blank time courses were obtained from cell-free wells. Media were prepared using DMEM 5030 and contained 2 mM HEPES and 2 mM MES, 25 mM glucose, supplemented with 10% FBS, 1% penicillin–streptomycin mixture. B: Cumulative H^+ production and O_2 consumption, calculated using Equations (7) and (8). C: Data from A and B replotted as a function of cell number, measured by CTO fluorescence. Plots with white background relate to end-point pH and O_2, and plots with grey background relate to cumulative H^+ production and O_2 consumption. The black star symbol denotes data from cell-free wells. Plots represent a mean of 3 biological repeats.

3.3.9. The assessment of metabolic responses

The described assay could be used to assess the altered metabolic response to changes in the substrate concentration. To test this hypothesis, MIA PaCa-2 and PANC-1 cells were seeded at high density (70,000 a well) and left to adhere overnight. Then, the culture medium was replaced with 100 µL of highly-buffered medium containing 20 mM HEPES, fluorescent dyes and as primary substrate 25 mM of either glucose or galactose. Each well was sealed by the addition of 150 µL mineral oil and the plate was transferred into the plate reader for time-course measurements over next 17 hours. As oxidation of galactose to pyruvate requires an additional conversion that 'costs' 2 ATP molecules, the galactose-triggered glycolysis doesn't produce any net ATP, which forces the cells to remodel their metabolism towards oxidative phosphorylation. In line with literature data, the shift towards increased oxygen consumption following the replacement of glucose with galactose was observed in both tested cell lines (Figure 3.7A). Additionally, the metabolic rewiring was confirmed by a decrease in acid-production (Figure 3.7B).

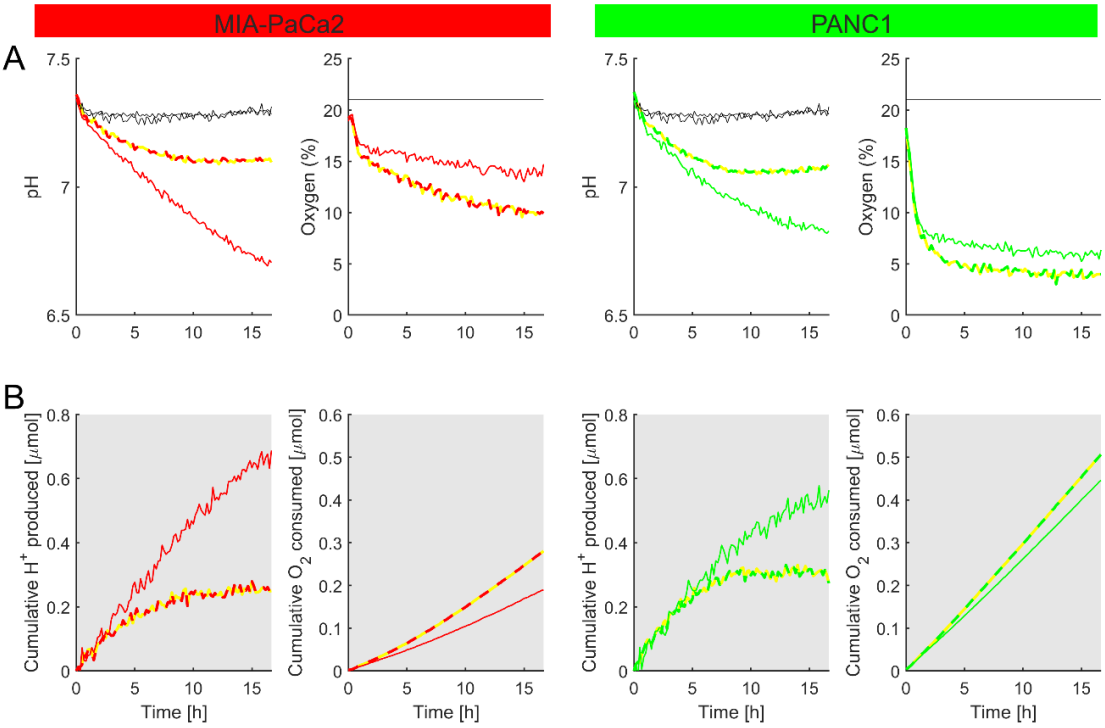


Figure 3.7 Assessment of cell response following a change in the metabolic substrate. A: Time courses of pH and O_2 measured for MIA PaCa-2 (red) and PANC-1 (green) cells seeded at 70,000 cells per well. Dashed double-colour lines depict media containing galactose (25 mM) instead of glucose. Media contained 20 mM HEPES, 25 mM glucose or galactose, 25 mM NaCl and was supplemented with 10% FBS, 1% penicillin–streptomycin mixture, 1% GlutaMAX, and 1% sodium pyruvate. B: The cumulative H^+ production and O_2 consumption, calculated using Equations (7) and (8). Plots represent a mean of 3 biological repeats.

Another area in which the assay can be successfully implemented is the screening of potential metabolic inhibitors or assessment of the response to these. To test whether the method is sensitive enough to resolve, possibly small, effects of metabolic inhibitors, MIA PaCa-2 and PANC-1 cells were plated at high density (70,000 a well) and left to attach overnight. The next day, the culture medium was discarded and 100 µL of highly-buffered medium containing 20 mM HEPES, a mixture of fluorescent dyes with or without 10 µM rotenone was added to each well. The plate was covered with mineral oil and transferred into the plate reader for measurements. As expected, the addition of rotenone, which inhibited the electron transport chain, decreased oxygen consumption and elevated acid production in both tested cell lines (Figure 3.8).

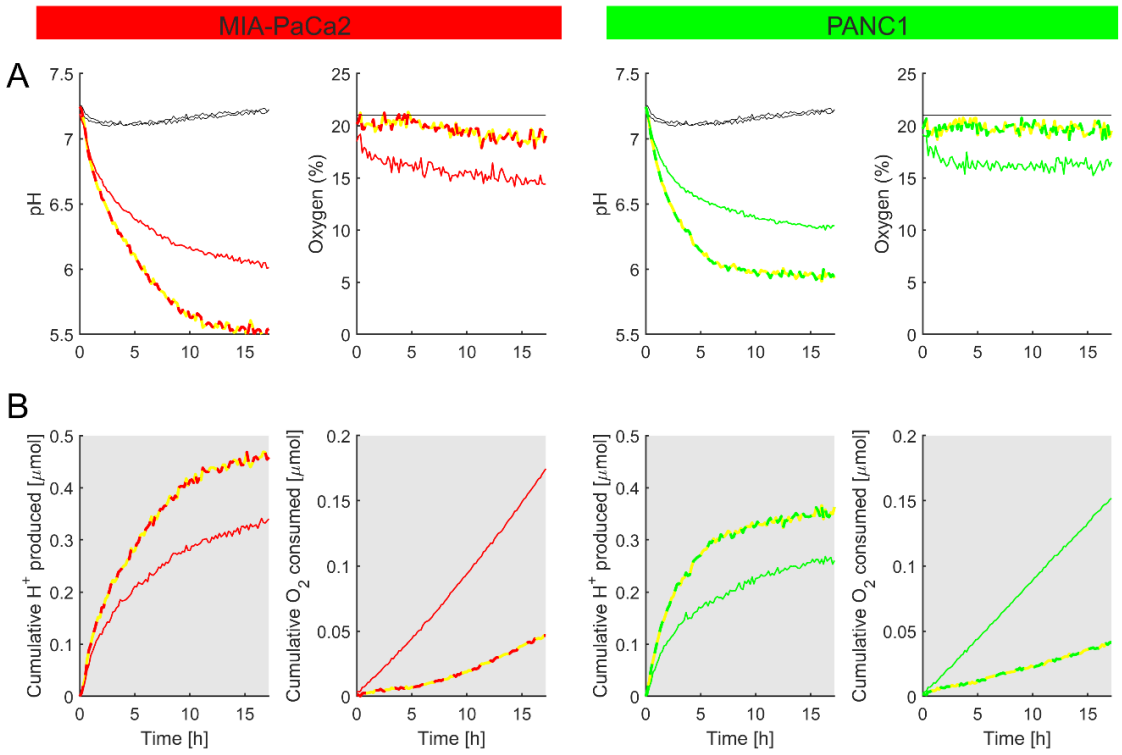


Figure 3.8 Assessment of the effect of metabolic inhibitors. A: Time courses of pH and O_2 for MIA PaCa-2 (red) and PANC-1 (green) plated at 70,000 cells per well. The metabolic substrate was glucose throughout. Media contained 2 mM HEPES and 2 mM MES, 25 mM glucose, supplemented with 10% FBS, 1% penicillin–streptomycin mixture, 1% GlutaMAX, and 1% sodium pyruvate. Dashed double-colour lines correspond to the effect of 10 µM rotenone. B: The cumulative H^+ production and O_2 consumption, calculated using Equations (7) and (8). Plots represent a mean of 3 biological repeats.

3.4. Discussion

This chapter provides a comprehensive description of the fluorescence-based assay that allows for the assessment of the interplay between glycolytic and oxidative metabolism in adherent cancer cells. The developed method is easy to use, cost-effective, and provides reliable and resolvable readings. Although several methods of cell metabolism phenotyping are currently available, none enables simultaneous reporting of both glycolytic and oxidative flux in real-time with control for cell density while maintaining relatively low running cost. Although the described assay is superior when compared with Seahorse measurements or commercially available pH and O_2 sensor pre-coated plates, it still comes with limitations. Unfortunately, the assay does not provide readings taken at a single-cell resolution. Therefore, it cannot be used to identify the metabolic rates of individual cells. It only provides a mean measurement of the total probed population, which is not useful when studying cell heterogeneity. Additional problems might occur, when the effects of lipophilic compounds are assessed as these might be absorbed by the layer of oil. A similar issue might apply to lipophilic ingredients of the culture medium, especially during long-term (longer than 24 hours) experiments. Furthermore, this specific setup uses the non-volatile buffering provided by HEPES and MES, which requires the plate to be maintained in a CO_2-free atmosphere, resulting in non-physiological conditions. This method has been extensively used in this thesis and provides important insights into the heterogeneity of metabolic phenotypes of used pancreatic ductal adenocarcinoma cell lines.

3.5. Key findings

1. The described method provides cost-effective metabolic profiling of adherent cells in terms of glycolytic and oxidative metabolism measured over prolonged periods of time;
2. The pH indicator, HPTS, provides ratiometric readings, while the oxygen sensor was adapted to a similar principle using the isosbestic point for HPTS as a reference;
3. In order to achieve resolvable readings of oxygen consumption an oil-imposed diffusion barrier for oxygen was implemented;
4. Cell tracker orange was used as an internal control for cell density, which is stable regardless of pH and oxygen tension.

Chapter 4. Description of the glycolytic metabolism and its control by pH in Pancreatic Ductal Adenocarcinoma

A hundred years ago Otto Warburg discovered a phenomenon of cancer cells relying on glycolysis even in the abundance of oxygen, the phenomenon later termed the Warburg effect. Since then many studies have shed light on how cancer cells manage to overcome the disadvantages of this reliance on a less energetically efficient pathway, some of which include upregulated glucose uptake, enhanced fatty acid oxidation and augmented autophagy. Elevated glycolysis, a hallmark of solid tumours, leads to pronounced extracellular acidosis, which is known to impact cell metabolism. In this Chapter the metabolic profile of a panel of six Pancreatic Ductal Adenocarcinoma cell lines is assessed and the feedback circuit between glycolysis and its end-products (lactate and protons) is characterized. This project tests the therapeutic potential of lactic acid efflux inhibitors and describes the cues that do and do not have the capacity to influence the glycolytic rate, and thus the fate of the cancer cell itself.

4.1. Introduction

Deregulated metabolism has been recognised as a hallmark of cancer. It is a feature that facilitates growth and helps to evade controlling cues that under physiological conditions would curb the metabolic rate and limit cell proliferation (322). Glycolytic metabolism, the first, and the least energetically efficient part of the glucose-oxidation pathway results in the production of pyruvate. This molecule can either enter the tricarboxylic acid cycle and feed oxidative phosphorylation, or undergo transformation into lactate, which is extruded out of the cell (398). The latter often happens in hypoxic tissues and in cancer cells, which even under aerobic conditions tend to favour glycolysis over oxidative phosphorylation, in a phenomenon termed the Warburg effect (102, 399, 400). This enhanced glycolysis leads to pronounced extracellular lactic acidosis (102), which further contributes to metabolic deregulation, as it facilitates evasion of immune recognition (401) and promotes more aggressive phenotypes (295). Accumulated in the extracellular space, lactic acid is known to control glycolysis, creating a negative feedback circuit. If that circuit is the main regulator of glycolytic metabolism, it would mean that a certain threshold of extracellular lactic acid levels is allowed to accumulate before glycolytic metabolism is shut down and the cell is starved. That situation could be a possibility, only if the cell is mostly reliant on glycolysis without any metabolic component of respiration. Such control could be a disadvantage for tumours unless excessive lactic acidosis is prevented by efficient diffusion and lactate uptake by adjacent cells (to be used in oxidative phosphorylation), as it would provide a limit for glycolytic metabolism. There are several potential points of control that might participate in the feedback loop. One, known since

1969 is the pH-dependent control of glycolytic enzymes (402). The optimum pH for glycolytic enzymes activity falls within the alkaline range (>6.9 for hexokinase and phosphofructokinase (403), 7.8 - 8.5 for glucokinase (404)), which means that in the event of intracellular acidification, this branch of metabolism is no longer available. Another element of metabolism regulation might be either the uptake of substrates or the extrusion of the end products. In case of oxidative phosphorylation, where the products are volatile and membrane-permeable like CO_2 or H_2O, either is unlikely to influence metabolic rates significantly. On the contrary, the glycolytic end-product, lactic acid cannot simply diffuse across the lipid bilayer and needs to dissociate into H^+ and lactate, and in this form is carried out of the cell via monocarboxylate transporters. This family of proteins comprises several transporters that catalyse passive, proton-coupled and bidirectional transport of lactate, pyruvate and ketone bodies. The MCTs might participate in metabolic control as they are strategically positioned on the cell surface and might sense the extracellular lactic acid levels and regulate the pathway accordingly. This Chapter provides a description of glycolytic and oxidative metabolism assayed across a panel of PDAC cell lines, investigates the therapeutic potential of MCT-targeted inhibitors and characterizes the feedback circuits that control metabolism in cancer cells.

4.2. Results

4.2.1. The negative feedback of pH on metabolic acid production

Glycolytic and oxidative metabolism are the main two pathways of ATP production in cells. It is a common phenomenon for cancer cells to rely on less energetically efficient glycolysis. However, the ratio of cell dependence on oxidative and glycolytic metabolism is often cell line dependent and can fluctuate depending on nutrient availability and conditions found within the microenvironment. Negative feedback circuits controlling the rates of enzymatic reactions are common in biology. In order to assess whether extracellular acidity feeds back on cell metabolism, five Pancreatic Ductal Adenocarcinoma cell lines of different metabolic profiles were seeded in high density onto a 96-well plate. The combination of high cell number, low buffering capacity and low volume of medium ensured that potential equilibrium, i.e. the extracellular pH that would inhibit further metabolic acidification would be reached within 16 hours. A detailed description of the method can be found in Chapter 2. Figure 4.1A depicts the exemplar time-course of extracellular acidification observed in BxPC-3 cells. Initially, the rate of pH change is rapid. However, in time it decelerates until the steady-state is reached, (around pH 6.6), which prevents further metabolic acid production. This pH point marks the limit for acidification that can be reached as a result of BxPC-3 cells' metabolism within a closed environment. In fact, this phenomenon was observed in the remaining cell lines, (Fig.4.1B), as their metabolic acid production rate was negatively affected by the accumulation of extracellular acidity. Among these, PANC-1 was identified as the most persistent acid-producer, as it continued to acidify the extracellular space until pH 6 was reached.

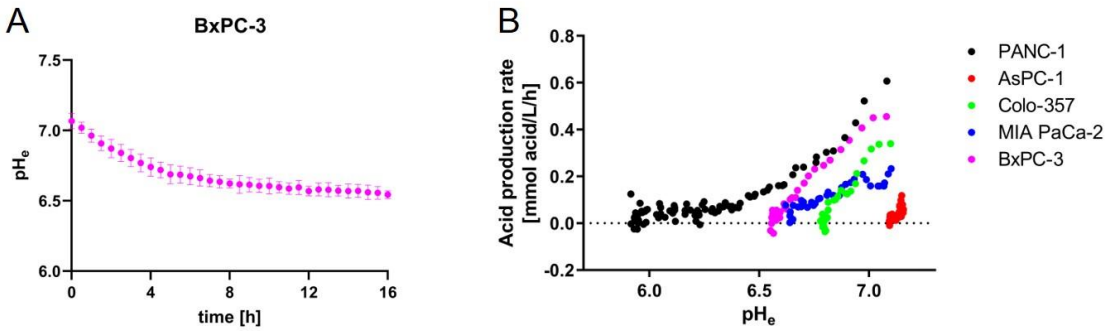


Figure 4.1 pH-induced feedback loop on metabolic acid production. A: Example time-course of medium acidification measured over 16h in BxPC-3 cell line. pHe- extracellular pH. Data shown as mean ± SEM. B: Metabolic acid production rate of PDAC cells slows down as acid accumulates within the extracellular compartment.

4.2.2. The interplay between glycolytic and oxidative metabolism depends on available nutrients

The maximal limits of extracellular pH for each cell line, identified in the previous section might be influenced by available metabolic substrates. As glucose can fuel both glycolysis and oxidative phosphorylation, its fate is dependent on the metabolic profile of the cell at a given time and the conditions found within the microenvironment. Under hypoxia, even respiration-dependent cells will not be able to fully oxidise glucose. On the other hand, mitochondrial substrates, like glutamine and pyruvate both enter the tricarboxylic acid cycle in the form of alpha-ketoglutarate and acetyl coenzyme A, respectively. Supplementing the medium with respiratory substrates therefore would show the cell preference for either the glycolytic or oxidative branch of metabolism, inferred from the change in maximum acidification.

The Pancreatic Ductal Adenocarcinoma cell lines were seeded at high density onto a 96-well plate as described previously. This time, however, the lightly-buffered medium was supplemented with 1% glutamine and 1% sodium pyruvate. The time-courses of medium acidification were recorded and the data recalculated into cumulative acid

production. To account for potential acidity resulting from oxidative phosphorylation (CO_2) the endpoint measurements of medium lactate were taken.

The metabolic acid production was greater in all cell lines when glucose was the only available substrate (Fig.4.2A). The addition of glutamine and pyruvate decreased acid production and revealed differences between the metabolic profiles of the cell lines. The only cell line that did not respond to a change in medium composition was PANC-1, which acidified to a similar extent regardless of nutrient availability. To confirm the glycolytic origin of medium acidity, extracellular lactate was measured at the endpoint and plotted against the cumulative H^+ produced (Fig.4.2B). When assayed in a medium containing only glucose all tested cell lines produced equal amounts of lactate and protons suggesting that all acidity was the end-product of glycolysis. Supplementing the medium with mitochondrial substrates disrupted the H^+:lactate ratio and decreased lactate and acid production in most cell lines, except for PANC-1.

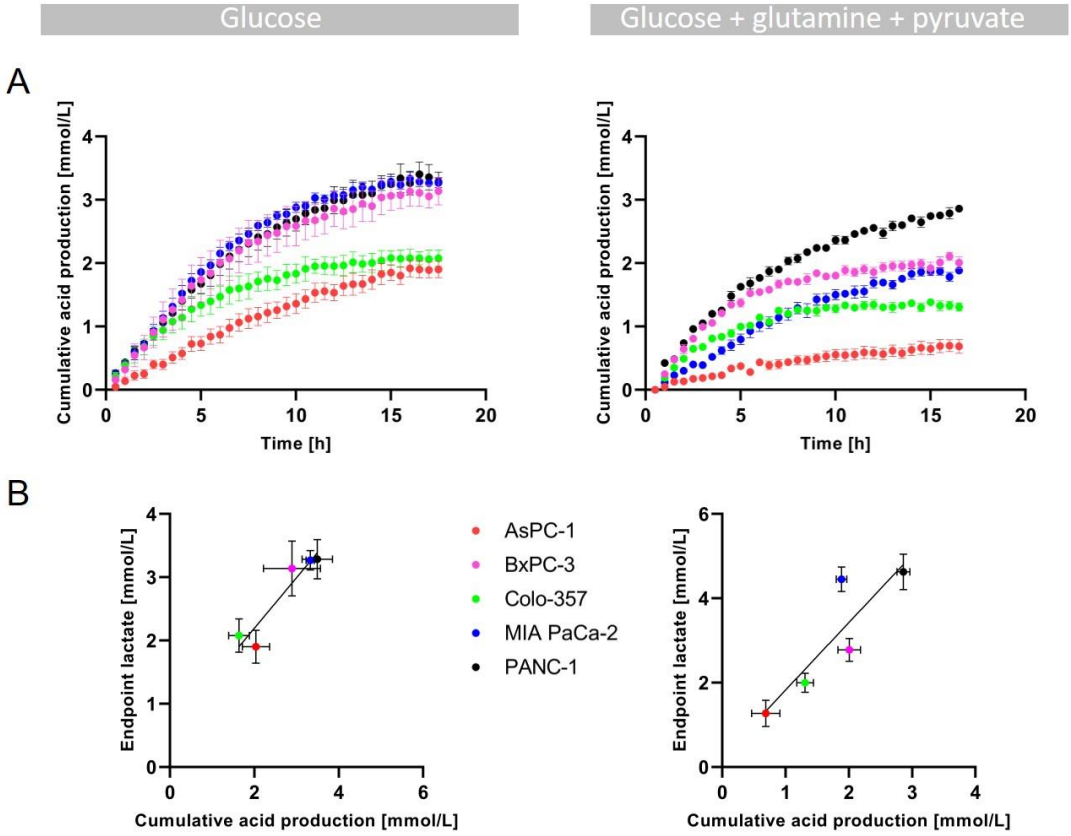


Figure 4.2 Metabolic acid production is dependent on available nutrients. A: Cumulative acid production in PDAC cells maintained in a medium containing either glucose only, or supplemented with glucose, glutamine and sodium pyruvate measured over 17 h. The addition of respiratory substrates (glutamine, pyruvate) decreases acid production and stimulates different responses in tested cell lines. B: Lactate produced measured in the medium after 17 h incubation plotted against cumulative acid production. A linear relationship between the two indicates that all acidity is of glycolytic origin. Maintaining PDAC cells in medium containing glucose only leads to higher lactate production and equimolar ratio of H^+ and lactate indicates glycolytic metabolism. Supplementing the medium with glutamine and pyruvate decreases lactate production and results in shifted H^+:lactate ratio suggesting a higher extent of respiration.

4.2.3. The effect of pH on glucose uptake

The inhibitory actions of extracellular acidity on glycolytic metabolism could be a result of decreased uptake of glucose under acidic conditions. This was verified by allowing cells to load with fluorescent glucose derivative, 2-(N-(7-nitrobenz-2-oxa-1,3-diazol-4-yl)amino)-2-deoxyglucose (2-NBDG) for 15 minutes in normal Tyrode-based solution titrated to pH ranging from 6.1 to 7.7. After the loading period, the solution was washed off by superfusion and the fluorescence of 2-NBDG was imaged. The uptake of fluorescent glucose derivative was found to be relatively insensitive to extracellular pH and did not change throughout the experiment (Fig.4.3).

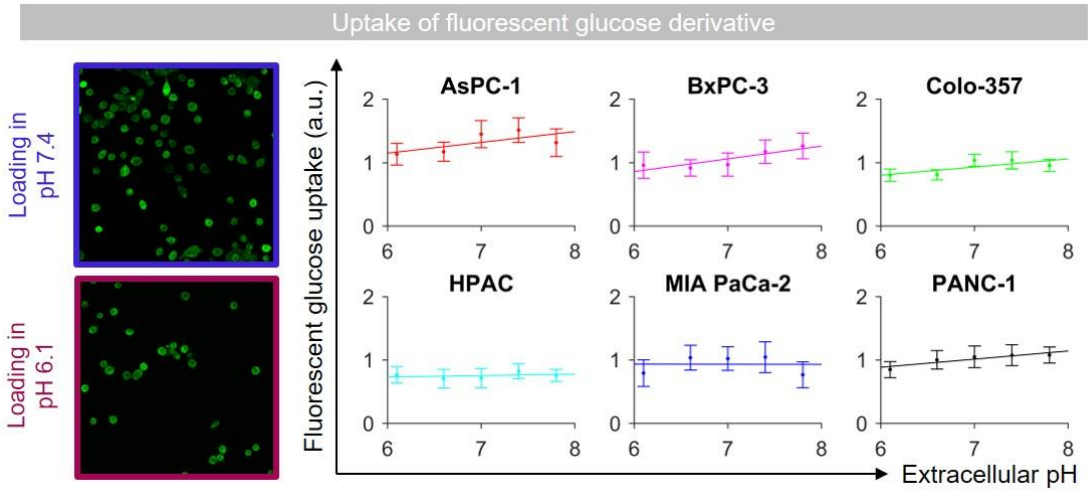


Figure 4.3 pH sensitivity of glucose uptake. Representative images showing uptake of fluorescent glucose derivative, 2-NBDG, at neutral and acidic pH. The plots depict the pH-sensitivity of glucose uptake in a panel of PDAC cell lines, no effect of pH on glucose uptake was observed. Data plotted as mean ± SD.

4.2.4. Glycolytic metabolism is inhibited by extracellular pH but not lactate

In the previous section, it was confirmed that lactic acid (glycolytic) flux is inhibited by low extracellular pH. Protons, however, represent only one of two products of glycolysis. To assess whether the negative feedback circuit is formed by protons or lactate, the sensitivity of glycolytic metabolism to its end products was tested by measuring the medium acidification rate with varying starting pH and lactate concentrations.

As depicted in Figure 4.4, extracellular pH had a strong inhibitory effect on lactic acid production, as opposed to lactate, which had only a mild effect. This indicates that the negative feedback circuit on glycolytic metabolism is mostly pH-dependent.

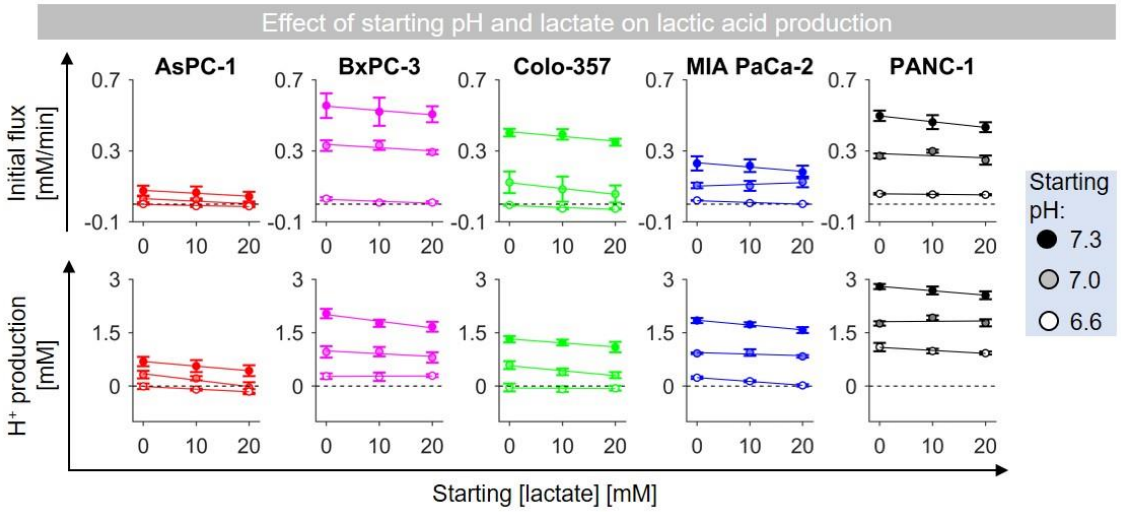


Figure 4.4 Effect of glycolytic end products, extracellular lactate and protons, on metabolic acid production rate. The initial lactic acid flux is strongly inhibited by low extracellular pH, as opposed to extracellular lactate, which has only a mild effect on metabolic acid production. The effect is observed in tested all PDAC cell lines, regardless of their baseline metabolic rates. The data are plotted as mean ± SEM.

4.2.5. *Negative feedback of extracellular pH can be disrupted by the increased buffering capacity*

The strong negative feedback of pH on cell glycolytic metabolism could be removed by increasing extrinsic buffering capacity, in this case, the buffering capacity of the culture medium. This would bind and scavenge the protons, allowing a more stable pH regardless of cell metabolic rates. This effect was tested by recording the time courses of extracellular acidification in a medium containing exogenous buffering provided by 5 mM acetate, propionate, butyrate, phosphate or imidazole. These buffers are characterised by different acid dissociation constants (pK_a), which are presented in Table 4.1. In fact, the addition of buffers of the pK_a closest to neutral (and starting) pH, phosphate and imidazole, significantly elevated metabolic acid production in MIA PaCa-2 and PANC-1 cell lines. Moreover, this effect was present regardless of the type of buffers used. Increasing the medium buffering capacity with 30 mM HEPES elevated glycolysis in both tested cell lines, while reducing the extracellular acidification rate. The increase in buffering also reduced the demand for oxygen (Fig.4.5B). Furthermore, the effect of buffering capacity on metabolic acid production was dose-dependent (Fig.4.5C).

Table 4.1 Acid dissociation constants (pK_a) of selected buffering agents at room temperature (RT).

Buffering agent	*pK_a at RT*	*Reference*
Acetate	4.54	(405)
Propionate	4.75	(406)
Butyrate	4.81	(407)
MES	6.15	(408)
Phosphate	6.82	(409)
Imidazole	6.95	(410)
HEPES	7.55	(360)

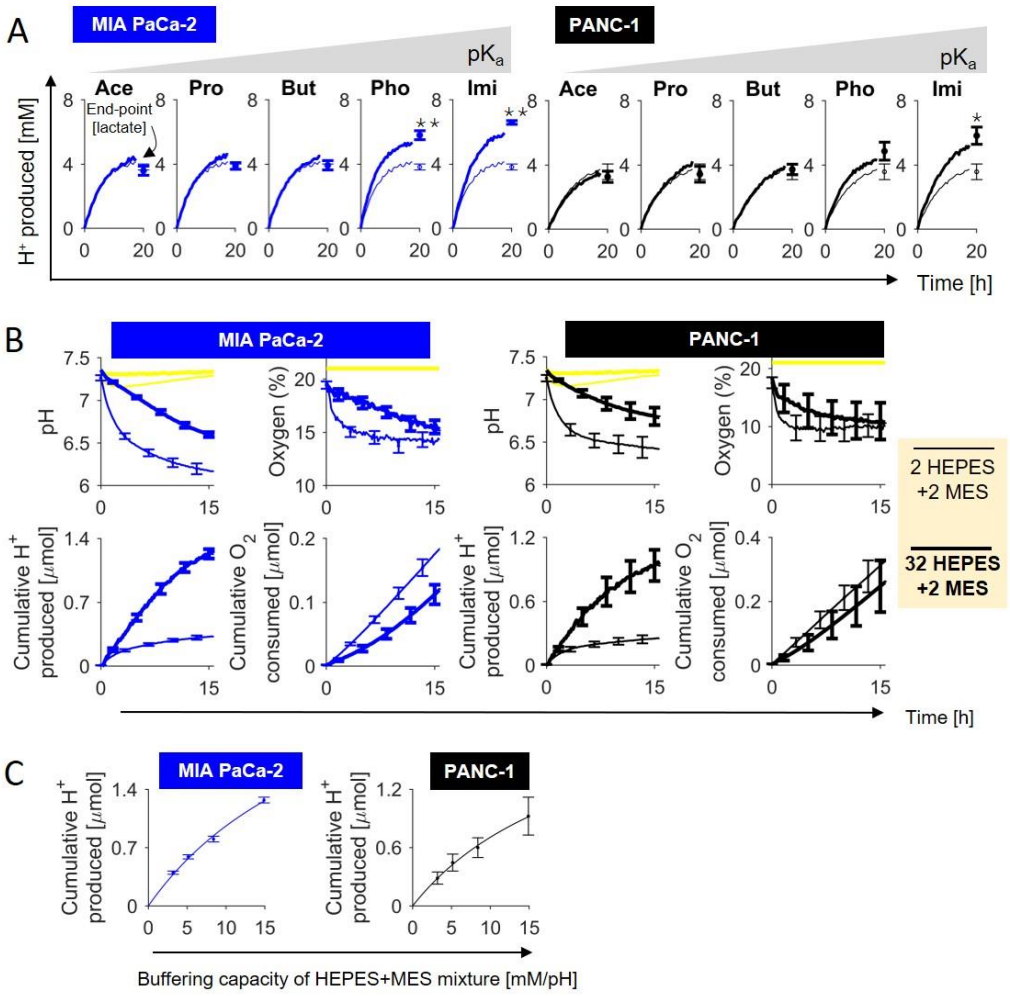


Figure 4.5 Increased medium buffering capacity removes negative feedback of extracellular pH and elevates glycolysis. A: Increasing medium buffering capacity by the addition of 5 mM phosphate and imidazole elevates glycolytic metabolism in MIA PaCa-2 and PANC-1 cells. Ace- acetate, Pro- propionate, But- butyrate, Pho- phosphate, Imi-imidazole. The data are strengthened by medium lactate measured at the end-point. B: Increasing medium buffering capacity by the addition of 30 mM HEPES maintains pHe at more stable levels and increases metabolic acid production and reduced oxygen consumption. Thick lines represent high buffering provided by 32 mM HEPES and thin depict low buffering conditions- 2 mM HEPES. Yellow lines represent cell-free controls. C: The effect of increased buffering capacity provided by HEPES and MES mixture elevates metabolic acid production in MIA PaCa-2 and PANC-1 cells. The effect of medium buffering on metabolic acid production is dose-dependent. Data plotted as mean ± SEM. Experiments from panels B and C have been conducted in collaboration with an undergraduate student, Hannah Williams.

The effects of medium buffering capacity on cell metabolism were confirmed using physiological buffering provided by CO_2/HCO_3^-. The low buffering conditions were achieved by the addition of 2.9 mM $NaHCO_3$ and maintaining the cells in a 0.5% CO_2 enriched atmosphere, as these conditions match the pH of 24 mM $NaHCO_3$ at 5% CO_2, i.e. both equilibrate to pHe 7.4. The buffering was increased by the addition of 50 mM

HEPES or 20 mM MES. The pK_a of MES is much lower than that of HEPES (6.15 vs 7.55), which makes it an unsuitable buffer at physiological, neutral pH. For this reason, the addition of MES served as a control for pH-independent effects of non-volatile buffering. Similarly, to previous experiments, increasing physiological buffering with addition of HEPES maintained more stable extracellular pH, and as expected, the addition of MES did not yield the same result, due to the extracellular pH being outside its optimal range (Fig.4.6A). Higher buffering increased metabolic acid production, however, no effects on oxygen consumption were observed (Fig.4.6B). Furthermore, the proliferation of cells cultured in a medium of low buffering was significantly reduced compared to cells exposed to higher buffering, regardless of the type of buffering agent used (Fig.4.6C).

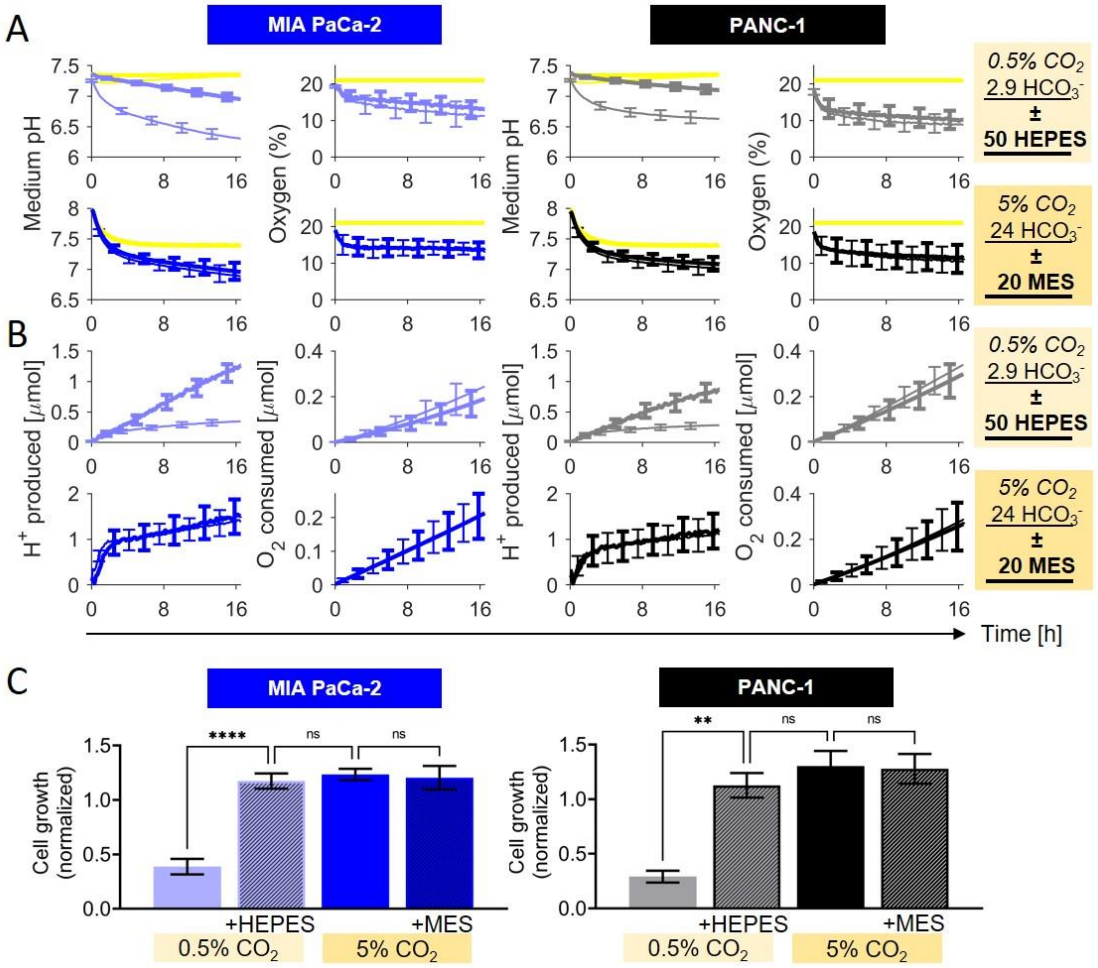


Figure 4.6 Increasing buffering capacity with volatile buffers elevates glycolysis. A: Time course of medium acidification and oxygen consumption of cells incubated for 17 h at low physiological buffering with and without supplementing buffering provided by HEPES and MES buffers. Yellow lines represent cell-free controls. As depicted in the legend on the right, thin lines represent the effects of low buffering attained by the addition of 2.9 mM NaHCO3, and bold lines represent increased buffering achieved by the addition of 2.9 mM NaHCO3 and 50 mM HEPES. Increasing already high buffering capacity (24 mM NaHCO3 +20 mM MES) does not affect cell metabolism. B: Increasing low physiological buffering by addition of 50 mM HEPES elevates metabolic acid production. Increasing already high physiological buffering by the addition of MES does not further enhance glycolytic metabolism. C: Increasing medium buffering capacity promotes cell proliferation irrespective of the type of buffering agent used. The significance was calculated with ordinary ANOVA with Tukey's multiple comparisons test. These data have been collected by FHS student, Hannah Williams.

The inhibitory effects of low extracellular pH on cell metabolism were confirmed using the Seahorse Analyzer. The cell metabolism was assessed at baseline, in standard, lightly buffered medium, and after injection with acidic media, which created stepwise acidification ranging from pH 4.4 to 7.4. The second, alkaline injection restored the initial, neutral pH. Extracellular acidification rate corresponding to glycolytic metabolism

was highly pH-dependent, with complete inhibition observed at pH 6 (Figure 4.7A). The striking similarity of the pH-sensitivity curves between the cell lines suggests a conserved mechanism of pH-induced glycolysis inhibition. On the contrary, the oxygen consumption rate was unaffected by changes to extracellular pH (Figure 4.7B).

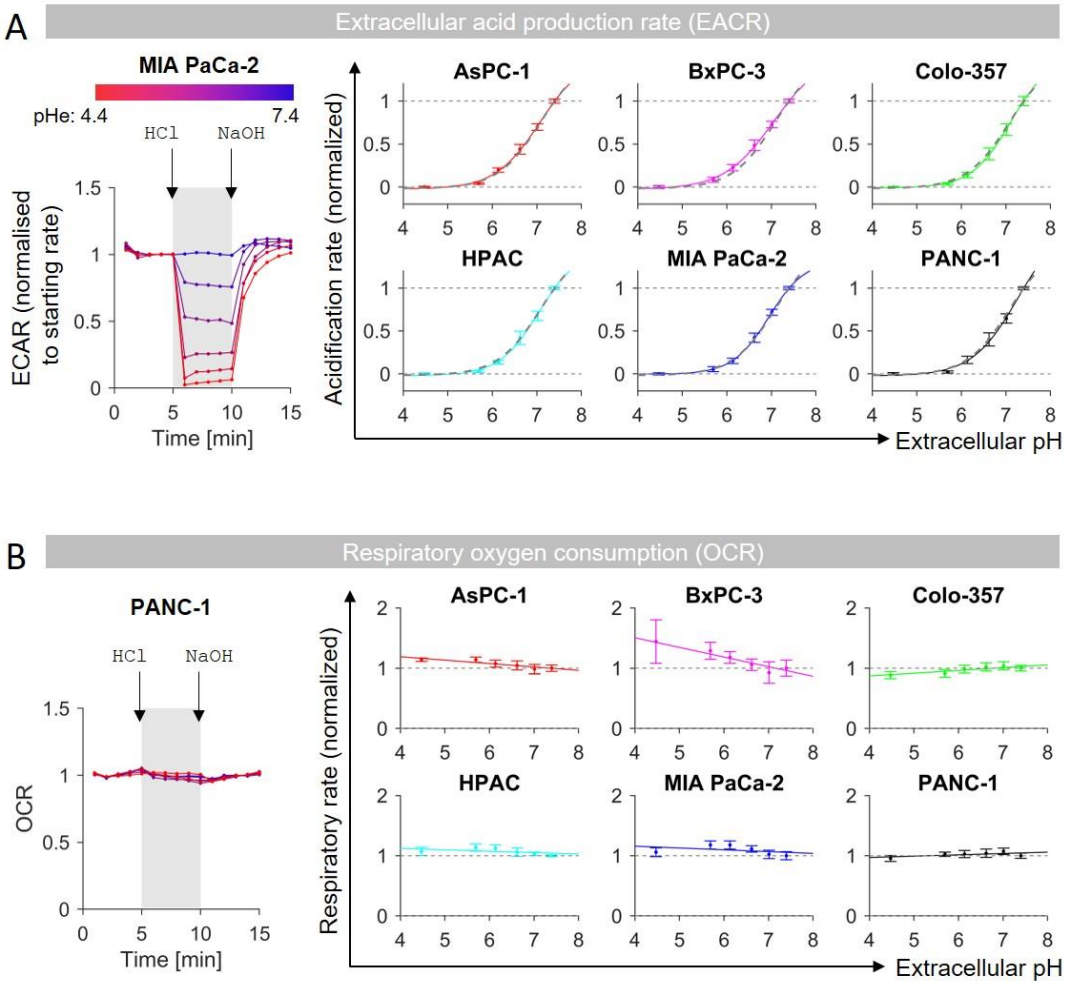


Figure 4.7 Effect of pH on glycolytic and oxidative metabolism. A: Representative plot depicting extracellular acidification rate (ECAR) in response to injections with acidic and alkaline media. Extracellular acidification rate is strongly pH dependent, with complete inhibition observed at pH 6, the result is strikingly conserved between tested cell lines. Data plotted as a mean ± SEM. B: Representative plot of oxygen consumption rate (OCR) in response to injections of acidic and alkaline media. The oxygen consumption rate is insensitive to changes in extracellular pH. Data plotted as a mean ± SEM.

4.2.6. Membrane permeability

The data shown previously strongly indicate that a pH-related mechanism controls glycolysis. This point of control might be at the final glycolytic step, which is the lactic acid extrusion through the Monocarboxylate Transporters. This family of proteins are commonly expressed and catalyse the passive, bidirectional and proton-coupled transport of monocarboxylates, i.e. pyruvate, lactate and ketone bodies (411, 412). The transporters have been widely studied in muscle physiology. During extensive exercise, high concentrations of lactic acid are produced and excreted into the extracellular space leading to transient lactic acidosis in the muscle tissue (413). More recently, MCTs have gained interest in cancer, as their lactic acid removal stabilizes glycolytic metabolism and allows cancers to grow and proliferate (414). The abundance of these proteins, both in cell lines and tumours as well as their surface expression inspired the idea of pharmacological inhibition, which, in theory, should reduce the glycolytic potential of the cell and in turn reduce tumour growth. Several MCT inhibitors have been designed and some of them entered clinical trials (415). However, to this day, no MCT inhibitor has been approved for therapeutic use. Here, the assumed link between the glycolytic rate of the cell and MCT-based lactic acid transport, as well as the efficiency of MCT inhibitors to reduce glycolytic flux was evaluated.

The MCT permeability was assayed by recording the rate of intracellular pH change in cells pre-equilibrated in normal Tyrode solution containing 30 mM sodium lactate. The cells seeded on Lab-Tek slides were loaded for 10 min with the intracellular pH reporter, cSNARF1. The cells were loaded with lactate by superfusion with 30 mM

lactate containing normal Tyrode for 5 minutes, after which, the solution was rapidly exchanged for lactate free, which triggered the efflux. Note that the solution exchange was very rapid, and happened within 25 ms, which removed the possibility of recording the effects of mixing artefacts. After allowing cells to extrude the lactate for 2 minutes, the lactate-containing solution was introduced again. The MCT permeability was calculated by multiplying the rate of pHi change by intrinsic buffering capacity. The intrinsic buffering capacity of PDAC cells was assessed using the previously described ammonium removal method. The protocol is described in detail in Chapter 2.

The MCT permeability in a panel of six pancreatic ductal adenocarcinoma cell lines was assessed. The MCT activity was cell line dependent, with MIA PaCa-2 cells showing the highest mean permeability (Fig.4.8).

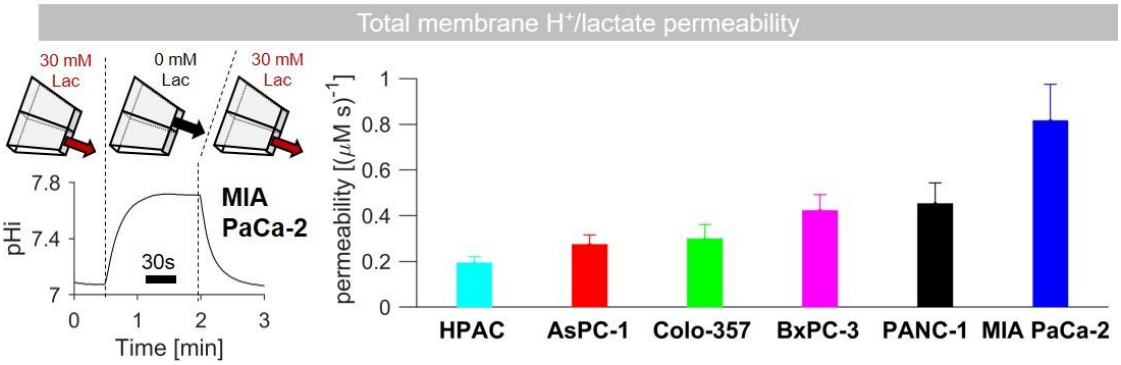


Figure 4.8 MCT permeability in PDAC cell lines. On the left the exemplar time-course of intracellular pH change enforced by solution exchange. On the right permeability of PDAC cells, ranked from the lowest to highest, shown as mean ± SEM.

To assess the potential link between the MCT permeability and glycolytic metabolism regulation, the glycolytic rate of cells was measured using two separate methods. At first, in the acute setting, by assessing the rate of intracellular acidification following the inhibition of lactic acid efflux with a non-selective MCT inhibitor, α-cyano-4-OH-cinnamate (CHC). The baseline pHi was measured by superfusion with

normal Tyrode at pH 7.4. Next, the superfusate was exchanged for a solution containing 2 mM CHC. To ensure that enforced intracellular acidification is not compensated for by the activity of NHE-1, its inhibitor, dimethyl amiloride (DMA) at 30 µM was added to both microstreams. The metabolic lactic acid production in mM/min is shown in Figure 4.9A. The second method used to assay the glycolytic rate was measuring the time courses of medium acidification during 17-hour incubation (Fig.4.9B). The cells were seeded at high density (50,000/well) in black 96-well plates. On the next day, the standard culture medium was exchanged for 100 µL of lightly buffered (2 mM HEPES, 2 mM MES-containing) medium with cSNARF1-dextran. The conjugation of cSNARF1 with dextran prevented the dye from entering the cells and ensured probing only extracellular pH. The plate was put into the Cytation 5 plate reader and the measurements were taken every 30 minutes over the next 17 hours. Afterwards, the medium was removed and frozen at -20°C for biochemical lactate measurements. The linear relationship between cumulative protons excreted into the medium and final lactate concentration confirms the glycolytic source of acidity (Fig.4.9C).

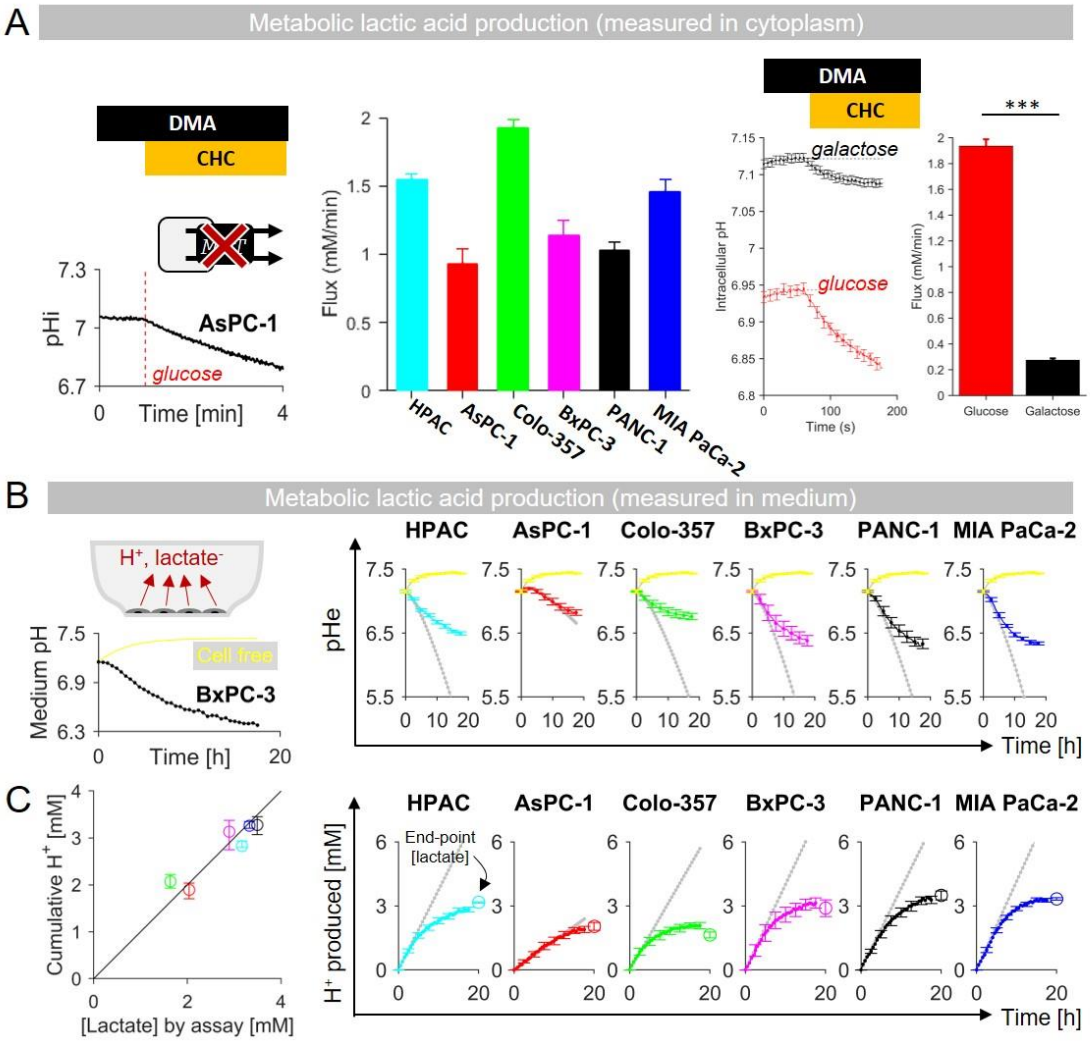


Figure 4.9 Glycolytic rate of PDAC cells. A: Metabolic lactic acid production, measured in the cytoplasm within 5 minutes of pan-MCT inhibition. On the left exemplar time-course of intracellular acidification following the MCT inhibition, on the middle bars representing cell line-dependent flux of lactic acid. On the right, the exemplar time course of cell acidification when superfused with a solution containing either glucose or galactose confirming the accuracy of the method. B: Metabolic lactic acid production measured in the culture medium. On the left, the exemplar time course of medium acidification, of the cell line-specific time courses of medium acidification. The final lactic acid concentration in the medium is plotted as a dot and colour-coded to match each cell line. Yellow lines indicate cell-free wells and grey depict the initial acidification rate. C: The linear relationship between cumulative H^+ excreted and medium lactate concentration measured at the end-point of the assay. Data plotted as mean of three biological repeats ± SEM.

Irrespectively of the method used to assay the glycolytic rate of cells, there was only a weak correlation between lactic acid production rate and MCT permeability across the range of tested PDAC cell lines (Fig.4.10) suggesting that some other factor, rather that MCT activity alone sets the glycolytic rate of cells.

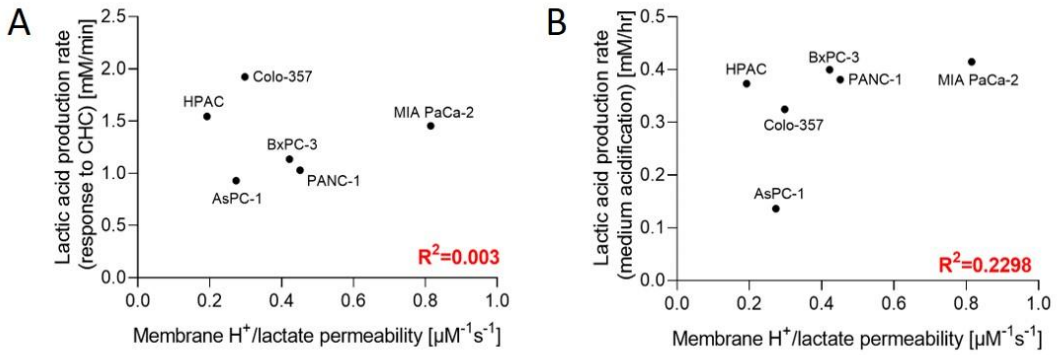


Figure 4.10 The correlation between MCT permeability and rate of cellular lactic acid production. A: Lack of correlation between lactic acid production rate assessed via cytoplasm acidification and membrane permeability to lactic acid, R2=Pearson's coefficient. B: Lack of correlation between lactic acid production rate assayed via medium acidification and membrane permeability to lactic acid.

4.2.7. The pH dependence of MCT permeability

Because low extracellular pH was found to be a potent inhibitor of glycolytic metabolism (as opposed to lactate) the assessment of pHe effects on lactic acid extrusion, i.e. MCT permeability was necessary. To measure the activity of the transporter in response to pH, cSNARF1-containing cells were loaded with lactate by superfusion with 30 mM lactate-containing solution at neutral pH. After a 5-minute period of equilibration, the solution was exchanged for lactate-free titrated to pH ranging from 5.7 to 7.4. MCT permeability was strongly pH dependent with complete abrogation of lactic acid flux below pH 6. This effect was remarkably conserved between the cell lines, regardless of the expression pattern of various MCT isoforms (Fig.4.12A).

Even activation of hypoxic signalling, by 48-hour-long incubation with 1 mM dimethyloxalylglycine (DMOG, which increases the expression of MCT4 isoform (121)) prior to experiments did not affect the pH sensitivity of lactic acid transport (Fig.4.12B), confirming that the pHe-MCT permeability relationship is universal regardless

of the type of isoform expressed. DMOG-induced hypoxic signalling activation was confirmed (Fig.4.11).

The experiments conducted so far revealed that glycolytic metabolism was negatively affected by one of two end-products of glycolysis: extracellular acidity and not extracellular lactate. The striking resemblance of pH-sensitivity of extracellular acidification rate and MCT permeability might suggest a conservative MCT-oriented mechanism of glycolytic rate regulation, but further research is required.

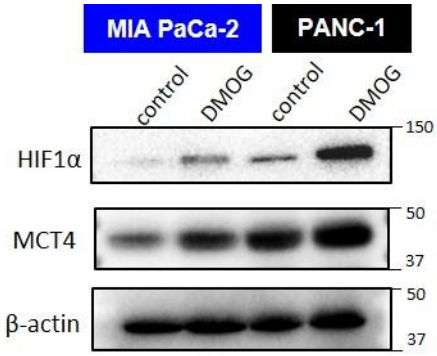


Figure 4.11 Treatment with DMOG activates hypoxic signalling in PDAC cells. MIA PaCa-2 and PANC-1 cells were incubated with 1 mM DMOG at normoxic oxygen conditions for 48h prior to lysate preparation.

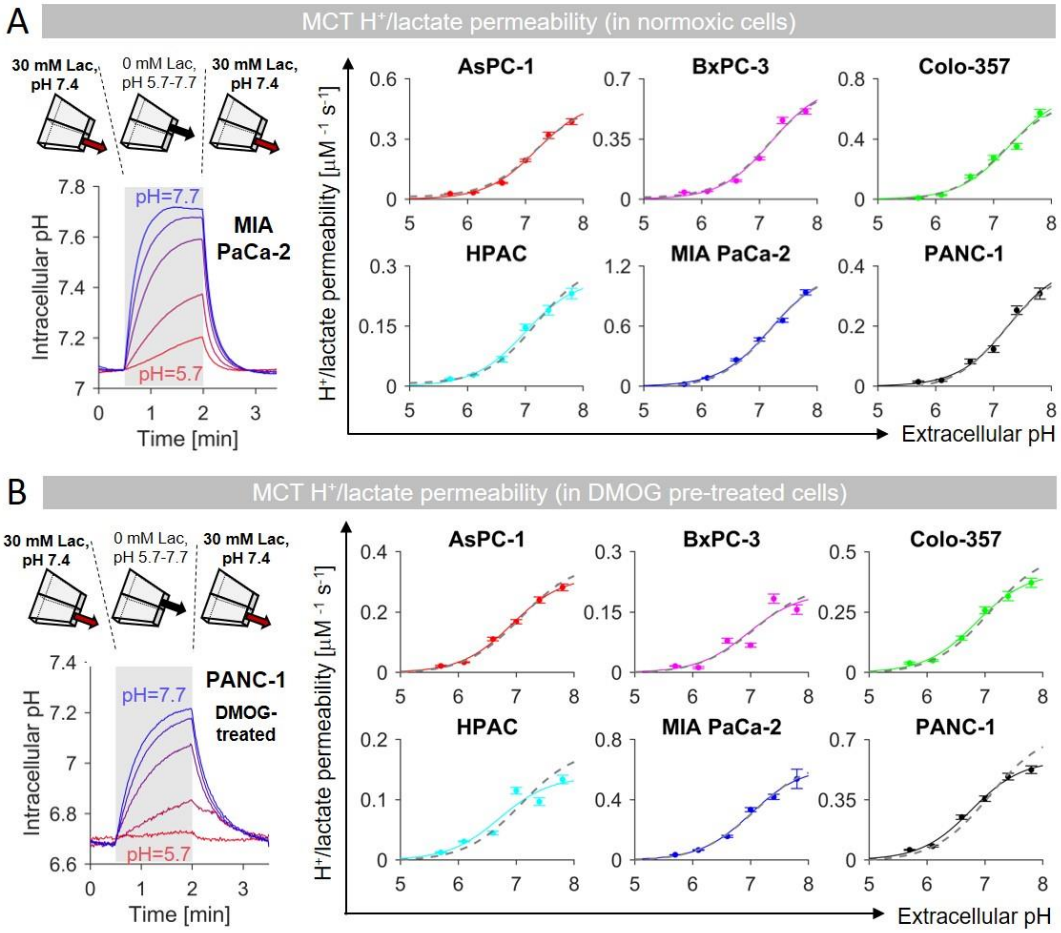


Figure 4.12 pH dependence of MCT permeability. A: Representative plot showing the experimental setting. Cells were loaded with lactate by superfusion at pH 7.4, next the lactate release was triggered by exchanging the lactate-free solution of pH ranging from 5.7 to 7.7. The rate of intracellular pH change was recalculated into the pH sensitivity of permeability. Membrane permeability to lactic acid was strongly pH dependent, with a complete abrogation of transport observed at pH 6. This effect was conserved in all tested PDAC cell lines, and was irrespective to MCT isoforms expressed. Grey lines show the mean for all six lines. Data plotted as mean ± SEM. B: Representative plot showing the experimental setting. The MCT permeability of cells with activated hypoxic signalling (cells incubated with 1 mM DMOG for 48 hours prior to experiments) is similarly pH dependent as normoxic cells. Grey lines show mean for all six lines. Data plotted as mean ± SEM.

4.2.8. MCT inhibitors reduce permeability but fail to limit the glycolytic flux

The appeal of MCT inhibitors comes from the assumption that a reduction in permeability of the transporter will abrogate the flux, thus, inhibiting glycolysis and starving cancer cells, rendering them unable to grow. For that reason, several inhibitors have been designed including SR13800 (416), AR-C155858 (417), 7AAC2 (418), and others developed by Astra Zeneca (419, 420). After initial success, only one managed to enter the clinical trials, AZD3965 (421). These compounds are specific inhibitors targeting MCT-1 and/or MCT-2. The only selective inhibitor towards MCT4, and to a lesser extent MCT-1, is syrosingopine (422). In this section, the capacity of MCT inhibitors to reduce the permeability of the transporter was confirmed and cell lines dependent on MCT-1 and MCT-2 activity were identified.

The reduction of the MCT permeability (P_{MCT}) was confirmed following the treatment with all inhibitors, with significant reductions in activity following the addition of 1 µM SR and ARC. The 1 µM dose of syrosingopine created only a mild effect of about a 30% reduction in P_{MCT} and increasing the dose to 10 µM led to about a 50% decrease in membrane permeability to lactic acid (Fig.4.13A). All tested cell lines expressed, however small amounts of MCT-1, with the highest expression observed in MIA PaCa-2 cells. The expression of MCT-2 isoform was also universal, however, only half of the tested cell lines expressed MCT-4, including BxPC-3, Colo-357 and PANC-1 (Fig.4.13B). The dependence of lactate membrane permeability on MCT-1 and MCT-2 was assessed based on cell response to A-RC inhibitor, and two cell lines of opposite phenotypes, highly sensitive to A-RC, MIA PaCa-2 cells and non-responsive PANC-1, were selected for further analysis.

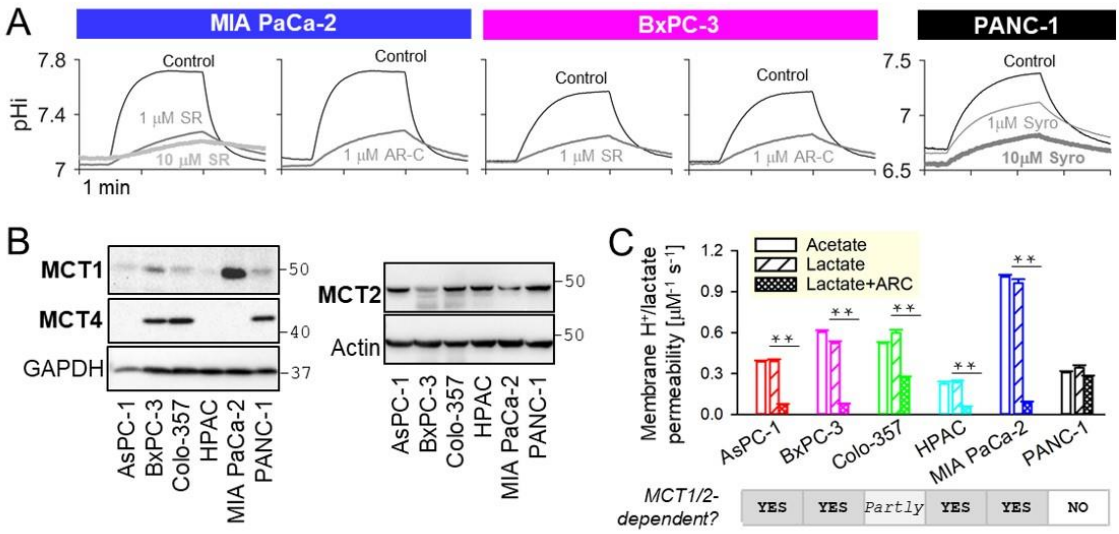


Figure 4.13 Pharmacological inhibitors successfully reduce the permeability of the monocarboxylate transporters. A: Exemplar plots of MCT permeability with or without the inhibitors: AR-C155858 (A-RC), SR13800 (SR), syrosingopine (Syro). B: Western blot confirming the expression of MCT 1, 2 and 4 isoforms in tested cell lines. C: Sensitivity of membrane permeability to lactic acid to A-RC (MCT-1/2 inhibition).

However, the sole reduction of permeability is no guarantee that lactic acid flux will be reduced as well. In case of MCTs, which carry a proton and a lactate ion across the membrane, the flux of lactic acid (J_{lac}) will depend not only on permeability of the transporter itself (P_{MCT}), but also on the driving force, here represented by a gradient of lactate (Δlac, see Equation 9 below).

$$Jlac = PMCT * \Delta lac \quad (9)$$

According to that Equation 9, a reduction in permeability, e.g. created by pharmacological inhibition could be compensated for by an increase in lactate gradient. To test this hypothesis, the time courses of medium acidification with and without the addition of various MCT inhibitors, AR-C155858 (AR-C), α-cyano-4-OH-cinnamate (CHC), SR13800 (SR) and syrosingopine (Syro), were recorded and compared with measurements of lactate excreted into the medium after the experiment. The equivalent doses were highly potent in reducing the MCT permeability as confirmed

previously (Fig.4.13). However, none of the inhibitors had an effect on total acid flux, which remained unaltered regardless of the treatment (Fig.4.14A-B). Additionally, no decrease in lactic acid excretion was observed when medium lactate measurements were performed (Fig.4.14C-D).

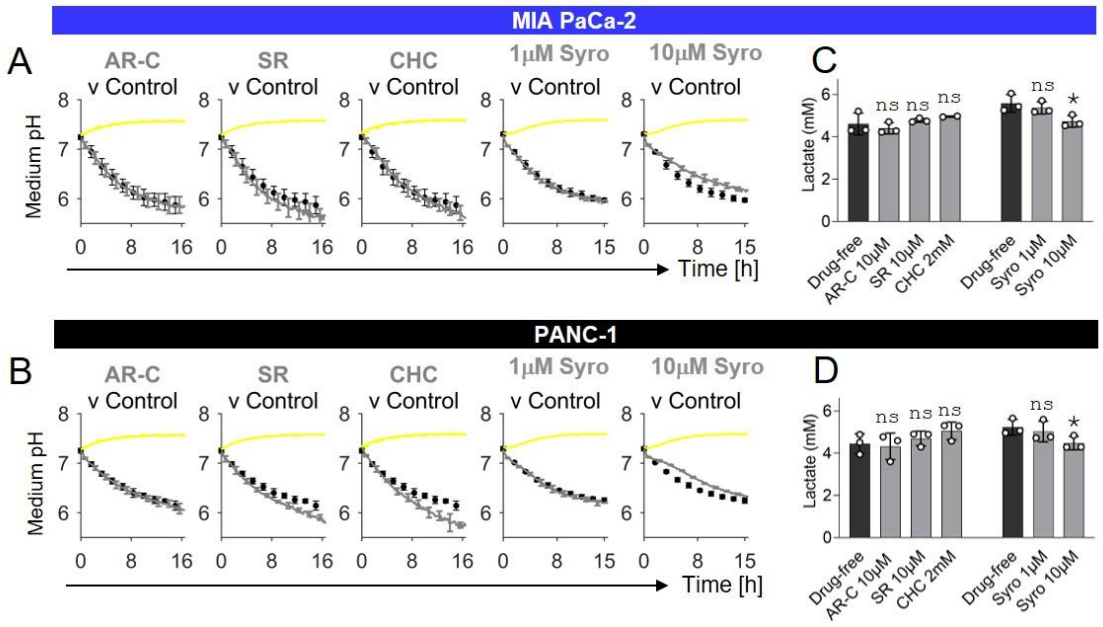


Figure 4.14 Pharmacological MCT inhibition does not impact the glycolytic flux. A&B: The time course of medium acidification with the addition of 10 µM AR-C (AR-C155858), 10 µM, SR (SR13800), 10 µM Syro (Syrosingopine) and 2 mM CHC (α-cyano-4-OH-cinnamate) in MIA PaCa-2 and PANC-1 cells. Data plotted as mean ± SEM. C&D: Lactate production [mM] after 17 h incubation with the inhibitors AR-C, SR, CHC and Syro remains unaltered.

According to Equation 1, the lactate flux could potentially be maintained even at reduced permeability due to increased lactic acid gradient. The pharmacological MCT inhibition, despite decreasing permeability, does not impact cell metabolism itself, neither glycolytic nor oxidative. The metabolic assay revealed that MCT-1 inhibitor, SR13800, does not affect metabolic acid production and oxygen consumption in either cell line (Fig.4.15), allowing for the cell to continue its metabolism. This, in turn, could lead to increased accumulation of intracellular lactate (as a reduction in permeability will render lactic acid efflux less efficient, at least initially), which corresponds

to the increased driving force. This would then compensate for the reduction in membrane permeability and leave the overall lactate flux unaltered. This hypothesis was tested by assessing the total protein lactylation following the treatment with inhibitors. The suitability of total protein lactylation as a marker for intracellular lactate concentration was evaluated by comparing its levels between untreated, control cells cultured in standard medium for 17 hours, cells maintained in medium, where glucose was substituted by galactose (negative control), and cells cultured in the medium supplemented with 30 mM sodium lactate (positive control). The representative blots and semi-quantification of total protein lactylation are presented in Figure 4.16.

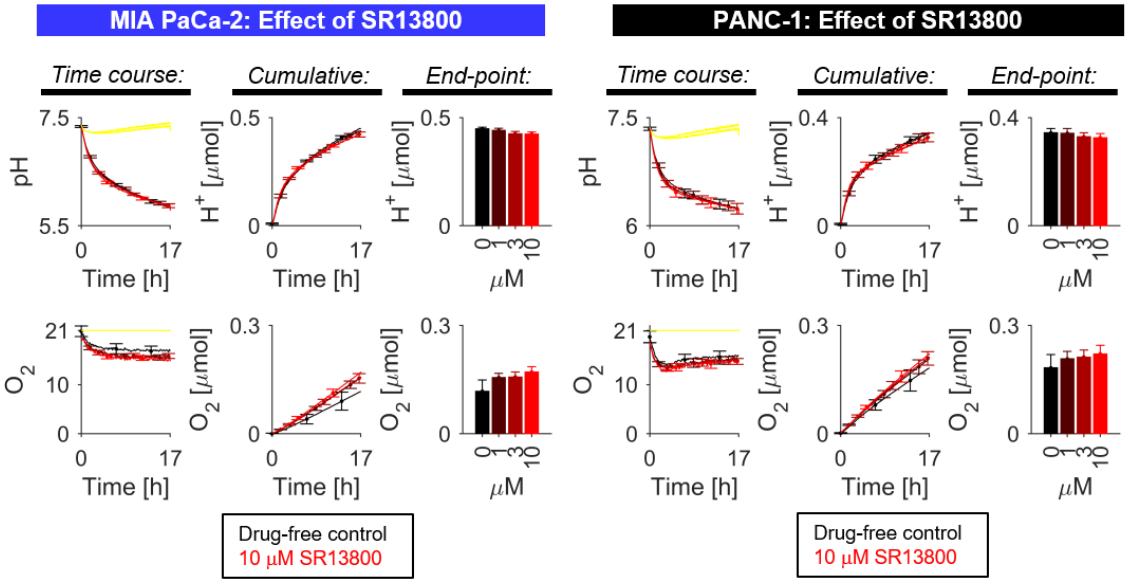


Figure 4.15 Pharmacological MCT inhibition does not affect cell metabolism. Treatment with increasing doses of SR13800 does not impact metabolic acid production or cell oxygen consumption in either of tested cell lines. Data plotted as mean ± SEM.

Assessment of total protein lactylation revealed that it was significantly increased following the treatment with the MCT inhibitors, ARC and CHC. These results support the notion that MCT-based lactic acid transport is auto-regulated and cannot be significantly affected by a change to permeability only. A reduction in permeability will be compensated for by an increase in the driving force (here: lactate gradient),

which will rescue the glycolytic flux even at low permeability. With that regard, the auto-regulation of MCT-based transport poses a vital survival mechanism for cells, as it protects them from metabolic inhibition, which unfortunately renders the actions of MCT inhibitors unfeasible in a clinical setting. The previously reported anti-cancer effects of MCT inhibitors might therefore be a result of a non-MCT specific mechanism of action, or from the toxicity of high cytoplasmic lactate concentrations.

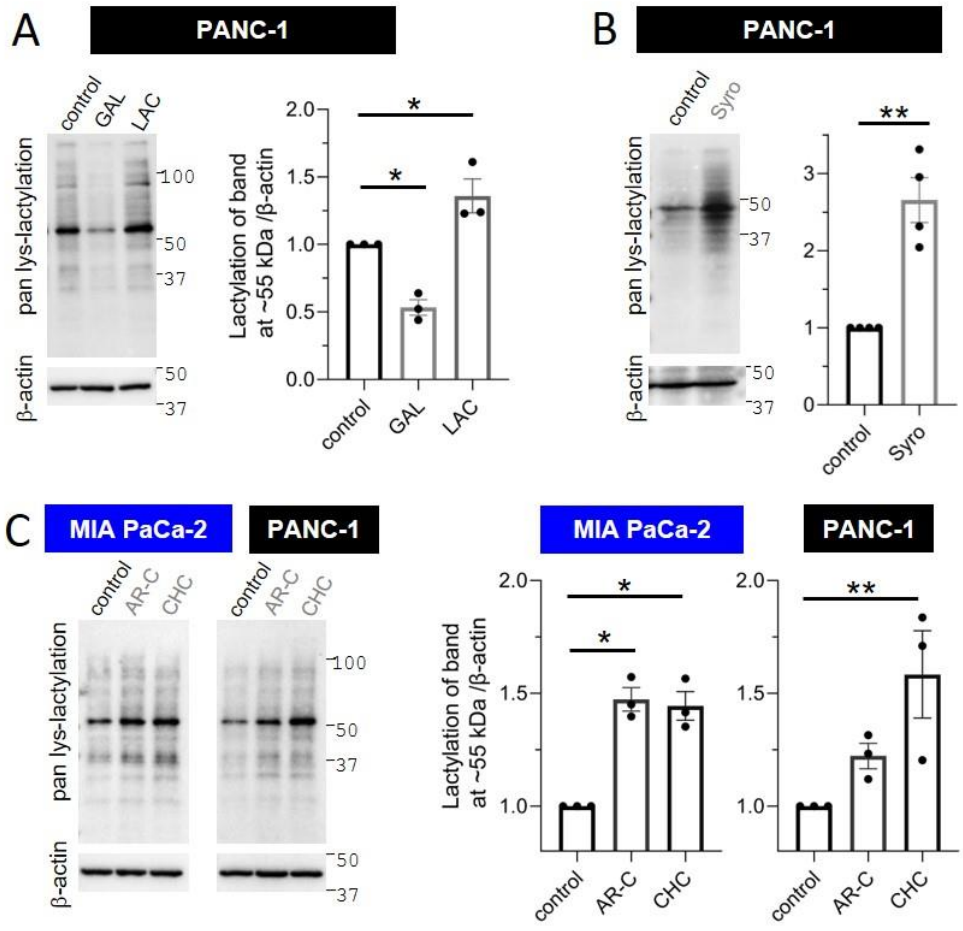


Figure 4.16 Pharmacological MCT inhibition increases total protein lactylation. A: Total protein lactylation compared between cells cultured in standard medium (control), medium containing galactose instead of glucose (GAL, negative control) and medium supplemented with 30 mM sodium lactate (positive control). Substitution of glucose for galactose decreases overall protein lactylation, and incubation of the cell with a medium containing exogenous lactate increases total protein lactylation. B: Treatment with 10 µM of syrosingopine (Syro) significantly elevates total protein lactylation in PANC-1 cells. The representative blot and semi-quantification of 3 biological experiments, the data are presented as mean ± SEM. C: Treatment with 10 µM of AR-C155858 (AR-C) and 10 µM α-cyano-4-OH-cinnamate (CHC) significantly elevates total protein lactylation in MIA PaCa-2 and PANC-1 cells. The representative blot and semi-quantification of 3 biological experiments, the data are presented as mean ± SEM.

4.2.9. The coupling between intra- and extracellular pH

The extracellular pH in healthy tissues is tightly controlled and does not exceed the range between 7.35-7.45 (423). The mechanisms of pH control become deregulated in cancer, which impacts both intra- and extracellular compartments. The tumour milieu, especially in highly glycolytic solid tumours is significantly more acidic than adjacent tissues reaching values of 6.3 (279, 284). On the contrary, the intracellular pH of cancer cells has been reported as alkaline (424). Overall, pH dynamics is of high importance in cancer, and the coupling between intracellular and extracellular pH needs to be measured in order to accurately assess the inhibitory mechanisms of pH. The response of the cytoplasmic compartment to extracellular acidity was tested at single-cell resolution by equilibrating cSNARF1-containing cells with a normal Tyrode solution of pH 7.4. Next, the solution was rapidly exchanged to another one, of acidic pH, 6.1 and 5.7. The intracellular acidification was recorded for two minutes, after which the initial, neutral solution was reintroduced. The intracellular response to acute extracellular acidification is depicted in Figure 4.17A. All tested cell lines acidified in response to superfusion with acidic solution, however the response varied among cell lines, with BxPC-3 and PANC-1 being the most susceptible to changes in microenvironmental pH. The coupling between intra- and extracellular pH was investigated further by imaging cSNARF1 fluorescence of cells pre-equilibrated in media of pH ranging from 5.7 to 7.7. On average extracellular acidification of 1 pH unit decreased intracellular pH of PDAC cells by 0.6 of unit (Fig.4.17B).

This pHe-pHi relationship suggests that all inhibitory effects of extracellular acidity on glycolytic metabolism and MCT permeability might reflect the ingress of H^+ into

the cytoplasmic compartment, rather than a direct inhibitory effect on the monocarboxylate transporters.

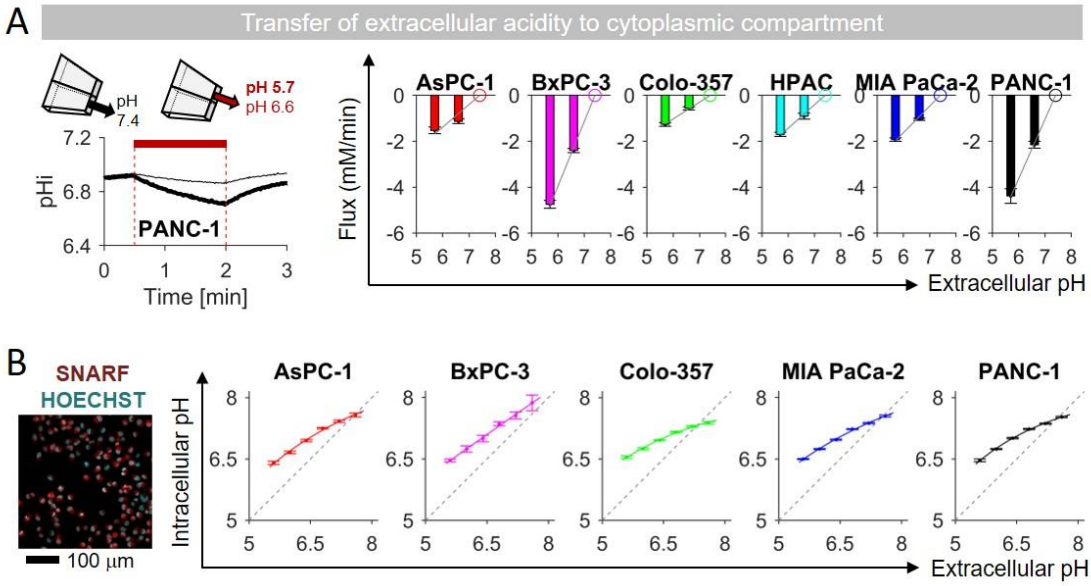


Figure 4.17 Transfer of extracellular acidity into the cytoplasm. A: Representative plot depicting the experimental setup. Cells loaded with cSNARF1 were equilibrated at neutral pH, next the solution was exchanged to one titrated to pH 6.6 or 5.7. The rate of intracellular acidification was recorded for 2 minutes, after which the initial, neutral solution was reintroduced. PDAC cells acidify in response to acute acidification of the extracellular compartment, with the strongest acidification observed in BxPC-3 and PANC-1 cell lines. B: Representative image showing cells loaded with cSNARF1 and Hoechst used to analyse the coupling between intra- and extracellular pH. The relationship between the intra- and extracellular pH in a panel of PDAC cell lines. Data shown as mean ± SEM.

4.2.10. The intracellular pH as a factor setting the glycolytic rate of cells

To accurately distinguish between the direct effects of extracellular pH on cell metabolism, and secondary actions on the cytoplasmic compartment, the cells were incubated in a low chloride medium. The use of the medium with minimal chloride concentration impairs the activity of members of the anion exchanger protein family, including Anion Exchanger 2 (AE2), which under normal conditions exchanges a single HCO_3^- ion for a single Cl^- (425). Substitution of normal medium to low chloride inactivates AEs as one of the substrates necessary for the transport is missing. This approach traps all HCO_3^- (that otherwise would have been removed from the cell) inside the cytoplasm, raising intrinsic buffering and intracellular pH (426). The alkalization of the intracellular compartment without affecting extracellular pH evoked by incubation in a low chloride medium was confirmed in MIA PaCa-2 and PANC-1 cell lines (Fig.4.18A). This in turn elevated metabolic acid production in both tested cell lines (Fig.4.18B), confirming that glycolytic metabolism is primarily controlled by intracellular pH, rather than extracellular conditions.

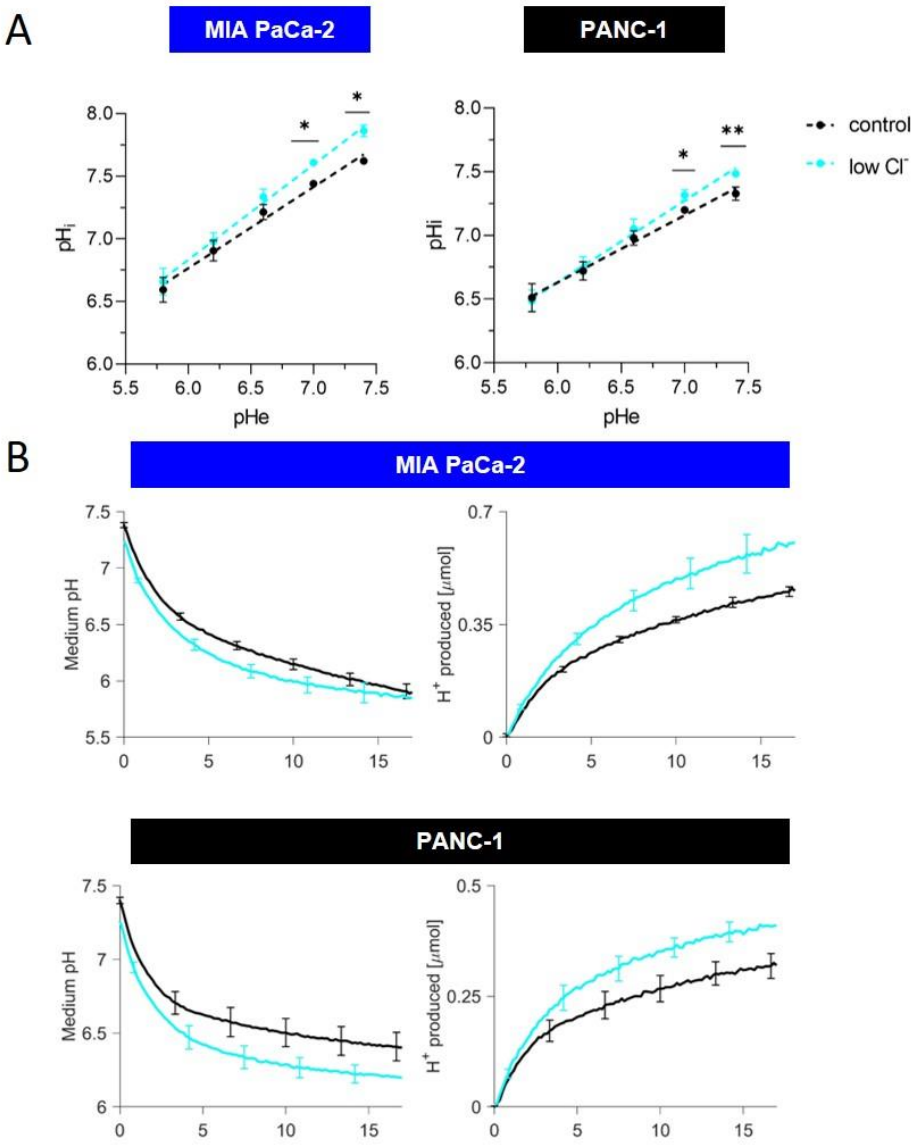


Figure 4.18 The effect of intracellular pH on glycolytic metabolism of PDAC cell lines. A: Incubation in low chloride medium increases intracellular pH without affecting extracellular pH. B: Increased intracellular pH facilitates metabolic acid production in MIA PaCA-2 and PANC-1 cell lines. Data shown as mean ± SEM. Black lines denote cells incubated in standard medium, and cyan low chloride medium.

4.3. Discussion

This Chapter provides a description of glycolytic and oxidative metabolism in Pancreatic Ductal Adenocarcinoma cell lines, with the focus on glycolysis and the cues with the capacity to influence the glycolytic rate. The baseline glycolytic metabolism is cell line dependent and does not respond to the accumulation of its two end-products equally, as the effects of extracellular lactate are negligible, while extracellular pH has a strong negative feedback on glycolysis. This feedback can be disrupted by increasing buffering capacity of the medium, which based on the chemical characteristics of the buffering provided efficiently scavenges protons and maintains a more stable extracellular pH. Furthermore, it was confirmed that the inhibitory effects of extracellular protons come from intracellular acidification rather than a direct effect on MCTs. The limitations of MCT-targeted inhibitors were evaluated, which revealed that even though efficient at reducing permeability, the inhibitors do not affect the overall lactic acid flux. One possible explanation could be an autoregulatory mechanism, which rescues lactic acid flux by a compensatory increase in driving force.

Glycolysis is understood to be allosterically controlled at the level of three irreversible reactions catalysed by hexokinase (427), phosphofructokinase (428), and pyruvate kinase (429) all of which respond to the concentrations of substrates. A similar mechanism could apply to monocarboxylate transporters, which strategically positioned on the cell membrane, could be affected by extracellular levels of glycolytic end-products (lactate and protons) and shut down the efflux and possibly the glycolysis itself. The assumption that inhibition of MCT permeability will adequately limit glycolytic metabolism is widespread, and led to development of several MCT inhibitors,

all of which supposedly target and subsequently starve the Warburg effect-dependent cancer cells. As confirmation of the inhibitory actions, these studies point out the increased intracellular lactate build-up (416, 430-433), reduction in cellular lactate uptake (433), and treatment-induced reduction in proliferation (434, 435). Unfortunately, that is not the sole interpretation of the data. The elevated intracellular lactate levels following the treatment with inhibitors have also been observed in this Chapter, however, contrary to literature, it was supported by permeability measurements and prolonged lactic acid flux recordings, taken at more physiologically relevant time periods. The comprehensive explanation of autoregulatory mechanism of MCT-based lactic acid transport was proposed, in which reduction of permeability, allows for cytoplasmic lactate build-up until the increase in lactate gradient will rescue the flux even at reduced permeability. The idea of MCT-operated lactic acid export auto-regulation is novel and has not yet been suggested. This phenomenon is well understood and has been reported previously in case of RyR-type calcium channels, which are insensitive to exogenous modulators (affecting permeability), as similarly to MCTs, the flux is maintained via compensatory gradient increase (436). The cytotoxic effects of pharmacological MCT inhibition are not challenged here, but their proposed mechanism of action is. Several reports observed a mild reduction in tumour volume after the administration of MCT inhibitors (437-440). This, however, seems unlikely to ever be efficient as a monotherapy, not only due to limited actions on glycolytic metabolism but mainly the metabolic plasticity, which would protect the cell in the event of glycolytic shutdown (441). Although, the concomitant inhibition of both the glycolytic and oxidative branches of the metabolism seems to be an efficient way to induce cell death (422). It is possible that cytoplasmic lactate build-up, even though

not blocking glycolysis, renders other effects that are damaging for the cells. These may include reported previously regulatory properties of lactate (442).

Previous studies have attempted to alleviate extracellular acidity, by systemic buffer administration (443) or dietary interventions (354). The reported effects of these approaches on tumour load are inconsistent, some indicate a mild reduction in tumour volume (299, 353), while others describe a lack of effect (444), or even a small increase in the size of the primary tumour (445), which is consistent with the data presented in this Chapter. Increased buffering, regardless of the type of buffering agent, elevated glycolytic metabolism by removing the negative impact of low extracellular pH and fuelled cell proliferation. Apart from reported effects on tumour burden, alkalizing the microenvironment restored immune functions (446) and decreased metastasis incidence (352, 353, 444), due to removing the selection pressure posed by acidity, however, the effects of acid treatment on cell phenotypes and metabolic profiles will be discussed further in Chapter 6.

An important factor to consider when assessing the glycolytic metabolism is the coupling between the intracellular and extracellular pH. Although many reports indicate numerous effects of alkaline or acidic extracellular pH (343), it is crucial to remember that the intracellular and extracellular compartments are not isolated from one another. The observed phenomena rarely correspond to direct effects of the pH within the microenvironment. Obviously, the cytoplasm is separated from the extracellular space with a lipid bilayer, which may not be permeable to every molecule. H^+ can flow through it by simple diffusion (447), and via the actions of a number of acid-extruders and loaders (448). This Chapter provides characteristics

of pH dynamics between the intra- and extracellular compartments, with the extent of acidity ingress into the cytoplasm by simple diffusion. The most probable cause of pH-induced glycolysis inhibition is the indirect action of extracellular protons on intracellular pH, which, when acidic, inhibits the pH-sensitive glycolytic enzymes (449, 450), mostly, hexokinase and phosphofructokinase, which are reported to be inhibited at a relatively high pH of 6.9 (403, 451). Therefore, the main cue setting the glycolytic rate is the pH-dependent activity of glycolytic enzymes.

4.4. Key findings

1. Accumulation of extracellular protons feeds back negatively on cellular metabolic acid production;
2. Metabolic acid production is negatively affected by extracellular protons, but not [lactate], although both are end-products of glycolysis;
3. Increasing medium buffering capacity removes the negative feedback of pH and elevates glycolytic metabolism and proliferation *in vitro*;
4. The permeability of Monocarboxylate Transporters and the glycolytic rate of cells are not correlated;
5. The Monocarboxylate Transporter-based lactic acid transport is auto-regulated and cannot be influenced by a sole change to permeability caused by pharmacological inhibition;
6. The glycolytic rate of cells is ultimately set by intracellular pH, which changes in response to extracellular acidity.

Chapter 5. Characterising cellular heterogeneity in terms of lactic acid efflux capacity and its metabolic consequences

Cellular heterogeneity within a tumour is essential for somatic evolution because it presents a vast number of phenotypes for selection but is also considered a crucial barrier to successful therapy. The diversity of clones covering various permutations of phenotypes ensures that there are always groups of cells with better survival prospects, even as microenvironmental conditions change, thereby securing continued tumour growth. The most studied source of heterogeneity relates to inherited differences in genotype (e.g. mutations) or stable epigenetic changes. However, a role for more dynamic mechanisms that are not hard-wired in the genome cannot be excluded; for example, feedback mechanisms involving signalling molecules that maintain different phenotypic states in a dynamic equilibrium. Various forms of metabolic heterogeneity may provide tumours with a means of surviving chemical selection pressures, such as variations in oxygen tension, extracellular pH and waste product accumulation. This way, the heterogeneity is maintained as a protective mechanism against changes to the microenvironment, which arise as a result of cell metabolism and tissue architecture. In this Chapter, the concept of metabolic heterogeneity is tested in a panel of Pancreatic Ductal Adenocarcinoma cell lines, and possible mechanisms involving feedback circuits that maintain heterogeneity are investigated.

5.1. Introduction

Heterogeneity relates to the diversity of phenotypes present in a population of cells from the same origin (452). In detail, intra-tumour heterogeneity describes subclonal diversity observed within the same cancer, while inter-tumour heterogeneity corresponds to differences observed between tumours originating from the same tissue compared among a cohort of individuals (452). Both types may arise as a result of genome instability (453, 454), different oncogenic transformation trajectories (resulting from a varied panel of driver mutations (455)) and can include changes to both genome (456), and epigenome (457). The inter-tumour heterogeneity, however may be further influenced by the sex of the individual (more specifically by the levels of sex-specific hormones), received therapies (458), and medications administered for concomitant diseases such as metformin (459, 460). Genomic instability and subclonal tissue architecture are not constant either; either may change over time in response to microenvironmental cues, or response to therapeutics (458, 461). According to canonical models, intra-heterogeneity is driven by selection pressures in the microenvironment (462). For instance, the cells residing at the tumour core are exposed to radically different conditions than those at the periphery (463). These differences may become apparent as a result of varied tissue architechture, distance to, and quality of vasculature (464), immune cell infiltration (462), and vicinity of stroma-producing extracellular matrix components (465, 466). The latter is particularly important in PDAC, where desmoplastic reaction provides the tumour with a thick fibrous layer, difficult to penetrate for the immune cells (467). All these elements impact solute diffusion and may result in local acidosis, hypoxia and

waste product accumulation, all of which are selection pressures able to test the cells for fitness, thus facilitating cancer evolution (462).

The heterogeneity of the metabolic profile can be a result of both genetic mutations and external conditions. However, the latter seems to have the more prominent role in triggering, or unmasking diversity, as cells of the same genotype placed within different environments will manifest distinctly different behaviours. As described in Chapter 4, glycolytic metabolism is particularly sensitive to acidosis. Low extracellular pH will shut down glycolysis because the ensuing fall in cytoplasmic pH inhibits glycolytic enzymes. In contrast, the rate of respiration is less sensitive to extracellular pH and is, instead, dependent on oxygen tension. This generates a complex feedback circuit in which glycolysis acidifies the environment to block further glycolysis, forcing cells to become more respiratory, which, in turn, produces hypoxia that blocks respiration. These interactions will result in a dynamic balance between glycolytic and respiratory phenotypes. Inevitably, some cellular phenotypes will be better prepared to survive these conditions whilst others will be forced into dormancy, senescence or apoptosis unless coupled with other more fit cell clones (468). In order to remain responsive to microenvironments, that could change rapidly and profoundly, heterogeneity of a metabolic phenotype may require feedback circuits rather than rely solely on genomic factors. Such mechanisms would require autocrine or paracrine signals that cycle cells between different states, ultimately resulting in an equilibrium between various metabolic profiles.

Studying cancer heterogeneity requires methods of single-cell resolution, which is challenging *in vitro* and especially *in vivo*. The development of single-cell omics

technology allows for the assessment of the mutatome, transcriptome and proteome variety observed between cells (469). However, the cell phenotype and metabolic profile remain elusive because actual metabolic fluxes are not stoichiometrically related to gene expression or protein levels. Thus metabolic fluxes cannot be appropriately predicted from transcriptomic or proteomic datasets. Most techniques for studying metabolism (e.g. Seahorse assay or the fluorimetric method described in Chapter 3) report values that are representative of the population, while lacking cellular resolution of information. This makes it necessary to separate distinct populations prior to conducting experiments.

The aim of this Chapter is to assess metabolic heterogeneity in Pancreatic Ductal Adenocarcinoma cell lines and investigate the underlying mechanisms maintaining this phenomenon.

5.2. Results

5.2.1. Cells of any one cell line manifest heterogeneity of glycolytic phenotype

To assess the potential heterogeneity of cell glycolytic phenotype, the cells were seeded onto Lab Tek slides and left to adhere overnight. The next day, the cells were loaded with cSNARF1 and superfused with HEPES-buffered solution containing 5-N,N-dimethylamiloride (DMA), ensuring stable extracellular pH and lack of NHE-1 involvement. The glycolytic rate was recorded at a single-cell resolution and inferred from the rate of intracellular acidification following the superfusion with a solution containing a non-specific MCT inhibitor (α-cyano-4-OH-cinnamate, CHC). The experimental protocol and the exemplar time-courses of high and low glycolytic cells are shown in Figure 5.1A. The inhibitor traps all produced lactic acid within the intracellular space and the rate of acidification, multiplied by intrinsic buffering capacity (which is cell line-specific) provides the estimate of the glycolytic rate. The observed glycolytic phenotype was heterogenous between and within the populations of tested PDAC cell lines, with PANC-1 and MIA PaCa-2 manifesting the widest distribution of tested phenotype (Fig.5.1B).

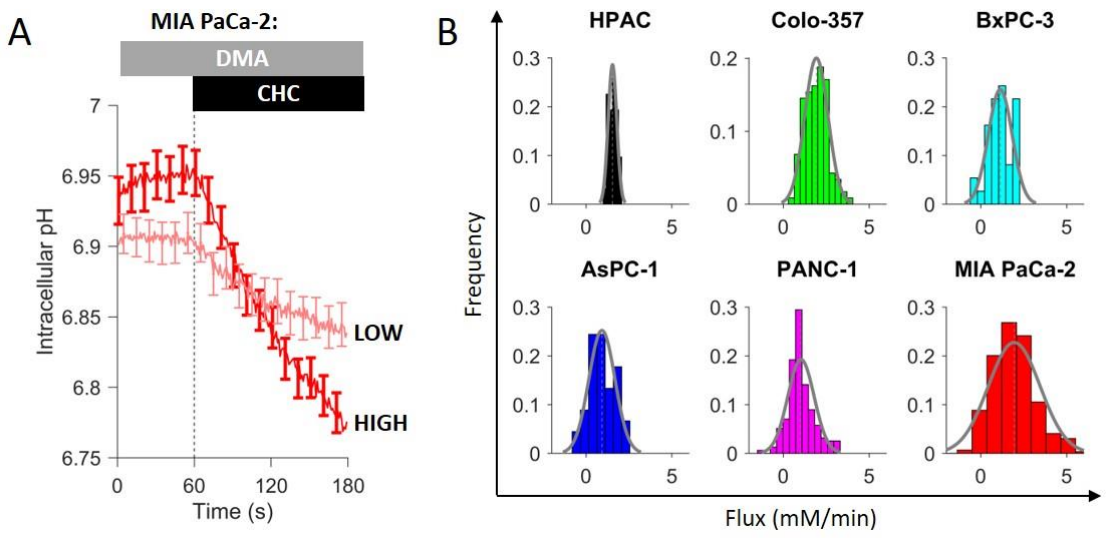


Figure 5.1 Assessment of the heterogeneity of glycolytic rate in PDAC cell lines. A: Example plots depicting the glycolytic rate measurement protocol. The glycolytic rate was inferred from the change in intracellular pH following the MCT inhibition with pan-inhibitor CHC (2 mM). The experiments were performed in CO_2/HCO_3^- free buffer (to block HCO_3^- transport) containing 5-N,N-dimethylamiloride (DMA; 30 mM; to block Na^+/H^+ exchange). Time course of intracellular pH in cSNARF1-loaded MIA PaCa-2 cells averaged for cells with the highest (top 20%) and lowest (bottom 20%) glycolytic rate (measured from the pHi slope in response to CHC) from a population of ~299 cells/five biological repeats. B. Frequency distributions for glycolytic rate measured in six PDAC cell lines, ranked by increasing variance. Best fit to Gaussian distribution. N=48 (AsPC-1), 37 (BxPC-3), 117 (Colo-357), 31 (HPAC), 299 (MIA PaCa-2), 157 (PANC-1) from at least two biological repeats.

5.2.2. Cancer cells manifest heterogeneity in terms of their lactic acid removal capacity

Heterogeneity of glycolytic phenotype was confirmed by measuring the membrane's permeability to lactic acid, a readout of the cell's capacity to carry an efflux of the end product of glycolysis, lactic acid. Most of this permeability is due to the activity of monocarboxylate transporters (MCT) and was measured in cells seeded on Lab-Tek slides and allowed to adhere overnight. Next, the cells were loaded with cSNARF1 and equilibrated by superfusion with lactate-containing solution. Using superfusion, lactic acid efflux was triggered by removing the lactate from the solution and the following alkalinisation of the intracellular space was recorded. Solution changes were rapid to ensure that the pHi response is a measure of lactic acid efflux

that is not rate-limited by solution switching. Similar to previous experiments, the MCT permeability was calculated by multiplying the rate of pHi change by intrinsic buffering capacity. The exemplar time-courses of intracellular pH change between cells of low and high MCT permeability are depicted in Figure 5.2A. The capacity to extrude lactic acid was cell-line dependent, with HPAC and AsPC-1 showing the lowest mean MCT activity and least variation among tested populations. Cells of the MIA PaCa-2 line manifested the highest mean MCT permeability and widest variation. The frequency and distribution of MCT activity in PDAC cell lines ranked from lowest to highest is depicted in Figure 5.2B. Because of the degree of heterogeneity in glycolytic rate and MCT permeability, MIA PaCa-2 cells were selected as an exemplar cells of large metabolic heterogeneity.

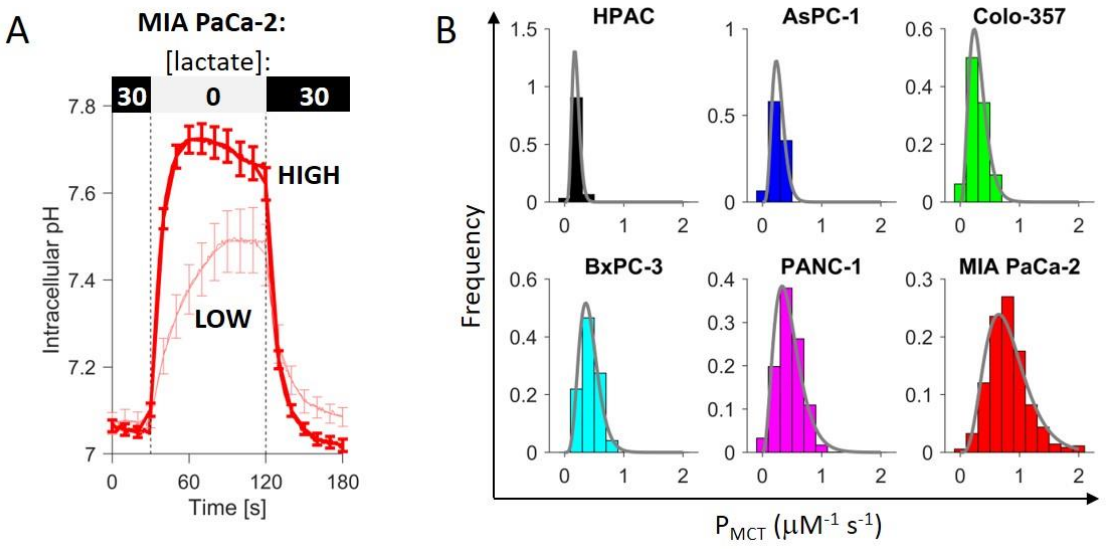


Figure 5.2 Variation of cell lactic acid efflux capabilities in PDAC cell lines. A: The cell potential to efflux lactic acid (MCT permeability) was assessed by loading the cells with lactate and recording the time-course of intracellular alkalinisation upon solution exchange to lactate-free. The intracellular pH was tracked by assessing the fluorescence of cSNARF1. The plots depict the time-courses of intracellular pH change evoked in MIA PaCa-2 cells (high- average of top 15%, and low-average of bottom 15%) by lactate removal. B: Frequency of P_{MCT} distribution among PDAC cell lines, ranked by increasing variance. Best fit to Gamma distribution. N=138 (AsPC-1), 196 (BxPC-3), 128 (Colo-357), 52 (HPAC), 304 (MIA PaCa-2), 187 (PANC-1) from at least four biological repeats.

5.2.3. *The heterogeneity of lactic acid removal capacity is not related to the cell cycle phase*

Previous experiments revealed that the MIA PaCa-2 cell line maintained high heterogeneity in terms of glycolytic rate and lactic acid permeability. Interestingly, assessment of MCT permeability identified cells with essentially no MCT activity (~0 $\mu M^{-1}s^{-1}$) alongside the cells of pronounced activity (~2 $\mu M^{-1}s^{-1}$). Enhanced glycolytic metabolism in the latter subpopulation would give cells a proliferative advantage in environments that are hypoxic but not yet profoundly acidic. However, if the environment becomes substantially acidic, high MCT capacity is less advantageous. The mechanism that generates this spectrum of glycolytic phenotype is not clear. One possibility is an association between metabolic profile and cell cycle stage as this provides a means of cycling between different cell states. To test this possibility, the MCT permeability of cells co-stained with GFP-conjugated geminin and Hoechst was measured. The second fluorescent reporter, Kusabira-Orange 2-conjugated Chromatin Licensing and DNA Replication Factor 1 (CDT1) provided by the FUCCI kit, had to be omitted due to spectral overlap with the fluorescence of cSNARF1. Hoechst 33342 was used to distinguish the cells with doubled amount of DNA, thus depicting S and G2 phases. The exemplar image of cells loaded with cSNARF1, Hoechst and GFP-geminin is shown in Figure 5.3. Regardless of the approach used, no correlation between MCT permeability and cell cycle stage was observed.

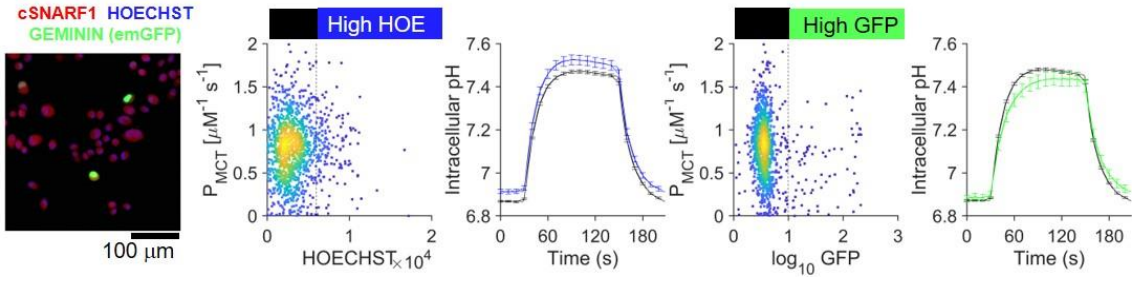


Figure 5.3 Relating the MCT permeability to the cell cycle phase. Image of MIA PaCa-2 expressing GFP-tagged geminin, stained with Hoechst and cSNARF1. P_{MCT} plotted as a function of total Hoechst fluorescence within the cell boundaries, or mean GFP fluorescence within the cell boundaries. No clear correlation between the cell cycle stage and P_{MCT} was observed. Mean time courses of intracellular pH for the corresponding cell subpopulations gated by Hoechst or GFP signal. Results from 3 biological repeats.

5.2.4. Cells sorted by their glycolytic phenotype manifest different metabolic profile

The finding that the cell cycle stage does not affect the glycolytic phenotype of MIA PaCa-2 cells does not exclude the possibility that cells of a low glycolytic rate are compensated by increased oxidative phosphorylation. To test this, subpopulations at the extremes of the glycolytic profile distribution were extracted from the mixed population for further analysis. The cells of low and high MCT permeability were separated via FACS, as described in detail in Section 2.2.10. First, the cells were loaded with cSNARF1, centrifuged and the medium was replaced with one containing 60 mM lactate. The cells were equilibrated at high lactate concentration for 5 minutes and prior to sorting the medium was replaced with lactate-free. This allowed the separation of the cells according to their intracellular pH (which corresponds to lactic acid content) in real-time, thus separating those with the highest capacity to vent lactic acid (largest pHi transient) from those of low permeability (smallest pHi transient). To ensure only extreme cell populations are collected the sorting window was limited to 10 minutes. After sorting, the cells were seeded on a 96-well plate and maintained in culture for up to 2 weeks. At 24 hours after separation, the metabolic profile of collected cells was assessed using the fluorimetric assay described in detail

in Chapter 3. Cells sorted according to their capacity to extrude lactic acid presented distinctly different metabolic profiles, with "MCT-high" cells showing increased glycolytic acid production and respiratory oxygen consumption, as compared to "MCT-low" cells (Figure 5.4). Interestingly, this phenotype was short-lived because the difference between the two populations disappeared within a week of culture. This transient behaviour suggests that there is a dynamic equilibrium between "MCT-high" and "MCT-low" cells, and if one population is removed, over time, the system restores balance. This cycling thus ensures that metabolic heterogeneity is maintained.

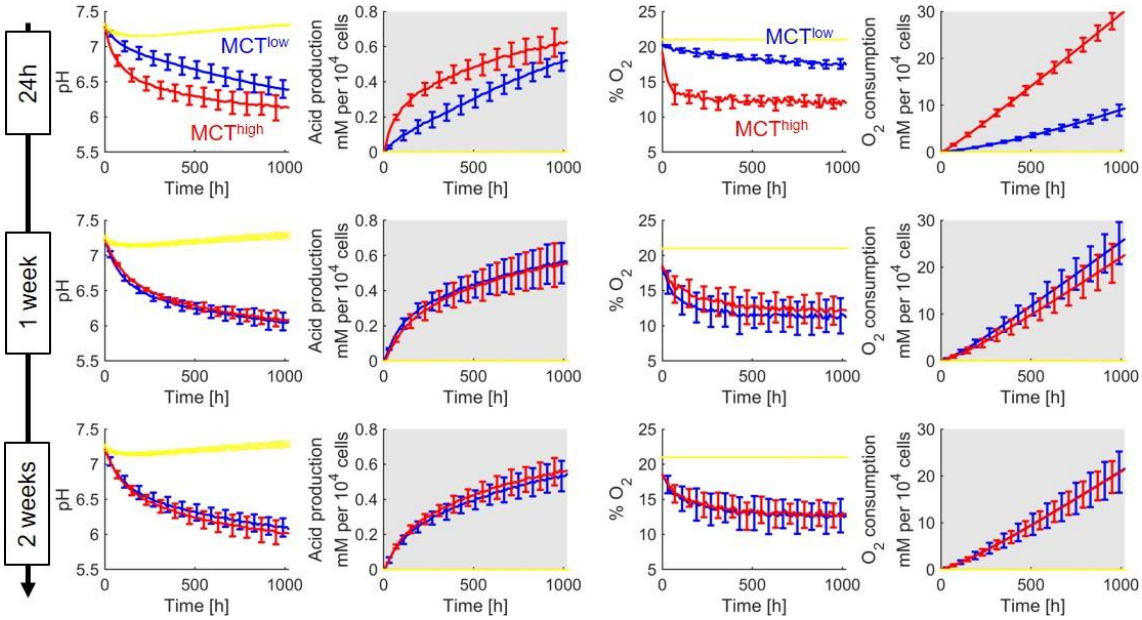


Figure 5.4 Cells of different MCT permeability status present different metabolic profiles. Metabolic profile of cells FACS-sorted according to their MCT permeability at 24 hours, 1-week and 2-weeks post sorting assayed via fluorimetric recordings of extracellular acidification and oxygen consumption rates. Red lines correspond to cells of high MCT permeability status, and blue to low. Yellow lines represent extracellular pH and oxygen levels in cell-free controls. A clear difference between the MCT-low and MCT-high subpopulations is visible after 24h in both the glycolytic acid production and oxygen consumption ($P<0.001$). The difference is lost within one week in culture. Panels depict: extracellular pH, cumulative acid production calculated from the pH time-course, medium O_2, and cumulative oxygen consumption calculated from O_2 time-course.

5.2.5. Cells of a high glycolytic profile have a proliferative advantage

Before other possible causes of temporally increased metabolism profile were investigated, it was necessary to confirm that a particular metabolic profile provides a proliferative advantage. To confirm this, cells from three sorting experiments were seeded at low density onto a 96-well plate and allowed to grow for four days. The period of experiments needed to be long enough for cells to proliferate (the reported doubling time of MIA PaCa-2 cells is 40 h (26)), but shorter than the time it takes for metabolic differences to collapse. After four days the cells were fixed and the total biomass produced was compared. This experiment confirmed that increased metabolic rates of MCT-high subpopulation provide cells with a proliferative advantage over the MCT-low group (Figure 5.5). As such, this difference in growth would predict that the MCT-high phenotype would eventually become dominant in the bulk population, so some sort of corrective mechanism must be responsible for sustaining the MCT-low population. One possibility is that cells alternate between the two phenotypes dynamically and that this leads to an apparent constancy of the MCT-high and MCT-low subpopulations.

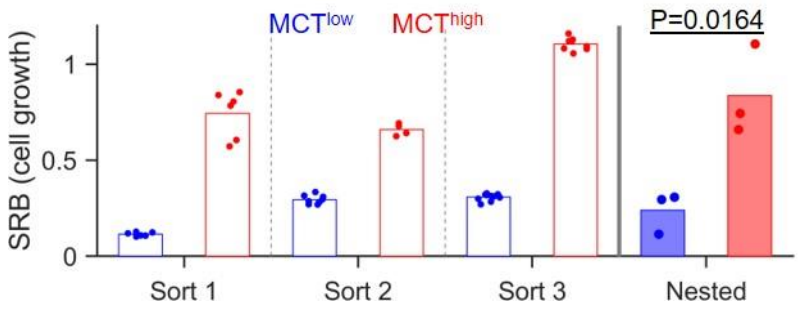


Figure 5.5 High MCT permeability status is associated with proliferative advantage. Cell growth assay (SRB) performed after 4 days of culture of MCT-low (blue) and MCT-high (red) subpopulations (N=3 sorts, each with 5-8 technical repeats; nested t-test).

5.2.6. Cells sorted according to the lactic acid venting capacity present distinctly different gene expression patterns

To investigate possible mechanisms underpinning the cycling between the two metabolic sub-populations, samples of MCT-high and MCT-low cells from four independent flow-cytometric sortings were subjected to poly-A mRNA sequencing. The MCT-high and MCT-low subpopulations were well resolved on principle component analysis (Figure 5.6A) and showed distinct patterns of gene expression when analysed for differential gene expression using the DESeq2 package (Figure 5.6B). Analysis of transcriptomic data identified a number of genes whose expression was elevated in MCT-high cells (Figure 5.6C). Strikingly, none of these differentially expressed genes (DEGs) belonged to the canonical glycolytic or respiratory pathways, indicating that the fundamental differences in metabolic rate are not due to a general upregulation of those pathways (Figure 5.6D). Similarly, the lack of cell cycle-related genes among these differentially expressed genes confirms that observed metabolic phenotype is not associated with the cell cycle phase. This unexpected finding indicates that heterogeneity of metabolic rate is more likely driven by components beyond transcription, for example, through a clock mechanism produced by a complex signalling pathway. These observations also suggest that sorting of cells by expression of genes belonging to glycolytic or respiratory pathways would not necessarily identify phenotypes of high and low metabolic rate. Pathway analysis highlighted the IL6R-STAT3 pathway as upregulated in MCT-high cells, which is consistent with the established role of IL6 signalling in stimulating the metabolic rate. Moreover, hierarchical ingenuity pathway analysis (IPA) indicated STAT3 at the centre of over-activated pathways in MCT-high cells (Figure 5.6E).

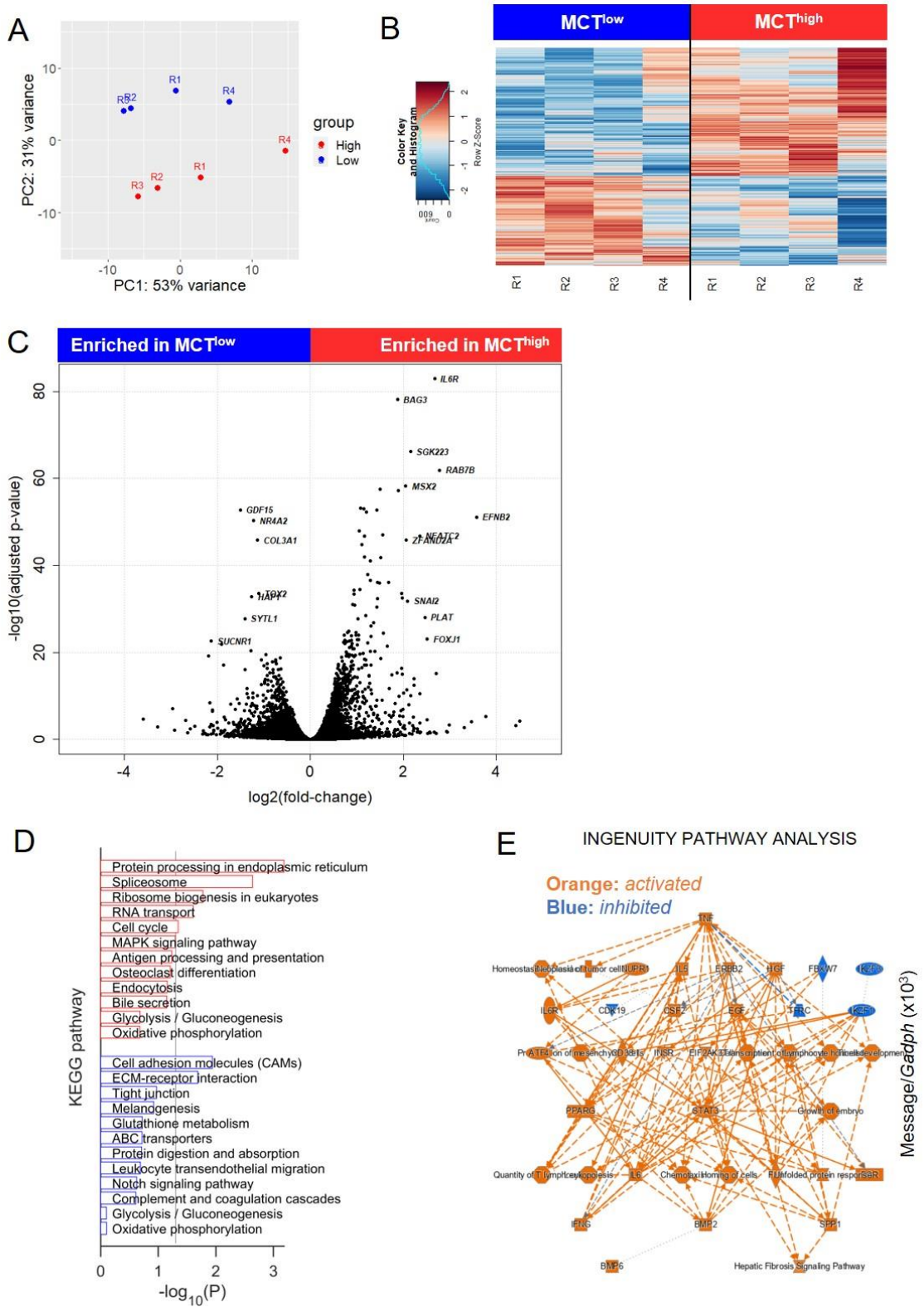

A
PC2: 31% variance
PC1: 53% variance
group
High
Low
B
MCTlow
MCThigh
Color Key and Histogram
Row Z-Score
C
Enriched in MCTlow
Enriched in MCThigh
-log10(adjusted p-value)
log2(fold-change)
IL6R
BAG3
SGK223
RAB7B
MSX2
EFNB2
GDF15
NR4A2
COL3A1
SNAI2
PLAT
FOXJ1
SYTL1
SUCNR1
D
KEGG pathway
Protein processing in endoplasmic reticulum
Spliceosome
Ribosome biogenesis in eukaryotes
RNA transport
Cell cycle
MAPK signaling pathway
Antigen processing and presentation
Osteoclast differentiation
Endocytosis
Bile secretion
Glycolysis / Gluconeogenesis
Oxidative phosphorylation
Cell adhesion molecules (CAMs)
ECM-receptor interaction
Tight junction
Melanogenesis
Glutathione metabolism
ABC transporters
Protein digestion and absorption
Leukocyte transendothelial migration
Notch signaling pathway
Complement and coagulation cascades
Glycolysis / Gluconeogenesis
Oxidative phosphorylation
-log10(P)
E
INGENUITY PATHWAY ANALYSIS
Orange: activated
Blue: inhibited
Message/Gadph (x10³)
TNF
PPARG
STAT3
BMP2
SPP1
BMP6
Hepatic Fibrosis Signaling Pathway

Figure 5.6 MCT permeability status correlated with differential gene expression. A: Principle component (PC) analysis of samples prepared from four independent experiments shows good separation on PC2 according to glycolytic phenotype inferred from P_{MCT}. R refers to sorting repeat (1-4). B: Heatmap showing differentially expressed genes (DEGs): expression of 1510 genes is higher in MCT-low cells and expression of 2156 genes is higher in MCT-high cells (cut-off: adjusted P<0.05). C: Volcano plot showing DEGs enriched in MCT-high or MCT-low cells. D: KEGG pathway analysis by GAGE showing 8 pathways with the lowest p-value plus "glycolysis/gluconeogenesis" and "oxidative phosphorylation" for reference. The horizontal line shows a significance cut-off (P=0.05). Analysis performed for DEGs in MCT-high (red) and MCT-low (blue) cells. E: Results of hierarchical ingenuity pathway analysis, indicating STAT3 among the key activated processes in MCT-high cells.

5.2.7. Differential gene expression is observed in subpopulations of MIA PaCa-2 cell line, but not PANC-1

A group of differentially expressed genes identified in transcriptome analysis with reported potential to upregulate glycolysis was selected for validation via reverse transcription-quantitative polymerase chain reaction (RT-qPCR). In order to assess whether the same cell subpopulations are present in PANC-1 cell line (which ranked second to MIA PaCa-2 with regard to the width of both lactic acid efflux capacity and glycolytic rate distribution) both MIA PaCa-2 and PANC-1 cells were FAC-sorted according to their MCT activity as described in Section 2.2.10. To avoid loss of a transient metabolic profile, samples were not maintained in culture and were processed immediately after sorting. The sorting protocol and exemplar dot plots showing the transient populations of high MCT activity in MIA PaCa-2 and PANC-1 are depicted in Figure 5.7.

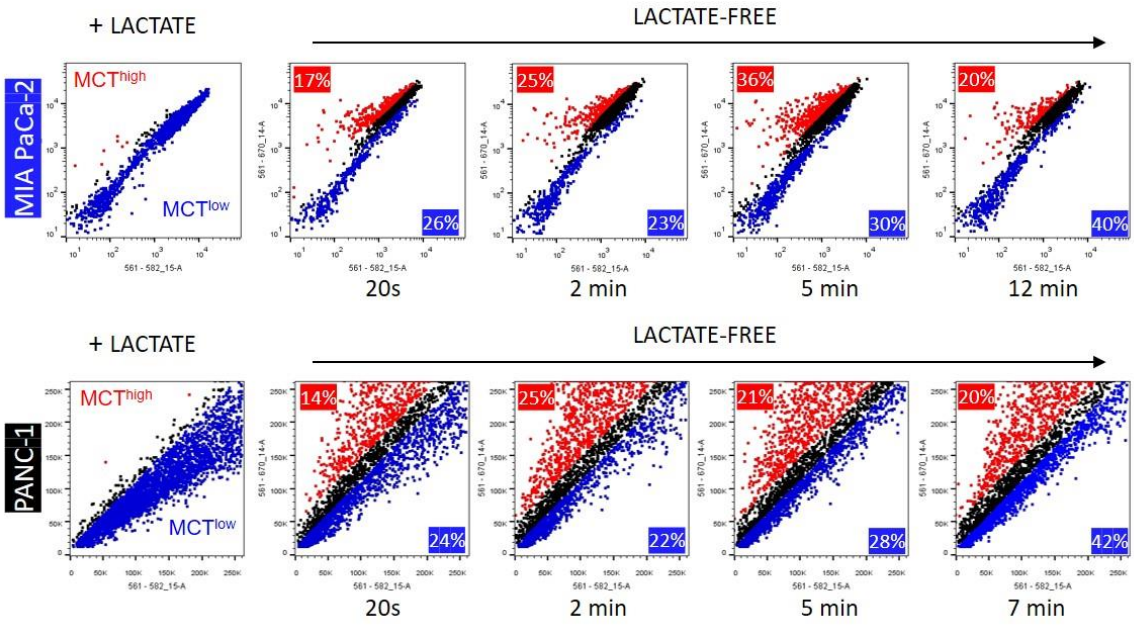


Figure 5.7 Stability of MCT-high and MCT-low populations during separation by FACS. Exemplar dot plots showing the changes in subpopulations in time. For MIA PaCa-2 logarithmic scale was used and for PANC-1 linear. The blue dots correspond to MCT-low (acidic) cells and the red depict the transient MCT-high (alkaline) population. Lactic acid efflux triggered by medium change peaked around 5 minutes since the start of sorting for MIA PaCa-2, in PANC-1 MCT-high population was smaller and formed a more stable population.

Differential expression of 7 out of 9 selected genes was confirmed in MIA PaCa-2, including interleukin 6 receptor (IL6R), interleukin 6 signal transducer (IL6ST), ephrin B2 (EFNB2), BAG cochaperone 3 (BAG3), forkhead fox J1 (FOXJ1), ubiquitin specific peptidase 38 (USP38) and heparin-binding EGF-like growth factor (HBEGF). Interestingly, the expression of solute carrier family 16 member 1 (SLC16A1), a gene coding for MCT-1, by the activity of which the cells were separated, was found unaltered between the groups (Fig.5.8). This lack of stoichiometric coupling between transcript level and functional outcome result strengthens the notion that expression level alone cannot accurately predict phenotype. Even though, PANC-1 cells presented only the second-widest glycolytic phenotype frequency distribution compared to MIA PaCa-2, sorting by MCT activity failed to separate distinguished populations. This suggests

that subpopulations of different P_{MCT}-related metabolic profile might be a cell line-specific phenomenon, which is not present in the PANC-1 cell line.

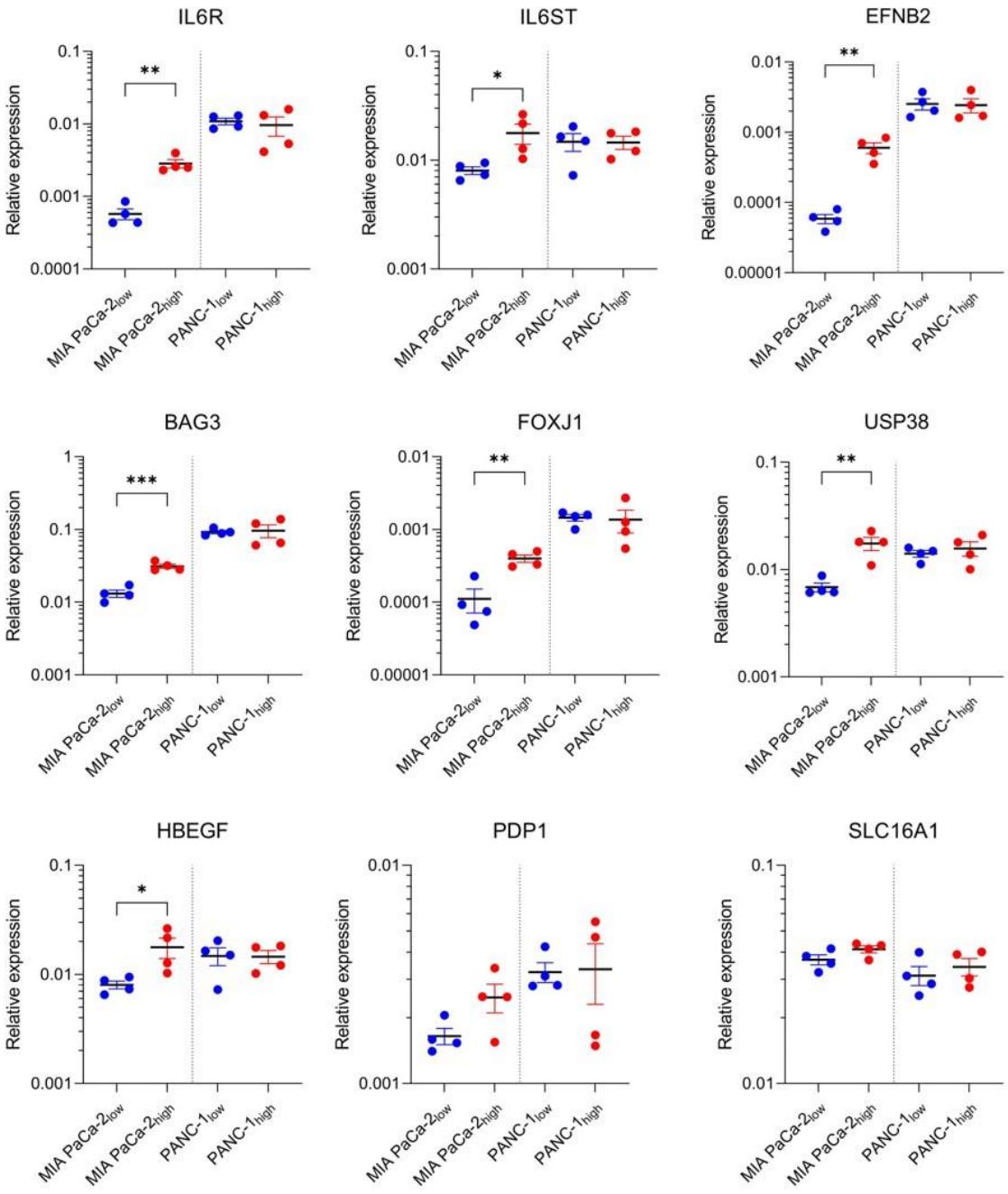


Figure 5.8 Validation of differentially expressed genes between high and low MCT subpopulations in MIA PaCa-2 and PANC-1 cells. The expression of selected differentially expressed genes (DEGs) was measured in MIA PaCa-2 and PANC-1 cells via RT-qPCR after sorting according to the P_{MCT} status. The plots show mean relative expression in 4 biological repeats. The significance between low and high groups was calculated by t-test and is indicated with asterisks were relevant.

5.2.8. Interleukin 6 production in vitro

Interleukin 6 (IL6) signalling is an important pathway for maintaining tissue homeostasis. IL6 has been identified as crucial in several processes including tissue regeneration, bone metabolism and the antibacterial response. It is a vital immune regulatory molecule, which with its versatile function can either induce (470), or prevent inflammation (471). The important role of IL6 signalling is indisputable *in vivo*, as it contributes to a vast range of pathologies including immune disorders (472), Castleman's syndrome (473), graft vs host disease (474), and multiple cancers (152-156). Although, it is understood that elevated IL6 levels in serum are part of a systemic response to cancer and may facilitate the progression of the disease by maintaining chronic inflammation (475, 476). In a clinical setting the main source of IL6 are the immune cells, including macrophages and monocytes. Therefore, the relevance of IL6 signalling in an *in vitro* setting, lacking the infiltrating immune cells needed to be assessed. To answer this question, the ability of PDAC cell lines to produce IL6 was tested by assessing the IL6 synthesis in MIA PaCA-2 and PANC-1 lysates. As the IL6 production is reported to be under a positive control of STAT3 signalling, the effects of STAT3 inhibition induced by treatment with napabucasin were also measured. As shown in Figure 5.9A, at baseline levels of IL6 were 2-fold higher in MIA PaCa-2 cell line than PANC-1. Also, STAT3 blockade lead to reduction in the cytokine synthesis to the similar levels observed in PANC-1 cells. This was further confirmed by unaltered STAT3 phosphorylation in PANC-1 cells following the treatment with napabucasin (Fig.5.9B). Thus, an activated STAT3 pathway signals to raise IL6 levels, which is a form of positive feedback. The released IL6 may act on the source

cell (autocrine signalling) or influence neighbouring cells (paracrine signalling) and thus spread the message of STAT3 activation.

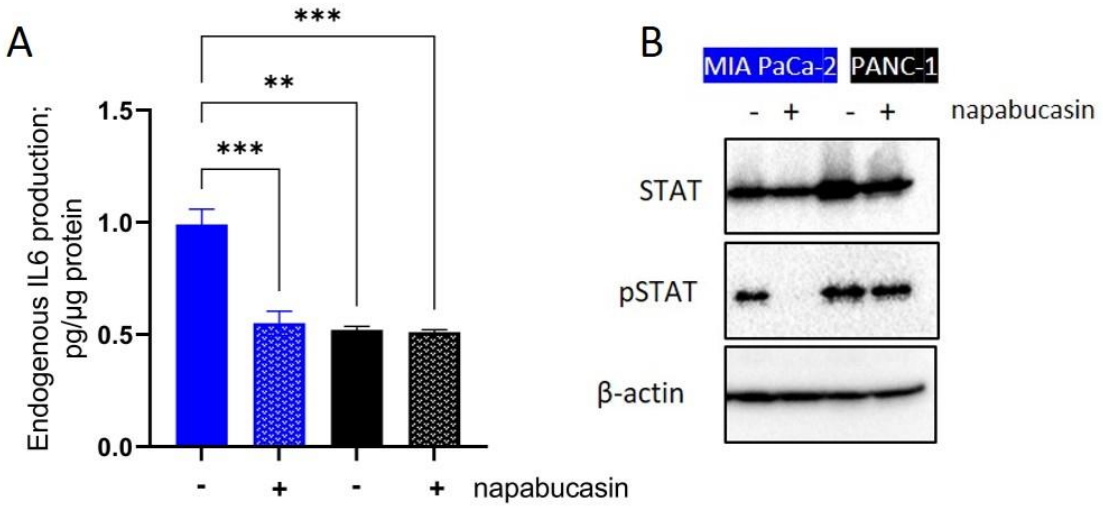


Figure 5.9 Interleukin 6 production *in vitro*. The levels of interleukin 6 production measured in 36 µg protein lysate of MIA PaCa-2, PANC-1 cells treated with 0.2 µM napabucasin for 48h. Data shown as the mean of three experiments ± SEM. The significance was calculated using ordinary ANOVA with Tukey's multiple comparisons test. B: Expression of STAT and phosphorylated STAT in MIA PaCa-2 and PANC-1 cells with and without napabucasin treatment (0.5 µM, 4 h), β-actin used as a loading control.

5.2.9. Subpopulations sorted by IL6R expression present different transient glycolytic phenotypes

To confirm the association of increased IL6R expression with higher metabolic rate identified by transcriptome analysis, MIA PaCa-2 cells were stained with fluorescent antibody against membrane-IL6R and sorted according to the receptor expression. The viability of collected subpopulations was confirmed by live imaging with calcein, MitoTracker and Hoechst identifying mitochondria and nuclei respectively (Figure 5.10A). The analysis of MitoTracker fluorescence revealed increased mitochondria count in the IL6R-high subpopulation in two independent sorting experiments (Figure 5.10B). The metabolic profile of the sorted cells was assessed via a fluorimetric approach as described previously (the detailed method description can

be found in Chapter 3). Due to the low number of IL6R-high cells collected during the experiments (the fluorimetric assay requires a large number of cells to deliver resolvable recordings), both subpopulations were acutely treated with 100 ng/mL recombinant IL6 for the duration of the assay, which enabled the observation of the resolvable differences between the groups. In line with previous experiments, high IL6R expression was observed in a small fraction of the total population (10-20%) and this expression status upon stimulation with IL6 resulted in increased glycolytic phenotype that was not maintained long-term and dissipated within one week of culture (Fig.5.10C). The low cell density made it unfeasible to assess the oxidative metabolism, as a high cell number is required for appropriate measurements of oxygen consumption (a large number of cells is more likely to produce a resolvable change in dissolved oxygen levels, which can be identified by a shift in fluorescence). Therefore, the oxidative metabolism of the subpopulation could not be assessed.

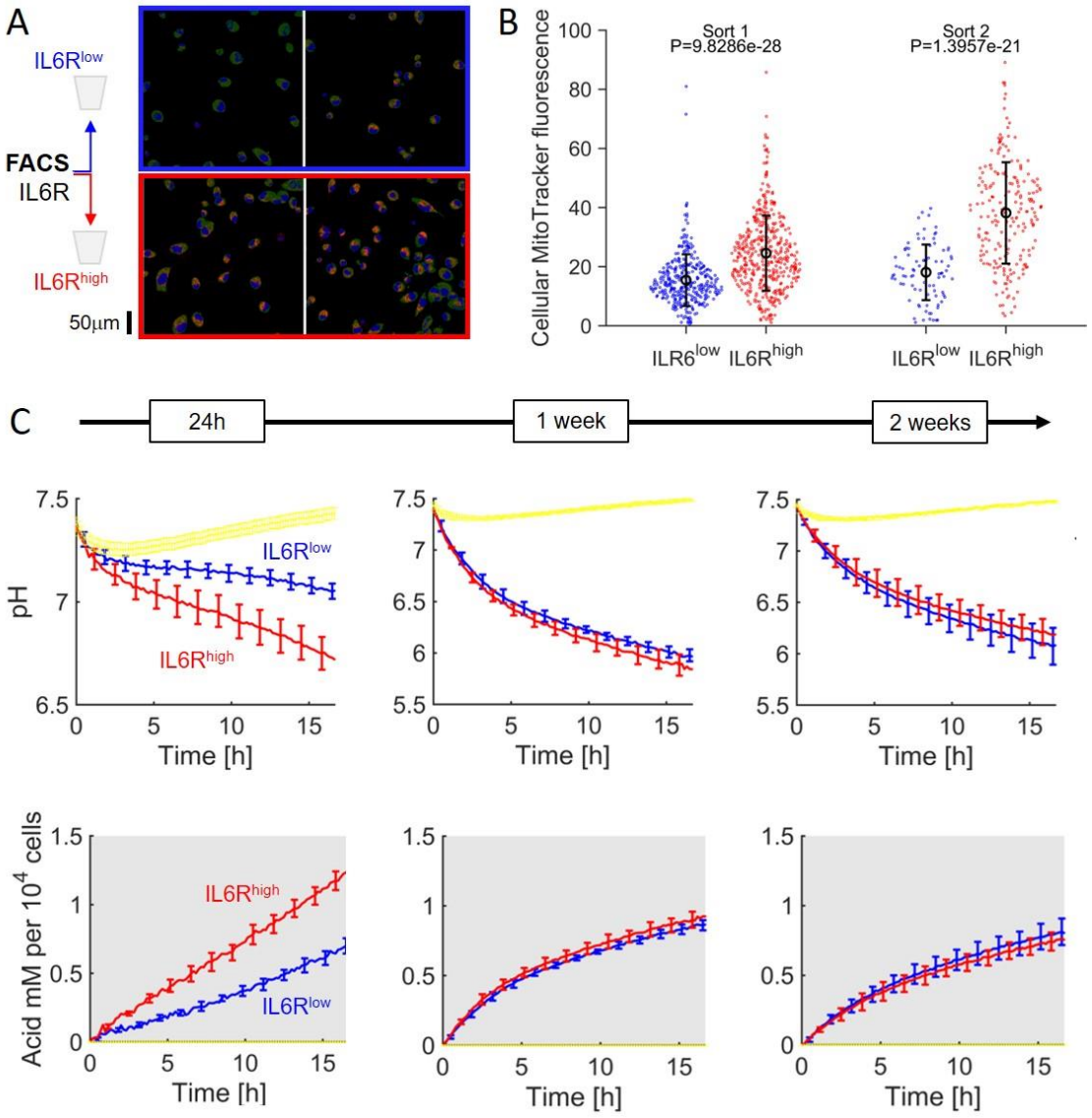


Figure 5.10 Cell phenotype associated with IL6R expression. A: Exemplar images of MIA PaCa2 cells sorted by IL6R expression to separate top and bottom fractions. Subpopulations were seeded for live-cell imaging with MitoTracker Red to stain mitochondria; calcein was used to mark the cytoplasm and Hoechst identified nuclei. B: The analysis of MitoTracker fluorescence between low and high IL6R cells. Cellular MitoTracker fluorescence was averaged within the cell boundaries. Data from two separate sorting experiments. Significance testing by t-test. C: The glycolytic profile of cells sorted by their IL6R expression was measured using the fluorimetric assay after 24 h, 1 week or 2 weeks in culture. In order to obtain resolvable differences despite low cell number, both subpopulations were acutely treated with 100 ng/mL recombinant IL6. A subpopulation of high IL6R expression (red) showed increased glycolytic metabolism when compared to low IL6R status (blue), however, this phenotype was transient and dissipated within 1 week. Yellow lines correspond to cell-free controls. Data normalised to 10,000 cells.

5.2.10. STAT3 inhibition causes metabolism collapse in MIA PaCa-2 but not PANC-1 cells

To confirm whether the metabolic phenotypes observed within the cell line population are controlled via IL6 signalling, the response of MIA PaCa-2 and PANC-1 cell lines to STAT3 inhibitor, napabucasin was assessed. Cells were seeded at high density and acutely treated with increasing doses of napabucasin (0.5, 1, 2 µM) for the duration of the assay. Although both cell lines express IL6R and produce endogenous IL6, the effects of STAT3 inhibition differed distinctly between the cell lines (Fig.5.11). MIA PaCa-2 cells were highly sensitive to napabucasin in a dose-dependent manner, with a complete shutdown of glycolysis observed after acute treatment with 1 µM of the inhibitor. On the contrary, PANC-1 cells were unaffected by the same doses of the napabucasin and continued glycolysis regardless of the treatment.

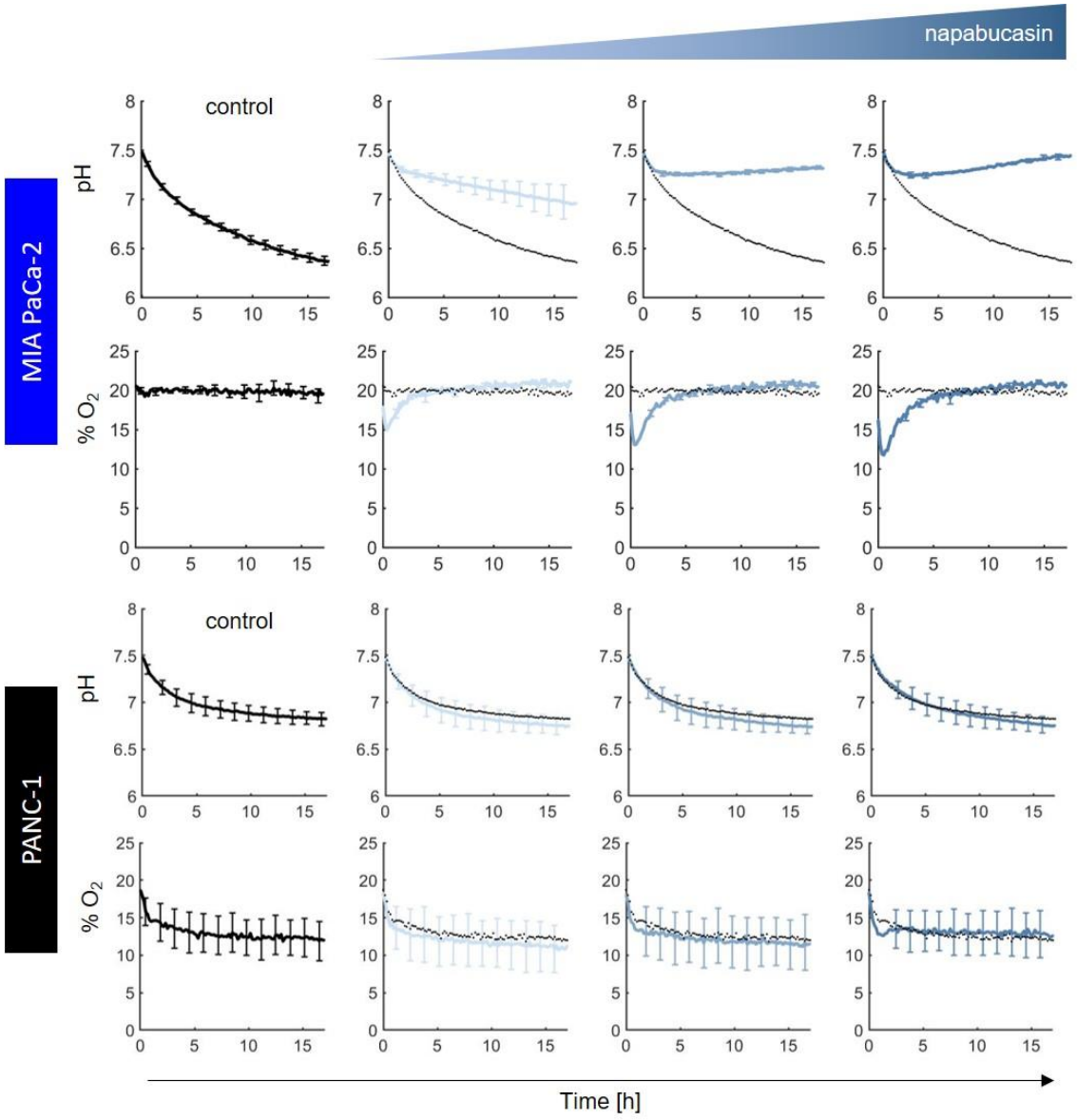


Figure 5.11 Impact of STAT3 inhibition on metabolic profile. Cells treated acutely with increasing doses of napabucasin (0.5, 1, 2 µM) for the duration of the assay (17 hours). The medium pH corresponds to glycolytic metabolism and % O_2 to oxidative phosphorylation. Metabolic acid production in MIA PaCa-2 cell line is strongly inhibited by treatment with napabucasin, with complete collapse observed at 1 µM dose. The same doses do not affect the metabolic rates of PANC-1 cells. Control, untreated cells are marked in black and cells treated with increasing doses are marked with darker blue. Data plotted as mean ± SEM. In collaboration with Ms. Bobby White.

5.2.11. The heterogeneity of IL6 signalling among PDAC cell lines

To assess the distribution of IL6 signalling among PDAC cell lines, the expression of IL6 receptor and its downstream effector, STAT3 was measured. The representative raw images showing protein expression and post-analysis images showing cells with the dominance of either protein are depicted in Figure 5.12A. The distribution of IL6R/STAT3 expression is shown in Figure 5.12B, and the cell lines were ranked from the smallest to largest heterogeneity. Similar to previous experiments, both MIA PaCa-2 and PANC-1 cells showed the greatest heterogeneity among the tested panel.

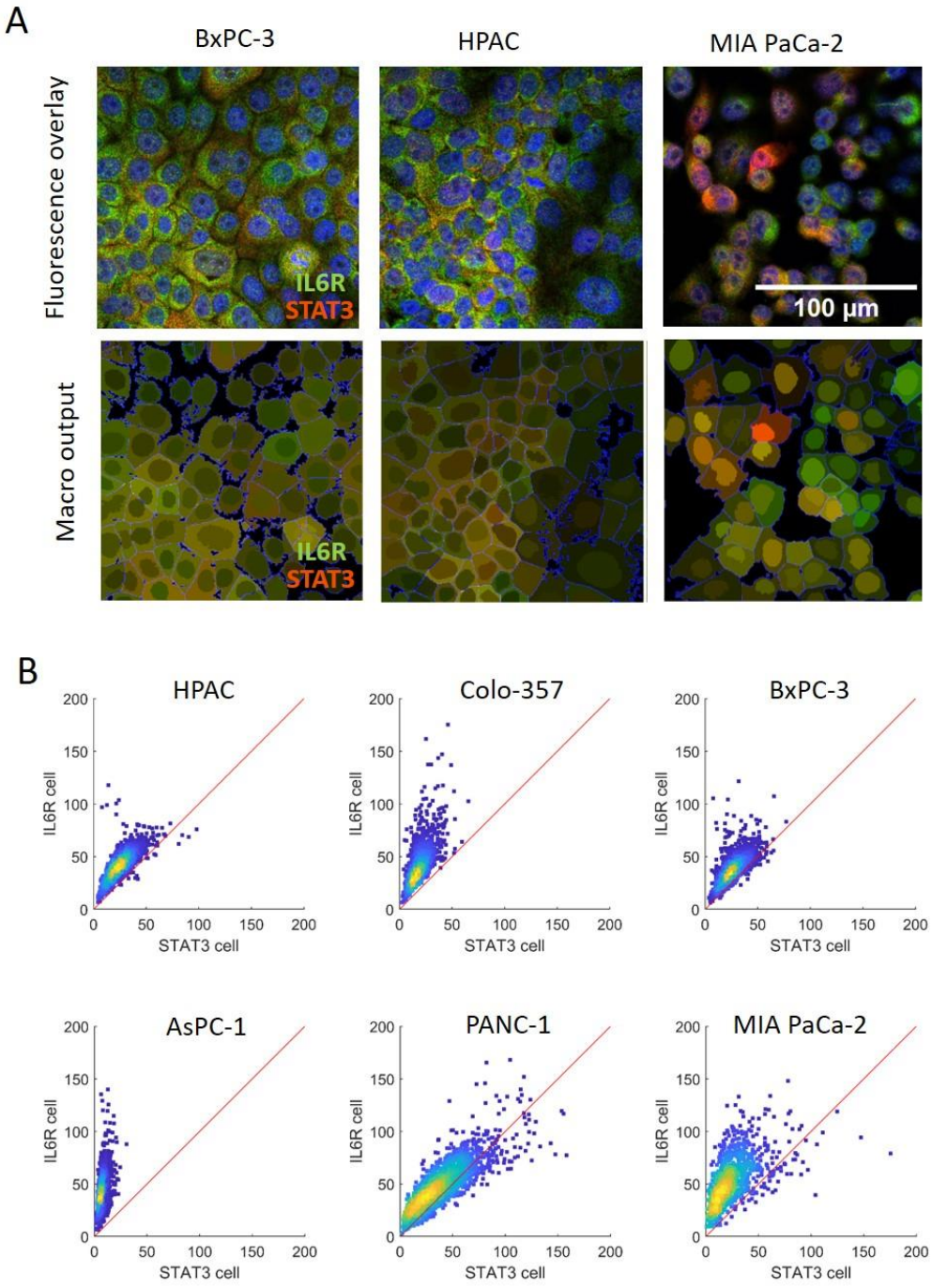


Figure 5.12 Heterogeneity of IL6R expression and STAT3 activation among PDAC cell lines. A: Exemplar raw images showing expression of IL6R (green), STAT3 (red) and cell nuclei (blue) and corresponding images showing the images post-analysis. Each cell was identified based on the nucleus signal, and the expression of IL6R and STAT3 within the cytoplasm and the nucleus was averaged. Cells imaged as red show a dominance of STAT3 expression, while cells with more IL6R expression appear as green. B: Distribution of IL6R and STAT3 expression among PDAC cell lines ranked from smallest to largest. The greatest intra-population heterogeneity in terms of IL6R/STAT3 expression ratio for PANC-1 and MIA PaCa-2 cell lines was confirmed. The experiments were conducted in collaboration with Ms. Bobby White.

5.2.12. The heterogeneity of IL6R expression in vivo

To confirm whether the IL6 signalling heterogeneity observed previously is only an *in vitro* phenomenon or whether it represents a distinct characteristic of the cell line regardless of the conditions, MIA PaCa-2 cells were injected subcutaneously into athymic mice for xenograft formation. The tumours were allowed to grow for 8 weeks and the mice were euthanised when the tumour volume reached 1 cm^3. Next, the tissues were collected, formalin-fixed and embedded in paraffin. Sections were then stained for IL6R and STAT3 expression and the diversity of this ratio was analysed.

Figure 5.13A depicts the image analysis of stained tissue sections showing cells marked as green, red or yellow depending on the dominance of IL6R, STAT3, or uniform expression of both, respectively. Figure 5.13B shows the localisation of IL6R and STAT3-dominant cells (either green or red) while omitting cells of average expression of the proteins (grey). Cells classed as IL6R or STAT3 dominant showed an increased or decreased ratio of IL6R:STAT3 by 50% when compared with a tumour-wide median. The distribution of IL6R and STAT3 expression in tested tissues is shown in Figure 5.13C. As all tumours are formed from MIA PaCa-2 cell line, no drastic differences between the sections were expected. All imaged tissue slices manifested wide distribution of IL6R and STAT3 expression, confirming that observed heterogeneity is maintained *in vivo*. Additionally, some level of inter-tumour heterogeneity has been observed, which might be attributed to different conditions of the microenvironment, further shaping the tumour population.

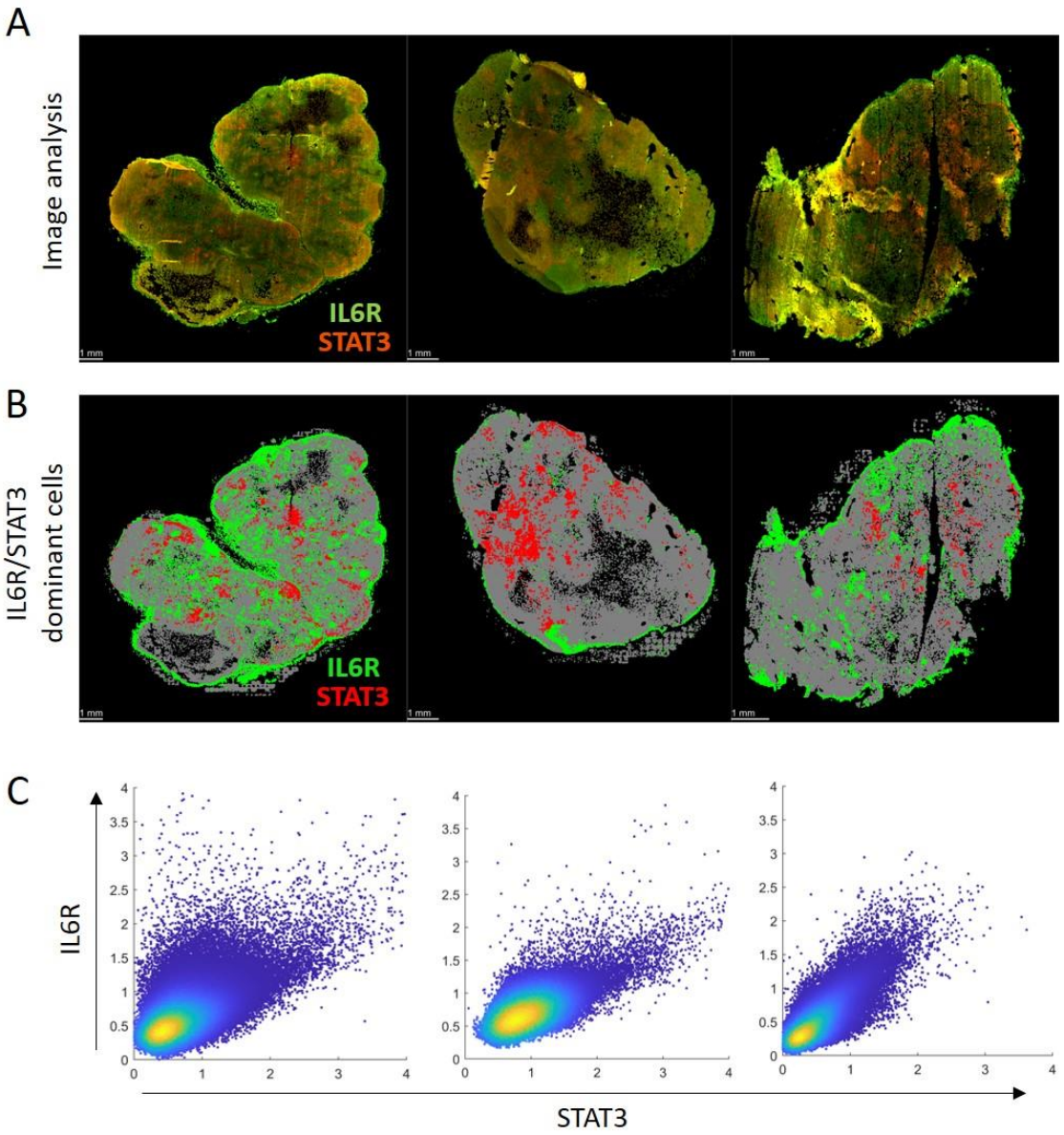


Figure 5.13 The heterogeneity of IL6R is maintained *in vivo*. A: Analysis of fluorescent staining of MIA PaCa-2 xenografts. Each cell is marked by green if IL6R expression is dominant over STAT3, or red if STAT3-dominant. Yellow cells show similar levels of both proteins. B: The image shows IL6R/STAT3 ratio dominant cells omitting those of average fluorescence intensity (grey). In cells highlighted in green the ratio is 50% above the median (IL6R dominance), and in red cells where this ratio is 50% below the median (STAT3 dominance). C: Distribution of IL6R and STAT3 expression in three different MIA PaCa-2 xenografts confirming the IL6R heterogeneity *in vivo*.

5.2.13. IL6R expression impacts the heterogeneity of lactic acid efflux

To confirm whether IL6R expression has the capacity to influence the population distribution of lactic acid efflux, MIA PaCa-2 cells were transfected with IL6R-targeted siRNA. The transfection efficacy was about 50% (Fig.5.14B). Knockdown of IL6R expression in MIA PaCa-2 cells, although incomplete, created a profound shift in the distribution of MCT permeability towards lower activity, thus confirming the relationship between high IL6R expression and glycolytic phenotype (Fig.5.13A).

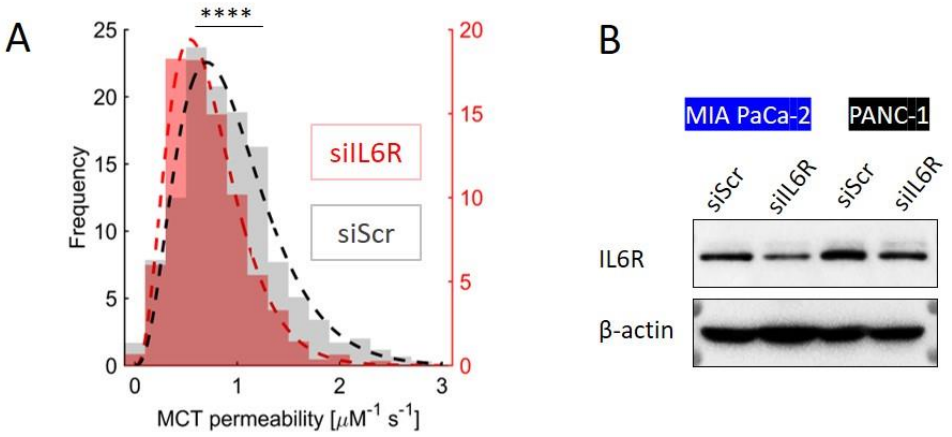


Figure 5.14 IL6R expression influences the heterogeneity of lactic acid efflux. A: The distribution of MCT permeability in MIA PaCa-2 cells transfected with siRNA against IL6R (siIL6R) or scrambled control (siScr). Data from three biological repeats are shown as a distribution with dashed lines depicting best fit. The significance was calculated using the Kolmogorov-Smirnov test. B: Representative western blot showing the efficacy of IL6R knockdown in MIA PaCa-2 and PANC-1 cells.

5.2.14. STAT3 inhibition increases IL6R-expressing population in MIA PaCa-2 but not PANC-1 cells

The transient character of the metabolic profile of MCT-sorted cells suggests an element of feedback that maintains subpopulations in balance, ostensibly by means of signalling. The IL6 signalling has been previously reported to be affected by random shedding of the receptor-mediated by the activity of metalloproteinases, especially a disintegrin and metalloproteinase 10 (ADAM-10) and 17 (477, 478). This cleavage would create a number of unbound IL6R-IL6 complexes, which could activate cells that under physiological conditions do not express the receptor. As binding of IL6 to its receptor triggers the phosphorylation and nucleus translocation of STAT3, where it acts as a transcription activator, the impact of STAT3 inhibition on the level of the active surface receptor was assessed. Additionally, the metalloproteinase-mediated cleavage of IL6R in MIA PaCa-2 and PANC-1 cells was tested. To investigate whether the surface expression of IL6R is under transcriptional control of STAT3 or if it is affected by random receptor cleavage the cells were treated for 48 hours with STAT3 inhibitor, napabucasin, and non-selective metalloproteinase inhibitor marimastat. Then, the viable cells were stained for surface-expressed IL6R followed by fixation and staining for total STAT3 expression and FACS analysis (Fig.5.15). Marimastat-sensitive metalloproteinase-mediated cleavage of IL6R did not affect receptor levels in either of the cell lines. On the contrary, STAT3 inhibition increased surface expression of IL6R in MIA PaCa-2 cells by 20-fold confirming that IL6 signalling in these cells is controlled by STAT3-mediated feedback circuit (Fig.5.16). In this model, activation of STAT3 is expected to stimulate glycolysis rapidly and reduce IL6R expression on a slower time

scale, whilst also stimulating IL6 synthesis and release. In this feedback circuit, a cell cycles from high glycolytic activity to low (delayed negative feedback), and spreads this influence via IL6 to neighbouring cells in a paracrine mechanism.

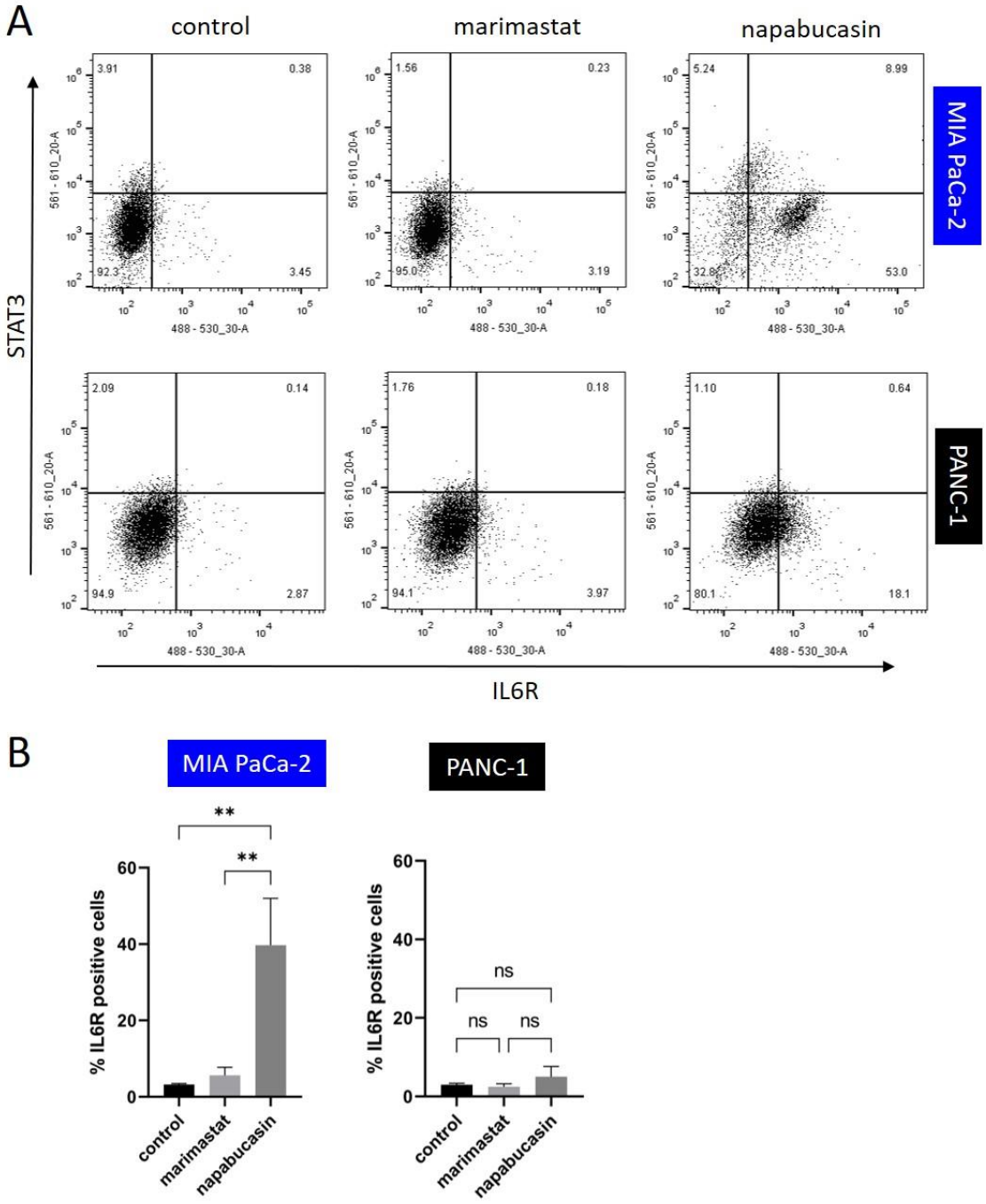


Figure 5.15 STAT3 inhibition increases surface expression of IL6R. A: Representative dot plots showing the expression of IL6R and total STAT3 in control and marimastat (1µM, 48 h) and napabucasin-treated (0.5 µM, 48 h) cells. Broad-spectrum metalloproteinase inhibition with marimastat does not affect the surface expression of IL6R nor STAT3. On the contrary, STAT3 inhibition by napabucasin elevates the surface expression of IL6R in MIA PaCa-2, but not PANC-1 cells. B: Quantification of IL6R-positive cells observed between treatments. Data shown as mean ± SEM. Mean calculated from three independent biological repeats. The significance was calculated using ordinary ANOVA with Tukey's multiple comparisons test.

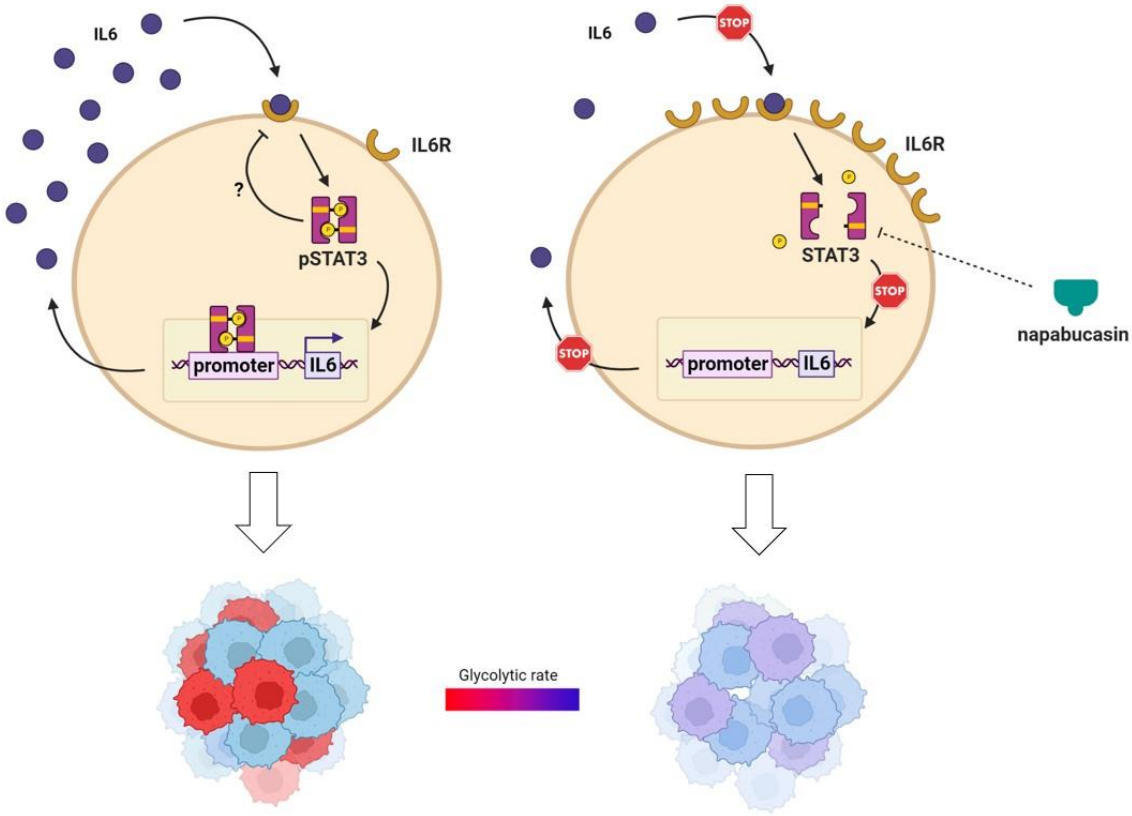


Figure 5.16 Proposed feedback circuit controlling the number of active surface receptors and heterogeneity of glycolytic metabolism in MIA PaCa-2 cell line. Binding of IL6 to IL6R induces a downstream cascade leading to STAT3 phosphorylation and dimerization. STAT3 dimers are translocated into the nucleus where they bind to the IL6 promoter region and stimulate transcription of the ligand. The negative feedback between STAT3 activation and IL6R controls the number of active receptors. The abundance of the ligand ensures stable pathway activation resulting in stimulation of glycolysis as well as the turnover of the receptor creating the glycolytic-heterogeneity within the population. Treatment with napabucasin prevents phosphorylation of STAT3 and the positive loop between the IL6 binding and synthesis is impaired. Shortage of the ligand prevents activation of IL6 signalling and lack of negative feedback increases the number of surface receptors removing cycling and creating a more metabolically homogenous population. As a result of negative feedback, the cell cycles between a high and low metabolic rate: in a high IL6R state, IL6 binding activates STAT3 and glycolysis but also evokes a slower downregulation of IL6R. Once this negative influence is fully implemented, the cell becomes unresponsive to interleukin and its glycolytic rate decreases. Without the stimulation of the IL6R-STAT3 pathway, receptor expression increases, without being hindered by activated STAT3.

5.3. Discussion

This Chapter described the metabolic heterogeneity in Pancreatic Ductal Adenocarcinoma cell lines, and how this arises and is maintained. The data shown here challenge the classical understanding that selection pressures in the environment drive the occurrence of metabolic phenotype diversity because the measured heterogeneity of glycolytic metabolism was observed within the population of the same cell line and under uniform *in vitro* conditions. An innovative, FACS-based protocol allowed the separation of distinct metabolic subpopulations according to the activity (rather than expression) of Monocarboxylate Transporters. Transcriptome analysis of collected subgroups surprisingly revealed a lack of difference in expression of canonical glycolytic pathway genes, and indicated interleukin 6 signalling as a driver of the phenotype. Interestingly, the expression of SLC16A1 (coding for MCT-1), by the activity of which the cells were separated was found unaltered, which confirms that assessment of expression alone, when it comes to metabolic phenotype might not be appropriate.

The IL6 signalling pathway is a crucial element of many pathologies, including cancer. Elevated serum IL6 levels are a hallmark of a systemic response to cancer (479), and have been suggested as a diagnostic and prognostic marker (480), with high levels indicative of poor prognosis due to cachexia (481). However, the causal mechanism of IL6 signalling on oncogenic transformation is still debated (482). *In vivo*, high IL6 synthesis is maintained via the activity of myeloid cells (483), and activated stroma, mainly cancer-associated fibroblasts (484, 485). Some reports indicated the capacity of tumour cells themselves to produce the cytokine (486, 487), however, the extent of

the endogenous synthesis in comparison to other components seems to be marginal. In this Chapter, the endogenous IL6 production by pancreatic cell lines *in vitro* was assessed, which confirms the autocrine/paracrine mechanism of this signalling in cancer. The binding of IL6 to its receptor, IL6R, results in classical or trans-signalling and a cascade of downstream events including the JAK-mediated phosphorylation of STAT, mostly STAT3 (488). The link between IL6 signalling and the regulation of glycolytic metabolism has been reported previously. IL6, via phosphorylation of STAT3, has been shown to promote the expression of glycolytic enzymes including hexokinase 2 and 6-phosphofructo-2-kinase (212), although in this study no difference in the expression of these genes between subpopulations of diverse glycolytic phenotypes was observed. Another mechanism by which IL6 enhances glycolysis is the increase of glucose uptake via stimulation of GLUT4 membrane translocation (489). The role of IL6 has been implicated in various metabolic disorders, including insulin resistance and diabetes, however, the reported effects of the signalling activation are often contradicting (490). This might be a result of the pleiotropic character of this cytokine and the fact that its actions seem to be particularly context-dependent (491). A positive feedback loop between STAT3 activation and increased ligand synthesis has been reported previously (196). Here this circuit was confirmed as the endogenous cancer cell IL6 synthesis was reduced following STAT3 inhibition. Additionally, negative feedback acting on the receptor levels is reported here, which is essential for explaining how a cell cycles between a high and low metabolic state. The inter-tumour heterogeneity of STAT3 status has been observed before in pancreatic cancer models, and the IL6 signal transducer (IL6ST) was identified as a key regulator of STAT3 phosphorylation (492). Similarly to data shown in this Chapter, the authors identified

MIA PaCa-2 cells as dependent on IL6ST-induced STAT3 signalling in driving aggressive phenotype of cancer but did not observe similar behaviour in PANC-1 cell line (492). Although PANC-1 cells ranked only second to MIA PaCa-2 in terms of the diversity of glycolytic phenotype, none of the differentially expressed genes identified in MIA PaCa-2 was validated in PANC-1. This suggests that either the FACS protocol separating the cells by lactic acid efflux capacity has failed, or that the subpopulations found in PANC-1 and MIA PaCa-2 are not phenotypically alike. The transient character of observed glycolytic phenotypes suggests a short-lived underlying transcriptional or signalling mechanism as opposed to a genomic mechanism, which should produce clones of stable metabolic profiles. It has been shown, that following extraction of the subpopulation from the parent cell line within a week the subgroups lose their distinctive metabolic profiles. However, while lost between separated cells, the phenotypes are maintained within the total population, suggesting that it is in each cell's fate to manifest both phenotypes in due course. This cycling pattern of metabolic profile could be explained by ligand-driven desensitisation of the IL6R receptor, as previously proposed (493, 494). Although the desensitisation of IL6 signalling would be an attractive explanation of IL6R-related metabolic cycling the timeline of reduced sensitivity cannot explain the metabolic profiles observed in this Chapter. Fisher et al., (2004) observed a gap in STAT3 activation during continuous stimulation with IL6 in hepatoma cells. This gap occurred at 2 hours after the initial stimulation and lasted for the next 2 hours before the sensitivity was regained. The authors reported that the desensitisation was not mediated by changes to either IL6R nor IL6ST membrane expression, but by activation of JAK kinases (494). A similar desensitisation period was observed in a model of pancreatic cancer. Upon steady IL6 treatment, the reduction in pSTAT3 levels occurred

at 1 and 2 hours after the onset of the stimulation. The sensitivity was regained after 4 hours despite ongoing IL6 stimulation consistent with previous reports. The authors studied the response of several PDAC cell lines, including MIA PaCa-2 and PANC-1 also researched in this Chapter. However, the STAT3 activation time-course was reported only in one tested cell line, HPAC, while others were omitted (495). As the turnover of IL6R and IL6ST is extremely rapid, with half-life not exceeding 2.5 h and membrane translocation of mature proteins happening within 45 minutes (496), it is unlikely that desensitisation could explain the cycling of metabolic phenotypes observed here which were maintained for at least 48 hours before dissipating after 1 week in culture. Another mechanism that might contribute to desensitisation is the random cleavage of the receptors (either IL6R or IL6ST) mediated by metalloproteinases such as ADAM-10 and ADAM-17 as reported previously (497-499). This is contradictory to data obtained by Fisher and colleagues, who found no changes to surface receptor expression during desensitisation (494). Similarly, treatment with marimastat, a pan-metalloproteinase inhibitor failed to affect the membrane expression of IL6R in this Chapter. Perhaps, the cleavage-mediated shedding of the receptor is not available due to insufficient expression of the enzymes or the sub-optimal *in vitro* conditions. The phenomenon of transient metabolic phenotypes is strengtened by data obtained by Kondo et al., (2021), who observed that the regenerative glucose metabolism heterogeneity of breast cancer cell lines is under the control of PIK3 signalling, chromatin state and actin dynamics (500). The metabolic profiles tracked by the authors with fluorescent glucose probes were maintained by both parent and daughter cells for at least 3 divisions, which is in line with the time-frame observed in this Chapter. PI3K signalling sugessted by the researchers as a cause of heterogeneity might also be relevant here,

as IL6 has been reported to activate PI3K (501), alongside STAT3 and JAK1 and 2 (151). Summing up, this Chapter explored metabolic heterogeneity in a model of pancreatic cancer. Glycolytic phenotype assessed as the capacity to extrude lactic acid and the glycolytic rate of cells was found to be diverse in a panel of tested cell lines, with profound intra-population heterogeneity observed in MIA PaCa-2 and PANC-1 cell lines. Separating MIA PaCa-2 cells according to their MCT permeability releaved distinct metabolic populations of transient character, which returned to parent phenotype within a week. These populations differed significantly in terms of global gene expression, with IL6 signalling enriched in highly glycolytic subgroup. The cells were found sensitive to STAT3 inhibition, which reduced glycolysis, and decreased endogenous IL6 synthesis, while simultaneously elevating membrane-bound IL6R levels. Due to inconsistencies between reported time-frame of ligand overload-triggered desensitisation and both half-life and regenerative character of metabolic phenotypes observed here, an IL6-synthesis oriented feedback has been proposed (Fig.5.16). Binding of the ligand to IL6R causes a dimerisation with IL6ST, which in turn activates Janus kinases and allows for phosphorylation and dimerisation of STAT3. These dimers are transported into the nucleus where they bind to IL6 promoter. This in turn triggers its transcription and creates a positive loop between IL6 signalling and its production and stimulates glycolysis. At the same time, activation of STAT3 feeds back negatively on membrane IL6R levels, restricting the number of active receptors. This way, the activated cell produces the ligand to stimulate local cells, while simultenously becoming desensitised by a reduction in receptor expression. Thus, the phenotype is being 'transferred' onto another cell causing the observed cycling. The napabucasin-mediatated STAT3 inhibition prevents its phosphorylation and activation abrogating

its transcription regulating acitivity which elminates both positive impact on IL6 production and a negative effect on IL6R expression. This creates a system with limited IL6 in the microenvironment which is eventually used. Lack of both the ligand and the negative impact of activated STAT prevents the internalisation of the receptors and increases the number of active membrane-bound receptors. This creates more homogenous and less glycolytic total population of decreased proliferative advantage.

However, as this phenomenon was observed only in one cell line it might not represent a universal mechanism. It is unclear why PANC-1 cells were insensitive towards STAT3 inhibition and did not harbour a similar metabolic population as MIA PaCa-2 cells. The differential responses of these cell lines to napabucasin have been studied by Froeling and colleagues, who proved that napabucasin undergoes bioactivation by binding to oxidoreductases, particularly NAD(P)H:quinone oxidoreductase-1 (NQO1). As NQO1 is not expressed in PANC-1 cells they are protected from negative effects of the inhibitor (502). Furthermore, it is likely that the glycolytic activation in PANC-1 cells is not modulated via IL6 signalling, but by another pathway. This however could not be easily elucidated without global transcriptomic and proteomic studies which are beyond the scope of this Chapter. Another lead that warrants investigation is the impact of IL6 signalling on transcriptional regulation of the receptors IL6R and IL6ST. Furthermore, rapid glycolysis collapse was observed following the acute treatment with napabucasin. As the mechanism by which IL6-STAT3 elevates glycolysis was attributed to transcriptional activation of glycolytic enzymes and glucose transporter expression it is unclear how it could affect the glycolytic rate so rapidly. The more plausible mechanism seems to be signalling-based, which would have the capacity to mediate more immediate effects observed within minutes from drug

administration (503). Although napabucasin has been extensively studied, most of the research is focused on its actions in a clinical setting (504-512) rather than mechanism per se (513). Several napabucasin-triggered actions have been reported, including a confirmed inhibition of STAT3 phosphorylation (514), however, some non-specific effects may be involved. Future work will need to address the mechanism by which STAT3 stimulates IL6 production yet inhibits IL6R expression.

5.4. Key findings

1. Pancreatic Ductal Adenocarcinoma cell lines manifest inter- and intra-tumour heterogeneity of glycolytic phenotype and lactic acid efflux capacity;
2. High lactic acid efflux capacity phenotype correlates with increased metabolism but this phenotype is not maintained long-term and dissipates within a week;
3. Cells sorted according to the lactic acid efflux capacity present distinctly different gene expression patterns;
4. Cells sorted based on IL6R expression manifest increased glycolytic metabolism, but as the phenotype is transient;
5. The heterogeneity of IL6R expression in MIA PaCa-2 cells is maintained *in vivo*;
6. Intra-tumour heterogeneity of glucose metabolism is maintained by the feedback circuit between the IL6 signalling and IL6 synthesis, even under selection pressure-free *in vitro* conditions.

Chapter 6. Comparing and contrasting the effects of acid selection versus acid adaptation on pH-related cellular phenotypes

Extracellular acidosis, resulting from poor perfusion and enhanced glycolytic activity, is a common feature of the tumour microenvironment. Chronic acidity has been associated with a number of effects including enhanced cell motility, decreased adhesion, deregulated metabolism, evasion of immune recognition and extracellular matrix remodelling, all of which contribute to elevated metastatic potential and more advanced disease stage. Although interest in studying acidity-driven cell behaviours and underlying mechanisms is widespread, typically inadequate efforts are made to distinguish whether the observed changes are related to an adaptation of cells to acidity or whether they are a product of selection. This is particularly problematic for assays that measure population-averaged parameters that lack single-cell granularity, necessary for testing whether sub-populations may have been selected for or against. For selection to occur, acidity must be strong enough to eliminate unfit clones before they may adapt, thus the original disturbance must be adequately fast. On the contrary, cells may adapt to acidosis if given sufficient time to respond, such as when the rate of acidification is sufficiently slow to evoke an iterative process of fine-tuning fitness. In this Chapter, the effects of selection by acidity and acid-adaptation of a panel of Pancreatic Ductal Adenocarcinoma cell lines are compared and contrasted.

6.1. Introduction

Extracellular acidosis is a chemical signature of solid tumours (515). The enhanced aerobic glycolysis (516) and aberrant vascular perfusion (517) contribute to a reduction of pH up to a point at which cells no longer produce acid (i.e. the steady-state at which glycolysis is effectively shut down). Low tumour extracellular pH is often associated with increased primary tumour load, and an overall more advanced stage of the disease (281). As it facilitates evasion of immune recognition by impairing the function of immune cells (401, 518) and increasing motility (332, 519) and selecting for more aggressive cell clones (463), acidity has been recognised as a crucial factor driving initiation of metastasis (297, 342, 520). In most normal tissues, interstitial pH is tightly controlled within 0.1 unit of pH 7.4 due to excellent diffusive coupling with blood (521). Some tissues, however, might be exposed to more pronounced fluctuations in extracellular pH (522). One of such organs is the exocrine pancreas which is responsible for secreting large fluxes of bicarbonate ions at the apical membrane which causes interstitial pH to fall, particularly in the postprandial period (523). The concentration of HCO_3 in pancreatic juice can reach 150 mM (345). Following the stimulation with secretin, apical efflux of HCO_3^- into the ductal lumen (524, 525) is linked stoichiometrically to H^+ secretion into the interstitium (345, 526). This way, the ductal cells are bathed in acidic conditions that may facilitate oncogenic transformation (341). The effects of acidity on cancer biology including cell metabolism (527), adhesion (333), proliferation, motility (528), as well as immune recognition are widely studied (529, 530). There are, however, concerns about how to interpret the data because the manner in which pH had been manipulated was often not adequately reported

to distinguish whether the outcomes are a product of acid adaptation, selection, or a mixture of both. Additional problems are caused by a lack of consensus when it comes to the understanding of the terms such as 'acid-selection' and 'acid-adaptation', which seem to differ significantly between different laboratories and the fact that although adaptation-oriented research is a popular topic, selection seems to be studied mostly in theoretical models (531-535). These factors significantly impact cell responses and might influence the interpretation of obtained data. This issue has been reviewed previously in the article written by the Author and Professor Pawel Swietach and the discrepancies found between studies have been discussed (536). The effects triggered by extracellular acidosis reported in literature are combined in Table 6.1, with indication of the method used to manipulate pH and duration of acidic treatment.

Table 6.1 Examples of acidity-triggered cellular responses. Table modified based on a review written by the author and Prof. Pawel Swietach (536).

Model	*Method of manipulating pHe*	*Duration under acidosis*	*Target pHe*	*Reported cell response*	*Reference*
Breast cancer: MCF-7, MCF10-AT, MDA-mb-231, MCF10 and MCF10AT	Medium supplemented with 25 mmol/L of PIPES and HEPES and the pH adjusted to 7.4 or 6.7.	Acute: 72h and prolonged: 3 months	6.7	Resistance to anoikis, elevated collagen production, upregulated ECM remodelling enzymes: TGM2, LOXL2	(537)
Colorectal cancer: HCT116, SW480, LoVo, SW620, and HT29	Medium maintained in a 5% CO_2 atmosphere at 37 °C. The medium was supplemented with 25 mM HEPES and PIPES and the pH was adjusted.	Acute, 24h	6.5	Increased ASIC2 expression, ASIC2-driven invasion	(538)
Glioma: U87MG, T98G, U251	Medium supplemented with 25 mM HEPES and the pH adjusted to 6.8; 6.7; 6.6; 6.5	Acute, 24h	6.8, 6.7, 6.6, 6.5	Induced stem-cell phenotype, increased OXPHOS, upregulated IL22,	(539)

				GUCA2B, CYP24A1, OR6P1	
Breast cancer: MCF-7, ZR-75-1, T47D, MDA-MB-231 and MDA-MB-157	Medium adjusted to acidic pH with HCl.	Acute, 24h	6.7	Metabolic reprogramming to oxidative PPP and glutaminolysis	(296)
Pancreatic cancer: PANC-1, AsPC-1; Cervical cancer: HeLa; Glioma: T98G; Colorectal cancer: SW620	pH was manipulated by varying concentration of $NaHCO_3$ in a CO_2-rich atmosphere. pH 7.4: 8mM, pH 6.8 2mM	Acute, 24h	6.8	Decreased adhesion, SREBP2 activation, IDI1 and PDK4 upregulation	(540)
Mesenchymal Stem Cells, Melanoma: A375M6	Medium adjusted to acidic pH.	Acute, 24h	6.6-6.7	Low pH-exposed MSC enhanced *in vivo* melanoma growth, acidosis of tumour microenvironment potentiated the pro-tumoral activity of MSC	(541)
Melanoma: MV3	$NaHCO_3$-free medium supplemented with HEPES (10 mmol/L) and adjusted to the respective experimental pH.	Acute, 24h	7.0; 6.8; 6.4	Reduced cell-to-cell adhesion, invasion, increased cell-surface adhesion	(542)
Breast cancer: MCF7, SUM52PE	Medium supplemented with 25 mM HEPES, adjusted to the acidic pH.	Acute, 24h	6.7	Inhibition of canonical hypoxia response and activation of UPR and inflammation	(543)
Glioblastoma: U87-MG, HTB-14; Cervical cancer: HeLa, CCL-2; Mouse Lewis lung carcinoma: LLC1, CRL-1642; Glioma: GL261	Medium adjusted to acidic pH.	Acute, 24h	6.6; 6.2; 6.0	Increased uptake of lipoproteins via Proteoglycan-Dependent Endocytosis	(297)
Glioblastoma: LN229	Medium adjusted to the desired pH with 2N HCl.	Acute, 3h	6.2; 3.4	Increased surface cholesterol elevated proliferative and stem-like potential	(544)
BREAST CANCER: MCF-7, MDA-MB-468, MDA-MB-231, AND SKBR3	Medium adjusted to pH 6.5.	Acute, 48h	6.5	Decreased glycolysis, elevated glutaminolysis and fatty acid synthesis	(295)
Melanoma: Me30966, Mel501, WM793, A375, SK-Mel-28	pH was manipulated by varying concentration of $NaHCO_3$ in a CO_2-rich atmosphere.	Acute, up to 24h	6.8, 6.5	Induced autophagy, mTOR inhibition, activated AMPK,	(292)

				reduced glucose and amino-acid uptake	
Breast cancer: MDA-MB-231, MCF7; Pancreatic cancer: PANC-1	pH was manipulated by varying concentration of $NaHCO_3$ in a CO_2-rich atmosphere, the osmolality was maintained by adjusting NaCl.	Prolonged, 1 month	6.5	Metabolic deregulation, ECM remodelling, altered cell cycle regulation, induced DNA damage response. Elevated expression of SCNN1A, CACNG4, ASIC1, SCN1B, IFITM1	(545)
Melanoma: C8161	Slow conditioning over 1.5 months with 0.15 pH units drop every two weeks.	Prolonged, 1.5 months	6.7	Increased invasion, motility, altered gene expression relating to: cell cycle, inflammation, Wnt signalling, apoptosis, IL-2, cell adhesion	(546)
Lewis lung carcinoma: LLCm1	Cells were adapted to acidic pH by serial passaging through media of stepwise decreasing pH (7.0, 6.8, and 6.5) until pH 6.2 was reached. The cells were maintained for 2–4 weeks at each pH.	Prolonged, 3 months	6.2	Increased metastatic activity through MMPs, increased migration and invasion	(547)
Colorectal cancer: SW480, SW620	Medium supplemented with 25 mM HEPES and PIPES, pH adjusted to 6.5.	Prolonged, 3 months	6.5	Increased invasion and metastasis, altered chromatin accessibility including DNA remodelling-associated pathways, HDAC, SIRT1 pathway, DNA methylation	(548)
Breast cancer: MDA-MB-231, HS766T	Cells were cultured and passaged directly in acidic medium.	Prolonged, 3 months	6.7	Cytoplasmic vacuolated phenotype, elevated autophagy, in mouse model autophagy was reduced by systemic treatment with sodium bicarbonate	(293)

Melanoma: Mel501; Breast cancer: MCF7ac; Prostate cancer: PC3ac	Cells allowed to acidify in an unbuffered medium for 5 days, then passaged and moved to a medium of pH 6.5.	Prolonged, 3-4 weeks	7; 6.75; 6.5	Remodelled lipid composition towards longer, unsaturated acyl chains, upregulation of genes involved in acyl chain desaturation, elongation and phospholipid transfer	(549)
Melanoma: Me30966; Prostate cancer: LNCaP; Osteosarcoma: SaOS2; Breast cancer: SKBR3; Colorectal cancer: HCT116	Cells allowed to acidify in an unbuffered medium for 5 days, then passaged and moved to a medium of pH 6.5.	Prolonged, 3-4 weeks	6.5	Increased exosome release	(550)
Cervical cancer: SiHa; Head and neck cancer: FaDu; Colorectal cancer: HCT-116	Medium supplemented with 25 mmol/L of both PIPES and HEPES, pH adjusted to 6.5	Prolonged, 8-10 weeks	6.5	Increased mitochondrial protein acetylation, switch to fatty acid oxidation	(527)

The aim of this Chapter is to assess the effects of a slow versus fast acid-treatment protocol on the metabolic profile of Pancreatic Ductal Adenocarcinoma cell lines. These protocols aim to distinguish between acid selection and adaptation to acidity on the basis of the rate of pH change.

6.2. Results

6.2.1. pH sensitivity of PDAC cell lines

To accurately select the most appropriate acid-treatment protocols, several factors must be considered. First is the cell line's specific extracellular pH sensitivity. The choice of medium pH selected for acidic treatment must fall within the range that at least some number of cells are able to withstand; otherwise, the cells will be killed excessively. Next, the realistic range of pH the cells may be expected to experience must be considered. This is a range of pH cells experience as a result of their own metabolism, assessed in Section 4.2.2. For all tested PDAC cell lines, the metabolic acid production was inhibited by pH 6, thus choosing a pH point below that threshold would subject the cells to supra-physiological (and irrelevant) conditions. The pH-sensitivity of PDAC cell proliferation was assessed over this range by seeding cells at low density and maintaining the cells at various pH points, enforced by titrating HCO_3^- concentrations, and allowing growth for 7 days. On the final day, the cells were fixed and the biomass produced was stained with SRB and its absorbance measured. The optimal pH for most tested cell lines fell within the pH range of 7.0-7.6. The AsPC-1 cell line was most vulnerable to acidity, with growth inhibition observed just below pH 7.0 (Fig.6.1). Based on these results, pHe values chosen for further experiments were set to a level that reduces the total biomass by 90%; e.g. for MIA PaCa-2 it was 6.3, and 6.5 for PANC-1.

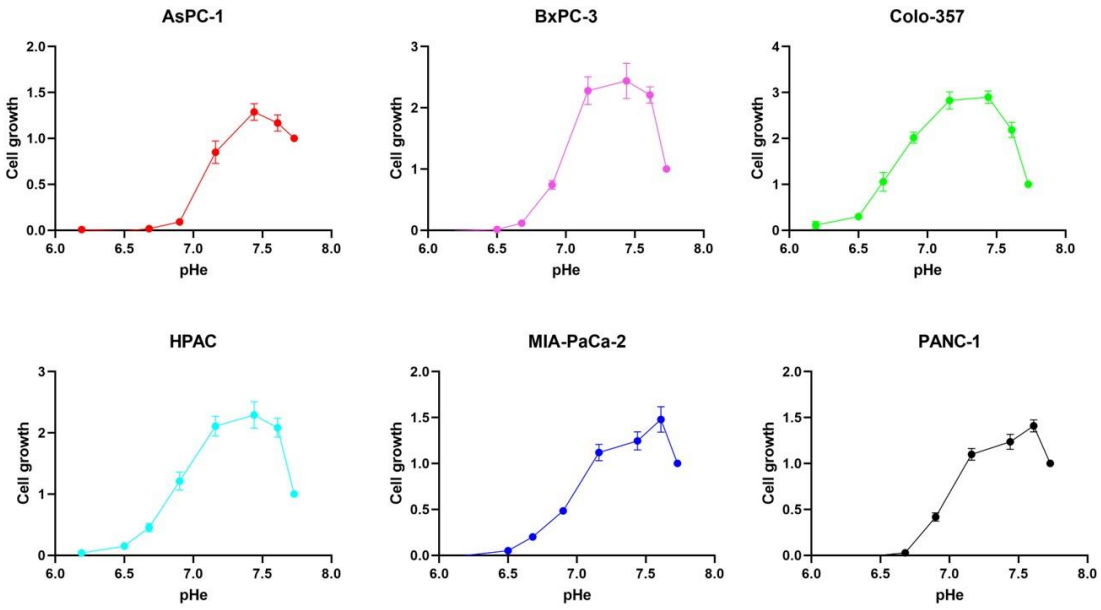


Figure 6.1 pH sensitivity of PDAC cell lines. Cells cultured for 7 days in a medium of pH ranging from 6.4 to 7.8 obtained by manipulating the $NaHCO_3$ concentration. The cell growth was assayed from the mean biomass produced after the period of the experiment. Data plotted as a mean ± SEM.

6.2.2. Impact of acidosis on the heterogeneity of glycolytic phenotypes

Previous Chapters established that metabolic acid production is blocked by pH below 6 and that cells of MIA PaCa-2 and PANC-1 lines show a wide distribution of both glycolytic metabolism and lactic acid efflux potential, two measures of metabolic heterogeneity. This suggests that upon exposure to an acidic environment, cells that normally have a low glycolytic capacity may reach a critical level of flux that is unable to sustain growth; in contrast, cells with a high MCT activity may still have the necessary reserve to remain viable. This predicts that acid selection should change the distribution of MCT activity by eliminating MCT-low cells, i.e. shifting the distribution to higher median values. However, it is also possible that cells with low MCT capacity have a high respiratory rate, i.e. do not need glycolysis for survival, whereas MCT-high cells are less oxidative. In such a scenario, acid selection would eliminate cells with low respiratory capacity, i.e. the higher MCT population, thereby shifting the distribution to the left.

These alternative scenarios were tested by comparing MCT activity in time-matched cultures maintained in a medium of neutral pH (7.4) or acidic pH (6.3 for MIAPaCa-2, 6.5 for PANC-1), after which, the MCT permeability of cells, compared to controls was assessed.

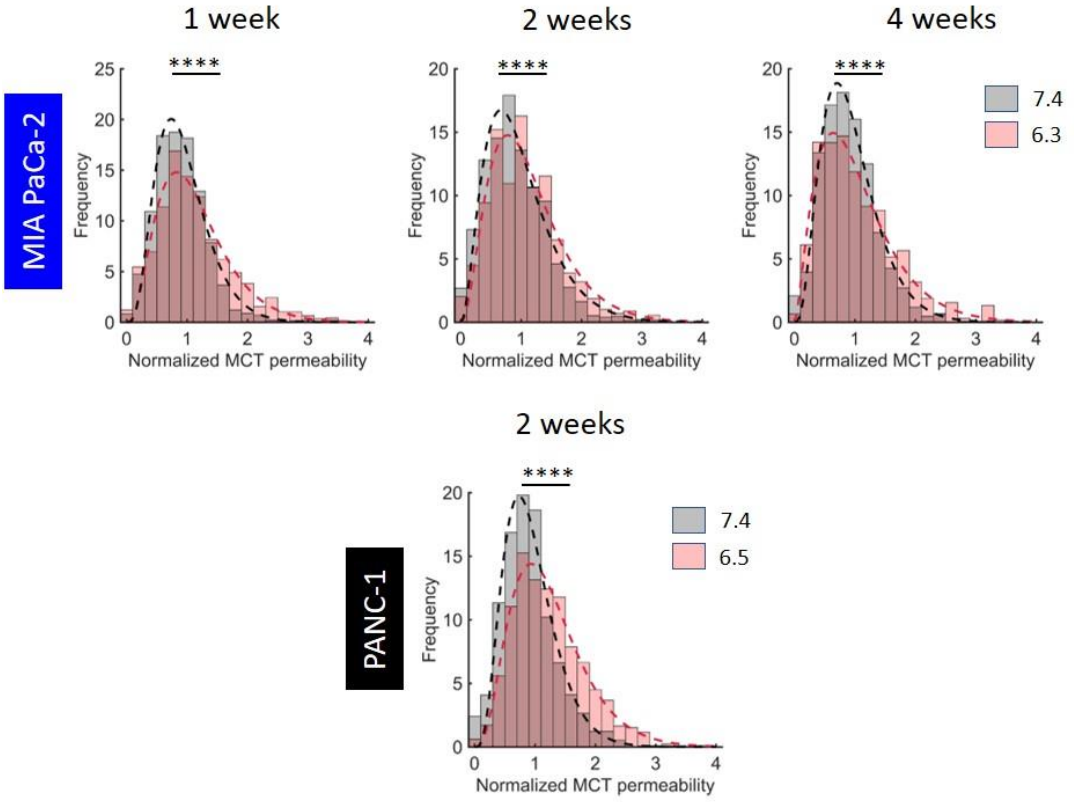


Figure 6.2 Acid treatment induces a shift in MCT permeability in PDAC cells. MIA PaCa-2 and PANC-1 cells selected by low pH and maintained in culture for 1, 2 or 4 weeks prior to MCT permeability measurements. The acid treatment created a significant shift towards higher MCT permeability, although the shift was of a small magnitude. No time dependence was observed. The most pronounced shift was observed in PANC-1 cells after 2 weeks of acid selection. Data shown as the mean of at least three repeats (3-5), significance was calculated using the Kolmogorov-Smirnov and Fisher test for meta-analysis.

The acidic treatment created a subtle but statistically significant shift towards the population of higher permeability in MIA PaCa-2 cells, and the effect was not influenced by the duration of the treatment. The most pronounced effect of low pH on MCT distribution was observed in PANC-1 cells after two weeks of acidic treatment (Fig.6.2). This finding indicates that acid selection has only a modest effect on the phenotypic

composition of PDAC populations, but provides evidence that cells with low MCT activity are more vulnerable to acidity and have weaker survival prospects at low pHe. These cells presumably lack the oxidative capacity to compensate for the loss of glycolytic flux at low pH. This is in line with data presented in Section 5.2.4, where high-MCT phenotype correlated with increased both glycolytic and oxidative rates.

6.2.3. Effects of acid treatment on metabolic profile

Next, the effects of various acid treatments were assessed in terms of metabolic profile. It is widely accepted that acidic conditions lead to metabolic reprogramming towards more oxygen-dependent phenotypes, as this branch of metabolism is essentially pH-insensitive. To confirm this notion and to distinguish between the effects on acid selection and acid adaptation, the metabolic profile of acid-treated cells was measured fluorimetrically. Here, selection and adaptation were implemented by controlling the rate at which pH was changed, with slower changes favouring the latter. For selection to occur, acidity needs to be strong enough and implemented rapidly to eliminate the majority of unfit phenotypes from the population. This will happen only if the chosen acidic pH is low enough based on the cell line-specific pH-sensitivity curves and if the pH is changed rapidly. To select cells by acidity, the medium was rapidly exchanged from physiological to acidic and maintained stable for the following two weeks (by regular medium changes). To adapt cells to acidity, a cell-metabolism-oriented approach was used. Rather than choosing an artificial rate of pH change e.g. by replacing the medium with more and more acidic every few days, the cells were seeded at high density (corresponding to 70% confluency) and placed in medium of physiological pH to acidify at their own pace depending on cellular acid production.

The pH of the medium was monitored by the change in colour of phenol red, and once sufficiently low pH was attained the medium was replaced with fresh, acidic one, of pH 6.5 or 6.3 depending on the cell line, and maintained in that medium for the remainder of the 2 weeks. After the period of acid treatment, the cells were seeded onto a 96-well plate as described in detail in Chapter 3, and the interplay between the oxidative and glycolytic metabolism was assessed.

Contrary to the canonical view that inhibiting glycolysis increases reliance on oxidative phosphorylation, the acidic treatment decreased the glycolytic acid production rate in MIA PaCa-2 cells, without triggering a compensatory rise in oxygen consumption (Fig.6.3). On the contrary, in the more oxygen-dependent PANC-1 cells, glycolysis was less profoundly affected by acidity but the oxygen consumption decreased. Overall, acidic conditions decreased metabolic rates in cells, but the exact effects seem to be mostly dependent on the baseline metabolic profile of selected cell lines. To help stabilise pHe at the acidic level, a second series of experiments used MES buffer to supplement the otherwise low buffering capacity of CO_2/HCO_3^- at low pH. This modification of the protocol during the adaptation/selection phase did not, however, influence the results.

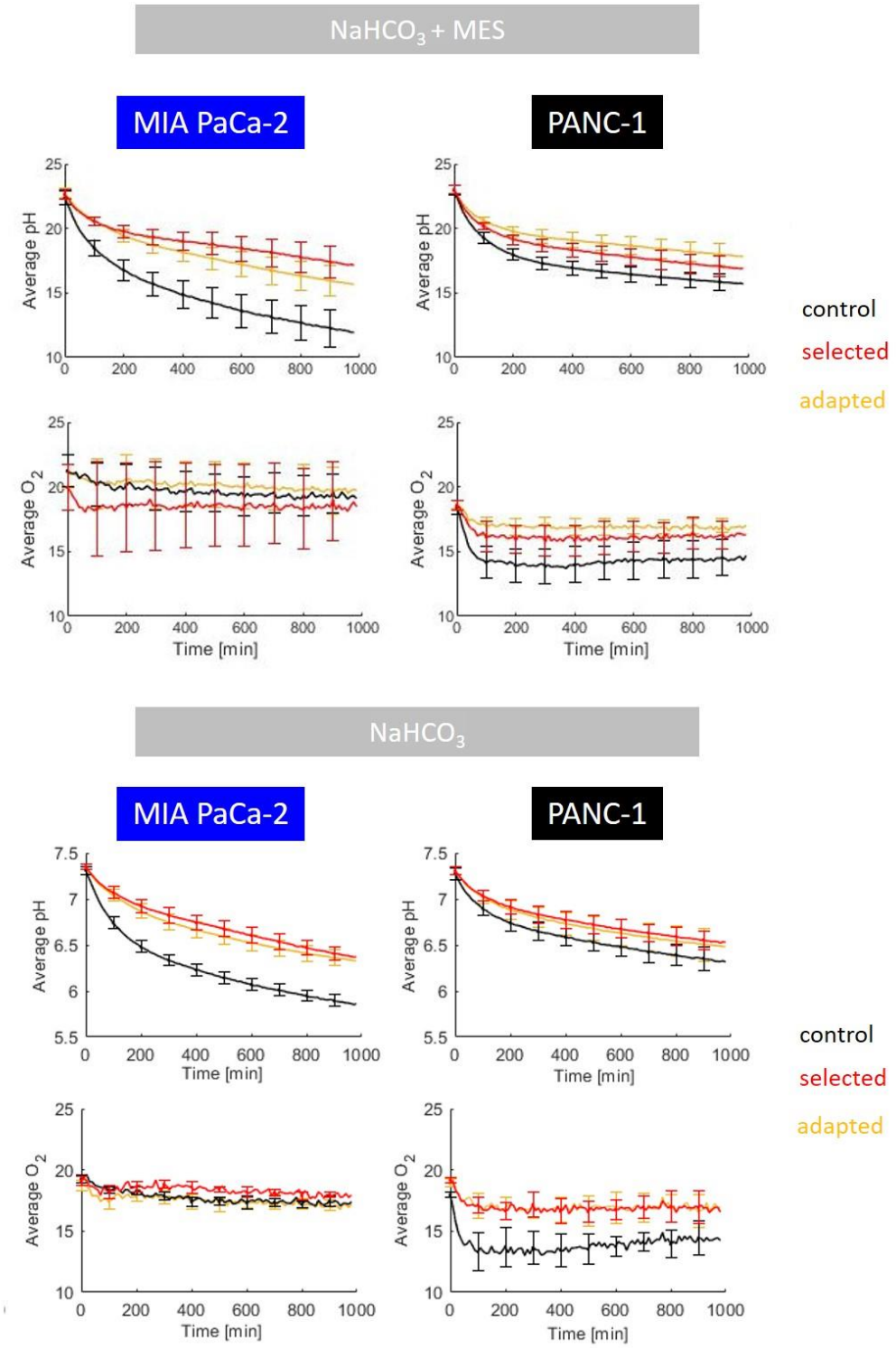


Figure 6.3 Acidic treatment alters the metabolic profile of PDAC cells. Cells selected by acidity and adapted to acid were seeded for metabolic profile assessment. As prolonged acid treatment decreased cell adhesion, the data were normalised to the number of cells. Acidic treatment (regardless of the type) decreased metabolic acid production in MIA PaCa-2 cells, no changes to oxidative metabolism were observed. Contrary effects were observed in PANC-1 cells, where acidic treatment did not significantly alter metabolic acid production but decreased oxygen consumption. Cells maintained in media where buffering was provided by a combination of $NaHCO_3$ and MES showed greater variability than those cultured in $NaHCO_3$ alone. Data shown as mean ± SEM of 3-6 biological repeats.

6.2.4. Effects of acid-selection and adaptation on intracellular pH

Chapter 4 described the effects of pH on glycolytic metabolism. In Section 4.2.10 the intracellular pH was confirmed as a main cue controlling the glycolytic rate of cells and showed that more alkaline intracellular pH elevates glycolysis. As acidic treatment was found to decrease both glycolytic and oxidative metabolism it was necessary to assess what impact it had on the intracellular pH of cells. MIA PaCa-2 and PANC-1 were subjected to acid treatment (selection and adaptation) as described previously. After two weeks of maintaining the cells under acidic conditions, the cells were seeded on poly-L-lysine coated Ibidi 96-well plates for high throughput intracellular pH imaging. Strikingly, prolonged acid treatment elevated intracellular pH by ~0.6 unit in both cell lines irrespectively of the rate of pH change (Fig.6.4A). Not only did the mean intracellular pH increase, but when studied at single-cell resolution, the acidic treatment also created a population shift towards a more alkaline phenotype (Fig.6.4B).

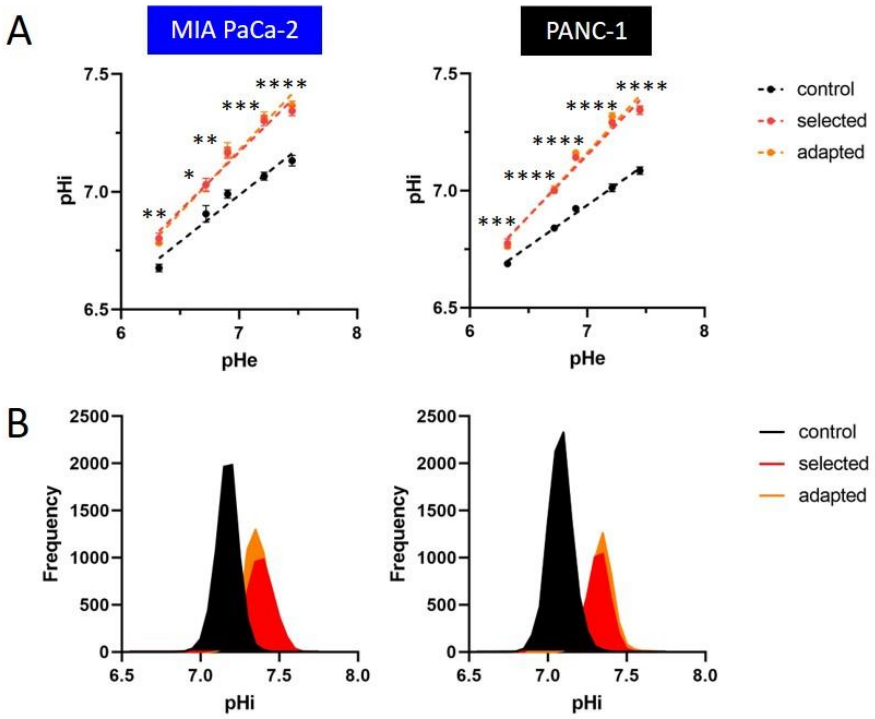


Figure 6.4 Acid treatment alkalinizes intracellular pH of PDAC cells. A: The cells were subjected to acid adaptation and selection by acidity as described before. After two weeks of acidic treatment, the cells were seeded for high-throughput pH imaging. Maintaining the cells in acidic conditions, regardless of the source of acidity and rate of pH change raises intracellular pH by ~0.6 pH unit in both PDAC cell lines. Data shown as the mean of 5 repeats ± SEM. Significance calculated with two-way ANOVA and multiple comparisons Tuckey's test. B: Acidic treatment shifts the population towards more alkaline rather than selectively killing cells of lower intracellular pH.

6.2.5. Anion Exchanger 2 undergoes degradation under acidic conditions

Since intra- and extracellular pH are thermodynamically coupled, a fall in extracellular pH will be accompanied by corresponding acidification of the intracellular compartment. The coupling between intra- and extracellular pH among PDAC cell lines has been measured in Section 4.2. This pHe-pHi relationship is maintained by the activity of several acid-extruders and acid-loaders including Na^+-H^+ Exchanger 1 (551, 552), Anion Exchanger 2 (553), Anion Exchanger 3 (554), SLC26A3 (555), SLC26A6 (556) and Na^+/HCO_3^- co-transporters (557, 558). The role of these proteins in regulating intracellular pH in response to microenvironment acidosis has been extensively studied by Dr. Johanna Michl (Swietach Lab, University of Oxford) in a model of colorectal

cancer. A similar rise in intracellular pH was observed as an adaptation mechanism in response to chronic acidity. This effect has been mediated by acid-triggered degradation of an acid loader, Anion Exchanger 2, which under physiological circumstances exchanges Cl^- for HCO_3^- ion. Inhibition of its activity, whether by degradation of the transporter or by removing the extracellular substrate (placing the cells in a low chloride medium, which was used in Section 4.2.10) elevates intracellular pH by trapping HCO_3^- inside the cytoplasm increasing intrinsic buffering (Michl et al., under review). To test, whether the same AE2 degradation-dependent mechanism is responsible for elevated intracellular pH in response to acidity in pancreatic cancer, the expression of AE2 in cells adapted to low pH was measured. The representative blot showing the expression of AE2 tested in cells maintained in either neutral or acidic conditions is depicted in Figure 5. Acid adaptation led to the loss of AE2 expression in both tested cell lines confirming the association between intracellular pH increase and AE2 function in acid adaptation (Fig.6.5).

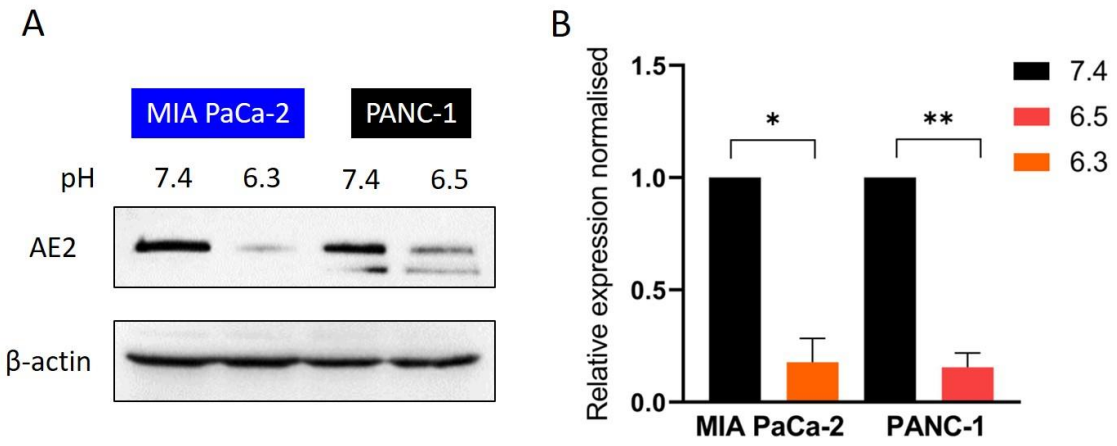


Figure 6.5 Anion Exchanger 2 degradation under acidic conditions. A: The representative western blot depicting the loss of Anion Exchanger 2 (AE2) expression triggered by acid adaptation. The effects are observed in both tested cell lines. B: Semi-quantification of AE2 expression relative to β-actin. Data shown as the mean of three repeats ± SEM. Significance was calculated with paired t-test.

6.3. Discussion

This Chapter studied the effects of acid selection and acid adaptation on PDAC cell phenotypes. To trigger the selection, the pressure needs to be strong enough to eliminate the majority of unfit phenotypes from the population and rapid enough to stop cells from adjusting. By comparison, adaptation may arise if the rate at which the pressure is presented is slow and allows cells time to respond. These triggers have been designed based on cell line-dependent pH sensitivity. For acid selection, rather than designing an arbitrary pH treatment, an informed and cell line-specific approach was used. To adapt cells to low pH, the cells were seeded at high density in a neutral medium and allowed to acidify at their own pace. This eliminated the problem of choosing a potentially too steep rate of pH change, which might not be attainable *in vivo*, and could have resulted in a degree of selection rather than adaptation alone. The success of these differential approaches was confirmed when the cell density was compared. The selection resulted in a loss of the majority of unfit clones, which did not proliferate at a comparable rate to control cells, while adapted cells grew in high number and required regular splitting during the remainder of the two-week-long period of acidic treatment.

The elevated expression of Monocarboxylate Transporters has been identified in several types of cancer and is considered an unfavourable prognostic marker in renal (559), endometrial (560), cervical (561), liver (561), lung (562), and pancreatic cancer (561). High expression of MCT-1 and MCT-4 has been observed at metastatic sites and is considered a crucial factor in disease recurrence (563). This increase could represent a compensatory mechanism of cancer cells to sustain high metabolic rates

by steady lactic acid efflux, or to preserve metabolic activity under acidosis. Additionally, the activity of MCT-4 has been implicated in maintaining alkaline intracellular pH (564). The tested cell lines manifested high intra-population heterogeneity in terms of the capacity to extrude lactate (the read-out of mean MCT activity). Acidic treatment mildly increased the fraction of cells with higher permeability, which indicates that some MCT-low clones had been eliminated. This indicates that cells with low MCT transport capacity have a survival disadvantage at low pH. Strikingly, acidic conditions did not evoke a rise in O_2 consumption, a plausible pathway compensating for acid-inhibited glycolysis. However, the overall effect of acidity on the distribution of MCT phenotype was modest at best and is unlikely to be critical in acid resistance. This shift may be compensatory to ensure that lactic acid efflux is maintained even at low extracellular pH, but whether it has been accompanied by increased expression of MCTs is unclear, though acidosis-triggered upregulation of acid extruders has been reported (565).

Tumours are characterised by a reversed pH gradient when compared to healthy tissue, with alkaline cytoplasmic pH and an acidic microenvironment (566-570). This notion has been challenged as low extracellular pH has been proposed to result in elevated proton influx with magnitude depending on the pH gradient (565). Rolver et al., (2021), observed an intracellular compartment in PANC-1 cells following the 4-week acid adaptation to pH 6.5 as acidic, not exceeding pH 7.0 (565). This is partially in line with the data presented in this Chapter. Although, similarly to literature data, pHi measured at extracellular pH of 6.5 did not exceed the acidic range, the consistent alkalinisation of the cytoplasmic compartment by about 0.6 pH unit across the tested pHe range (6.3-7.5) in both cell lines subjected to acidic treatment was observed. As monocarboxylate transporters have been implicated in intracellular pH regulation, with loss of expression

leading to lower cytosolic pH (571-573), the increase in population MCT permeability might have contributed to elevated intracellular pH observed here. However, as the magnitude of the MCT activity shift was mild, it is unlikely to be the only factor triggering the alkalinisation. It was proposed that this effect might be mediated by acidity-triggered loss of Anion Exchanger 2. Under physiological conditions, AE2 exchanges chloride for bicarbonate, thus causing cytoplasm to acidify. Reducing extracellular Cl^- is expected to reverse this process. This approach has been exploited in Chapter 4, where placing cells in a medium of low chloride concentration elevated the intracellular pH of cells without affecting pHe. It has been observed that selective raise in intracellular pH alone is sufficient to trigger dysplasia and create an oncogenic phenotype (574). This is further enhanced by pHi-mediated activation of arginine to histidine mutant proteins (575, 576). White et al., (2017) reported that the tumorigenic effects of arginine to histidine mutations in *EGFR* and *TP53* were attenuated by lowering intracellular pH. Also, this effect was specific to only arginine to histidine substitutions and was not observed in proteins harbouring other genetic alterations (575). If AE2 degradation is the first response to chronic acidosis, it might be that a direct cause of carcinogenesis is in fact the elevated intracellular pH, rather than microenvironment acidosis. Additionally, low AE2 expression has been linked to increased migration and evasion of apoptosis in a model of head and neck cancer (577), and it was observed that gastric cancer is characterised by a reduction in AE2 expression when compared with adjacent healthy tissue which correlated with dedifferentiation and poorer prognosis (578). Although some reports seem to confirm the association between reduced AE2 expression with more aggressive cell behaviour, the data are variable and largely dependent on the type of cancer. Perhaps these differences

in reported actions of AE2 could be explained by the pH conditions within the microenvironment, and therefore be dependent on unique tumour metabolism, or manifest themselves only at a certain stage (correlating with pH in the tumour milieu). Although the exposure to chronic acidosis increased the intracellular pH of cells by around half of a unit, in theory preventing the acidity-exposed cell from the glycolytic shutdown (579-581), it was not accompanied by elevated acid production. On the contrary, the oxidative metabolism rates in PANC-1 and glycolytic in MIA PaCa-2 cells following acidic treatment were slightly reduced, suggesting that low pH triggered more dormant phenotype, which is in line with data obtained by Gao and others (295, 582, 583). Although, reported previously acidosis-triggered metabolic reprogramming towards oxidative phosphorylation (296, 539, 584), was not observed here, the downregulation of glycolysis is in line with literature reports (292, 295). Moreover, the decrease in metabolic acid production might have contributed to elevated pHi phenotype (565). Perhaps the timeline of experiments was not long enough to reveal all acid-adaptation mechanisms and the common incubation period post-selection attenuated the potential differences between the groups.

Chronic acidosis has been recognised as a driver of oncogenic transformation. Acid adaptation has been reported to increase proliferation and lead to overall greater tumour size (585). These findings are contradictory to the data shown in this Chapter, as the observed reduction in overall metabolic rates would not sustain high proliferation. This lack of consensus might be a result of different adaptation protocols or the length of adaptation itself. The two-week-long adaptation used here, might not be sufficient to observe the full scope of adaptive response, which has been studied after longer periods of adaptation ranging from 1 to 3 months (293, 546-548). However,

if chronic acidosis reduces the metabolic rates how can it correspond to more aggressive phenotypes? Perhaps the energy demand necessary for sustained proliferation can be met due to elevated autophagy (294, 586-588), increased glutaminolysis (295, 296), and lipid droplet accumulation (589, 590), all of which are well-established responses of acid-exposed cancer cells. Additionally, the persistent selection pressure of accumulated extracellular acid despite stalling the growth of the primary tumour may facilitate cancer evolution by selecting for most aggressive clones well prepared for local invasion and formation of distant metastasis. Acidosis further propagates metastasis by maintaining alkaline intracellular pH, which by increasing mutation rates creates a more diverse group of genotypes to test for fitness, further accelerating cancer evolution.

Summing up, this Chapter revealed that acid-exposed cells, whether subjected to selection by steep pH-change or more mild adaptive approach respond in a similar way, by a reduction in metabolic rates, and AE2-dependent increase in intracellular pH. Furthermore, acid treatment influenced the MCT permeability by shifting the total population towards the phenotype of higher activity in order to sustain efficient lactic acid efflux even under acidic conditions.

6.4. Key findings

1. Acidity impacts MCT permeability by shifting the population towards higher activity to sustain lactic acid efflux;
2. Selection by acidity and acid adaptation raise intracellular pH in the same manner;
3. Acid treatment reduces the glycolytic rate in MIA PaCa-2 cells without affecting oxygen consumption, the contrary effect is observed in PANC-1, in which oxidative metabolism decreases following culture at low pH;
4. Chronic acid treatment elevates intracellular pH which is associated to the loss of Anion Exchanger 2 expression.

Chapter 7. Concluding remarks and future directions

The results described in this Thesis provide a comprehensive characterization of the role of acidity in shaping the metabolic profile of pancreatic ductal adenocarcinoma cells. Using a novel fluorimetric approach (Chapter 3), I quantified acid production in a panel of cell lines and described the feedback mechanisms that regulate metabolism. Using rapid solution switching (Chapter 4), I characterised the membrane permeability to lactic acid, the principal non-volatile acid produced by PDAC cells. I used this as a measure of glycolytic capacity to sort cells by FACS and study metabolic heterogeneity (Chapter 5). I also characterised the cell responses to selection by acidity and acid adaptation (Chapter 6). Based on this, I described feedback circuits that determine steady-state extracellular pH and also the phenotypic composition of cells in terms of metabolic rate. The overview of the signalling pathways and transporters studied in this Thesis is summarized in Figure 7.1.

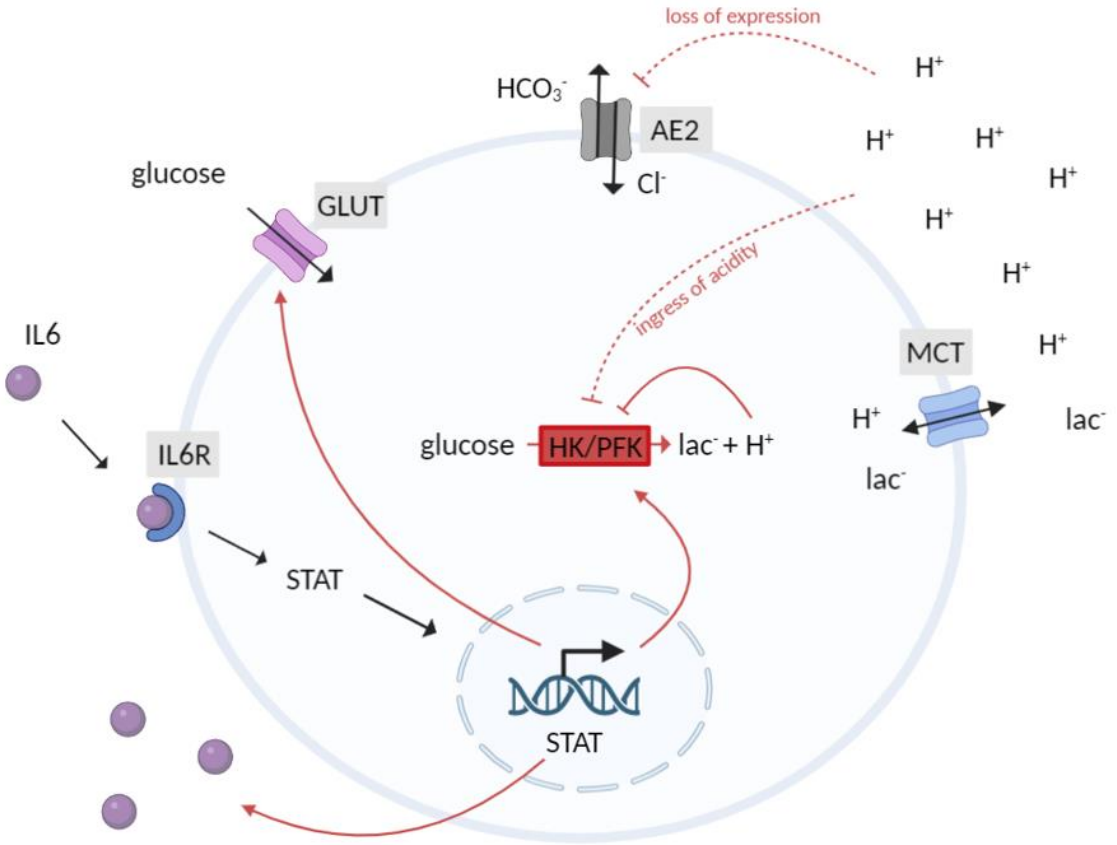


Figure 7.1 The overview of main signalling pathways and transporters studied in this project with indicated feedback control between them. In a glycolysis-dependent pancreatic cancer cell, glucose is converted into unstable lactic acid, which easily dissociates into a lactate anion and a proton. To prevent acidification of the cytoplasm, which inhibits glycolytic enzymes, glycolytic end-products are released into the microenvironment via monocarboxylate transporters. Extracellular acidosis is associated with the loss of anion exchanger 2 expression, which traps HCO3- inside the cytoplasm raising its pH. However, low extracellular pH by promoting the ingress of protons into the cytoplasm indirectly inhibits glycolytic enzymes limiting glycolysis. The binding of interleukin 6 to its receptor triggers a downstream cascade of events leading to phosphorylation and dimerization of signal transducer and activator of transcription, which translocates to the nucleus and stimulates expression of interleukin 6, glycolytic enzymes and glucose transporters promoting glycolytic phenotype. GLUT- glucose transporter, AE2-anion exchanger 2, MCT- monocarboxylate transporter, IL6-interleukin 6, IL6R, interleukin 6 receptor, HK-hexokinase, PFK-phosphofructokinase, STAT- signal transducer and activator of transcription.

In Chapter 4, I explained how acidity, generated as the end-product of metabolism, feeds back on glycolysis, a major supplier of non-volatile acid. In a closed system, such as that *in vitro* and (to a degree) in poorly-perfused tumours, this feedback circuit determines the lowest possible extracellular pH that can be attained. Extracellular pH stabilises when lactic acid production is blocked and cannot further acidify

the extracellular space; this remains until the system vents acidity by other means, such as diffusion. I found this feedback to be a universal feature of all PDAC cells, which operates via intracellular pH sensors represented by glycolytic enzymes. The coupling between intra- and extracellular is altered in cells exposed to chronic acidosis, due to the downregulation of a key acid-loader that maintains intracellular pH at a more alkaline level (Chapter 6). Furthermore, I described how glycolytic flux through H^+-monocarboxylate transporters (MCTs) is auto-regulated and cannot be affected by a sole change to permeability. This finding indicates that pharmacological inhibition of MCT activity cannot proportionately reduce glycolytic rate, and challenges their clinical utility. Strikingly, metabolically-generated acid does not affect respiration, at least acutely. This provides respiring cells with a major survival advantage in acidic niches, which inhibit metabolism in glycolysis-dependent phenotypes. This is in line with recent studies from the lab, showing that mitochondrial genes are essential for survival in acidic environments (Michl et al., 2022).

In Chapter 5, I studied the intra-population heterogeneity of metabolic profile using single-cell technologies, specifically in terms of glycolytic rate and the cellular capacity to export lactic acid. I observed significant diversity among cell lines, with MIA PaCa-2 cells showing the most profound and stable heterogeneity. By sorting cells according to lactic acid permeability, I was able to describe the gene expression signature of cells at the low and high ends of the distribution (referred to as MCT-low and MCT-high). The MCT-high subpopulation manifested increased respiratory and glycolytic rates with larger numbers of mitochondria. Moreover, RNA sequencing revealed cells of high permeability to have elevated expression of genes related to STAT3 signalling, of which

IL6 receptor (IL6R) was the most prominent. Strikingly, these key differences between MCT-low and MCT-high cells were transient and reverted to the parent phenotype within 2 weeks. Sorting by IL6R expression confirmed the link between receptor expression and elevated metabolic rate. Further work using a pharmacological and genetic approach showed that the IL6-IL6R-STAT3 axis includes feedback that produces spontaneously oscillating behaviour. This explains why sorted subpopulations lost their distinctive phenotype over time, and also underpins the mechanisms by which cells can alternate between high and low metabolic rates. This heterogeneity was confirmed *in vivo* in MIA PaCa-2 xenografts. This feedback challenges a canonical view that heterogeneity is predominantly set by a local variation in the environment or stable genetic differences. Instead, I show that it can also be a result of an intrinsic feature of MIA PaCa-2 cells that operates via the IL6-IL6R-STAT3 pathway which includes negative feedback. This is strengthened, by persistent heterogeneity observed *in vitro* under uniform environmental conditions. I postulate that this cycling of metabolic profiles facilitates disease progression without excessively acidifying the microenvironment. As a result, tumours can proliferate (in groups of cells at a time) without the risk of metabolic inhibition. The pathway requires further interrogation to explain why only some cell lines manifest cycling of metabolic activity, and whether it can be exploited therapeutically.

Chapter 6 focused on the responses of PDAC cells to extracellular pH over longer periods of time. To study this, I undertook two strategies: (i) I allowed the cells to acidify extracellular space at an endogenous rate corresponding to glycolytic metabolism, or (ii) I immediately exposed cells to a highly acidic medium by an experimental

intervention. In the former, the rate of pH change is slower which increases the ability of cells to adapt to changing conditions. In contrast, the latter is more likely to produce irreversible selection favouring fit phenotypes as the time frame might not be sufficient to allow for an adaptive response. In terms of effects on metabolic profile and intracellular pH regulation, selection and adaptation produced the same phenotype with decreased metabolic rate and an elevated cytoplasmic pH. This finding challenges the notion that acidity selects irreversibly; instead, acidosis may force cells to adapt, e.g. by downregulating the acid-loading anion exchanger AE2.

Summing up, this doctoral project mechanistically described: (i) how extracellular acidity arises in PDAC, and which cues regulate it, (ii) how cells respond to acute and chronic acidosis, (iii) and how the interplay between cytokines and metabolism can produce metabolic heterogeneity, providing the cells with a survival advantage. Although several fundamental processes were described, further research, especially *in vivo*, is required to confirm their relevance in a clinical setting.

References

1. Kleeff J, Korc M, Apte M, La Vecchia C, Johnson CD, Biankin AV, et al. Pancreatic cancer. Nat Rev Dis Primers. 2016;2:16022.

2. De La Cruz MS, Young AP, Ruffin MT. Diagnosis and management of pancreatic cancer. Am Fam Physician. 2014;89(8):626-32.

3. Sturm N, Ettrich TJ, Perkhofer L. The Impact of Biomarkers in Pancreatic Ductal Adenocarcinoma on Diagnosis, Surveillance and Therapy. Cancers (Basel). 2022;14(1).

4. Apte MV, Park S, Phillips PA, Santucci N, Goldstein D, Kumar RK, et al. Desmoplastic reaction in pancreatic cancer - Role of pancreatic stellate cells. Pancreas. 2004;29(3):179-87.

5. Sung H, Ferlay J, Siegel RL, Laversanne M, Soerjomataram I, Jemal A, et al. Global Cancer Statistics 2020: GLOBOCAN Estimates of Incidence and Mortality Worldwide for 36 Cancers in 185 Countries. CA Cancer J Clin. 2021;71(3):209-49.

6. Ushio J, Kanno A, Ikeda E, Ando K, Nagai H, Miwata T, et al. Pancreatic Ductal Adenocarcinoma: Epidemiology and Risk Factors. Diagnostics (Basel). 2021;11(3).

7. Wong MCS, Jiang JY, Liang M, Fang Y, Yeung MS, Sung JJY. Global temporal patterns of pancreatic cancer and association with socioeconomic development. Sci Rep. 2017;7(1):3165.

8. Chan JM, Gong Z, Holly EA, Bracci PM. Dietary patterns and risk of pancreatic cancer in a large population-based case-control study in the San Francisco Bay Area. Nutr Cancer. 2013;65(1):157-64.

9. Papier K, Kakkoura MG, Guo Y, Knuppel A, Pei P, Tong TYN, et al. Intakes of major food groups in China and UK: results from 100,000 adults in the China Kadoorie biobank and UK biobank. Eur J Nutr. 2022.

10. Klein AP, Brune KA, Petersen GM, Goggins M, Tersmette AC, Offerhaus GJA, et al. Prospective risk of pancreatic cancer in familial pancreatic cancer kindreds. Cancer Res. 2004;64(7):2634-8.

11. Giardiello FM, Offerhaus JGA, Lee DH, Krush A, Tersmette AC, Booker SV, et al. Increased Risk of Thyroid and Pancreatic-Carcinoma in Familial Adenomatous Polyposis. Gastroenterology. 1993;104(4):A404-A.

12. Watson P, Vasen HFA, Mecklin JP, Bernstein I, Aarnio M, Jarvinen HJ, et al. The risk of extra-colonic, extra-endometrial cancer in the Lynch syndrome. International Journal of Cancer. 2008;123(2):444-9.

13. Kastrinos F, Mukherjee B, Tayob N, Wang F, Sparr J, Raymond VM, et al. Risk of Pancreatic Cancer in Families With Lynch Syndrome. Jama-J Am Med Assoc. 2009;302(16):1790-5.

14. Moran A, O'Hara C, Khan S, Shack L, Woodward E, Maher ER, et al. Risk of cancer other than breast or ovarian in individuals with BRCA1 and BRCA2 mutations. Fam Cancer. 2012;11(2):235-42.

15. Risch HA, McLaughlin JR, Cole DEC, Rosen B, Bradley L, Fan I, et al. Population BRCA1 and BRCA2 mutation frequencies and cancer penetrances: A kin-cohort study in Ontario, Canada. Jnci-J Natl Cancer I. 2006;98(23):1694-706.

16. Duell E, Lucenteforte E, La Vecchia C, Bracci P, Holly E, Li DH, et al. Pancreatitis and pancreatic cancer risk: A pooled analysis in the international pancreatic pancer case-control consortium (PanC4). Cancer Res. 2009;69.

17. Duell EJ, Lucenteforte E, Olson SH, Bracci PM, Li D, Risch HA, et al. Pancreatitis and pancreatic cancer risk: a pooled analysis in the International Pancreatic Cancer Case-Control Consortium (PanC4). Ann Oncol. 2012;23(11):2964-70.

18. Ekbom A, Mclaughlin JK, Karlsson BM, Nyren O, Gridley G, Adami HO, et al. Pancreatitis and Pancreatic-Cancer - a Population-Based Study. J Natl Cancer I. 1994;86(8):625-7.

19. Raimondi S, Lowenfels AB, Morselli-Labate AM, Maisonneuve P, Pezzilli R. Pancreatic cancer in chronic pancreatitis; aetiology, incidence, and early detection. Best Pract Res Cl Ga. 2010;24(3):349-58.

20. Sharma A, Chari ST. Pancreatic Cancer and Diabetes Mellitus. Curr Treat Options Gastroenterol. 2018;16(4):466-78.

21. Cui YF, Andersen DK. Diabetes and pancreatic cancer. Endocr-Relat Cancer. 2012;19(5):F9-F26.

22. Saad AM, Turk T, Al-Husseini MJ, Abdel-Rahman O. Trends in pancreatic adenocarcinoma incidence and mortality in the United States in the last four decades; a SEER-based study. BMC Cancer. 2018;18(1):688.

23. Siegel RL, Miller KD, Jemal A. Cancer Statistics, 2017. CA Cancer J Clin. 2017;67(1):7-30.

24. World Health Organisation Mortality Database, Retrieved from: https://platform.who.int/mortality/themes/theme-details/topics/topic-details/MDB/malignant-neoplasms [Internet]. 2022.

25. Morgan RT, Woods LK, Moore GE, Quinn LA, McGavran L, Gordon SG. Human cell line (COLO 357) of metastatic pancreatic adenocarcinoma. Int J Cancer. 1980;25(5):591-8.

26. Yunis AA, Arimura GK, Russin DJ. Human pancreatic carcinoma (MIA PaCa-2) in continuous culture: sensitivity to asparaginase. Int J Cancer. 1977;19(1):128-35.

27. Lieber M, Mazzetta J, Nelson-Rees W, Kaplan M, Todaro G. Establishment of a continuous tumor-cell line (panc-1) from a human carcinoma of the exocrine pancreas. Int J Cancer. 1975;15(5):741-7.

28. Ghandi M, Huang FW, Jane-Valbuena J, Kryukov GV, Lo CC, McDonald ER, et al. Next-generation characterization of the Cancer Cell Line Encyclopedia. Nature. 2019;569(7757):503-508.

29. Deer EL, Gonzalez-Hernandez J, Coursen JD, Shea JE, Ngatia J, Scaife CL, et al. Phenotype and genotype of pancreatic cancer cell lines. Pancreas. 2010;39(4):425-35.

30. Aubert M, Crotte C, Bernard JP, Lombardo D, Sadoulet MO, Mas E. Decrease of human pancreatic cancer cell tumorigenicity by alpha1,3galactosyltransferase gene transfer. Int J Cancer. 2003;107(6):910-8.

31. Fukasawa M, Korc M. Vascular endothelial growth factor-trap suppresses tumorigenicity of multiple pancreatic cancer cell lines. Clin Cancer Res. 2004;10(10):3327-32.

32. Miknyoczki SJ, Chang H, Klein-Szanto A, Dionne CA, Ruggeri BA. The Trk tyrosine kinase inhibitor CEP-701 (KT-5555) exhibits significant antitumor efficacy in preclinical xenograft models of human pancreatic ductal adenocarcinoma. Clin Cancer Res. 1999;5(8):2205-12.

33. Kern SE, Pietenpol JA, Thiagalingam S, Seymour A, Kinzler KW, Vogelstein B. Oncogenic Forms of P53 Inhibit P53-Regulated Gene-Expression. Science. 1992;256(5058):827-30.

34. Lillemoe KD, Hwang, Thompson JC, Townsend CM, Vickers SM, Beauchamp RD, et al. Gene therapy for primary and metastatic pancreatic cancer with intraperitoneal retroviral vector bearing the wild-type p53 gene - Discussion. Surgery. 1998;124(2):150-1.

35. Donehower LA, Harvey M, Slagle BL, Mcarthur MJ, Montgomery CA, Butel JS, et al. Mice Deficient for P53 Are Developmentally Normal but Susceptible to Spontaneous Tumors. Nature. 1992;356(6366):215-21.

36. Jacks T, Remington L, Williams BO, Schmitt EM, Halachmi S, Bronson RT, et al. Tumor Spectrum Analysis in P53-Mutant Mice. Curr Biol. 1994;4(1):1-7.

37. Riley T, Sontag E, Chen P, Levine A. Transcriptional control of human p53-regulated genes. Nat Rev Mol Cell Bio. 2008;9(5):402-12.

38. Menendez D, Inga A, Resnick MA. The expanding universe of p53 targets. Nat Rev Cancer. 2009;9(10):724-37.

39. Rivlin N, Brosh R, Oren M, Rotter V. Mutations in the p53 Tumor Suppressor Gene: Important Milestones at the Various Steps of Tumorigenesis. Genes Cancer. 2011;2(4):466-74.

40. Bamford S, Dawson E, Forbes S, Clements J, Pettett R, Dogan A, et al. The COSMIC (Catalogue of Somatic Mutations in Cancer) database and website. Brit J Cancer. 2004;91(2):355-8.

41. Kim ST, Lim DH, Jang KT, Lim T, Lee J, Choi YL, et al. Impact of KRAS Mutations on Clinical Outcomes in Pancreatic Cancer Patients Treated with First-line Gemcitabine-Based Chemotherapy. Molecular Cancer Therapeutics. 2011;10(10):1993-9.

42. Gysin S, Salt M, Young A, McCormick F. Therapeutic strategies for targeting ras proteins. Genes Cancer. 2011;2(3):359-72.

43. Guerra C, Schuhmacher AJ, Canamero M, Grippo PJ, Verdaguer L, Perez-Gallego L, et al. Chronic pancreatitis is essential for induction of pancreatic ductal adenocarcinoma by K-Ras oncogenes in adult mice. Cancer Cell. 2007;11(3):291-302.

44. Sousa CM, Biancur DE, Wang X, Halbrook CJ, Sherman MH, Zhang L, et al. Pancreatic stellate cells support tumour metabolism through autophagic alanine secretion. Nature. 2016;536(7617):479-83.

45. Golay HG, Barbie DA. Targeting cytokine networks in KRAS-driven tumorigenesis. Expert Rev Anticanc. 2014;14(8):869-71.

46. Hamarsheh S, Gross O, Brummer T, Zeiser R. Immune modulatory effects of oncogenic KRAS in cancer. Nature Communications. 2020;11(1).

47. Mori T, Miura K, Aoki T, Nishihira T, Mori S, Nakamura Y. Frequent Somatic Mutation of the Mts1/Cdk4i (Multiple Tumor-Suppressor Cyclin-Dependent Kinase-4

Inhibitor) Gene in Esophageal Squamous-Cell Carcinoma. Cancer Res. 1994;54(13):3396-7.

48. Sharpless NE, Sherr CJ. Forging a signature of in vivo senescence (vol 15, pg 397, 2015). Nat Rev Cancer. 2015;15(8).

49. Weber JD, Jeffers JR, Rehg JE, Randle DH, Lozano G, Roussel MF, et al. p53-independent functions of the p19(ARF) tumor suppressor. Genes Dev. 2000;14(18):2358-65.

50. Sherr CJ. The INK4a/ARF network in tumour suppression. Nat Rev Mol Cell Bio. 2001;2(10):731-7.

51. Zhao R, Choi BY, Lee MH, Bode AM, Dong ZG. Implications of Genetic and Epigenetic Alterations of CDKN2A (p16(INK4a)) in Cancer. Ebiomedicine. 2016;8:30-9.

52. Serrano M, Hannon GJ, Beach D. A New Regulatory Motif in Cell-Cycle Control Causing Specific-Inhibition of Cyclin-D/Cdk4. Nature. 1993;366(6456):704-7.

53. Chen JY, Li DH, Killary AM, Sen S, Amos CI, Evans DB, et al. Polymorphisms of p16, p27, p73, and MDM2 Modulate Response and Survival of Pancreatic Cancer Patients Treated with Preoperative Chemoradiation. Ann Surg Oncol. 2009;16(2):431-9.

54. Schutte M, Hruban RH, Geradts J, Maynard R, Hilgers W, Rabindran SK, et al. Abrogation of the Rb/p16 tumor-suppressive pathway in virtually all pancreatic carcinomas. Cancer Res. 1997;57(15):3126-30.

55. Moore PS, Sipos B, Orlandini S, Sorio C, Real FX, Lemoine NR, et al. Genetic profile of 22 pancreatic carcinoma cell lines - Analysis of K-ras, p53, p16 and DPC4/Smad4. Virchows Arch. 2001;439(6):798-802.

56. Li YY, Chen HP, Hardy TM, Tollefsbol TO. Epigenetic Regulation of Multiple Tumor-Related Genes Leads to Suppression of Breast Tumorigenesis by Dietary Genistein. Plos One. 2013;8(1).

57. Majid S, Kikuno N, Nelles J, Noonan E, Tanaka Y, Kawamoto K, et al. Genistein induces the p21WAF1/CIP1 and p16INK4a tumor suppressor genes in prostate cancer cells by epigenetic mechanisms involving active chromatin modification. Cancer Res. 2008;68(8):2736-44.

58. Kensler TW, Egner PA, Agyeman AS, Visvanathan K, Groopman JD, Chen JG, et al. Keap1-Nrf2 Signaling: A Target for Cancer Prevention by Sulforaphane. Top Curr Chem. 2013;329:163-77.

59. Nandakumar V, Vaid M, Katiyar SK. (-)-Epigallocatechin-3-gallate reactivates silenced tumor suppressor genes, Cip1/p21 and p16INK4a, by reducing DNA methylation and increasing histones acetylation in human skin cancer cells. Carcinogenesis. 2011;32(4):537-44.

60. Blackford A, Serrano OK, Wolfgang CL, Parmigiani G, Jones S, Zhang XS, et al. SMAD4 Gene Mutations Are Associated with Poor Prognosis in Pancreatic Cancer. Clinical Cancer Research. 2009;15(14):4674-9.

61. De Bosscher K, Hill CS, Nicolas FJ. Molecular and functional consequences of Smad4 C-terminal missense mutations in colorectal tumour cells. Biochemical Journal. 2004;379:209-16.

62. Li Y, Basti A, Yalcin M, Relogio A. Circadian Dysregulation of the TGFbeta/SMAD4 Pathway Modulates Metastatic Properties and Cell Fate Decisions in Pancreatic Cancer Cells. iScience. 2020;23(10):101551.

63. Thuault S, Tan EJ, Peinado H, Cano A, Heldin CH, Moustakas A. HMGA2 and Smads co-regulate SNAIL1 expression during induction of epithelial-to-mesenchymal transition. J Biol Chem. 2008;283(48):33437-46.

64. Syed V. TGF-beta Signaling in Cancer. J Cell Biochem. 2016;117(6):1279-87.

65. Wang ZS, Li YX, Zhan SX, Zhang L, Zhang S, Tang Q, et al. SMAD4 Y353C promotes the progression of PDAC. Bmc Cancer. 2019;19(1).

66. David CJ, Huang YH, Chen M, Su J, Zou Y, Bardeesy N, et al. TGF-beta Tumor Suppression through a Lethal EMT. Cell. 2016;164(5):1015-30.

67. Iacobuzio-Donahue CA, Fu B, Yachida S, Luo M, Abe H, Henderson CM, et al. DPC4 gene status of the primary carcinoma correlates with patterns of failure in patients with pancreatic cancer. J Clin Oncol. 2009;27(11):1806-13.

68. Ezrova Z, Nahacka Z, Stursa J, Werner L, Vlcak E, Kralova Viziova P, et al. SMAD4 loss limits the vulnerability of pancreatic cancer cells to complex I inhibition via promotion of mitophagy. Oncogene. 2021;40(14):2539-52.

69. Wang F, Xia X, Yang C, Shen J, Mai J, Kim HC, et al. SMAD4 Gene Mutation Renders Pancreatic Cancer Resistance to Radiotherapy through Promotion of Autophagy. Clin Cancer Res. 2018;24(13):3176-85.

70. Yachida S, Jones S, Bozic I, Antal T, Leary R, Fu B, et al. Distant metastasis occurs late during the genetic evolution of pancreatic cancer. Nature. 2010;467(7319):1114-7.

71. Yu J, Blackford AL, Dal Molin M, Wolfgang CL, Goggins M. Time to progression of pancreatic ductal adenocarcinoma from low-to-high tumour stages. Gut. 2015;64(11):1783-9.

72. Nishida K, Kaneko T, Yoneda M, Nakagawa S, Ishikawa T, Yamane E, et al. Doubling time of serum CA 19-9 in the clinical course of patients with pancreatic cancer and its significant association with prognosis. J Surg Oncol. 1999;71(3):140-6.

73. Jones S, Zhang XS, Parsons DW, Lin JCH, Leary RJ, Angenendt P, et al. Core signaling pathways in human pancreatic cancers revealed by global genomic analyses. Science. 2008;321(5897):1801-6.

74. Waddell N, Pajic M, Patch AM, Chang DK, Kassahn KS, Bailey P, et al. Whole genomes redefine the mutational landscape of pancreatic cancer. Nature. 2015;518(7540):495-501.

75. Biankin AV, Waddell N, Kassahn KS, Gingras MC, Muthuswamy LB, Johns AL, et al. Pancreatic cancer genomes reveal aberrations in axon guidance pathway genes. Nature. 2012;491(7424):399-405.

76. Bailey P, Chang DK, Nones K, Johns AL, Patch AM, Gingras MC, et al. Genomic analyses identify molecular subtypes of pancreatic cancer. Nature. 2016;531(7592):47-+.

77. McDonald OG, Li X, Saunders T, Tryggvadottir R, Mentch SJ, Warmoes MO, et al. Epigenomic reprogramming during pancreatic cancer progression links anabolic glucose metabolism to distant metastasis. Nat Genet. 2017;49(3):367-76.

78. Lomberk G, Blum Y, Nicolle R, Nair A, Gaonkar KS, Marisa L, et al. Distinct epigenetic landscapes underlie the pathobiology of pancreatic cancer subtypes. Nature Communications. 2018;9.

79. Offeddu GS, Haase K, Wan Z, Possenti L, Nguyen HT, Gillrie MR, et al. Personalized models of breast cancer desmoplasia reveal biomechanical determinants of drug penetration. bioRxiv. 2021:2021.12.12.472296.

80. Das S, Shapiro B, Vucic EA, Vogt S, Bar-Sagi D. Tumor Cell-Derived IL1beta Promotes Desmoplasia and Immune Suppression in Pancreatic Cancer. Cancer Res. 2020;80(5):1088-101.

81. Collisson EA, Sadanandam A, Olson P, Gibb WJ, Truitt M, Gu SD, et al. Subtypes of pancreatic ductal adenocarcinoma and their differing responses to therapy. Nat Med. 2011;17(4):500-U140.

82. Janky R, Binda MM, Allemeersch J, Van den Broeck A, Govaere O, Swinnen JV, et al. Prognostic relevance of molecular subtypes and master regulators in pancreatic ductal adenocarcinoma. Bmc Cancer. 2016;16.

83. Kim S, Kang MJ, Lee S, Bae S, Han S, Jang JY, et al. Identifying molecular subtypes related to clinicopathologic factors in pancreatic cancer. Biomed Eng Online. 2014;13.

84. Moffitt RA, Marayati R, Flate EL, Volmar KE, Loeza SGH, Hoadley KA, et al. Virtual microdissection identifies distinct tumor- and stroma-specific subtypes of pancreatic ductal adenocarcinoma. Nat Genet. 2015;47(10):1168-1178.

85. Moffitt RA, Network CGAR. Integrated genomic characterization of pancreatic ductal adenocarcinoma and the confounding role of purity. Cancer Res. 2016;76.

86. Veenstra VL, Garcia-Garijo A, van Laarhoven HW, Bijlsma MF. Extracellular Influences: Molecular Subclasses and the Microenvironment in Pancreatic Cancer. Cancers. 2018;10(2).

87. Principe DR, Underwood PW, Korc M, Trevino JG, Munshi HG, Rana A. The Current Treatment Paradigm for Pancreatic Ductal Adenocarcinoma and Barriers to Therapeutic Efficacy. Front Oncol. 2021;11:688377.

88. Moore M. Activity of gemcitabine in patients with advanced pancreatic carcinoma - A review. Cancer. 1996;78(3):633-8.

89. Conroy T, Hammel P, Hebbar M, Ben Abdelghani M, Wei AC, Raoul JL, et al. FOLFIRINOX or Gemcitabine as Adjuvant Therapy for Pancreatic Cancer. N Engl J Med. 2018;379(25):2395-406.

90. Rinehart J, Adjei AA, Lorusso PM, Waterhouse D, Hecht JR, Natale RB, et al. Multicenter phase II study of the oral MEK inhibitor, CI-1040, in patients with advanced non-small-cell lung, breast, colon, and pancreatic cancer. J Clin Oncol. 2004;22(22):4456-62.

91. Singh A, Settleman J. Oncogenic K-ras "addiction" and synthetic lethality. Cell Cycle. 2009;8(17):2676-7.

92. Ying HQ, Kimmelman AC, Lyssiotis CA, Hua SJ, Chu GC, Fletcher-Sananikone E, et al. Oncogenic Kras Maintains Pancreatic Tumors through Regulation of Anabolic Glucose Metabolism. Cell. 2012;149(3):656-70.

93. Identifier: NCT04799431, Neoantigen-Targeted Vaccine Combined With Anti-PD-1 Antibody for Patients With Stage IV MMR-p Colon and Pancreatic Ductal Cancer. Bethesda (MD):National Library of Medicine. 2022 [cited 11.11.2022]. Available from: https://clinicaltrials.gov/ct2/show/NCT04799431.

94. Identifier: NCT03727880, Study of Pembrolizumab With or Without Defactinib Following Chemotherapy as a Neoadjuvant and Adjuvant Treatment for Resectable Pancreatic Ductal Adenocarcinoma. Bethesda (MD): National Library of Medicine. 2022 [cited 11.11.2022]. Available from: https://clinicaltrials.gov/ct2/show/NCT03727880.

95. Identifier: INCB106385, Alone or in Combination With Immunotherapy in Advanced Solid Tumors. Bethesda (MD): National Library of Medicine. 2022 [cited 11.11.2022]. Available from: https://clinicaltrials.gov/ct2/show/NCT04580485.

96. Overbeek KA, Levink IJM, Koopmann BDM, Harinck F, Konings I, Ausems M, et al. Long-term yield of pancreatic cancer surveillance in high-risk individuals. Gut. 2022;71(6):1152-60.

97. Pavlova NN, Thompson CB. The Emerging Hallmarks of Cancer Metabolism. Cell Metab. 2016;23(1):27-47.

98. Jose C, Bellance N, Rossignol R. Choosing between glycolysis and oxidative phosphorylation: a tumor's dilemma? Biochim Biophys Acta. 2011;1807(6):552-61.

99. De Luca A, Fiorillo M, Peiris-Pages M, Ozsvari B, Smith DL, Sanchez-Alvarez R, et al. Mitochondrial biogenesis is required for the anchorage-independent survival and propagation of stem-like cancer cells. Oncotarget. 2015;6(17):14777-95.

100. Ancey PB, Contat C, Meylan E. Glucose transporters in cancer - from tumor cells to the tumor microenvironment. Febs J. 2018;285(16):2926-43.

101. Lincet H, Icard P. How do glycolytic enzymes favour cancer cell proliferation by nonmetabolic functions? Oncogene. 2015;34(29):3751-9.

102. Warburg O, Wind F, Negelein E. The Metabolism of Tumors in the Body. J Gen Physiol. 1927;8(6):519-30.

103. Halestrap AP, Wilson MC. The monocarboxylate transporter family--role and regulation. IUBMB Life. 2012;64(2):109-19.

104. Hui S, Ghergurovich JM, Morscher RJ, Jang C, Teng X, Lu WY, et al. Glucose feeds the TCA cycle via circulating lactate. Nature. 2017;551(7678):115-+.

105. Faubert B, Li KY, Cai L, Hensley CT, Kim J, Zacharias LG, et al. Lactate Metabolism in Human Lung Tumors. Cell. 2017;171(2):358-371.

106. Koppenol WH, Bounds PL, Dang CV. Otto Warburg's contributions to current concepts of cancer metabolism. Nat Rev Cancer. 2011;11(5):325-37.

107. Cho ES, Cha YH, Kim HS, Kim NH, Yook JI. The Pentose Phosphate Pathway as a Potential Target for Cancer Therapy. Biomol Ther (Seoul). 2018;26(1):29-38.

108. Kruiswijk F, Labuschagne CF, Vousden KH. p53 in survival, death and metabolic health: a lifeguard with a licence to kill. Nat Rev Mol Cell Bio. 2015;16(7):393-405.

109. Barron CC, Bilan PJ, Tsakiridis T, Tsiani E. Facilitative glucose transporters: Implications for cancer detection, prognosis and treatment. Metabolism. 2016;65(2):124-39.

110. Liu YH, Hu CM, Hsu YS, Lee WH. Interplays of glucose metabolism and KRAS mutation in pancreatic ductal adenocarcinoma. Cell Death & Disease. 2022;13(9).

111. Nie K, Li J, He X, Wang Y, Zhao Q, Du M, et al. COX6B2 drives metabolic reprogramming toward oxidative phosphorylation to promote metastasis in pancreatic ductal cancer cells. Oncogenesis. 2020;9(5):51.

112. Russell S, Xu L, Kam Y, Abrahams D, Ordway B, Lopez AS, et al. Proton export upregulates aerobic glycolysis. BMC Biol. 2022;20(1):163.

113. Buchakjian MR, Kornbluth S. The engine driving the ship: metabolic steering of cell proliferation and death. Nat Rev Mol Cell Bio. 2010;11(10):715-27.

114. Ast T, Mootha VK. Oxygen and mammalian cell culture: are we repeating the experiment of Dr. Ox? Nat Metab. 2019;1(9):858-60.

115. Fan J, Kamphorst JJ, Mathew R, Chung MK, White E, Shlomi T, et al. Glutamine-driven oxidative phosphorylation is a major ATP source in transformed mammalian cells in both normoxia and hypoxia. Mol Syst Biol. 2013;9:712.

116. Wilson DF. Oxidative phosphorylation: unique regulatory mechanism and role in metabolic homeostasis. Journal of Applied Physiology. 2017;122(3):611-9.

117. Korzeniewski B. Regulation of oxidative phosphorylation during work transitions results from its kinetic properties. Journal of Applied Physiology. 2014;116(1):83-94.

118. Chiche J, Brahimi-Horn MC, Pouyssegur J. Tumour hypoxia induces a metabolic shift causing acidosis: a common feature in cancer. J Cell Mol Med. 2010;14(4):771-94.

119. Korzeniewski B, Rossiter HB. Each-step activation of oxidative phosphorylation is necessary to explain muscle metabolic kinetic responses to exercise and recovery in humans. J Physiol. 2015;593(24):5255-68.

120. Zhang D, Tang ZY, Huang H, Zhou GL, Cui C, Weng YJ, et al. Metabolic regulation of gene expression by histone lactylation. Nature. 2019;574(7779):575-580.

121. Dovmark TH, Saccomano M, Hulikova A, Alves F, Swietach P. Connexin-43 channels are a pathway for discharging lactate from glycolytic pancreatic ductal adenocarcinoma cells. Oncogene. 2017;36(32):4538-50.

122. Rabinowitz JD, Enerback S. Lactate: the ugly duckling of energy metabolism. Nat Metab. 2020;2(7):566-71.

123. Sonveaux P, Vegran F, Schroeder T, Wergin MC, Verrax J, Rabbani ZN, et al. Targeting lactate-fueled respiration selectively kills hypoxic tumor cells in mice. J Clin Invest. 2008;118(12):3930-42.

124. Tennant DA, Duran RV, Gottlieb E. Targeting metabolic transformation for cancer therapy. Nat Rev Cancer. 2010;10(4):267-77.

125. Hollinshead KER, Parker SJ, Eapen VV, Encarnacion-Rosado J, Sohn A, Oncu T, et al. Respiratory Supercomplexes Promote Mitochondrial Efficiency and Growth in Severely Hypoxic Pancreatic Cancer. Cell Rep. 2020;33(1):108231.

126. Xie JS, Wu H, Dai CY, Pan QR, Ding ZH, Hu DQ, et al. Beyond Warburg effect - dual metabolic nature of cancer cells. Sci Rep-Uk. 2014;4.

127. Frezza C, Zheng L, Tennant DA, Papkovsky DB, Hedley BA, Kalna G, et al. Metabolic Profiling of Hypoxic Cells Revealed a Catabolic Signature Required for Cell Survival. Plos One. 2011;6(9).

128. Perera RM, Bardeesy N. Pancreatic Cancer Metabolism: Breaking It Down to Build It Back Up. Cancer Discov. 2015;5(12):1247-61.

129. Islam MM, Goertzen A, Singh PK, Saha R. Exploring the metabolic landscape of pancreatic ductal adenocarcinoma cells using genome-scale metabolic modeling. iScience. 2022;25(6):104483.

130. Taga T, Hibi M, Hirata Y, Yamasaki K, Yasukawa K, Matsuda T, et al. Interleukin-6 Triggers the Association of Its Receptor with a Possible Signal Transducer, Gp130. Cell. 1989;58(3):573-81.

131. Radharani NNV, Yadav AS, Nimma R, Kumar TVS, Bulbule A, Chanukuppa V, et al. Tumor-associated macrophage derived IL-6 enriches cancer stem cell population and promotes breast tumor progression via Stat-3 pathway. Cancer Cell International. 2022;22(1).

132. Tanaka T, Narazaki M, Kishimoto T. IL-6 in Inflammation, Immunity, and Disease. Csh Perspect Biol. 2014;6(10).

133. Calabrese LH, Rose-John S. IL-6 biology: implications for clinical targeting in rheumatic disease. Nat Rev Rheumatol. 2014;10(12):720-7.

134. Waage A, Brandtzaeg P, Halstensen A, Kierulf P, Espevik T. The Complex Pattern of Cytokines in Serum from Patients with Meningococcal Septic Shock - Association between Interleukin-6, Interleukin-1, and Fatal Outcome. J Exp Med. 1989;169(1):333-8.

135. Kraakman MJ, Kammoun HL, Allen TL, Deswaerte V, Henstridge DC, Estevez E, et al. Blocking IL-6 trans-signaling prevents high-fat diet-induced adipose tissue macrophage recruitment but does not improve insulin resistance. Cell Metab. 2015;21(3):403-16.

136. van Hall G, Steensberg A, Sacchetti M, Fischer C, Keller C, Schjerling P, et al. Interleukin-6 stimulates lipolysis and fat oxidation in humans. J Clin Endocr Metab. 2003;88(7):3005-10.

137. Hodes GE, Pfau ML, Leboeuf M, Golden SA, Christoffel DJ, Bregman D, et al. Individual differences in the peripheral immune system promote resilience versus susceptibility to social stress. P Natl Acad Sci USA. 2014;111(45):16136-41.

138. Lakatos P, Foldes J, Horvath C, Kiss L, Tatrai A, Takacs I, et al. Serum interleukin-6 and bone metabolism in patients with thyroid function disorders. J Clin Endocr Metab. 1997;82(1):78-81.

139. Patsalos O, Dalton B, Himmerich H. Effects of IL-6 Signaling Pathway Inhibition on Weight and BMI: A Systematic Review and Meta-Analysis. Int J Mol Sci. 2020;21(17).

140. Ito H. IL-6 and Crohn's disease. Curr Drug Targets Inflamm Allergy. 2003;2(2):125-30.

141. Mavragani CP, Spyridakis EG, Koutsilieris M. Adult-Onset Still's Disease: From Pathophysiology to Targeted Therapies. Int J Inflam. 2012;2012:879020.

142. Serada S, Fujimoto M, Mihara M, Koike N, Ohsugi Y, Nomura S, et al. IL-6 blockade inhibits the induction of myelin antigen-specific Th17 cells and Th1 cells in experimental autoimmune encephalomyelitis. P Natl Acad Sci USA. 2008;105(26):9041-6.

143. Greenhill CJ, Rose-John S, Lissilaa R, Ferlin W, Ernst M, Hertzog PJ, et al. IL-6 trans-signaling modulates TLR4-dependent inflammatory responses via STAT3. J Immunol. 2011;186(2):1199-208.

144. Buchert M, Burns CJ, Ernst M. Targeting JAK kinase in solid tumors: emerging opportunities and challenges. Oncogene. 2016;35(8):939-51.

145. Baran P, Nitz R, Grotzinger J, Scheller J, Garbers C. Minimal Interleukin 6 (IL-6) Receptor Stalk Composition for IL-6 Receptor Shedding and IL-6 Classic Signaling. Journal of Biological Chemistry. 2013;288(21):14756-68.

146. Jones SA, Horiuchi S, Topley N, Yamamoto N, Fuller GM. The soluble interleukin 6 receptor: mechanisms of production and implications in disease. Faseb Journal. 2001;15(1):43-58.

147. Rosean TR, Tompkins VS, Tricot G, Holman CJ, Olivier AK, Zhan FH, et al. Preclinical validation of interleukin 6 as a therapeutic target in multiple myeloma. Immunol Res. 2014;59(1-3):188-202.

148. Kuhn KA, Manieri NA, Liu TC, Stappenbeck TS. IL-6 Stimulates Intestinal Epithelial Proliferation and Repair after Injury. Plos One. 2014;9(12).

149. Schaper F, Rose-John S. Interleukin-6: Biology, signaling and strategies of blockade. Cytokine Growth F R. 2015;26(5):475-87.

150. McLoughlin RM, Jenkins BJ, Grail D, Williams AS, Fielding CA, Parker CR, et al. IL-6 trans-signaling via STAT3 directs T cell infiltration in acute inflammation. P Natl Acad Sci USA. 2005;102(27):9589-94.

151. Johnson DE, O'Keefe RA, Grandis JR. Targeting the IL-6/JAK/STAT3 signalling axis in cancer. Nat Rev Clin Oncol. 2018;15(4):234-48.

152. Miura T, Mitsunaga S, Ikeda M, Shimizu S, Ohno I, Takahashi H, et al. Characterization of Patients With Advanced Pancreatic Cancer and High Serum Interleukin-6 Levels. Pancreas. 2015;44(5):756-63.

153. Culig Z, Puhr M. Interleukin-6: A multifunctional targetable cytokine in human prostate cancer. Mol Cell Endocrinol. 2012;360(1-2):52-8.

154. Dethlefsen C, Hojfeldt G, Hojman P. The role of intratumoral and systemic IL-6 in breast cancer. Breast Cancer Res Tr. 2013;138(3):657-64.

155. Sanguinete MMM, De Oliveira PH, Martins A, Micheli DC, Tavares-Murta BM, Murta EFC, et al. Serum IL-6 and IL-8 Correlate with Prognostic Factors in Ovarian Cancer. Immunol Invest. 2017;46(7):677-88.

156. Riedel F, Zaiss I, Herzog D, Gotte K, Naim R, Hormann K. Serum levels of interleukin-6 in patients with primary head and neck squamous cell carcinoma. Anticancer Research. 2005;25(4):2761-5.

157. Wu CT, Chen MF, Chen WC, Hsieh CC. The role of IL-6 in the radiation response of prostate cancer. Radiat Oncol. 2013;8.

158. Knupfer H, Preiss R. Serum interleukin-6 levels in colorectal cancer patients-a summary of published results. Int J Colorectal Dis. 2010;25(2):135-40.

159. Duffy SA, Taylor JMG, Terrell JE, Islam M, Li Y, Fowler KE, et al. Interleukin-6 predicts recurrence and survival among head and neck cancer patients. Cancer. 2008;113(4):750-7.

160. Chang CH, Hsiao CF, Yeh YM, Chang GC, Tsai YH, Chen YM, et al. Circulating interleukin-6 level is a prognostic marker for survival in advanced nonsmall cell lung cancer patients treated with chemotherapy. International Journal of Cancer. 2013;132(9):1977-85.

161. Kotowicz B, Fuksiewicz M, Jonska-Gmyrek J, Bidzinski M, Kowalska M. The assessment of the prognostic value of tumor markers and cytokines as SCCAg, CYFRA 21.1, IL-6, VEGF and sTNF receptors in patients with squamous cell cervical cancer, particularly with early stage of the disease. Tumor Biol. 2016;37(1):1271-8.

162. Chen MF, Chen PT, Lu MS, Lin PY, Chen WC, Lee KD. IL-6 expression predicts treatment response and outcome in squamous cell carcinoma of the esophagus. Mol Cancer. 2013;12.

163. Rupert JE, Narasimhan A, Jengelley DHA, Jiang Y, Liu J, Au E, et al. Tumor-derived IL-6 and trans-signaling among tumor, fat, and muscle mediate pancreatic cancer cachexia. J Exp Med. 2021;218(6).

164. White JP. IL-6, cancer and cachexia: metabolic dysfunction creates the perfect storm. Transl Cancer Res. 2017;6(Suppl 2):S280-S5.

165. Formica V, Cereda V, Nardecchia A, Tesauro M, Roselli M. Immune reaction and colorectal cancer: Friends or foes? World J Gastroentero. 2014;20(35):12407-19.

166. Zhou L, Lopes JE, Chong MM, Ivanov, II, Min R, Victora GD, et al. TGF-beta-induced Foxp3 inhibits T(H)17 cell differentiation by antagonizing RORgammat function. Nature. 2008;453(7192):236-40.

167. Chen W, Jin W, Hardegen N, Lei KJ, Li L, Marinos N, et al. Conversion of peripheral CD4+CD25- naive T cells to CD4+CD25+ regulatory T cells by TGF-beta induction of transcription factor Foxp3. J Exp Med. 2003;198(12):1875-86.

168. Hodge DR, Peng B, Cherry JC, Hurt EM, Fox SD, Kelley JA, et al. Interleukin 6 supports the maintenance of p53 tumor suppressor gene promoter methylation. Cancer Res. 2005;65(11):4673-82.

169. Wei LH, Kuo ML, Chen CA, Chou CH, Lai KB, Lee CN, et al. Interleukin-6 promotes cervical tumor growth by VEGF-dependent angiogenesis via a STAT3 pathway. Oncogene. 2003;22(10):1517-27.

170. Ohno Y, Kitamura H, Takahashi N, Ohtake J, Kaneumi S, Sumida K, et al. IL-6 down-regulates HLA class II expression and IL-12 production of human dendritic cells to impair activation of antigen-specific CD4(+) T cells. Cancer Immunol Immunother. 2016;65(2):193-204.

171. Kitamura H, Kamon H, Sawa S, Park SJ, Katunuma N, Ishihara K, et al. IL-6-STAT3 controls intracellular MHC class II alphabeta dimer level through cathepsin S activity in dendritic cells. Immunity. 2005;23(5):491-502.

172. Condamine T, Gabrilovich DI. Molecular mechanisms regulating myeloid-derived suppressor cell differentiation and function. Trends Immunol. 2011;32(1):19-25.

173. Lo CW, Chen MW, Hsiao M, Wang SA, Chen CA, Hsiao SM, et al. IL-6 Trans-Signaling in Formation and Progression of Malignant Ascites in Ovarian Cancer. Cancer Res. 2011;71(2):424-34.

174. Liu CC, Lin JH, Hsu TW, Su K, Li AF, Hsu HS, et al. IL-6 enriched lung cancer stem-like cell population by inhibition of cell cycle regulators via DNMT1 upregulation. Int J Cancer. 2015;136(3):547-59.

175. Sun Q, Shang Y, Sun F, Dong X, Niu J, Li F. Interleukin-6 Promotes Epithelial-Mesenchymal Transition and Cell Invasion through Integrin beta6 Upregulation in Colorectal Cancer. Oxid Med Cell Longev. 2020;2020:8032187.

176. Xiao J, Gong YN, Chen Y, Yu DH, Wang XY, Zhang XX, et al. IL-6 promotes epithelial-to-mesenchymal transition of human peritoneal mesothelial cells possibly through the JAK2/STAT3 signaling pathway. Am J Physiol-Renal. 2017;313(2):F310-F8.

177. Jing B, Wang T, Sun B, Xu J, Xu D, Liao Y, et al. IL6/STAT3 Signaling Orchestrates Premetastatic Niche Formation and Immunosuppressive Traits in Lung. Cancer Res. 2020;80(4):784-97.

178. Mikucki ME, Fisher DT, Ku AW, Appenheimer MM, Muhitch JB, Evans SS. Preconditioning thermal therapy: Flipping the switch on IL-6 for anti-tumour immunity. Int J Hyperther. 2013;29(5):464-73.

179. Fisher DT, Chen Q, Skitzki JJ, Muhitch JB, Zhou L, Appenheimer MM, et al. IL-6 trans-signaling licenses mouse and human tumor microvascular gateways for trafficking of cytotoxic T cells. Journal of Clinical Investigation. 2011;121(10):3846-59.

180. Sharma MD, Hou DY, Baban B, Koni PA, He YK, Chandler PR, et al. Reprogrammed Foxp3(+) Regulatory T Cells Provide Essential Help to Support Cross-presentation and CD8(+) T Cell Priming in Naive Mice. Immunity. 2010;33(6):942-54.

181. Chen Q, Fisher DT, Clancy KA, Gauguet JM, Wang WC, Unger E, et al. Fever-range thermal stress promotes lymphocyte trafficking across high endothelial venules via an interleukin 6 trans-signaling mechanism. Nat Immunol. 2006;7(12):1299-308.

182. Evans SS, Wang WC, Bain MD, Burd R, Ostberg JR, Repasky EA. Fever-range hyperthermia dynamically regulates lymphocyte delivery to high endothelial venules. Blood. 2001;97(9):2727-33.

183. Mitchem JB, Brennan DJ, Knolhoff BL, Belt BA, Zhu Y, Sanford DE, et al. Targeting Tumor-Infiltrating Macrophages Decreases Tumor-Initiating Cells, Relieves Immunosuppression, and Improves Chemotherapeutic Responses. Cancer Res. 2013;73(3):1128-41.

184. Oh K, Lee OY, Shon SY, Nam O, Ryu PM, Seo MW, et al. A mutual activation loop between breast cancer cells and myeloid-derived suppressor cells facilitates spontaneous metastasis through IL-6 trans-signaling in a murine model. Breast Cancer Res. 2013;15(5).

185. Angelo LS, Talpaz M, Kurzrock R. Autocrine interleukin-6 production in renal cell carcinoma: Evidence for the involvement of p53. Cancer Res. 2002;62(3):932-40.

186. Zhang L, Badgwell DB, Bevers JJ, 3rd, Schlessinger K, Murray PJ, Levy DE, et al. IL-6 signaling via the STAT3/SOCS3 pathway: functional analysis of the conserved STAT3 N-domain. Mol Cell Biochem. 2006;288(1-2):179-89.

187. Lang R, Pauleau AL, Parganas E, Takahashi Y, Mages J, Ihle JN, et al. SOCS3 regulates the plasticity of gp130 signaling. Nature Immunology. 2003;4(6):546-50.

188. Wang Y, van Boxel-Dezaire AH, Cheon H, Yang J, Stark GR. STAT3 activation in response to IL-6 is prolonged by the binding of IL-6 receptor to EGF receptor. Proc Natl Acad Sci U S A. 2013;110(42):16975-80.

189. Fong YM, Moldawer LL, Marano M, Wei H, Tatter SB, Clarick RH, et al. Endotoxemia Elicits Increased Circulating Beta-2-Ifn/Il-6 in Man. Journal of Immunology. 1989;142(7):2321-4.

190. Kohase M, Henriksen-DeStefano D, May LT, Vilcek J, Sehgal PB. Induction of beta 2-interferon by tumor necrosis factor: a homeostatic mechanism in the control of cell proliferation. Cell. 1986;45(5):659-66.

191. Kohase M, May LT, Tamm I, Vilcek J, Sehgal PB. A Cytokine Network in Human-Diploid Fibroblasts - Interactions of Beta-Interferons, Tumor-Necrosis-Factor, Platelet-Derived Growth-Factor, and Interleukin-1. Molecular and Cellular Biology. 1987;7(1):273-80.

192. Linnskog R, Mohapatra P, Moradi F, Prasad CP, Andersson T. Demonstration of a WNT5A-IL-6 positive feedback loop in melanoma cells: Dual interference of this loop more effectively impairs melanoma cell invasion. Oncotarget. 2016;7(25):37790-802.

193. Peng CY, Liao YW, Lu MY, Yang CM, Hsieh PL, Yu CC. Positive Feedback Loop of SNAIL-IL-6 Mediates Myofibroblastic Differentiation Activity in Precancerous Oral Submucous Fibrosis. Cancers (Basel). 2020;12(6).

194. Ogura H, Murakami M, Okuyama Y, Tsuruoka M, Kitabayashi C, Kanamoto M, et al. Interleukin-17 promotes autoimmunity by triggering a positive-feedback loop via interleukin-6 induction. Immunity. 2008;29(4):628-36.

195. Lee J, Nakagiri T, Oto T, Harada M, Morii E, Shintani Y, et al. IL-6 amplifier, NF-kappaB-triggered positive feedback for IL-6 signaling, in grafts is involved in allogeneic rejection responses. J Immunol. 2012;189(4):1928-36.

196. Chang Q, Bournazou E, Sansone P, Berishaj M, Gao SP, Daly L, et al. The IL-6/JAK/Stat3 feed-forward loop drives tumorigenesis and metastasis. Neoplasia. 2013;15(7):848-62.

197. Garg M, Potter JA, Abrahams VM. Identification of microRNAs That Regulate TLR2-Mediated Trophoblast Apoptosis and Inhibition of IL-6 mRNA. Plos One. 2013;8(10).

198. Rossato M, Curtale G, Tamassia N, Castellucci M, Mori L, Gasperini S, et al. IL-10-induced microRNA-187 negatively regulates TNF-alpha, IL-6, and IL-12p40 production in TLR4-stimulated monocytes. Proc Natl Acad Sci U S A. 2012;109(45):E3101-10.

199. Xu Z, Xiao SB, Xu P, Xie Q, Cao L, Wang D, et al. miR-365, a novel negative regulator of interleukin-6 gene expression, is cooperatively regulated by Sp1 and NF-kappaB. J Biol Chem. 2011;286(24):21401-12.

200. Zhang L, Li JY, Wang Q, Meng GP, Lv XJ, Zhou H, et al. The relationship between microRNAs and the STAT3-related signaling pathway in cancer. Tumor Biol. 2017;39(7).

201. Pedersen BK. Muscular Interleukin-6 and Its Role as an Energy Sensor. Med Sci Sport Exer. 2012;44(3):392-6.

202. Wolsk E, Mygind H, Grondahl TS, Pedersen BK, van Hall G. IL-6 selectively stimulates fat metabolism in human skeletal muscle. Am J Physiol-Endoc M. 2010;299(5):E832-E40.

203. Inoue H, Ogawa W, Asakawa A, Okamoto Y, Nishizawa A, Matsumoto M, et al. Role of hepatic STAT3 in brain-insulin action on hepatic glucose production. Cell Metabolism. 2006;3(4):267-75.

204. Trinh B, Peletier M, Simonsen C, Plomgaard P, Karstoft K, Pedersen BK, et al. Blocking endogenous IL-6 impairs mobilization of free fatty acids during rest and exercise in lean and obese men. Cell Rep Med. 2021;2(9).

205. Carey AL, Steinberg GR, Macaulay SL, Thomas WG, Holmes AG, Ramm G, et al. Interleukin-6 increases insulin-stimulated glucose disposal in humans and glucose uptake and fatty acid oxidation in vitro via AMP-activated protein kinase. Diabetes. 2006;55(10):2688-97.

206. Tammineni P, Anugula C, Mohammed F, Anjaneyulu M, Larner AC, Sepuri NB. The import of the transcription factor STAT3 into mitochondria depends on GRIM-19, a component of the electron transport chain. J Biol Chem. 2013;288(7):4723-32.

207. Gough DJ, Corlett A, Schlessinger K, Wegrzyn J, Larner AC, Levy DE. Mitochondrial STAT3 Supports Ras-Dependent Oncogenic Transformation. Science. 2009;324(5935):1713-6.

208. Cheng X, Peuckert C, Wolfl S. Essential role of mitochondrial Stat3 in p38(MAPK) mediated apoptosis under oxidative stress. Sci Rep. 2017;7(1):15388.

209. Patel SB, Nemkov T, Stefanoni D, Benavides GA, Bassal MA, Crown BL, et al. Metabolic alterations mediated by STAT3 promotes drug persistence in CML. Leukemia. 2021;35(12):3371-82.

210. Demaria M, Giorgi C, Miano V, Misale S, Suski JM, Esposito G, et al. A stat3-mediated metabolic switch is involved in tumour transformation and stat3 addiction. Febs J. 2011;278:229-.

211. Tosic I, Frank DA. STAT3 as a mediator of oncogenic cellular metabolism: Pathogenic and therapeutic implications. Neoplasia. 2021;23(12):1167-78.

212. Ando M, Uehara I, Kogure K, Asano Y, Nakajima W, Abe Y, et al. Interleukin 6 enhances glycolysis through expression of the glycolytic enzymes hexokinase 2 and 6-

phosphofructo-2-kinase/fructose-2,6-bisphosphatase-3. J Nippon Med Sch. 2010;77(2):97-105.

213. Han J, Meng Q, Xi Q, Zhang Y, Zhuang Q, Han Y, et al. Interleukin-6 stimulates aerobic glycolysis by regulating PFKFB3 at early stage of colorectal cancer. Int J Oncol. 2016;48(1):215-24.

214. Kumari N, Das A, Bhatt AN. Interleukin-6 confers radio-resistance by inducing Akt-mediated glycolysis and reducing mitochondrial damage in cells. J Biochem. 2020;167(3):303-14.

215. Wang T, Fahrmann JF, Lee H, Li YJ, Tripathi SC, Yue C, et al. JAK/STAT3-Regulated Fatty Acid beta-Oxidation Is Critical for Breast Cancer Stem Cell Self-Renewal and Chemoresistance. Cell Metab. 2018;27(1):136-50 e5.

216. Gao P, Wang LL, Liu J, Dong FY, Song W, Liao L, et al. Dihydroartemisinin inhibits endothelial cell tube formation by suppression of the STAT3 signaling pathway. Life Sci. 2020;242.

217. Fahmi A, Smart N, Punn A, Jabr R, Marber M, Heads R. p42/p44-MAPK and PI3K are sufficient for IL-6 family cytokines/gp130 to signal to hypertrophy and survival in cardiomyocytes in the absence of JAK/STAT activation. Cell Signal. 2013;25(4):898-909.

218. Wegiel B, Bjartell A, Culig Z, Persson JL. Interleukin-6 activates PI3K/Akt pathway and regulates cyclin A1 to promote prostate cancer cell survival. Int J Cancer. 2008;122(7):1521-9.

219. Betts JC, Cheshire JK, Akira S, Kishimoto T, Woo P. The role of NF-kappa B and NF-IL6 transactivating factors in the synergistic activation of human serum amyloid A gene expression by interleukin-1 and interleukin-6. J Biol Chem. 1993;268(34):25624-31.

220. Lang Lehrskov L, Lyngbaek MP, Soederlund L, Legaard GE, Ehses JA, Heywood SE, et al. Interleukin-6 Delays Gastric Emptying in Humans with Direct Effects on Glycemic Control. Cell Metab. 2018;27(6):1201-11 e3.

221. Harder-Lauridsen NM, Krogh-Madsen R, Holst JJ, Plomgaard P, Leick L, Pedersen BK, et al. Effect of IL-6 on the insulin sensitivity in patients with type 2 diabetes 2. Am J Physiol-Endoc M. 2014;306(7):E769-E78.

222. Tsigos C, Papanicolaou DA, Kyrou I, Defensor R, Mitsiadis CS, Chrousos GP. Dose-dependent effects of recombinant human interleukin-6 on glucose regulation. J Clin Endocr Metab. 1997;82(12):4167-70.

223. Tsigos C, Papanicolaou DA, Defensor R, Mitsiadis CS, Kyrou I, Chrousos GP. Dose effects of recombinant human interleukin-6 on pituitary hormone secretion and energy expenditure. Neuroendocrinology. 1997;66(1):54-62.

224. Flint TR, Janowitz T, Connell CM, Roberts EW, Denton AE, Coll AP, et al. Tumor-Induced IL-6 Reprograms Host Metabolism to Suppress Anti-tumor Immunity. Cell Metab. 2016;24(5):672-84.

225. Choy EH, De Benedetti F, Takeuchi T, Hashizume M, John MR, Kishimoto T. Translating IL-6 biology into effective treatments. Nat Rev Rheumatol. 2020;16(6):335-45.

226. Coronavirus (COVID-19) Update: FDA Authorizes Drug for Treatment of COVID-19. Retrieved from: https://www.fda.gov/news-events/press-announcements/coronavirus-covid-19-update-fda-authorizes-drug-treatment-covid-19. [press release]. 2022.

227. Identifier: NCT03821246, Neoadjuvant Atezolizumab-Based Combination Therapy in Men With Localized Prostate Cancer Prior to Radical Prostatectomy. Bethesda (MD): National Library of Medicine. 2022. [cited: 15.11.2022]. Available from: https://clinicaltrials.gov/ct2/show/NCT03821246

228. Identifier: NCT05552001, A Study Evaluating the Efficacy and Safety of Multiple Immunotherapy-Based Treatment Combinations in Patients With Metastatic or Inoperable Locally Advanced Triple-Negative Breast Cancer. Bethesda (MD): National Library of Medicine. 2022. [cited: 15.11.2022]. Available from: https://www.clinicaltrials.gov/ct2/show/NCT05552001.

229. Identifier: NCT05033522, A Study Evaluating the Efficacy and Safety of Multiple Immunotherapy-Based Treatment Combinations in Patients With Advanced Liver Cancers (Morpheus-Liver). Bethesda (MD): National Library of Medicine. 2022. [cited: 15.11.2022]. Available from: https://clinicaltrials.gov/ct2/show/NCT05033522.

230. Identifier: NCT04408638, A Phase III Study Evaluating Glofitamab in Combination With Gemcitabine + Oxaliplatin vs Rituximab in Combination With Gemcitabine + Oxaliplatin in Participants With Relapsed/Refractory Diffuse Large B-Cell Lymphoma. Bethesda (MD): National Library of Medicine. 2022. [cited: 15.11.2022]. Available from: https://www.clinicaltrials.gov/ct2/show/NCT04408638.

231. Identifier: NCT03337698, A Study Of Multiple Immunotherapy-Based Treatment Combinations In Participants With Metastatic Non-Small Cell Lung Cancer (Morpheus-Non-Small Cell Lung Cancer). Bethesda (MD): National Library of Medicine. 2022. [cited: 15.11.2022]. Available from: https://clinicaltrials.gov/ct2/show/NCT03337698.

232. Identifier: NCT02767557, Study of Nab-Paclitaxel and Gemcitabine With or Without Tocilizumab in Pancreatic Cancer Patients. Bethesda (MD): National Library of Medicine. 2022. [cited: 15.11.2022]. Available from: https://www.clinicaltrials.gov /ct2/show/NCT02767557.

233. Identifier: NCT04940299, Tocilizumab, Ipilimumab, and Nivolumab for the Treatment of Advanced Melanoma, Non-Small Cell Lung Cancer, or Urothelial Carcinoma. Bethesda (MD): National Library of Medicine. 2022. [cited: 15.11.2022]. Available from: https://clinicaltrials.gov/ct2/show/NCT04940299.

234. Identifier: NCT04691817, Tocilizumab and Atezolizumab in Adults With Locally Advanced or Metastatic Non-Small Cell Lung Cancer Refractory to 1st Line Immune Checkpoint Inhibitor-Based Therapy. Bethesda (MD): National Library of Medicine. 2022. [cited: 15.11.2022]. Available from: https://clinicaltrials.gov/ct2/show/NCT04691817.

235. San-Miguel J, Blade J, Shpilberg O, Grosicki S, Maloisel F, Min CK, et al. Phase 2 randomized study of bortezomib-melphalan-prednisone with or without siltuximab (anti-IL-6) in multiple myeloma. Blood. 2014;123(26):4136-42.

236. Identifier: NCT02277093, Pacritinib to Inhibit JAK/STAT Signaling in Refractory Colorectal Cancer. Bethesda (MD): National Library of Medicine. 2022. [cited: 15.11.2022]. Available from: https://clinicaltrials.gov/ct2/show/NCT02277093.

237. Identifier: NCT02342353, Pacritinib in Patients With Endothelial Growth Factor (EGFR) Mutant Non-small Cell Lung Cancer (NSCLC) After EGFR Tyrosine Kinase Inhibitor (TKI). Bethesda (MD): National Library of Medicine. 2022. [cited: 15.11.2022]. Available from: https://clinicaltrials.gov/ct2/show/NCT02342353.

238. Identifier: NCT01620216, Targeted Therapy in Treating Patients With Relapsed or Refractory Acute Lymphoblastic Leukemia or Acute Myelogenous Leukemia. Bethesda (MD): National Library of Medicine. 2022. [cited: 15.11.2022]. Available from: https://clinicaltrials.gov/ct2/show/NCT01620216.

239. Identifier: NCT02323607, Pacritinib and Chemotherapy in Treating Patients With Acute Myeloid Leukemia and FLT3 Mutations. Bethesda (MD): National Library of Medicine. 2022. [cited: 15.11.2022]. Available from: https://clinicaltrials.gov/ct2/show/NCT02323607.

240. Identifier: NCT03425006, Pembrolizumab and Itacitinib (INCB039110) for Non-Small Cell Lung Cancer. Bethesda (MD): National Library of Medicine. 2022. [cited: 15.11.2022]. Available from: https://clinicaltrials.gov/ct2/show/NCT03425006.

241. Identifier: NCT02456675, INCB040093 and INCB040093 Combined With Itacitinib (INCB039110) in Relapsed/Refractory Hodgkin Lymphoma. Bethesda (MD):

National Library of Medicine. 2022. [cited: 15.11.2022]. Available from: https://clinicaltrials.gov/ct2/show/NCT02456675.

242. Identifier: NCT02265510, An Open-Label Study of a Novel JAK-inhibitor, INCB052793, Given to Patients With Advanced Malignancies. Bethesda (MD): National Library of Medicine. 2022. [cited: 15.11.2022]. Available from: https://clinicaltrials.gov/ct2/show/NCT02265510.

243. Identifier: NCT02119663, A Study of Ruxolitinib in Pancreatic Cancer Patients. Bethesda (MD): National Library of Medicine. 2022. [cited: 15.11.2022]. Available from: https://www.clinicaltrials.gov/ct2/show/NCT02119663.

244. Identifier: NCT00638378, Study of Ruxolitinib (INCB018424) Administered Orally to Patients With Androgen Independent Metastatic Prostate Cancer. Bethesda (MD): National Library of Medicine. 2022. [cited: 15.11.2022]. Available from: https://clinicaltrials.gov/ct2/show/NCT00638378.

245. Identifier: NCT02066532, Ruxolitinib in Combination With Trastuzumab in Metastatic HER2 Positive Breast Cancer. Bethesda (MD): National Library of Medicine. 2022. [cited: 15.11.2022]. Available from: https://clinicaltrials.gov/ct2/show/NCT02066532.

246. Identifier: NCT02583477, Phase Ib/II Study of MEDI4736 Evaluated in Different Combinations in Metastatic Pancreatic Ductal Carcinoma. Bethesda (MD): National Library of Medicine. 2022. [cited: 15.11.2022]. Available from: https://clinicaltrials.gov/ct2/show/NCT02583477.

247. Identifier: NCT03382340, IMX-110 in Patients With Advanced Solid Tumors. Bethesda (MD): National Library of Medicine. 2022. [cited: 15.11.2022]. Available from: https://clinicaltrials.gov/ct2/show/NCT03382340.

248. Identifier: NCT01711034, A Phase 1, Open-label, Multiple Dose Escalation Trial to Determine Safety and Tolerability of Once Daily OPB-111077 in Subjects With Advanced Cancer. Bethesda (MD): National Library of Medicine. 2022. [cited: 15.11.2022]. Available from: https://clinicaltrials.gov/ct2/show/NCT01711034.

249. Identifier: NCT02250170, Safety and Biomarker of OPB-111077 in Subjects With Advanced Solid Tumor. Bethesda (MD): National Library of Medicine. 2022. [cited: 15.11.2022]. Available from: https://clinicaltrials.gov/ct2/show/NCT02250170.

250. Identifier: NCT03197714, Clinical Trial of OPB-111077 in Patients With Relapsed or Refractory Acute Myeloid Leukaemia. Bethesda (MD): National Library of Medicine. 2022. [cited: 15.11.2022]. Available from: https://clinicaltrials.gov/ct2/show/NCT03197714.

251. Identifier: NCT01219543, A Phase I Study of AZD1480 in Patients With Advanced Solid Malignancies and Advanced Hepatocellular Carcinoma in the Escalation Phase, Non-Small Cell Lung Cancer(NSCLC) and Non-smokers With Lung Metastasis and Gastric Cancer and Solid Tumour in the Expansion Phase. Bethesda (MD): National Library of Medicine. 2022. [cited: 15.11.2022] Available from: https://clinicaltrials.gov/ct2/show/NCT01219543.

252. ClinicalTrials.gov [Internet]. Bethesda (MD): National Library of Medicine (US). [Internet]. 2022. Available from: https://clinicaltrials.gov/ct2/results?cond=cancer&term=&intr=Ruxolitinib&cntry=&state=&city=&dist=&Search=Search&recrs=a&recrs=b&recrs=d.

253. Genovese MC, Rubbert-Roth A, Smolen JS, Kremer J, Khraishi M, Gomez-Reino J, et al. Longterm Safety and Efficacy of Tocilizumab in Patients with Rheumatoid Arthritis: A Cumulative Analysis of Up to 4.6 Years of Exposure. J Rheumatol. 2013;40(6):768-80.

254. Morel J, Constantin A, Baron G, Dernis E, Flipo RM, Rist S, et al. Risk factors of serious infections in patients with rheumatoid arthritis treated with tocilizumab in the French Registry REGATE. Rheumatology. 2017;56(10):1746-54.

255. Monemi S, Berber E, Sarsour K, Wang JM, Lampl K, Bharucha K, et al. Incidence of Gastrointestinal Perforations in Patients with Rheumatoid Arthritis Treated with Tocilizumab from Clinical Trial, Postmarketing, and Real-World Data Sources. Rheumatol Ther. 2016;3(2):337-52.

256. Berend K, de Vries APJ, Gans ROB. Physiological Approach to Assessment of Acid-Base Disturbances. New Engl J Med. 2014;371(15):1434-45.

257. Imai K. [Acid-base equilibrium control system--red cell function]. Nihon Rinsho. 1992;50(9):2082-7.

258. Roos A, Boron WF. Intracellular pH. Physiol Rev. 1981;61(2):296-434.

259. Casey JR, Grinstein S, Orlowski J. Sensors and regulators of intracellular pH. Nat Rev Mol Cell Bio. 2010;11(1):50-61.

260. Aronson PS. Kinetic-Properties of the Plasma-Membrane Na+-H+ Exchanger. Annual Review of Physiology. 1985;47:545-60.

261. Cordat E, Casey JR. Bicarbonate transport in cell physiology and disease. Biochemical Journal. 2009;417:423-39.

262. Alper SL. Molecular physiology and genetics of Na+-independent SLC4 anion exchangers. Journal of Experimental Biology. 2009;212(11):1672-83.

263. Humphreys BD, Jiang LW, Chernova MN, Alper SL. Functional-Characterization and Regulation by Ph of Murine Ae2 Anion-Exchanger Expressed in Xenopus Oocytes. Am J Physiol-Cell Ph. 1994;267(5):C1295-C307.

264. Edlund GL, Halestrap AP. The kinetics of transport of lactate and pyruvate into rat hepatocytes. Evidence for the presence of a specific carrier similar to that in erythrocytes. Biochem J. 1988;249(1):117-26.

265. Halestrap AP, Price NT. The proton-linked monocarboxylate transporter (MCT) family: structure, function and regulation. Biochemical Journal. 1999;343:281-99.

266. Schwartz CE, Stevenson RE. The MCT8 thyroid hormone transporter and Allan-Herndon-Dudley syndrome. Best Pract Res Clin Endocrinol Metab. 2007;21(2):307-21.

267. Abplanalp J, Laczko E, Philp NJ, Neidhardt J, Zuercher J, Braun P, et al. The cataract and glucosuria associated monocarboxylate transporter MCT12 is a new creatine transporter. Hum Mol Genet. 2013;22(16):3218-26.

268. Felmlee MA, Jones RS, Rodriguez-Cruz V, Follman KE, Morris ME. Monocarboxylate Transporters (SLC16): Function, Regulation, and Role in Health and Disease. Pharmacol Rev. 2020;72(2):466-85.

269. Morris ME, Felmlee MA. Overview of the proton-coupled MCT (SLC16A) family of transporters: characterization, function and role in the transport of the drug of abuse gamma-hydroxybutyric acid. AAPS J. 2008;10(2):311-21.

270. Leu M, Kitz J, Pilavakis Y, Hakroush S, Wolff HA, Canis M, et al. Monocarboxylate transporter-1 (MCT1) protein expression in head and neck cancer affects clinical outcome. Sci Rep-Uk. 2021;11(1).

271. Chen X, Chen X, Liu F, Yuan QQ, Zhang KX, Zhou W, et al. Monocarboxylate transporter 1 is an independent prognostic factor in esophageal squamous cell carcinoma. Oncol Rep. 2019;41(4):2529-39.

272. Pinheiro C, Albergaria A, Paredes J, Sousa B, Dufloth R, Vieira D, et al. Monocarboxylate transporter 1 is up-regulated in basal-like breast carcinoma. Histopathology. 2010;56(7):860-7.

273. Pinheiro C, Longatto A, Scapulatempo C, Ferreira L, Martins S, Pellerin L, et al. Increased expression of monocarboxylate transporters 1, 2, and 4 in colorectal carcinomas. Virchows Arch. 2008;452(2):139-46.

274. Wilde L, Roche M, Domingo-Vidal M, Tanson K, Philp N, Curry J, et al. Metabolic coupling and the Reverse Warburg Effect in cancer: Implications for novel biomarker and anticancer agent development. Semin Oncol. 2017;44(3):198-203.

275. Roughton FJ, Booth VH. The manometric determination of the activity of carbonic anhydrase under varied conditions. Biochem J. 1946;40(2):309-19.

276. Swietach P, Hulikova A, Vaughan-Jones RD, Harris AL. New insights into the physiological role of carbonic anhydrase IX in tumour pH regulation. Oncogene. 2010;29(50):6509-21.

277. Andreucci E, Peppicelli S, Ruzzolini J, Bianchini F, Biagioni A, Papucci L, et al. The acidic tumor microenvironment drives a stem-like phenotype in melanoma cells. J Mol Med (Berl). 2020;98(10):1431-46.

278. Pillai SR, Damaghi M, Marunaka Y, Spugnini EP, Fais S, Gillies RJ. Causes, consequences, and therapy of tumors acidosis. Cancer Metast Rev. 2019;38(1-2):205-22.

279. Murdter TE, Friedel G, Backman JT, McClellan M, Schick M, Gerken M, et al. Dose optimization of a doxorubicin prodrug (HMR 1826) in isolated perfused human lungs: low tumor pH promotes prodrug activation by beta-glucuronidase. J Pharmacol Exp Ther. 2002;301(1):223-8.

280. Komarov DA, Ichikawa Y, Yamamoto K, Stewart NJ, Matsumoto S, Yasui H, et al. In Vivo Extracellular pH Mapping of Tumors Using Electron Paramagnetic Resonance. Analytical Chemistry. 2018;90(23):13938-45.

281. Anemone A, Consolino L, Conti L, Irrera P, Hsu MY, Villano D, et al. Tumour acidosis evaluated in vivo by MRI-CEST pH imaging reveals breast cancer metastatic potential. Brit J Cancer. 2021;124(1):207-16.

282. Tang YY, Xiao G, Shen ZW, Zhuang CY, Xie YD, Zhang XL, et al. Noninvasive Detection of Extracellular pH in Human Benign and Malignant Liver Tumors Using CEST MRI. Front Oncol. 2020;10.

283. Consolino L, Anemone A, Capozza M, Carella A, Irrera P, Corrado A, et al. Non-invasive Investigation of Tumor Metabolism and Acidosis by MRI-CEST Imaging. Front Oncol. 2020;10.

284. Chen MM, Chen CY, Shen ZW, Zhang XL, Chen YZ, Lin FF, et al. Extracellular pH is a biomarker enabling detection of breast cancer and liver cancer using CEST MRI. Oncotarget. 2017;8(28):45759-67.

285. Coman D, Huang Y, Rao JU, De Feyter HM, Rothman DL, Juchem C, et al. Imaging the intratumoral-peritumoral extracellular pH gradient of gliomas. NMR Biomed. 2016;29(3):309-19.

286. Ferrauto G, Di Gregorio E, Auboiroux V, Petit M, Berger F, Aime S, et al. CEST-MRI for glioma pH quantification in mouse model: Validation by immunohistochemistry. NMR Biomed. 2018;31(11):e4005.

287. Liu G, Li Y, Sheth VR, Pagel MD. Imaging in vivo extracellular pH with a single paramagnetic chemical exchange saturation transfer magnetic resonance imaging contrast agent. Mol Imaging. 2012;11(1):47-57.

288. Duwel S, Hundshammer C, Gersch M, Feuerecker B, Steiger K, Buck A, et al. Imaging of pH in vivo using hyperpolarized (13)C-labelled zymonic acid. Nat Commun. 2017;8:15126.

289. Samouilov A, Efimova OV, Bobko AA, Sun Z, Petryakov S, Eubank TD, et al. In vivo proton-electron double-resonance imaging of extracellular tumor pH using an advanced nitroxide probe. Anal Chem. 2014;86(2):1045-52.

290. Komarov DA, Ichikawa Y, Yamamoto K, Stewart NJ, Matsumoto S, Yasui H, et al. In Vivo Extracellular pH Mapping of Tumors Using Electron Paramagnetic Resonance. Anal Chem. 2018;90(23):13938-45.

291. Chen LQ, Pagel MD. Evaluating pH in the Extracellular Tumor Microenvironment Using CEST MRI and Other Imaging Methods. Adv Radiol. 2015;2015.

292. Marino ML, Pellegrini P, Di Lernia G, Djavaheri-Mergny M, Brnjic S, Zhang X, et al. Autophagy is a protective mechanism for human melanoma cells under acidic stress. J Biol Chem. 2012;287(36):30664-76.

293. Wojtkowiak JW, Rothberg JM, Kumar V, Schramm KJ, Haller E, Proemsey JB, et al. Chronic autophagy is a cellular adaptation to tumor acidic pH microenvironments. Cancer Res. 2012;72(16):3938-47.

294. Gao Y, Qi WW, Liu SH, Zhao SF, Lv J, Qiu WS. Acid-induced autophagy protects human gastric cancer cells from apoptosis by activating Erk1/2 pathway. Transl Cancer Res. 2019;8(4):1560-70.

295. Gao J, Guo Z, Cheng J, Sun B, Yang J, Li H, et al. Differential metabolic responses in breast cancer cell lines to acidosis and lactic acidosis revealed by stable isotope assisted metabolomics. Sci Rep. 2020;10(1):21967.

296. Lamonte G, Tang X, Chen JL, Wu J, Ding CK, Keenan MM, et al. Acidosis induces reprogramming of cellular metabolism to mitigate oxidative stress. Cancer Metab. 2013;1(1):23.

297. Menard JA, Christianson HC, Kucharzewska P, Bourseau-Guilmain E, Svensson KJ, Lindqvist E, et al. Metastasis Stimulation by Hypoxia and Acidosis-Induced Extracellular

Lipid Uptake Is Mediated by Proteoglycan-Dependent Endocytosis. Cancer Res. 2016;76(16):4828-40.

298. Wu H, Estrella V, Beatty M, Abrahams D, El-Kenawi A, Russell S, et al. T-cells produce acidic niches in lymph nodes to suppress their own effector functions. Nat Commun. 2020;11(1):4113.

299. Pilon-Thomas S, Kodumudi KN, El-Kenawi AE, Russell S, Weber AM, Luddy K, et al. Neutralization of Tumor Acidity Improves Antitumor Responses to Immunotherapy. Cancer Res. 2016;76(6):1381-90.

300. Calcinotto A, Filipazzi P, Grioni M, Iero M, De Milito A, Ricupito A, et al. Modulation of Microenvironment Acidity Reverses Anergy in Human and Murine Tumor-Infiltrating T Lymphocytes. Cancer Res. 2012;72(11):2746-56.

301. Riemann A, Ihling A, Thomas J, Schneider B, Thews O, Gekle M. Acidic environment activates inflammatory programs in fibroblasts via a cAMP-MAPK pathway. Biochim Biophys Acta. 2015;1853(2):299-307.

302. Magistretti PJ, Allaman I. Lactate in the brain: from metabolic end-product to signalling molecule. Nat Rev Neurosci. 2018;19(4):235-49.

303. Brizel DM, Schroeder T, Scher RL, Walenta S, Clough RW, Dewhirst MW, et al. Elevated tumor lactate concentrations predict for an increased risk of metastases in head-and-neck cancer. Int J Radiat Oncol. 2001;51(2):349-53.

304. Nikoobakht M, Shamshiripour P, Nekoo ZA, Haghmohammadi SF. Elevated Lactate and Total Protein Levels in Stereotactic Brain Biopsy Specimen; Potential Biomarkers of Malignancy and Poor Prognosis. Arch Iran Med. 2019;22(3):125-31.

305. Walenta S, Salameh A, Lyng H, Evensen JF, Mitze M, Rofstad EK, et al. Correlation of high lactate levels in head and neck tumors with incidence of metastasis. American Journal of Pathology. 1997;150(2):409-15.

306. Walenta S, Wetterling M, Lehrke M, Schwickert G, Sundfor K, Rofstad EK, et al. High lactate levels predict likelihood of metastases, tumor recurrence, and restricted patient survival in human cervical cancers. Cancer Res. 2000;60(4):916-21.

307. Sonveaux P, Copetti T, De Saedeleer CJ, Vegran F, Verrax J, Kennedy KM, et al. Targeting the Lactate Transporter MCT1 in Endothelial Cells Inhibits Lactate-Induced HIF-1 Activation and Tumor Angiogenesis. Plos One. 2012;7(3).

308. Perez-Escuredo J, Dadhich RK, Dhup S, Cacace A, Van Hee VF, De Saedeleer CJ, et al. Lactate promotes glutamine uptake and metabolism in oxidative cancer cells. Cell Cycle. 2016;15(1):72-83.

309. Lu H, Dalgard CL, Mohyeldin A, McFate T, Tait AS, Verma A. Reversible inactivation of HIF-1 prolyl hydroxylases allows cell metabolism to control basal HIF-1. J Biol Chem. 2005;280(51):41928-39.

310. Feichtinger RG, Lang R. Targeting L-Lactate Metabolism to Overcome Resistance to Immune Therapy of Melanoma and Other Tumor Entities. J Oncol. 2019;2019:2084195.

311. Nowell PC. The clonal evolution of tumor cell populations. Science. 1976;194(4260):23-8.

312. Chen H, Lin FQ, Xing K, He XL. The reverse evolution from multicellularity to unicellularity during carcinogenesis (vol 6, 6367, 2015). Nature Communications. 2015;6.

313. Ikehata H, Ono T. The mechanisms of UV mutagenesis. J Radiat Res. 2011;52(2):115-25.

314. Voordeckers K, Colding C, Grasso L, Pardo B, Hoes L, Kominek J, et al. Ethanol exposure increases mutation rate through error-prone polymerases. Nature Communications. 2020;11(1).

315. Blackford A, Parmigiani G, Kensler T, Wolfgang CL, Jones S, Zhang X, et al. Genetic Mutations Associated with Cigarette Smoking in Pancreatic Cancer. Lab Invest. 2009;89:308a-9a.

316. Loeb LA. Human cancers express mutator phenotypes: origin, consequences and targeting. Nat Rev Cancer. 2011;11(6):450-7.

317. Mengelbier LH, Karlsson J, Lindgren D, Valind A, Lilljebjorn H, Jansson C, et al. Intratumoral genome diversity parallels progression and predicts outcome in pediatric cancer. Nature Communications. 2015;6.

318. Foster KR. Biomedicine. Hamiltonian medicine: why the social lives of pathogens matter. Science. 2005;308(5726):1269-70.

319. Lambert G, Estevez-Salmeron L, Oh S, Liao D, Emerson BM, Tlsty TD, et al. An analogy between the evolution of drug resistance in bacterial communities and malignant tissues. Nat Rev Cancer. 2011;11(5):375-U138.

320. Marusyk A, Polyak K. Tumor heterogeneity: Causes and consequences. Bba-Rev Cancer. 2010;1805(1):105-17.

321. Hidalgo M. Pancreatic cancer. N Engl J Med. 2010;362(17):1605-17.

322. Hanahan D, Weinberg RA. Hallmarks of cancer: the next generation. Cell. 2011;144(5):646-74.

323. Steeg PS. Tumor metastasis: mechanistic insights and clinical challenges. Nat Med. 2006;12(8):895-904.

324. Yachida S, Iacobuzio-Donahue CA. The Pathology and Genetics of Metastatic Pancreatic Cancer. Arch Pathol Lab Med. 2009;133(3):413-22.

325. Luzzi KJ, MacDonald IC, Schmidt EE, Kerkvliet N, Morris VL, Chambers AF, et al. Multistep nature of metastatic inefficiency - Dormancy of solitary cells after successful extravasation and limited survival of early micrometastases. American Journal of Pathology. 1998;153(3):865-73.

326. Fares J, Fares MY, Khachfe HH, Salhab HA, Fares Y. Molecular principles of metastasis: a hallmark of cancer revisited. Signal Transduct Target Ther. 2020;5(1):28.

327. Birkbak NJ, McGranahan N. Cancer Genome Evolutionary Trajectories in Metastasis. Cancer Cell. 2020;37(1):8-19.

328. Robinson DR, Wu YM, Lonigro RJ, Vats P, Cobain E, Everett J, et al. Integrative clinical genomics of metastatic cancer. Nature. 2017;548(7667):297-303.

329. Yang D, Denny SK, Greenside PG, Chaikovsky AC, Brady JJ, Ouadah Y, et al. Intertumoral Heterogeneity in SCLC Is Influenced by the Cell Type of Origin. Cancer Discovery. 2018;8(10):1316-31.

330. Tasdogan A, Faubert B, Ramesh V, Ubellacker JM, Shen B, Solmonson A, et al. Metabolic heterogeneity confers differences in melanoma metastatic potential. Nature. 2020;577(7788):115-20.

331. Husing T, Lange L, Rauschner M, Riemann A, Thews O. Functional Impact of Acidosis-Regulated MicroRNAs on the Migration and Adhesion of Tumor Cells. Adv Exp Med Biol. 2021;1269:151-5.

332. Riemann A, Schneider B, Gundel D, Stock C, Gekle M, Thews O. Acidosis Promotes Metastasis Formation by Enhancing Tumor Cell Motility. Adv Exp Med Biol. 2016;876:215-20.

333. Riemann A, Rauschner M, Giesselmann M, Reime S, Haupt V, Thews O. Extracellular Acidosis Modulates the Expression of Epithelial-Mesenchymal Transition (EMT) Markers and Adhesion of Epithelial and Tumor Cells. Neoplasia. 2019;21(5):450-8.

334. Zhang YJ, Xu LL, Wang P, Jian HZ, Shi XH, Jia M, et al. Phenotypic transition of tumor cells between epithelial- and mesenchymal-like state during adaptation to acidosis. Cell Cycle. 2019;18(16):1938-47.

335. Csaderova L, Debreova M, Radvak P, Stano M, Vrestiakova M, Kopacek J, et al. The effect of carbonic anhydrase IX on focal contacts during cell spreading and migration. Front Physiol. 2013;4.

336. Debreova M, Csaderova L, Burikova M, Lukacikova L, Kajanova I, Sedlakova O, et al. CAIX Regulates Invadopodia Formation through Both a pH-Dependent Mechanism and Interplay with Actin Regulatory Proteins. International Journal of Molecular Sciences. 2019;20(11).

337. Rothberg JM, Bailey KM, Wojtkowiak JW, Ben-Nun Y, Bogyo M, Weber E, et al. Acid-Mediated Tumor Proteolysis: Contribution of Cysteine Cathepsins. Neoplasia. 2013;15(10):1111-23.

338. Rozhin J, Sameni M, Ziegler G, Sloane BF. Pericellular Ph Affects Distribution and Secretion of Cathepsin-B in Malignant-Cells. Cancer Res. 1994;54(24):6517-25.

339. Guo W, Zhang YC, Guo SW, Mei Z, Liao HP, Dong H, et al. Tumor microbiome contributes to an aggressive phenotype in the basal-like subtype of pancreatic cancer. Communications Biology. 2021;4(1).

340. Geller LT, Barzily-Rokni M, Danino T, Jonas OH, Shental N, Nejman D, et al. Potential role of intratumor bacteria in mediating tumor resistance to the chemotherapeutic drug gemcitabine. Science. 2017;357(6356):1156-60.

341. Gatenby RA, Gillies RJ. Why do cancers have high aerobic glycolysis? Nat Rev Cancer. 2004;4(11):891-9.

342. Damaghi M, Tafreshi NK, Lloyd MC, Sprung R, Estrella V, Wojtkowiak JW, et al. Chronic acidosis in the tumour microenvironment selects for overexpression of LAMP2 in the plasma membrane. Nat Commun. 2015;6:8752.

343. Boedtkjer E, Pedersen SF. The Acidic Tumor Microenvironment as a Driver of Cancer. Annu Rev Physiol. 2020;82:103-26.

344. Case RM. Synthesis, intracellular transport and discharge of exportable proteins in the pancreatic acinar cell and other cells. Biol Rev Camb Philos Soc. 1978;53(2):211-354.

345. Case RM, Scratcherd T, Wynne RD. The origin and secretion of pancreatic juice bicarbonate. J Physiol. 1970;210(1):1-15.

346. Hickson JC. The secretion of pancreatic juice in response to stimulation of the vagus nerves in the pig. J Physiol. 1970;206(2):275-97.

347. Dubrasquet M, Roze C, Ling N, Florencio H. Inhibition of gastric and pancreatic secretions by cerebroventricular injections of gastrin-releasing peptide and bombesin in rats. Regul Pept. 1982;3(2):105-12.

348. Ishiguro H, Yamamoto A, Nakakuki M, Yi L, Ishiguro M, Yamaguchi M, et al. Physiology and pathophysiology of bicarbonate secretion by pancreatic duct epithelium. Nagoya J Med Sci. 2012;74(1-2):1-18.

349. Freedman SD. New concepts in understanding the pathophysiology of chronic pancreatitis. Int J Pancreatol. 1998;24(1):1-8.

350. Behrendorff N, Floetenmeyer M, Schwiening C, Thorn P. Protons Released During Pancreatic Acinar Cell Secretion Acidify the Lumen and Contribute to Pancreatitis in Mice. Gastroenterology. 2010;139(5):1711-20.

351. Archetti M. Heterogeneity and proliferation of invasive cancer subclones in game theory models of the Warburg effect. Cell Prolif. 2015;48(2):259-69.

352. Silva AS, Yunes JA, Gillies RJ, Gatenby RA. The potential role of systemic buffers in reducing intratumoral extracellular pH and acid-mediated invasion. Cancer Res. 2009;69(6):2677-84.

353. Ibrahim Hashim A, Cornnell HH, Coelho Ribeiro Mde L, Abrahams D, Cunningham J, Lloyd M, et al. Reduction of metastasis using a non-volatile buffer. Clin Exp Metastasis. 2011;28(8):841-9.

354. Ribeiro MD, Silva AS, Bailey KM, Kumar NB, Sellers TA, Gatenby RA, et al. Buffer Therapy for Cancer. J Nutr Food Sci. 2012;2:6.

355. The American Type Culture Collection. AsPC-1 [15.07.2022]. Available from: https://www.atcc.org/products/crl-1682.

356. The American Type Culture Collection. BxPC-3 [15.07.2022]. Available from: https://www.atcc.org/products/crl-1687.

357. The American Type Culture Collection. HPAC [15.07.2022]. Available from: https://www.atcc.org/products/crl-2119.

358. The American Type Culture Collection. MIA-PaCa-2 [15.07.2022]. Available from: https://www.atcc.org/products/crl-1420.

359. The American Type Culture Collection. PANC-1 [15.07.2022]. Available from: https://www.atcc.org/products/crl-1469.

360. PubChem Compound Summary for CID 23831 [Internet]. 2022 [cited Retrieved September 15, 2022]. Available from: https://pubchem.ncbi.nlm.nih.gov/compound/hepes.

361. Good NE, Winget GD, Winter W, Connolly TN, Izawa S, Singh RM. Hydrogen ion buffers for biological research. Biochemistry. 1966;5(2):467-77.

362. Goldsmith DJ, Hilton PJ. Relationship between intracellular proton buffering capacity and intracellular pH. Kidney Int. 1992;41(1):43-9.

363. Benyahia Z, Blackman MCNM, Hamelin L, Zampieri LX, Capeloa T, Bedin ML, et al. In Vitro and In Vivo Characterization of MCT1 Inhibitor AZD3965 Confirms Preclinical Safety Compatible with Breast Cancer Treatment. Cancers. 2021;13(3).

364. Corbet C, Bastien E, Draoui N, Doix B, Mignion L, Jordan BF, et al. Interruption of lactate uptake by inhibiting mitochondrial pyruvate transport unravels direct antitumor and radiosensitizing effects. Nature Communications. 2018;9.

365. Michl J, Park KC, Swietach P. Evidence-based guidelines for controlling pH in mammalian live-cell culture systems. Commun Biol. 2019;2:144.

366. Vichai V, Kirtikara K. Sulforhodamine B colorimetric assay for cytotoxicity screening. Nature Protocols. 2006;1(3):1112-6.

367. Love MI, Huber W, Anders S. Moderated estimation of fold change and dispersion for RNA-seq data with DESeq2. Genome Biol. 2014;15(12).

368. Livak KJ, Schmittgen TD. Analysis of relative gene expression data using real-time quantitative PCR and the 2(T)(-Delta Delta C) method. Methods. 2001;25(4):402-8.

369. Schindelin J, Arganda-Carreras I, Frise E, Kaynig V, Longair M, Pietzsch T, et al. Fiji: an open-source platform for biological-image analysis. Nat Methods. 2012;9(7):676-82.

370. Nonnenmacher Y, Palorini R, Hiller K. Determining Compartment-Specific Metabolic Fluxes. Methods Mol Biol. 2019;1862:137-49.

371. Guo J, Su Y, Zhang M. Circ_0000140 restrains the proliferation, metastasis and glycolysis metabolism of oral squamous cell carcinoma through upregulating CDC73 via sponging miR-182-5p. Cancer Cell Int. 2020;20:407.

372. O'Neill S, Porter RK, McNamee N, Martinez VG, O'Driscoll L. 2-Deoxy-D-Glucose inhibits aggressive triple-negative breast cancer cells by targeting glycolysis and the cancer stem cell phenotype. Sci Rep. 2019;9(1):3788.

373. Sun C, Liu X, Wang B, Wang Z, Liu Y, Di C, et al. Endocytosis-mediated mitochondrial transplantation: Transferring normal human astrocytic mitochondria into glioma cells rescues aerobic respiration and enhances radiosensitivity. Theranostics. 2019;9(12):3595-607.

374. Zhang J, Zhang Q. Using Seahorse Machine to Measure OCR and ECAR in Cancer Cells. Methods Mol Biol. 2019;1928:353-63.

375. Pirkmajer S, Chibalin AV. Serum starvation: caveat emptor. Am J Physiol Cell Physiol. 2011;301(2):C272-9.

376. Rashid MU, Coombs KM. Serum-reduced media impacts on cell viability and protein expression in human lung epithelial cells. J Cell Physiol. 2019;234(6):7718-24.

377. Benz K, Mollenhauer J. 3D Cultures of Disc-Chondrocytes. Optosensoric Online Monitoring of Oxygen and pH Kinetics2008 12.10.2021; 12:[54-9 pp.]. Available from: https://www.presens.de/knowledge/publications/application-note/3d-cultures-of-disc-chondrocytes-588.

378. V. Lorenz BR, A. Hermann, H. F. Abts. Quality Assessment of Primary Human Keratinocyte Cultures with Online Measurement of Oxygen and pH2012 12.10.2021; 4(2):[70-4 pp.]. Available from: http://ipimediaworld.com/wp-content/uploads/2012/06/Pages-from-IPI-Volume4-Issue2-11.pdf.

379. Heux S, Philippe B, Portais JC. High-throughput workflow for monitoring and mining bioprocess data and its application to inferring the physiological response of Escherichia coli to perturbations. Appl Environ Microbiol. 2011;77(19):7040-9.

380. John GT, Goelling D, Klimant I, Schneider H, Heinzle E. PH-sensing 96-well microtitre plates for the characterization of acid production by dairy starter cultures. J Dairy Res. 2003;70(3):327-33.

381. Kieninger J, Aravindalochanan K, Sandvik JA, Pettersen EO, Urban GA. Pericellular oxygen monitoring with integrated sensor chips for reproducible cell culture experiments. Cell Prolif. 2014;47(2):180-8.

382. Wu S, Wu S, Yi Z, Zeng F, Wu W, Qiao Y, et al. Hydrogel-Based Fluorescent Dual pH and Oxygen Sensors Loaded in 96-Well Plates for High-Throughput Cell Metabolism Studies. Sensors (Basel). 2018;18(2).

383. Arguello RJ, Combes AJ, Char R, Gigan JP, Baaziz AI, Bousiquot E, et al. SCENITH: A Flow Cytometry-Based Method to Functionally Profile Energy Metabolism with Single-Cell Resolution. Cell Metab. 2020;32(6):1063-75 e7.

384. Tanumihardja E, Slaats RH, van der Meer AD, Passier R, Olthuis W, van den Berg A. Measuring Both pH and O2 with a Single On-Chip Sensor in Cultures of Human Pluripotent Stem Cell-Derived Cardiomyocytes to Track Induced Changes in Cellular Metabolism. ACS Sens. 2021;6(1):267-74.

385. Hulikova A, Harris AL, Vaughan-Jones RD, Swietach P. Regulation of intracellular pH in cancer cell lines under normoxia and hypoxia. J Cell Physiol. 2013;228(4):743-52.

386. Jo J, Lee CH, Kopelman R, Wang X. In vivo quantitative imaging of tumor pH by nanosonophore assisted multispectral photoacoustic imaging. Nat Commun. 2017;8(1):471.

387. Bachmeier CJ, Trickler WJ, Miller DW. Drug efflux transport properties of 2',7'-bis(2-carboxyethyl)-5(6)-carboxyfluorescein acetoxymethyl ester (BCECF-AM) and its fluorescent free acid, BCECF. J Pharm Sci. 2004;93(4):932-42.

388. Contreras-Baeza Y, Sandoval PY, Alarcon R, Galaz A, Cortes-Molina F, Alegria K, et al. Monocarboxylate transporter 4 (MCT4) is a high affinity transporter capable of exporting lactate in high-lactate microenvironments. J Biol Chem. 2019;294(52):20135-47.

389. Hinton A, Sennoune SR, Bond S, Fang M, Reuveni M, Sahagian GG, et al. Function of a subunit isoforms of the V-ATPase in pH homeostasis and in vitro invasion of MDA-MB231 human breast cancer cells. J Biol Chem. 2009;284(24):16400-8.

390. Lucien F, Harper K, Pelletier PP, Volkov L, Dubois CM. Simultaneous pH measurement in endocytic and cytosolic compartments in living cells using confocal microscopy. J Vis Exp. 2014(86).

391. Ray A, Koo Lee YE, Epstein T, Kim G, Kopelman R. Two-photon nano-PEBBLE sensors: subcellular pH measurements. Analyst. 2011;136(18):3616-22.

392. Willoughby D, Schwiening CJ. Electrically evoked dendritic pH transients in rat cerebellar Purkinje cells. J Physiol. 2002;544(2):487-99.

393. Jiang Z, Yu X, Zhai S, Hao Y. Ratiometric Dissolved Oxygen Sensors Based on Ruthenium Complex Doped with Silver Nanoparticles. Sensors (Basel). 2017;17(3).

394. Lima S, Bonifacio RL, Azzellini GC, Coichev N. Ruthenium(II) tris(bipyridyl) ion as a luminescent probe for oxygen uptake on the catalyzed oxidation of HSO3-. Talanta. 2002;56(3):547-56.

395. Wang XD, Wolfbeis OS. Optical methods for sensing and imaging oxygen: materials, spectroscopies and applications. Chem Soc Rev. 2014;43(10):3666-761.

396. Grynkiewicz G, Poenie M, Tsien RY. A new generation of Ca2+ indicators with greatly improved fluorescence properties. J Biol Chem. 1985;260(6):3440-50.

397. Stern OV, M. Über die Abklingzeit der Fluoreszenz. Z Phys. 1919;20:183-1888.

398. Bacci G, Capanna R, Orlandi M, Mancini I, Bettelli G, Dallari D, et al. Prognostic significance of serum lactic acid dehydrogenase in Ewing's tumor of bone. Ric Clin Lab. 1985;15(1):89-96.

399. Koppenol WH, Bounds PL, Dang CV. Otto Warburg's contributions to current concepts of cancer metabolism. Nat Rev Cancer. 2011;11(5):325-37.

400. Racker E. Bioenergetics and the problem of tumor growth. Am Sci. 1972;60(1):56-63.

401. Wu H, Estrella V, Beatty M, Abrahams D, El-Kenawi A, Russell S, et al. T-cells produce acidic niches in lymph nodes to suppress their own effector functions. Nature Communications. 2020;11(1).

402. Halperin ML, Connors HP, Relman AS, Karnovsky ML. Factors that control the effect of pH on glycolysis in leukocytes. J Biol Chem. 1969;244(2):384-90.

403. Kumar DP, Tiwari A, Bhat R. Effect of pH on the stability and structure of yeast hexokinase A - Acidic amino acid residues in the cleft region are critical for the opening and the closing of the structure. Journal of Biological Chemistry. 2004;279(31):32093-9.

404. Simcikova D, Heneberg P. Identification of alkaline pH optimum of human glucokinase because of ATP-mediated bias correction in outcomes of enzyme assays. Sci Rep. 2019;9(1):11422.

405. Sodium acetate [Internet]. Sigma Aldrich. 2022 [cited 27.09.2022]. Available from: https://www.sigmaaldrich.com/GB/en/product/aldrich/229873.

406. DRUGBANK compound summary for DB03766 [Internet]. 2022 [cited 27.09.2022]. Available from: https://go.drugbank.com/drugs/DB03766.

407. Makowski Z, Lipinski K, Mazur-Kusnirek M. The Effects of Sodium Butyrate, Coated Sodium Butyrate, and Butyric Acid Glycerides on Nutrient Digestibility, Gastrointestinal Function, and Fecal Microbiota in Turkeys. Animals (Basel). 2022;12(14).

408. PubChem Compound Summary for CID 78165 [Internet]. 2022 [cited 27.09.2022]. Available from: https://pubchem.ncbi.nlm.nih.gov/compound/2-_N-Morpholino_ethanesulfonic-acid.

409. PubChem Compound Summary for CID 23672064, Monosodium phosphate [Internet]. 2022 [cited 28.09.2022]. Available from: https://pubchem.ncbi.nlm.nih.gov/compound/23672064#section=CAS.

410. PubChem Compound Summary for CID 795, Imidazole. [Internet]. 2022 [cited 27.09.2022]. Available from: https://pubchem.ncbi.nlm.nih.gov/compound/Imidazole.

411. Adijanto J, Philp NJ. The SLC16A Family of Monocarboxylate Transporters (MCTs)-Physiology and Function in Cellular Metabolism, pH Homeostasis, and Fluid Transport. Curr Top Membr. 2012;70:275-311.

412. Jackson VN, Halestrap AP. The kinetics, substrate, and inhibitor specificity of the monocarboxylate (lactate) transporter of rat liver cells determined using the fluorescent intracellular pH indicator, 2',7'-bis(carboxyethyl)-5(6)-carboxyfluorescein. Journal of Biological Chemistry. 1996;271(2):861-8.

413. Baker SK, McCullagh KJ, Bonen A. Training intensity-dependent and tissue-specific increases in lactate uptake and MCT-1 in heart and muscle. J Appl Physiol (1985). 1998;84(3):987-94.

414. Felmlee MA, Jones RS, Rodriguez-Cruz V, Follman KE, Morris ME. Monocarboxylate Transporters (SLC16): Function, Regulation, and Role in Health and Disease. Pharmacol Rev. 2020;72(2):466-85.

415. Identifier: NCT01791595, A Phase I Trial of AZD3965 in Patients With Advanced Cancer. Bethesda (MD): National Library of Medicine. 2022. [cited 11.04.2022.] Available from: https://www.clinicaltrials.gov/ct2/show/NCT01791595?intr=AZD3965 &draw=2&rank=1.

416. Khan A, Valli E, Lam H, Scott DA, Murray J, Hanssen KM, et al. Targeting metabolic activity in high-risk neuroblastoma through Monocarboxylate Transporter 1 (MCT1) inhibition. Oncogene. 2020;39(17):3555-70.

417. Ovens MJ, Davies AJ, Wilson MC, Murray CM, Halestrap AP. AR-C155858 is a potent inhibitor of monocarboxylate transporters MCT1 and MCT2 that binds to an intracellular site involving transmembrane helices 7-10. Biochem J. 2010;425(3):523-30.

418. Vander Linden C, Corbet C. Killing two birds with one stone: Blocking the mitochondrial pyruvate carrier to inhibit lactate uptake by cancer cells and radiosensitize tumors. Mol Cell Oncol. 2018;5(4).

419. Guile SD, Banticka JR, Cheshire DR, Cooper ME, Davis AM, Donald DK, et al. Potent blockers of the monocarboxylate transporter MCT1: Novel immunomodulatory compounds. Bioorg Med Chem Lett. 2006;16(8):2260-5.

420. Murray CM, Hutchinson R, Bantick JR, Belfield GP, Benjamin AD, Brazma D, et al. Monocarboxylate transporter MCT1 is a target for immunosuppression. Nat Chem Biol. 2005;1(7):371-6.

421. Halford SER, Jones P, Wedge S, Hirschberg S, Katugampola S, Veal G, et al. A first-in-human first-in-class (FIC) trial of the monocarboxylate transporter 1 (MCT1) inhibitor AZD3965 in patients with advanced solid tumours. Journal of Clinical Oncology. 2017;35.

422. Benjamin D, Robay D, Hindupur SK, Pohlmann J, Colombi M, El-Shemerly MY, et al. Dual Inhibition of the Lactate Transporters MCT1 and MCT4 Is Synthetic Lethal with Metformin due to NAD+ Depletion in Cancer Cells. Cell Rep. 2018;25(11):3047-58 e4.

423. Gatenby RA, Gawlinski ET, Gmitro AF, Kaylor B, Gillies RJ. Acid-mediated tumor invasion: a multidisciplinary study. Cancer Res. 2006;66(10):5216-23.

424. Hao GY, Xu ZP, Li L. Manipulating extracellular tumour pH: an effective target for cancer therapy. Rsc Adv. 2018;8(39):22182-92.

425. Alper SL, Darman RB, Chernova MN, Dahl NK. The AE gene family of Cl/HCO3-exchangers. J Nephrol. 2002;15 Suppl 5:S41-53.

426. Concepcion AR, Lopez M, Ardura-Fabregat A, Medina JF. Role of AE2 for pHi regulation in biliary epithelial cells. Front Physiol. 2013;4:413.

427. Ureta T, Lazo PA, Sols A. Allosteric inhibition of brain hexokinase by glucose 6-phosphate in the reverse reaction. Arch Biochem Biophys. 1985;239(2):315-9.

428. Kemp RG, Foe LG. Allosteric regulatory properties of muscle phosphofructokinase. Mol Cell Biochem. 1983;57(2):147-54.

429. El-Maghrabi MR, Claus TH, McGrane MM, Pilkis SJ. Influence of phosphorylation on the interaction of effectors with rat liver pyruvate kinase. J Biol Chem. 1982;257(1):233-40.

430. Noble RA, Bell N, Blair H, Sikka A, Thomas H, Phillips N, et al. Inhibition of monocarboxyate transporter 1 by AZD3965 as a novel therapeutic approach for diffuse large B-cell lymphoma and Burkitt lymphoma. Haematologica. 2017;102(7):1247-57.

431. Curtis NJ, Mooney L, Hopcroft L, Michopoulos F, Whalley N, Zhong HH, et al. Pre-clinical pharmacology of AZD3965, a selective inhibitor of MCT1: DLBCL, NHL and Burkitt's lymphoma anti-tumor activity. Oncotarget. 2017;8(41):69219-36.

432. Cassio F, Leao C, Vanuden N. Transport of Lactate and Other Short-Chain Monocarboxylates in the Yeast Saccharomyces-Cerevisiae. Appl Environ Microb. 1987;53(3):509-13.

433. Guan X, Rodriguez-Cruz V, Morris ME. Cellular Uptake of MCT1 Inhibitors AR-C155858 and AZD3965 and Their Effects on MCT-Mediated Transport of L-Lactate in Murine 4T1 Breast Tumor Cancer Cells. AAPS J. 2019;21(2):13.

434. Dong LQ, Lu DY, Chen R, Lin YP, Zhu HW, Zhang Z, et al. Proteogenomic characterization identifies clinically relevant subgroups of intrahepatic cholangiocarcinoma. Cancer Cell. 2022;40(1):70-87.

435. Vander Linden C, Corbet C, Bastien E, Martherus R, Guilbaud C, Petit L, et al. Therapy-induced DNA methylation inactivates MCT1 and renders tumor cells vulnerable to MCT4 inhibition. Cell Rep. 2021;35(9).

436. Eisner DA, Trafford AW, Diaz ME, Overend CL, O'Neill SC. The control of Ca release from the cardiac sarcoplasmic reticulum: regulation versus autoregulation. Cardiovasc Res. 1998;38(3):589-604.

437. Guan X, Morris ME. In Vitro and In Vivo Efficacy of AZD3965 and Alpha-Cyano-4-Hydroxycinnamic Acid in the Murine 4T1 Breast Tumor Model. AAPS J. 2020;22(4):84.

438. Hamdan L, Arrar Z, Al Muataz Y, Suleiman L, Negrier C, Mulengi JK, et al. Alpha Cyano-4-Hydroxy-3-Methoxycinnamic Acid Inhibits Proliferation and Induces Apoptosis in Human Breast Cancer Cells. Plos One. 2013;8(9).

439. Bola BM, Chadwick AL, Michopoulos F, Blount KG, Telfer BA, Williams KJ, et al. Inhibition of Monocarboxylate Transporter-1 (MCT1) by AZD3965 Enhances Radiosensitivity by Reducing Lactate Transport. Molecular Cancer Therapeutics. 2014;13(12):2805-16.

440. Van Hee VF, Labar D, Dehon G, Grasso D, Gregoire V, Muccioli GG, et al. Radiosynthesis and validation of (+/-)-[18F]-3-fluoro-2-hydroxypropionate ([18F]-FLac) as a PET tracer of lactate to monitor MCT1-dependent lactate uptake in tumors. Oncotarget. 2017;8(15):24415-28.

441. Al-Masri M, Paliotti K, Tran R, Halaoui R, Lelarge V, Chatterjee S, et al. Architectural control of metabolic plasticity in epithelial cancer cells. Communications Biology. 2021;4(1).

442. Baltazar F, Afonso J, Costa M, Granja S. Lactate Beyond a Waste Metabolite: Metabolic Affairs and Signaling in Malignancy. Front Oncol. 2020;10:231.

443. Ibrahim-Hashim A, Abrahams D, Enriquez-Navas PM, Luddy K, Gatenby RA, Gillies RJ. Tris-base buffer: a promising new inhibitor for cancer progression and metastasis. Cancer Med. 2017;6(7):1720-9.

444. Robey IF, Baggett BK, Kirkpatrick ND, Roe DJ, Dosescu J, Sloane BF, et al. Bicarbonate increases tumor pH and inhibits spontaneous metastases. Cancer Res. 2009;69(6):2260-8.

445. Voss NCS, Dreyer T, Henningsen MB, Vahl P, Honore B, Boedtkjer E. Targeting the Acidic Tumor Microenvironment: Unexpected Pro-Neoplastic Effects of Oral NaHCO3 Therapy in Murine Breast Tissue. Cancers. 2020;12(4).

446. Potzl J, Roser D, Bankel L, Homberg N, Geishauser A, Brenner CD, et al. Reversal of tumor acidosis by systemic buffering reactivates NK cells to express IFN-gamma and induces NK cell-dependent lymphoma control without other immunotherapies. Int J Cancer. 2017;140(9):2125-33.

447. Serowy S, Saparov SM, Antonenko YN, Kozlovsky W, Hagen V, Pohl P. Structural proton diffusion along lipid bilayers. Biophys J. 2003;84(2 Pt 1):1031-7.

448. Swietach P. What is pH regulation, and why do cancer cells need it? Cancer Metastasis Rev. 2019;38(1-2):5-15.

449. Luzia L, Lao-Martil D, Savakis P, van Heerden J, van Riel N, Teusink B. pH dependencies of glycolytic enzymes of yeast under in vivo-like assay conditions. Febs J. 2022.

450. Guppy M, Attwood PV, Hansen IA, Sabaratnam R, Frisina J, Whisson ME. pH, temperature and lactate production in human red blood cells: implications for blood storage and glycolytic control. Vox Sang. 1992;62(2):70-5.

451. Rapoport I, Rapoport TA, Rapoport SM. Analysis of pH-induced changes of the glycolysis of human erythrocytes. Acta Biol Med Ger. 1978;37(3):393-401.

452. Burrell RA, McGranahan N, Bartek J, Swanton C. The causes and consequences of genetic heterogeneity in cancer evolution. Nature. 2013;501(7467):338-45.

453. Merlo LMF, Pepper JW, Reid BJ, Maley CC. Cancer as an evolutionary and ecological process. Nat Rev Cancer. 2006;6(12):924-35.

454. Cahill DP, Kinzler KW, Vogelstein B, Lengauer C. Genetic instability and darwinian selection in tumours (Reprinted from Trends in Biochemical Science, vol 12, Dec., 1999). Trends Cell Biol. 1999;9(12):M57-M60.

455. Grossmann P, Cristea S, Beerenwinkel N. Clonal evolution driven by superdriver mutations. Bmc Evol Biol. 2020;20(1).

456. Vogelstein B, Papadopoulos N, Velculescu VE, Zhou SB, Diaz LA, Kinzler KW. Cancer Genome Landscapes. Science. 2013;339(6127):1546-58.

457. Dalgliesh GL, Furge K, Greenman C, Chen LN, Bignell G, Butler A, et al. Systematic sequencing of renal carcinoma reveals inactivation of histone modifying genes. Nature. 2010;463(7279):360-3.

458. Hunter C, Smith R, Cahill DP, Stephens P, Stevens C, Teague J, et al. A hypermutation phenotype and somatic MSH6 mutations in recurrent human malignant gliomas after alkylator chemotherapy. Cancer Res. 2006;66(8):3987-91.

459. Cioce M, Pulito C, Strano S, Blandino G, Fazio VM. Metformin: Metabolic Rewiring Faces Tumor Heterogeneity. Cells. 2020;9(11).

460. Tsai PC, Kuo HT, Hung CH, Tseng KC, Lai HC, Peng CY, et al. Metformin reduces hepatocellular carcinoma incidence after successful antiviral therapy in patients with diabetes and chronic hepatitis C in Taiwan. J Hepatol. 2022.

461. Ding L, Ley TJ, Larson DE, Miller CA, Koboldt DC, Welch JS, et al. Clonal evolution in relapsed acute myeloid leukaemia revealed by whole-genome sequencing. Nature. 2012;481(7382):506-10.

462. Junttila MR, de Sauvage FJ. Influence of tumour micro-environment heterogeneity on therapeutic response. Nature. 2013;501(7467):346-54.

463. Rohani N, Hao LL, Alexis MS, Joughin BA, Krismer K, Moufarrej MN, et al. Acidification of Tumor at Stromal Boundaries Drives Transcriptome Alterations Associated with Aggressive Phenotypes. Cancer Res. 2019;79(8):1952-66.

464. Ferrara N, Kerbel RS. Angiogenesis as a therapeutic target. Nature. 2005;438(7070):967-74.

465. Barcellos-Hoff MH, Ravani SA. Irradiated mammary gland stroma promotes the expression of tumorigenic potential by unirradiated epithelial cells. Cancer Res. 2000;60(5):1254-60.

466. Straussman R, Morikawa T, Shee K, Barzily-Rokni M, Qian ZR, Du JY, et al. Tumour micro-environment elicits innate resistance to RAF inhibitors through HGF secretion. Nature. 2012;487(7408):500-U118.

467. Provenzano PP, Cuevas C, Chang AE, Goel VK, Von Hoff DD, Hingorani SR. Enzymatic Targeting of the Stroma Ablates Physical Barriers to Treatment of Pancreatic Ductal Adenocarcinoma. Cancer Cell. 2012;21(3):418-29.

468. Monterisi S, Michl J, Hulikova A, Koth J, Bridges EM, Hill AE, et al. Solute exchange through gap junctions lessens the adverse effects of inactivating mutations in metabolite-handling genes. Elife. 2022;11.

469. Lee J, Hyeon DY, Hwang D. Single-cell multiomics: technologies and data analysis methods. Exp Mol Med. 2020;52(9):1428-42.

470. Kishimoto T. Interleukin-6: from basic science to medicine--40 years in immunology. Annu Rev Immunol. 2005;23:1-21.

471. Xing Z, Gauldie J, Cox G, Baumann H, Jordana M, Lei XF, et al. IL-6 is an antiinflammatory cytokine required for controlling local or systemic acute inflammatory responses. J Clin Invest. 1998;101(2):311-20.

472. Ishihara K, Hirano T. IL-6 in autoimmune disease and chronic inflammatory proliferative disease. Cytokine Growth Factor Rev. 2002;13(4-5):357-68.

473. Yoshizaki K, Matsuda T, Nishimoto N, Kuritani T, Taeho L, Aozasa K, et al. Pathogenic significance of interleukin-6 (IL-6/BSF-2) in Castleman's disease. Blood. 1989;74(4):1360-7.

474. Greco R, Lorentino F, Nitti R, Lupo Stanghellini MT, Giglio F, Clerici D, et al. Interleukin-6 as Biomarker for Acute GvHD and Survival After Allogeneic Transplant With Post-transplant Cyclophosphamide. Front Immunol. 2019;10:2319.

475. Mantovani A, Allavena P, Sica A, Balkwill F. Cancer-related inflammation. Nature. 2008;454(7203):436-44.

476. Grivennikov SI, Greten FR, Karin M. Immunity, inflammation, and cancer. Cell. 2010;140(6):883-99.

477. Schumacher N, Meyer D, Mauermann A, von der Heyde J, Wolf J, Schwarz J, et al. Shedding of Endogenous Interleukin-6 Receptor (IL-6R) Is Governed by A Disintegrin and Metalloproteinase (ADAM) Proteases while a Full-length IL-6R Isoform Localizes to Circulating Microvesicles. J Biol Chem. 2015;290(43):26059-71.

478. Matthews V, Schuster B, Schutze S, Bussmeyer I, Ludwig A, Hundhausen C, et al. Cellular cholesterol depletion triggers shedding of the human interleukin-6 receptor by ADAM10 and ADAM17 (TACE). J Biol Chem. 2003;278(40):38829-39.

479. Okada S, Okusaka T, Ishii H, Kyogoku A, Yoshimori M, Kajimura N, et al. Elevated serum interleukin-6 levels in patients with pancreatic cancer. Jpn J Clin Oncol. 1998;28(1):12-5.

480. Xu J, Ye Y, Zhang H, Szmitkowski M, Makinen MJ, Li P, et al. Diagnostic and Prognostic Value of Serum Interleukin-6 in Colorectal Cancer. Medicine (Baltimore). 2016;95(2):e2502.

481. Hagi T, Nakamura T, Iino T, Matsubara T, Asanuma K, Matsumine A, et al. The diagnostic and prognostic value of interleukin-6 in patients with soft tissue sarcomas. Sci Rep-Uk. 2017;7.

482. Tian G, Mi J, Wei XD, Zhao DM, Qiao LY, Yang CH, et al. Circulating interleukin-6 and cancer: A meta-analysis using Mendelian randomization. Sci Rep-Uk. 2015;5.

483. Akira S, Taga T, Kishimoto T. Interleukin-6 in Biology and Medicine. Adv Immunol. 1993;54:1-78.

484. Thongchot S, Vidoni C, Ferraresi A, Loilome W, Khuntikeo N, Sangkhamanon S, et al. Cancer-Associated Fibroblast-Derived IL-6 Determines Unfavorable Prognosis in Cholangiocarcinoma by Affecting Autophagy-Associated Chemoresponse. Cancers (Basel). 2021;13(9).

485. Cheteh EH, Sarne V, Ceder S, Bianchi J, Augsten M, Rundqvist H, et al. Interleukin-6 derived from cancer-associated fibroblasts attenuates the p53 response to doxorubicin in prostate cancer cells. Cell Death Discov. 2020;6(1).

486. Francis GM, Krohn EG, Woods KV, Buzaid AC, Grimm EA. Interleukin-6 production and secretion in human melanoma cell lines: regulation by interleukin-1. Melanoma Res. 1996;6(3):191-201.

487. Frassanito MA, Cusmai A, Iodice G, Dammacco F. Autocrine interleukin-6 production and highly malignant multiple myeloma: relation with resistance to drug-induced apoptosis. Blood. 2001;97(2):483-9.

488. Yu H, Lee H, Herrmann A, Buettner R, Jove R. Revisiting STAT3 signalling in cancer: new and unexpected biological functions. Nat Rev Cancer. 2014;14(11):736-46.

489. Carey AL, Steinberg GR, Macaulay SL, Thomas WG, Holmes AG, Ramm G, et al. Interleukin-6 increases insulin-stimulated glucose disposal in humans and glucose

uptake and fatty acid oxidation in vitro via AMP-activated protein kinase. Diabetes. 2006;55(10):2688-97.

490. Fuster JJ, Walsh K. The good, the bad, and the ugly of interleukin-6 signaling. EMBO J. 2014;33(13):1425-7.

491. Kistner TM, Pedersen BK, Lieberman DE. Interleukin 6 as an energy allocator in muscle tissue. Nat Metab. 2022;4(2):170-9.

492. Corcoran RB, Contino G, Deshpande V, Tzatsos A, Conrad C, Benes CH, et al. STAT3 plays a critical role in KRAS-induced pancreatic tumorigenesis. Cancer Res. 2011;71(14):5020-9.

493. Recasens M, Almolda B, Perez-Clausell J, Campbell IL, Gonzalez B, Castellano B. Chronic exposure to IL-6 induces a desensitized phenotype of the microglia. J Neuroinflamm. 2021;18(1).

494. Fischer P, Lehmann U, Sobota RM, Schmitz J, Niemand C, Linnemann S, et al. The role of the inhibitors of interleukin-6 signal transduction SHP2 and SOCS3 for desensitization of interleukin-6 signalling. Biochemical Journal. 2004;378:449-60.

495. Chen X, Tian J, Su GH, Lin J. Blocking IL-6/GP130 Signaling Inhibits Cell Viability/Proliferation, Glycolysis, and Colony Forming Activity in Human Pancreatic Cancer Cells. Curr Cancer Drug Targets. 2019;19(5):417-27.

496. Gerhartz C, Dittrich E, Stoyan T, Rosejohn S, Yasukawa K, Heinrich PC, et al. Biosynthesis and Half-Life of the Interleukin-6 Receptor and Its Signal Transducer Gp130. European Journal of Biochemistry. 1994;223(1):265-74.

497. Mullberg J, Schooltink H, Stoyan T, Gunther M, Graeve L, Buse G, et al. The soluble interleukin-6 receptor is generated by shedding. Eur J Immunol. 1993;23(2):473-80.

498. Garbers C, Kuck F, Aparicio-Siegmund S, Konzak K, Kessenbrock M, Sommerfeld A, et al. Cellular senescence or EGFR signaling induces Interleukin 6 (IL-6) receptor expression controlled by mammalian target of rapamycin (mTOR). Cell Cycle. 2013;12(21):3421-32.

499. Garbers C, Janner N, Chalaris A, Moss ML, Floss DM, Meyer D, et al. Species specificity of ADAM10 and ADAM17 proteins in interleukin-6 (IL-6) trans-signaling and novel role of ADAM10 in inducible IL-6 receptor shedding. J Biol Chem. 2011;286(17):14804-11.

500. Kondo H, Ratcliffe CDH, Hooper S, Ellis J, MacRae JI, Hennequart M, et al. Single-cell resolved imaging reveals intra-tumor heterogeneity in glycolysis, transitions

between metabolic states, and their regulatory mechanisms. Cell Rep. 2021;34(7):108750.

501. Zegeye MM, Lindkvist M, Falker K, Kumawat AK, Paramel G, Grenegard M, et al. Activation of the JAK/STAT3 and PI3K/AKT pathways are crucial for IL-6 trans-signaling-mediated pro-inflammatory response in human vascular endothelial cells. Cell Commun Signal. 2018;16.

502. Froeling FEM, Swamynathan MM, Deschenes A, Chio IIC, Brosnan E, Yao MA, et al. Bioactivation of Napabucasin Triggers Reactive Oxygen Species-Mediated Cancer Cell Death. Clin Cancer Res. 2019;25(23):7162-74.

503. Na S, Collin O, Chowdhury F, Tay B, Ouyang M, Wang Y, et al. Rapid signal transduction in living cells is a unique feature of mechanotransduction. Proc Natl Acad Sci U S A. 2008;105(18):6626-31.

504. Kawazoe A, Kuboki Y, Bando H, Fukuoka S, Kojima T, Naito Y, et al. Phase 1 study of napabucasin, a cancer stemness inhibitor, in patients with advanced solid tumors. Cancer Chemoth Pharm. 2020;85(5):855-62.

505. Taniguchi H, Masuishi T, Kawazoe A, Muro K, Kadowaki S, Bando H, et al. Phase I study of napabucasin in combination with FOLFIRI + bevacizumab in Japanese patients with metastatic colorectal cancer. Int J Clin Oncol. 2021;26(11):2017-24.

506. Sonbol MB, Bekaii-Saab T. A clinical trial protocol paper discussing the BRIGHTER study. Future Oncol. 2018;14(10):901-6.

507. Shitara K, Yodo Y, Iino S. A Phase I Study of Napabucasin Plus Paclitaxel for Japanese Patients With Advanced/Recurrent Gastric Cancer. In Vivo. 2019;33(3):933-7.

508. Noda N, Takagaki T, Yodo Y, Horibuchi Y, Iino S, Matsuki S, et al. Effects of a reactive oxygen species generator, napabucasin (BBI608), on tolerability, safety, pharmacokinetics, and QT/QTc interval in healthy volunteers. Pharmacol Res Perspect. 2021;9(5):e00874.

509. Kawazoe A, Kuboki Y, Shinozaki E, Hara H, Nishina T, Komatsu Y, et al. Multicenter Phase I/II Trial of Napabucasin and Pembrolizumab in Patients with Metastatic Colorectal Cancer (EPOC1503/SCOOP Trial). Clin Cancer Res. 2020;26(22):5887-94.

510. Jonker DJ, Nott L, Yoshino T, Gill S, Shapiro J, Ohtsu A, et al. Napabucasin versus placebo in refractory advanced colorectal cancer: a randomised phase 3 trial. Lancet Gastroenterol Hepatol. 2018;3(4):263-70.

511. Dai X, Karol MD, Hitron M, Hard ML, Goulet MT, McLaughlin CF, et al. Napabucasin Drug-Drug Interaction Potential, Safety, Tolerability, and Pharmacokinetics Following Oral Dosing in Healthy Adult Volunteers. Clin Pharmacol Drug Dev. 2021;10(8):824-39.

512. Dai X, Karol MD, Hitron M, Hard ML, Blanchard JE, Eraut N, et al. Mass balance and pharmacokinetics of an oral dose of (14) C-napabucasin in healthy adult male subjects. Pharmacol Res Perspect. 2021;9(1):e00722.

513. Hanafi M, Chen XD, Neamati N. Discovery of a Napabucasin PROTAC as an Effective Degrader of the E3 Ligase ZFP91. J Med Chem. 2021;64(3):1626-48.

514. Li Y, Song Z, Han Q, Zhao H, Pan Z, Lei Z, et al. Targeted inhibition of STAT3 induces immunogenic cell death of hepatocellular carcinoma cells via glycolysis. Mol Oncol. 2022;16(15):2861-80.

515. Vaupel P, Kallinowski F, Okunieff P. Blood-Flow, Oxygen and Nutrient Supply, and Metabolic Microenvironment of Human-Tumors - a Review. Cancer Res. 1989;49(23):6449-65.

516. Ward PS, Thompson CB. Metabolic reprogramming: a cancer hallmark even warburg did not anticipate. Cancer Cell. 2012;21(3):297-308.

517. Gillies RJ, Brown JS, Anderson ARA, Gatenby RA. Eco-evolutionary causes and consequences of temporal changes in intratumoural blood flow. Nat Rev Cancer. 2018;18(9):576-85.

518. Lardner A. The effects of extracellular pH on immune function. J Leukoc Biol. 2001;69(4):522-30.

519. Miret NV, Zarate LV, Erra Diaz F, Leguizamon MA, Pontillo CA, Chiappini FA, et al. Extracellular acidosis stimulates breast cancer cell motility through aryl hydrocarbon receptor and c-src kinase activation. J Cell Biochem. 2022;123(7):1197-206.

520. Gillies RJ, Verduzco D, Gatenby RA. Evolutionary dynamics of carcinogenesis and why targeted therapy does not work. Nat Rev Cancer. 2012;12(7):487-93.

521. Palmer AS, Miller AJ, Davis C, Greene R. Gas tensions in cardiac lymph as a reflection of the interstitial space of the heart. Angiology. 1998;49(9):735-41.

522. Niv Y, Fraser GM. The alkaline tide phenomenon. J Clin Gastroenterol. 2002;35(1):5-8.

523. Girard-Globa A, Bourdel G, Lardeux B. Regulation of protein synthesis and enzyme accumulation in the rat pancreas by amount and timing of dietary protein. J Nutr. 1980;110(7):1380-90.

524. Schaffalitzky de Muckadell OB, Fahrenkrug J, Watt-Boolsen S, Worning H. Pancreatic response and plasma secretin concentration during infusion of low dose secretin in man. Scand J Gastroenterol. 1978;13(3):305-11.

525. Fawcett AN. The relationship between flow and electrolyte secretion in the canine pancreas. Gut. 1970;11(8):700-8.

526. Ashley SW, Schwarz M, Alvarez C, Nguyen TN, Vdovenko A, Reber HA. Pancreatic Interstitial Ph Regulation - Effects of Secretory Stimulation. Surgery. 1994;115(4):503-9.

527. Corbet C, Pinto A, Martherus R, Santiago de Jesus JP, Polet F, Feron O. Acidosis Drives the Reprogramming of Fatty Acid Metabolism in Cancer Cells through Changes in Mitochondrial and Histone Acetylation. Cell Metab. 2016;24(2):311-23.

528. Rauschner M, Lange L, Husing T, Reime S, Nolze A, Maschek M, et al. Impact of the acidic environment on gene expression and functional parameters of tumors in vitro and in vivo. J Exp Clin Canc Res. 2021;40(1).

529. Huber V, Camisaschi C, Berzi A, Ferro S, Lugini L, Triulzi T, et al. Cancer acidity: An ultimate frontier of tumor immune escape and a novel target of immunomodulation. Semin Cancer Biol. 2017;43:74-89.

530. Damgaci S, Ibrahim-Hashim A, Enriquez-Navas PM, Pilon-Thomas S, Guvenis A, Gillies RJ. Hypoxia and acidosis: immune suppressors and therapeutic targets. Immunology. 2018;154(3):354-62.

531. Leroi AM, Koufopanou V, Burt A. Cancer selection. Nat Rev Cancer. 2003;3(3):226-31.

532. Fortunato A, Boddy A, Mallo D, Aktipis A, Maley CC, Pepper JW. Natural Selection in Cancer Biology: From Molecular Snowflakes to Trait Hallmarks. Cold Spring Harb Perspect Med. 2017;7(2).

533. Muller AWJ. Cancer is an adaptation that selects in animals against energy dissipation. Med Hypotheses. 2017;104:104-15.

534. Thomas F, Ujvari B, Renaud F, Vincent M. Cancer adaptations: Atavism, de novo selection, or something in between? Bioessays. 2017;39(8).

535. Voskarides K. Group Selection May Explain Cancer Predisposition and Other Human Traits' Evolution. J Mol Evol. 2018;86(3-4):184-6.

536. Blaszczak W, Swietach P. What do cellular responses to acidity tell us about cancer? Cancer Metastasis Rev. 2021;40(4):1159-76.

537. Damaghi M, Mori H, Byrne S, Xu L, Chen T, Johnson J, et al. Collagen production and niche engineering: A novel strategy for cancer cells to survive acidosis in DCIS and evolve. Evol Appl. 2020;13(10):2689-703.

538. Zhou ZH, Song JW, Li W, Liu X, Cao L, Wan LM, et al. The acid-sensing ion channel, ASIC2, promotes invasion and metastasis of colorectal cancer under acidosis by activating the calcineurin/NFAT1 axis. J Exp Clin Cancer Res. 2017;36(1):130.

539. Hu P, Li S, Tian N, Wu F, Hu Y, Li D, et al. Acidosis enhances the self-renewal and mitochondrial respiration of stem cell-like glioma cells through CYP24A1-mediated reduction of vitamin D. Cell Death Dis. 2019;10(1):25.

540. Kondo A, Yamamoto S, Nakaki R, Shimamura T, Hamakubo T, Sakai J, et al. Extracellular Acidic pH Activates the Sterol Regulatory Element-Binding Protein 2 to Promote Tumor Progression. Cell Rep. 2017;18(9):2228-42.

541. Peppicelli S, Bianchini F, Toti A, Laurenzana A, Fibbi G, Calorini L. Extracellular acidity strengthens mesenchymal stem cells to promote melanoma progression. Cell Cycle. 2015;14(19):3088-100.

542. Hofschroer V, Koch KA, Ludwig FT, Friedl P, Oberleithner H, Stock C, et al. Extracellular protonation modulates cell-cell interaction mechanics and tissue invasion in human melanoma cells. Sci Rep-Uk. 2017;7.

543. Tang X, Lucas JE, Chen JL, LaMonte G, Wu J, Wang MC, et al. Functional interaction between responses to lactic acidosis and hypoxia regulates genomic transcriptional outputs. Cancer Res. 2012;72(2):491-502.

544. John S, Sivakumar KC, Mishra R. Extracellular Proton Concentrations Impacts LN229 Glioblastoma Tumor Cell Fate via Differential Modulation of Surface Lipids. Front Oncol. 2017;7:20.

545. Yao J, Czaplinska D, Ialchina R, Schnipper J, Liu B, Sandelin A, et al. Cancer Cell Acid Adaptation Gene Expression Response Is Correlated to Tumor-Specific Tissue Expression Profiles and Patient Survival. Cancers (Basel). 2020;12(8).

546. Moellering RE, Black KC, Krishnamurty C, Baggett BK, Stafford P, Rain M, et al. Acid treatment of melanoma cells selects for invasive phenotypes. Clin Exp Metastasis. 2008;25(4):411-25.

547. Sutoo S, Maeda T, Suzuki A, Kato Y. Adaptation to chronic acidic extracellular pH elicits a sustained increase in lung cancer cell invasion and metastasis. Clin Exp Metastasis. 2020;37(1):133-44.

548. Zhou ZH, Wang QL, Mao LH, Li XQ, Liu P, Song JW, et al. Chromatin accessibility changes are associated with enhanced growth and liver metastasis capacity of acid-adapted colorectal cancer cells. Cell Cycle. 2019;18(4):511-22.

549. Urbanelli L, Buratta S, Logozzi M, Mitro N, Sagini K, Raimo RD, et al. Lipidomic analysis of cancer cells cultivated at acidic pH reveals phospholipid fatty acids remodelling associated with transcriptional reprogramming. J Enzyme Inhib Med Chem. 2020;35(1):963-73.

550. Logozzi M, Mizzoni D, Angelini DF, Di Raimo R, Falchi M, Battistini L, et al. Microenvironmental pH and Exosome Levels Interplay in Human Cancer Cell Lines of Different Histotypes. Cancers (Basel). 2018;10(10).

551. Brown DA, Melvin JE, Yule DI. Critical role for NHE1 in intracellular pH regulation in pancreatic acinar cells. Am J Physiol-Gastr L. 2003;285(5):G804-G12.

552. Cheng PC, Lin HY, Chen AS, Cheng RC, Su HC, Huang RC. The Na+/H+-Exchanger NHE1 Regulates Extra- and Intracellular pH and Nimodipine-sensitive [Ca2+](i) in the Suprachiasmatic Nucleus. Sci Rep-Uk. 2019;9.

553. Gawenis LR, Ledoussal C, Judd LM, Prasad V, Alper SL, Stuart-Tilley A, et al. Mice with a targeted disruption of the AE2 Cl-/HCO3- exchanger are achlorhydric. J Biol Chem. 2004;279(29):30531-9.

554. Kopito RR, Lee BS, Simmons DM, Lindsey AE, Morgans CW, Schneider K. Regulation of intracellular pH by a neuronal homolog of the erythrocyte anion exchanger. Cell. 1989;59(5):927-37.

555. Yin KF, Lei YJ, Wen X, Lacruz RS, Soleimani M, Kurtz I, et al. SLC26A Gene Family Participate in pH Regulation during Enamel Maturation. Plos One. 2015;10(12).

556. Ren PTL, Lyu YK, Overton J, Xu W, Chiamvimonvat N, Zhang XD. Functional Significance of Slc26a6 in Cardiac PH Regulation Revealed by ex vivo Confocal Imaging. Biophysical Journal. 2020;118(3):130a-1a.

557. Hulikova A, Vaughan-Jones RD, Swietach P. Dual role of CO2/HCO3(-) buffer in the regulation of intracellular pH of three-dimensional tumor growths. J Biol Chem. 2011;286(16):13815-26.

558. McIntyre A, Hulikova A, Ledaki I, Snell C, Singleton D, Steers G, et al. Disrupting Hypoxia-Induced Bicarbonate Transport Acidifies Tumor Cells and Suppresses Tumor Growth. Cancer Res. 2016;76(13):3744-55.

559. Cao YW, Liu Y, Dong Z, Guo L, Kang EH, Wang YH, et al. Monocarboxylate transporters MCT1 and MCT4 are independent prognostic biomarkers for the survival of patients with clear cell renal cell carcinoma and those receiving therapy targeting angiogenesis. Urol Oncol. 2018;36(6):311 e15- e25.

560. Latif A, Chadwick AL, Kitson SJ, Gregson HJ, Sivalingam VN, Bolton J, et al. Monocarboxylate Transporter 1 (MCT1) is an independent prognostic biomarker in endometrial cancer. BMC Clin Pathol. 2017;17:27.

561. Uhlen M, Zhang C, Lee S, Sjostedt E, Fagerberg L, Bidkhori G, et al. A pathology atlas of the human cancer transcriptome. Science. 2017;357(6352):660-71.

562. Eilertsen M, Andersen S, Al-Saad S, Kiselev Y, Donnem T, Stenvold H, et al. Monocarboxylate transporters 1-4 in NSCLC: MCT1 is an independent prognostic marker for survival. PLoS One. 2014;9(9):e105038.

563. Johnson JM, Cotzia P, Fratamico R, Mikkilineni L, Chen J, Colombo D, et al. MCT1 in Invasive Ductal Carcinoma: Monocarboxylate Metabolism and Aggressive Breast Cancer. Front Cell Dev Biol. 2017;5:27.

564. Chiche J, Le Fur Y, Vilmen C, Frassineti F, Daniel L, Halestrap AP, et al. In vivo pH in metabolic-defective Ras-transformed fibroblast tumors: key role of the monocarboxylate transporter, MCT4, for inducing an alkaline intracellular pH. Int J Cancer. 2012;130(7):1511-20.

565. Rolver MG, Holland, L.K.K., Prasad, N.S., Ponniah, M.i, Yao, J., Schnipper, J., Kramer, S., Elingaard-Larsen, L., Pedraz-Cuesta, E., Liu, B., Pardo, L.A., Sandelin A., Maeda, K., Pedersen, S.F. Chronic Acidosis Rewires Cancer Cell Metabolism Through PPARα Signaling. SSRN. 2021.

566. Reshkin SJ, Bellizzi A, Caldeira S, Albarani V, Malanchi I, Poignee M, et al. Na+/H+ exchanger-dependent intracellular alkalinization is an early event in malignant transformation and plays an essential role in the development of subsequent transformation-associated phenotypes. Faseb Journal. 2000;14(14):2185-97.

567. White KA, Grillo-Hill BK, Barber DL. Cancer cell behaviors mediated by dysregulated pH dynamics at a glance. Journal of Cell Science. 2017;130(4):663-9.

568. Griffiths JR, Stevens AN, Iles RA, Gordon RE, Shaw D. 31P-NMR investigation of solid tumours in the living rat. Biosci Rep. 1981;1(4):319-25.

569. Lee S, Axelsen TV, Andersen AP, Vahl P, Pedersen SF, Boedtkjer E. Disrupting Na+, HCO3--cotransporter NBCn1 (Slc4a7) delays murine breast cancer development. Oncogene. 2016;35(16):2112-22.

570. Voss NCS, Kold-Petersen H, Henningsen MB, Homilius C, Boedtkjer E. Upregulated Na+/H+-Exchange Protects Human Colon Cancer Tissue against Intracellular Acidification. Biomed Research International. 2019.

571. Baenke F, Dubuis S, Brault C, Weigelt B, Dankworth B, Griffiths B, et al. Functional screening identifies MCT4 as a key regulator of breast cancer cell metabolism and survival. Journal of Pathology. 2015;237(2):152-65.

572. Chiche J, Le Fur Y, Vilmen C, Frassineti F, Daniel L, Halestrap AP, et al. In vivo pH in metabolic-defective Ras-transformed fibroblast tumors: Key role of the monocarboxylate transporter, MCT4, for inducing an alkaline intracellular pH. International Journal of Cancer. 2012;130(7):1511-20.

573. Gerlinger M, Santos CR, Spencer-Dene B, Martinez P, Endesfelder D, Burrell RA, et al. Genome-wide RNA interference analysis of renal carcinoma survival regulators identifies MCT4 as a Warburg effect metabolic target (vol 227, pg 146, 2012). Journal of Pathology. 2015;236(4):146-56.

574. Grillo-Hill BK, Choi C, Jimenez-Vidal M, Barber DL. Increased H+ Efflux is Sufficient to Induce Dysplasia and Necessary for Viability with Oncogene Expression. Elife. 2015;4.

575. White KA, Ruiz DG, Szpiech ZA, Strauli NB, Hernandez RD, Jacobson MP, et al. Cancer-associated arginine-to-histidine mutations confer a gain in pH sensing to mutant proteins. Sci Signal. 2017;10(495).

576. Liu Y, White KA, Barber DL. Intracellular pH Regulates Cancer and Stem Cell Behaviors: A Protein Dynamics Perspective. Front Oncol. 2020;10:1401.

577. Shiozaki A, Hikami S, Ichikawa D, Kosuga T, Shimizu H, Kudou M, et al. Anion exchanger 2 suppresses cellular movement and has prognostic significance in esophageal squamous cell carcinoma. Oncotarget. 2018;9(40):25993-6006.

578. Wang T, Fei HJ, Yang Y, Jiang XS, Yan M, Zeng Z, et al. Expression of AE1/p16 promoted degradation of AE2 in gastric cancer cells. BMC Cancer. 2016;16:716.

579. Dietl K, Renner K, Dettmer K, Timischl B, Eberhart K, Dorn C, et al. Lactic Acid and Acidification Inhibit TNF Secretion and Glycolysis of Human Monocytes. Journal of Immunology. 2010;184(3):1200-9.

580. Miccoli L, Oudard S, Sureau F, Poirson F, Dutrillaux B, Poupon MF. Intracellular pH governs the subcellular distribution of hexokinase in a glioma cell line. Biochemical Journal. 1996;313:957-62.

581. Peak M, Alhabori M, Agius L. Regulation of Glycogen-Synthesis and Glycolysis by Insulin, Ph and Cell-Volume - Interactions between Swelling and Alkalinization in Mediating the Effects of Insulin. Biochemical Journal. 1992;282:797-805.

582. Park SY, Nam JS. The force awakens: metastatic dormant cancer cells. Exp Mol Med. 2020;52(4):569-81.

583. Peppicelli S, Andreucci E, Ruzzolini J, Laurenzana A, Margheri F, Fibbi G, et al. The acidic microenvironment as a possible niche of dormant tumor cells. Cell Mol Life Sci. 2017;74(15):2761-71.

584. Wu H, Ying M, Hu X. Lactic acidosis switches cancer cells from aerobic glycolysis back to dominant oxidative phosphorylation. Oncotarget. 2016;7(26):40621-9.

585. Damaghi M, Gillies R. Phenotypic changes of acid-adapted cancer cells push them toward aggressiveness in their evolution in the tumor microenvironment. Cell Cycle. 2017;16(19):1739-43.

586. Ying C, Jin CM, Zeng SY, Chao M, Hu X. Alkalization of cellular pH leads to cancer cell death by disrupting autophagy and mitochondrial function. Oncogene. 2022;41(31):3886-97.

587. Sheng J, Sun LB, Zhao SF, Qi WW, Lv J, Zhang ZG, et al. Acidic stress induces protective autophagy in SGC7901 cells. J Int Med Res. 2018;46(8):3285-95.

588. Pellegrini P, Strambi A, Zipoli C, Hagg-Olofsson M, Buoncervello M, Linder S, et al. Acidic extracellular pH neutralizes the autophagy-inhibiting activity of chloroquine: implications for cancer therapies. Autophagy. 2014;10(4):562-71.

589. Chen X, Liu H, Chen K, Guo Y, Mo T, Gao T. Inhibition of autophagy impairs free fatty acid-induced excessive lipid accumulation in hepatocellular carcinoma and hepatic cells. J Biosci. 2022;47.

590. Corbet C, Bastien E, Santiago de Jesus JP, Dierge E, Martherus R, Vander Linden C, et al. TGFbeta2-induced formation of lipid droplets supports acidosis-driven EMT and the metastatic spreading of cancer cells. Nat Commun. 2020;11(1):454.

Appendix

chemosensors

MDPI

Article

Cost-Effective Real-Time Metabolic Profiling of Cancer Cell Lines for Plate-Based Assays

Wiktoria Blaszczak †, Zhengchu Tan † and Pawel Swietach *

Department of Physiology, Anatomy & Genetics, University of Oxford, Oxford OX1 3PT, UK; wiktoria.blaszczak@dpag.ox.ac.uk (W.B.); zhengchu.tan11@imperial.ac.uk (Z.T.)
* Correspondence: pawel.swietach@dpag.ox.ac.uk; Tel.: +44-18-6528-2515
† These authors contributed equally to this work.

Abstract: A fundamental phenotype of cancer cells is their metabolic profile, which is routinely described in terms of glycolytic and respiratory rates. Various devices and protocols have been designed to quantify glycolysis and respiration from the rates of acid production and oxygen utilization, respectively, but many of these approaches have limitations, including concerns about their cost-ineffectiveness, inadequate normalization procedures, or short probing time-frames. As a result, many methods for measuring metabolism are incompatible with cell culture conditions, particularly in the context of high-throughput applications. Here, we present a simple plate-based approach for real-time measurements of acid production and oxygen depletion under typical culture conditions that enable metabolic monitoring for extended periods of time. Using this approach, it is possible to calculate metabolic fluxes and, uniquely, describe the system at steady-state. By controlling the conditions with respect to pH buffering, O_2 diffusion, medium volume, and cell numbers, our workflow can accurately describe the metabolic phenotype of cells in terms of molar fluxes. This direct measure of glycolysis and respiration is conducive for between-runs and even between-laboratory comparisons. To illustrate the utility of this approach, we characterize the phenotype of pancreatic ductal adenocarcinoma cell lines and measure their response to a switch of metabolic substrate and the presence of metabolic inhibitors. In summary, the method can deliver a robust appraisal of metabolism in cell lines, with applications in drug screening and in quantitative studies of metabolic regulation.

Keywords: cell lines; screening; acidity; hypoxia; glycolysis; respiration; flux; buffers; PDAC

check for updates

Citation: Blaszczak, W.; Tan, Z.; Swietach, P. Cost-Effective Real-Time Metabolic Profiling of Cancer Cell Lines for Plate-Based Assays. *Chemosensors* **2021**, *9*, 139. https://doi.org/10.3390/chemosensors9060139

Academic Editor: Pietro Salvo

Received: 18 May 2021
Accepted: 11 June 2021
Published: 13 June 2021

Publisher's Note: MDPI stays neutral with regard to jurisdictional claims in published maps and institutional affiliations.

Copyright: © 2021 by the authors. Licensee MDPI, Basel, Switzerland. This article is an open access article distributed under the terms and conditions of the Creative Commons Attribution (CC BY) license (https://creativecommons.org/licenses/by/4.0/).

1. Introduction

Cell growth and proliferation is ultimately powered by metabolic pathways that harness energy from substrates such as glucose [1,2]. Ever since the discovery that deregulated energetics is a hallmark of cancer [3], metabolic phenotyping has become a pillar of cancer research [3–5]. The two main energy-yielding pathways are glycolysis and respiration, and their rates can be gauged from the production of lactic acid and consumption of oxygen, respectively [6]. In tumors, glycolytic and respiratory fluxes can be very large, which explains their characteristic acidotic and hypoxic signatures [7–9]. Glycolytic and respiratory rates can be probed using dedicated platforms, such as Seahorse XF [10–12], or bespoke plates imprinted with pH and/or O_2 sensors for use with fluorescence or absorbance readers [13–18]. However, acid production and oxygen consumption are rarely measured under culture conditions over extended periods of time and then reported in terms of molar fluxes per cell. The Seahorse XF analyzer, for example, takes a snapshot of metabolic rates within a small but poorly controlled catchment of cells [19]. Data generated in this way are prone to measurement error, and as a result, comparisons between laboratories or even consecutive runs may not be advisable [20]. Measurements of pH or O_2 in bulk media require additional calculations to derive fluxes, but these are not always performed or reported [21,22]. Given that metabolism is a cellular process, it would be

prudent to normalize these flux estimates to the number of cells [23,24]. A concern for many laboratories are the prohibitive costs associated with metabolic profiling, which can make continuous or high-throughput measurements impractical, despite a strong scientific justification [17,25,26]

Here, we describe a simple, fluorescence-based protocol for measuring pH and O_2 simultaneously and in real-time using standard culture plates. We demonstrate how the method can determine acid production (J_{acid}) and oxygen consumption (J_{oxygen}) fluxes per cell as a function of time, including their approach to the steady-state. The method uses commercially available chemical sensors that reduce the cost of fluorescence substances to under 5 cents per plate. We also present a workflow for calculating fluxes from pH and O_2 time courses, and illustrate the utility of our approach in metabolically phenotyping various cancer cell lines using pancreatic ductal adenocarcinoma (PDAC) cells as an example. With the aid of this accessible and simple approach, our intention is to standardize the process of metabolic phenotyping. In doing so, our overarching objective is to improve data quality, exchange, and reproducibility.

2. Materials and Methods

2.1. Plates and Plate Readers

Suitable plates for metabolic phenotyping are those designed for use with fluorescence readers. For illustrative purposes, this study used flat-bottom, black 96-well plates (655090, Greiner, Kremsmünster, Austria) that can be read using a Cytation 5 device (BioTek, Agilent, Winooski, VT, USA) [27]. Excitation was provided by a monochromator, and fluorescence emission was detected sequentially at five wavelengths, which were optimized for the dye combination used. Optimal settings on our system were excitation wavelengths of 400, 416, 450, 460, and 540 nm, and the corresponding emissions were 510, 510, 620, 510, and 580 nm. For improved signal-to-noise ratio, fluorescence can be acquired in time-resolved mode (e.g., delay: 0 µs; acquisition: 500 µs).

2.2. Fluorescent Dyes and Drugs

HPTS (8-Hydroxypyrene-1,3,6-trisulfonic acid trisodium salt) and RuBPY (tris(bipyridine)ruthenium(II) chloride) were purchased from Sigma-Aldrich (H1529 and 224758, St Louis, MO, USA) and dissolved in water at stocks of 4 and 100 mM, respectively. To maintain a consistent molar ratio of HPTS and RuBPY, stocks were mixed accordingly (1:1 v/v) and stored at −20 °C. CellTracker Orange CMRA (CTO) was obtained from Invitrogen (C34551) and kept in DMSO stock (sc-202581, Santa Cruz Biotechnology). Rotenone (R8875, Sigma-Aldrich) was dissolved in DMSO and stored at −20 °C.

2.3. Media

Powdered DMEM medium was obtained from Sigma-Aldrich (D5030). This formulation was chosen because it could be supplemented with buffers, as desired [28]. HEPES (H3375), MES (M3671), glucose (G7021), galactose (G5388), and NaCl (S7653) were obtained from Sigma-Aldrich. Low-buffer medium was prepared by dissolving Phenol Red-Free DMEM 5030 powder in deionized water, then adding 2 mM HEPES, 2 mM MES, 40 mM NaCl, 25 mM glucose, 10% FBS, 1% penicillin–streptomycin mixture, 1% GlutaMAX, and 1% sodium pyruvate. After the ingredients dissolved completely, the medium was tittered to pH 7.4, at 37 °C with 0.4 M NaOH and filtered (0.22 µm pore). High-buffer media were prepared similarly, with the exception that 20 mM HEPES was used instead of 2 mM HEPES plus 2 mM MES, and NaCl was reduced to 25 mM NaCl.

2.4. Cells

Pancreatic ductal adenocarcinoma (PDAC) cell lines AsPC1, MIA-PaCa-2 and PANC1 were a gift from Prof. Anna Trauzold (Christian-Albrecht University, Kiel, Germany), maintained in RPMI (Sigma-Aldrich, R0883) supplemented with 10% FBS, 1% penicillin–streptomycin mixture, 1% GlutaMAX (35050-038, Gibco, Waltham, MA, USA), 1% sodium

pyruvate (11360-039, Gibco, Waltham, MA, USA), and used within passage 3–8 [29,30]. Adult mouse myocytes were isolated from Langendorff-perfused mice hearts using a previously published method [31,32]. Mice were killed humanely by an approved Schedule 1 method following ASPA regulations and University guidelines. Cells were kept in media for up to 20 h after isolation.

3. Results

3.1. Selecting Cost-Effective pH and Oxygen Probes for Assaying Glycolysis and Respiration

The criteria for appropriate pH- and O_2-sensitive dyes for a metabolic assay system are (i) low cost, (ii) non-toxicity to cells, (iii) impermeability to measure extracellular levels, (iv) temporal stability, (v) spectral compatibility, and (vi) ability to produce a calibrated signal. Furthermore, the ensemble spectral properties of the dye-pair must reserve a wavelength range for assessing cell numbers using fluorescent dyes, such as those of the CellTracker family. There are multiple pH-sensitive dyes available, including commonly used cSNARF derivatives [33,34], BCECF [35,36], and HPTS [37–39]. Of the three, HPTS has a superior value for money ($0.05 per μmole). Furthermore, HPTS is a ratiometric dye that can be calibrated, and its spectrum is shifted towards low wavelengths, giving spectral space for red-shifted O_2 sensors [40]. Conveniently, HPTS is membrane impermeable, chemically stable, and produces a very strong signal, which means that concentrations below 10 μM are usually sufficient. There are a number of O_2-sensing dyes, including those that are quenched by molecular oxygen [18,41–43]. A cost-effective dye that emits fluorescence in a range that has no overlap with HPTS is RuBPY.

The spectral characterization of HPTS and RuBPY was performed in a 96-well plate using a fluorescence plate reader. The degree of spectral overlap between HPTS and RuBPY fluorescence was measured in DMEM-based media buffered with 10 mM HEPES and 10 mM MES, and titrated to pH 6.0, 7.0, or 8.0 with 0.4 M NaOH and 0.5 N HCl. Excitation was delivered at wavelengths previously reported as suitable for HPTS in dual excitation mode (400 nm and 460 nm) and RuBPY in a single-excitation model (450 nm). The spectra, shown in Figure 1A, show a clear distinction between the dyes. Moreover, fluorescence emitted by HPTS, but not RuBPY, was pH-sensitive. To confirm that the choices of excitation wavelengths were optimal in the biological context of culture media, excitation spectra were probed at emission peaks of 510 nm for HPTS and 620 nm for RuBPY. The spectrum for HPTS was measured over a range of pH, from 6 to 8 (Figure 1B); the peaks producing maximal pH sensitivity for ratiometry were 400 nm and 460 nm. Excitation spectra intersected at 416 nm, which defines the pH-insensitive wavelength. This so-called isosbestic point is a useful reference point that relates to the concentration of HPTS. Unlike HPTS, RuBPY is not ratiometric, and its single excitation peak was 450 nm (Figure 1C). The lack of an oxygen-insensitive reference wavelength makes it difficult to calibrate RuBPY fluorescence into units of dissolved O_2. However, as the HPTS:RuBPY concentration ratio can be fixed by careful and consistent mixing, the HPTS isosbestic point could serve as a convenient reference point to O_2-sensitive RuBPY fluorescence. This is particularly useful for offsetting the effects of changes in volumes, such as evaporation, where both isosbestic HPTS and RuBPY would be affected equally.

In order to use the dyes in combination, it is first necessary to determine the concentrations that produce comparable peaks for best resolving power. HPTS and RuBPY were mixed in various molar ratios, and the emission spectra above 480 nm were recorded with 450 nm excitation—a wavelength that is sufficiently close to the excitation peaks of both dyes. A suitable combination of HPTS and RuBPY that produced a bimodal spectrum was determined empirically to be 2 μM and 50 μM, respectively. At this molar ratio, the spectral distinction between the dyes was >100 nm, and the optimal emission peaks for the pH- and O_2-sensitive channels were 510 nm and 620 nm, respectively (Figure 1D).

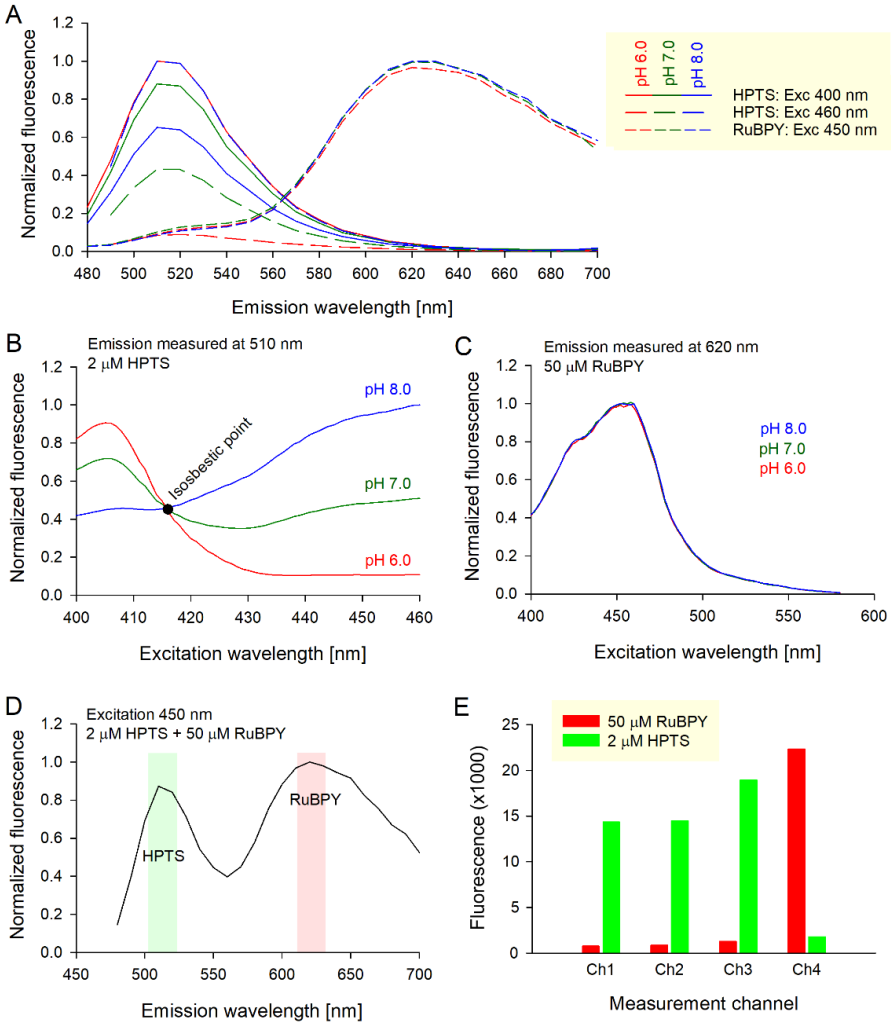


Figure 1. Spectral analyses of HPTS and RuBPY. (**A**) Emission spectra for HPTS and RuBPY measured separately in DMEM-based media buffered with 10 mM HEPES/10 mM MES and titrated to either pH 6.0, 7.0, or 8.0. (**B**) The excitation spectrum for HPTS fluorescence collected at its optimal emission (510 nm). Isosbestic point is the wavelength at which fluorescence is pH-insensitive. (**C**) The excitation spectrum for RuBPY fluorescence collected at its optimal emission (620 nm). Note the pH insensitivity. (**D**) Concentrations of HTPS (2 μM) and RuBPY (50 μM) determined empirically in DMEM-based media to produce comparable emission peaks when excited at 450 nm. (**E**) Test for fluorescence bleed-through between recording channels. Media contained either HTPS (2 μM) or RuBPY (50 μM) at pH 7.3, and measurement protocols were performed to obtain signals across all four channels sequentially (Ch1–Ch4). Ch1–Ch3 are nominally HPTS channels and found to detect a predominantly HPTS-emitted signal. Ch4 is nominally a RuBPY channel and detects a predominantly RuBPY-emitted signal.

Based on the optimization experiments performed, the most suitable measurements settings were determined to be:

- Ch1: Excitation 400 nm/emission 510 nm, optimized for HPTS fluorescence at low pH;
- Ch2: Excitation 460 nm/emission 510 nm, optimized for HPTS fluorescence at high pH;
- Ch3: Excitation 416 nm/emission 510 nm, optimized for pH-insensitive HPTS fluorescence as an O_2-insensitive reference to O_2-sensitive RuBPY;
- Ch4: Excitation 450 nm/emission 620 nm, optimized for RuBPY fluorescence, which is quenched by oxygen, i.e., inversely related to oxygen tension.

Ratios Ch2/Ch1 and Ch3/Ch4 increase with a rise in pH and oxygen, respectively. In order for these ratios to provide a truly selective measure of pH and O_2, the fluorescence

emitted by one dye cannot bleed-through to another's wavelength range. To test for bleed-through at the optimized settings, measurements were performed in wells that contained one dye only, and recordings on all four fluorescence channels are presented in Figure 1E. These data show that RuBPY-emitted fluorescence detected at the three, nominally HPTS channels (Ch1-3) is small (<5%) compared to the fluorescence emitted from HPTS-containing wells. This indicates minimal bleed-through and does not warrant a correction. Similarly, HTPS-emitted fluorescence detected at the RuBPY channel (Ch4) was <7% of the signal measured in RuBPY-containing wells. Again, there was no requirement to implement any correction factor for this minimal bleed-through.

3.2. Calibration of Signals to Units of pH and Oxygen Tension

Having optimized the wavelengths for detecting a pH-sensitive ratio (R_{pH} = Ch2/Ch1) and an O_2-sensitive ratio (R_{O2} = Ch3/Ch4), calibration curves were obtained by carefully titrating culture media pH to a value over the range 5–8 and altering O_2 tension. Media were buffered with 10 mM HEPES and 10 mM MES, but no bicarbonate because calibrations were performed in the absence of CO_2. The calibration curves were measured in atmospheric O_2 (21%) and then in hypoxia (<1% O_2). In order to maintain oxygen tension during the measurement period, wells were covered with 150 µL of mineral oil, which serves as a diffusion barrier to minimize oxygen ingress during the brief recording period. The calibration curves are presented in Figure 2.

Table 1. Best fit to calibration curves in Equations (1) and (2).

Calibration Variable	Best-Fit
pK_a	7.5383
r_{max}	3.9503
r_{min}	0.0603
r_{anoxia}	0.6945

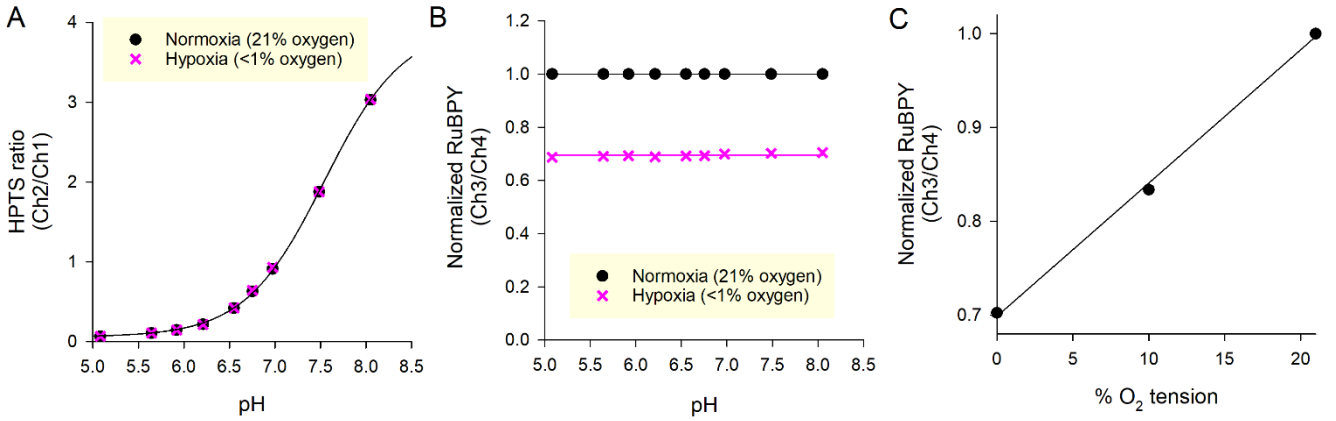


Figure 2. (**A**) The calibration curve for the HPTS ratio (Ch2/Ch1) in normoxic and hypoxic conditions. Best-fit to Equation (1) with constants listed in Table 1. (**B**) Hypoxia-sensitive ratio of isosbestic HPTS to RuBPY (as Ch3/Ch4). Hypoxia (<1% O_2) reduces the Ch3/Ch4 ratio but is pH-insensitive. (**C**) Three-point calibration for 0.1%, 10%, and 21% O_2.

HPTS provides a highly pH-sensitive ratio across the physiological range. The calibration curves in normoxia and hypoxia were superimposable, indicating that HPTS is insensitive to oxygen and reports a pH-selective signal (Figure 2A). The best-fit equation is the Grinkiewicz type:

$$pH = pK_a - \log_{10} \frac{r_{max} - R_{pH}}{R_{pH} - r_{min}} \quad (1)$$

RuBPY fluorescence was pH-insensitive but responded to hypoxia, which is consistent with the quenching effect of oxygen (Figure 2B). The ratio of isosbestic HPTS to RuBPY flu-

orescence was deemed adequately O_2-sensitive, and its calibration curve can be described using a modification of the Stern-Volmer equation (Figure 2C):

$$O_2 = 21 \times \left(1 - \frac{1 - R_{O2}/R_{normoxia}}{1 - r_{anoxia}}\right) \quad (2)$$

The value for $R_{normoxia}$ at 21% O_2, i.e., atmospheric, can be obtained in cell-free wells measured in parallel to wells that include cells. In contrast, r_{anoxia} must be obtained in separate experimental reads by placing plates in an O_2-free environment. In our system, the best-fit values are listed in Table 1. It is important that calibrations are determined for each laboratory individually to account for differences in equipment.

3.3. Converting pH and Oxygen Time Courses into Fluxes

The convertion of pH or O_2 time courses to molar fluxes must consider chemical buffering and whether the system being studied is open (i.e., can exchange freely with the atmosphere) or closed.

3.3.1. Buffering

Fluorescent dyes such as HPTS and RuBPY probe the level of free ligands, i.e., H^+ ions and O_2, respectively. It is, however, common for chemical systems to manifest buffering: pH buffering takes the form of H^+-binding weak acid/base pairs, whereas O_2 buffering can involve chelators such as hemoglobin. Fluxes of H^+ or O_2 caused by glycolysis and respiration should refer to the total concentration rather than the free pool. Thus, flux is best described as the product of buffering capacity and rate of change. Buffering can be quantified in terms of a buffer ratio (B), such as the number of molecules bound to buffer per free molecule. In most culture media, O_2 buffering is close to zero, and therefore the rate of change of measured O_2 gives an adequate estimate of flux. This can be used to describe oxygen flux (J_{O2}):

$$J_{O2} = \frac{d[O_2]^{total}}{dt} = \frac{d[O_2]^{free}}{dt} \times (1 + B) \approx \frac{d[O_2]^{free}}{dt} \quad (3)$$

H^+ ions, in contrast, can be heavily buffered; indeed, that is the rationale of including buffers such as HEPES in media formulations. By convention, pH buffering is described in terms of a buffering capacity (β) that may vary in a pH-dependent manner. Whilst it is appropriate to express acid flux in terms of H^+ ions, free H^+ ions are, by convention, reported as pH. Thus, the corresponding definition of buffering capacity is the concentration of acid added, divided by the pH change. Therefore, the acid flux (J_{H+}) is defined as follows:

$$J_{H+} = \frac{d[H^+]^{total}}{dt} = -\frac{dpH}{dt} \times \beta \quad (4)$$

Medium buffering capacity can be measured by adding known amounts of HCl or NaOH and measuring the resulting pH change. Figure 3A shows an exemplar recording of pH after sequential additions of 0.5 mM HCl to media from an alkaline starting pH and 0.5 mM NaOH to media from an acidic starting pH. For this experiment, media contained 2 mM HEPES and 2 mM MES to provide a low level of buffering. The calculated buffering capacity is plotted in Figure 3B.

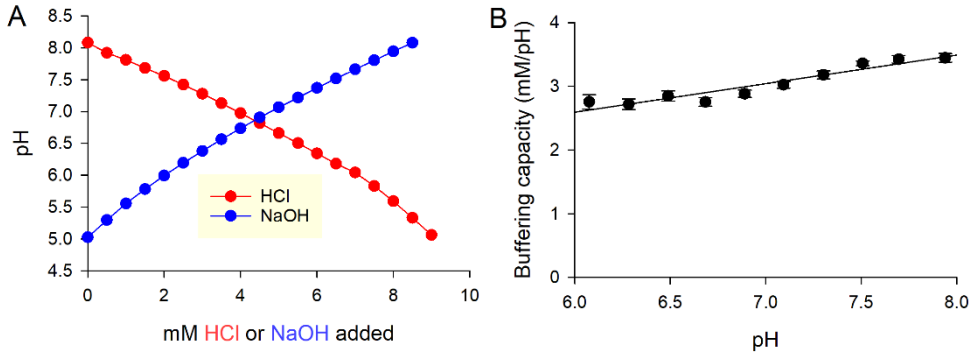


Figure 3. Measuring the pH buffering capacity. (**A**) Stepwise addition of 0.5 mM HCl or NaOH to media of undetermined buffering capacity. The inverse of the slope gives average buffering capacity for the entire pH range. (**B**) Buffering capacity expressed as the ratio of HCl (or NaOH) added to pH change, plotted against the midpoint of the pH change. The best fit line accounts for pH-sensitivity of buffering capacity. This function should be used whenever converting between pH changes and H^+ fluxes.

3.3.2. Open and Closed Systems

In a closed system, a change in O_2 or pH can be attributed to an internal process, such as respiration and glycolysis. Lactic acid is an example of a non-volatile acid, and media with glycolytic cells can be considered a closed system with respect to pH. Oxygen, in contrast, is gaseous, and any system that consumes (or produces) O_2 should be considered an open system in dynamic equilibrium with its immediate atmosphere. The exchange of O_2 between the well and its atmosphere introduces an additional flux that can be described by a permeability constant (P_{O2}) and gradient:

$$J_{O2}{}^{\text{exchange}} = P_{O2} \times ([O_2]_{\text{atm}} - [O_2]_{\text{well}}) \quad (5)$$

Thus, O_2 dynamics in a well that (i) contains respiring cells and (ii) is open to the atmosphere should be described as follows:

$$J_{O2}{}^{measured} = J_{O2}{}^{respiration} + J_{O2}{}^{exchange} \quad (6)$$

Using Equation (6), it is possible to calculate the respiratory flux from O_2 measurements once passive O_2 exchange is factored in. In order to calculate the latter, an a priori estimate of permeability is required. This will depend on various parameters, among which is oxygen diffusivity in media and the height of the column of a medium. A column of medium can support relatively fast gas diffusion, which risks that any change in medium O_2 would be difficult to resolve. To impose a controlled restriction on gas diffusion, media in wells were covered with a layer of mineral oil (Sigma-Aldrich, M5904, St Louis, MO, USA). The ensemble permeability P_{O2} across media and oil can be estimated in cell-free wells that had been pre-equilibrated in hypoxia (e.g., 0.1% O_2). Returning plates to the normal atmosphere of the plate reader drives O_2 ingress, which was reported using RuBPY (Figure 4A). The time course of re-oxygenation gives a measure of time constant, inversely related to P_{O2} (Figure 4B). This experiment was performed for a range of oil volumes to vary the diffusive restriction (Figure 4C). These data provide an estimate of the time constant of O_2 diffusion in the media and the effect that oil has on restricting gas diffusion. For 150 µL of mineral oil, P_{O2} is 0.029 min^{-1}. Applying this to Equation (6) enables real-time measurements of respiratory fluxes.

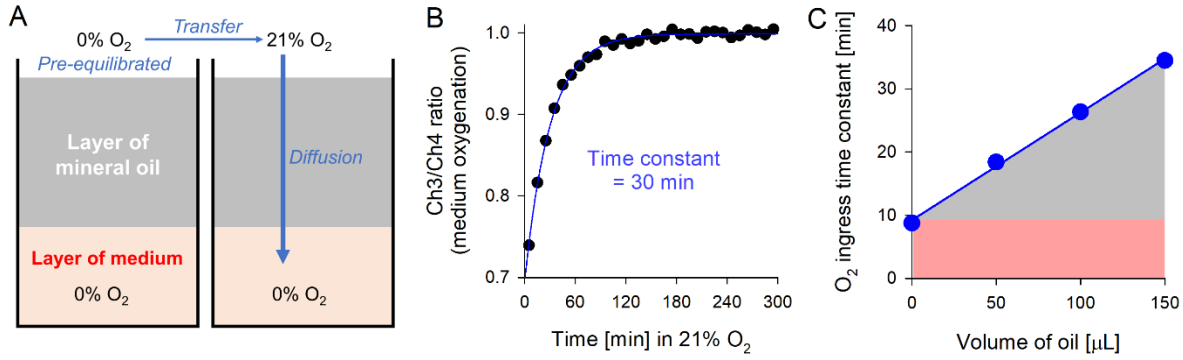


Figure 4. Characterizing the open system with respect to O_2 dynamics. (**A**) The protocol for measuring O_2 permeability across a layer of medium (typically 100 µL) and oil (varied between 0 and 150 µL). (**B**) Exemplar time course from well covered with 150 µL oil. Transferring a plate to an atmosphere of normal oxygen in the reader triggers re-oxygenation, which was monitored every 10 min. The best fit gives a time constant, which is inversely related to O_2 permeability. (**C**) Relationship between the time constant of O_2 ingress and the volume of oil added to wells. Red shading denotes time constant attributable to medium, and gray denotes that due to diffusion through oil.

3.4. Implementation of Assay to Metabolically Phenotype Cancer Cells

Proof-of-principle studies of glycolytic and respiratory fluxes were performed on pancreatic adenocarcinoma cell lines (AsPC1, MIA-PaCa-2, PANC1). Reported fluxes will depend on the density of cells; therefore, it was necessary to obtain a measure of cell count for normalization purposes.

3.4.1. Normalizing for Cell Number

The number of cells in a well can be estimated using fluorescent dyes loaded to cells; a higher signal would indicate higher density. The appropriate dye is required to be stable, membrane impermeant once loaded, spectrally non-overlapping with HTPS and RuBPY, as well as pH- and O_2-insensitive. Suitable candidates for cell counting are CellTracker dyes, and the optimal choice considering the spectral constraints is CellTracker Orange (CTO). The CTO emission spectrum is shown in Figure 5A. CTO fluorescence is resolvable from HPTS and RuBPY, as it is excited at a considerably higher wavelength (540 nm vs. <460 nm) (Figure 5B). As determined using serially-diluted human red blood cells, the CTO signal is linearly related to cell number (Figure 5C). A similar calibration curve can be obtained for adherent cells grown at the bottom of wells, as is shown for MIA-PaCa-2 and AsPC1 (Figure 5D). Note that the fluorescence per PDAC cell (0.455 F.U.) is higher than per red blood cell (0.19 F.U.) because the latter is smaller in size and contains hemoglobin, which absorbs some fluorescence.

The degree to which CTO is pH- and O_2-sensitive was determined experimentally by loading MIA PaCa-2 cells with the dye at 12.5 µM for 15 min, followed by superfusion maneuvers that change pH or O_2 levels. Cells were plated in LabTek slides that are suitable for superfusion. Superfusates contained 125 mM NaCl, 4.5 mM KCl, 11 mM glucose, 1 mM $CaCl_2$, 1 mM $MgCl_2$, and 20 mM HEPES, titrated to either pH 6.4 or 7.4. To make anoxic superfusates, solutions were bubbled in 100% N_2, and anoxia was stabilized chemically by the addition of 1 mM sodium dithionite, an oxygen scavenger. Superfusates were delivered to cells by a peristaltic pump and heated to 37 °C. Images were taken on a Leica confocal microscope using settings optimized previously for CTO. Fluorescence was first imaged under baseline conditions (normoxia of 21% O_2 and pH 7.4), and then after a change in pH to 6.4 (Figure 5E), allowing 10 min for equilibration, or change in O_2 tension to anoxic levels (Figure 5F), allowing 2 min for equilibration. Finally, superfusion was returned to baseline conditions. No effect of hypoxia or acidity was observed, indicating that CTO provides a stable fluorescence signal.

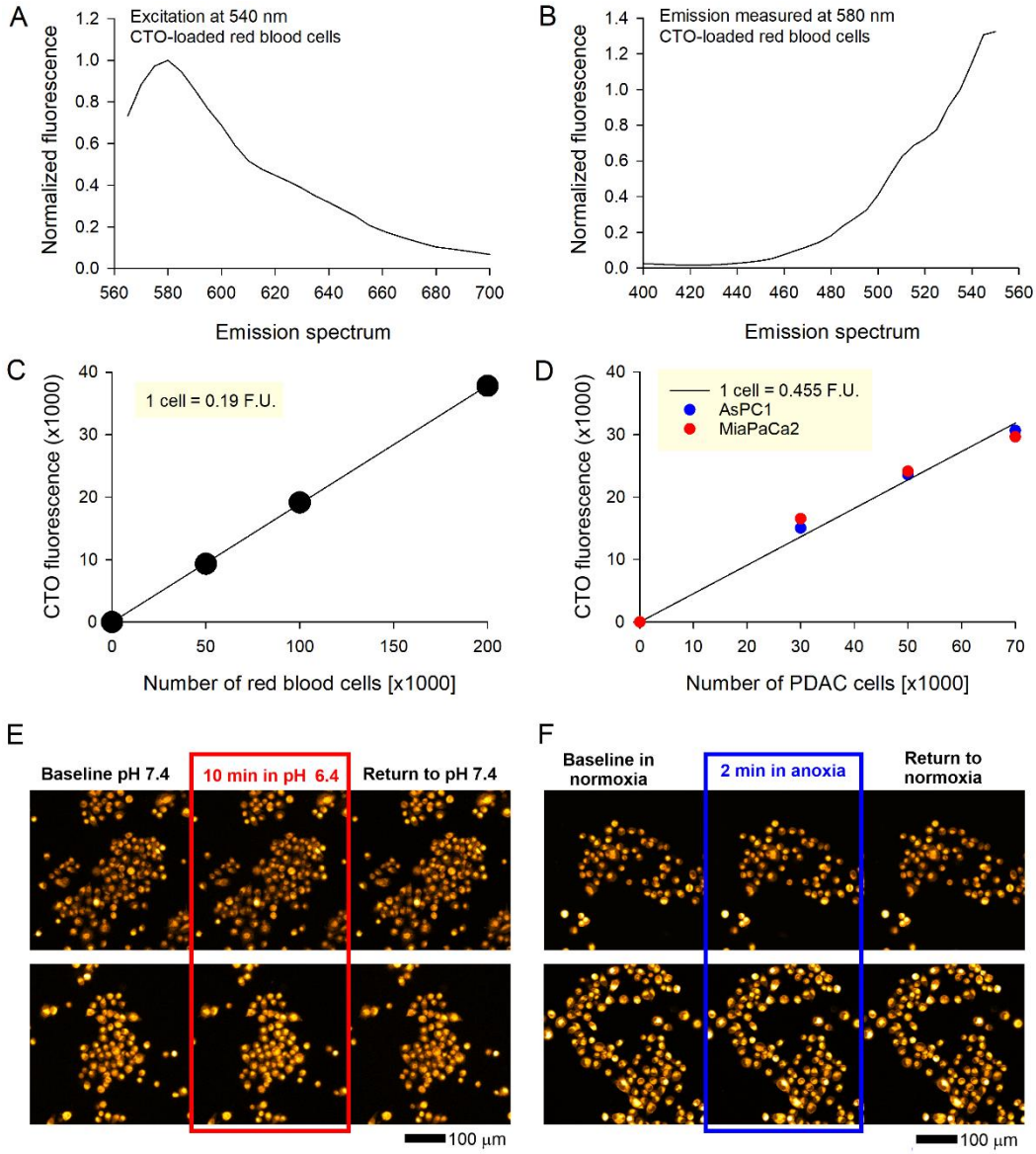


Figure 5. Using CellTracker Orange (CTO) to normalize for cell number. (**A**) The emission spectrum of CTO, excited at 540 nm. (**B**) The optimal CTO excitation is 540 nm, which ensures that the signal is resolvable from HPTS and RuBPY. (**C**) The correlation between CTO fluorescence and count of human red blood cells. (**D**) The correlating CTO signal with the number of plated AsPC1 and MIA-PaCa2 cells in wells of a 96-well plate. (**E**) Superfused MIA-PaCa2 cells imaged confocally. Fluorescence images taken during superfusion at pH 7.4 (baseline; 20 mM HEPES-buffered solution), after 10 min of superfusion at pH 6.4, and 10 min after returning to normal pH. Two exemplar experiments are shown. (**F**) Fluorescence images taken during superfusion in normoxic solution (baseline), after 2 min of superfusion in anoxic conditions (superfusate contained 1 mM dithionite, 100% N_2), and 2 min after returning to normoxia. Two exemplar experiments shown.

3.4.2. Real-Time Monitoring of Metabolic Fluxes

To monitor glycolytic and respiratory fluxes in real-time, AsPC1, MIA-PaCa2, and PANC1 cells were plated in 96-well plates at various cell densities (30k, 50k 70k) and left to adhere overnight. Next, the cells were loaded with 25 µM CTO for 15 min, after which media were replaced with 100 µL of a low-buffer formulation containing 2 µM HPTS and 50 µM RuBPY. Wells were immediately covered with a layer of mineral oil (150 µL), and the plate was inserted into a reader for recordings at regular intervals (e.g., 10 min). Some wells had no cells in order to measure background changes to pH during incubation and for obtaining reference values for normoxia ($R_{normoxia}$). Figure 6A shows a time course of

pH and O_2 for various densities of cells (30, 50, and 70k per well), including cell-free wells. This information was used to calculate cumulative acid production (C_{H+}) and oxygen consumption (C_{O2}), where V is the volume of the well:

$$C_{H+} = V \times \left(\sum_{t=0}^{T} J_{H+}{}^{cell} - \sum_{t=0}^{T} J_{H+}{}^{cell-free} \right) = V \times \left(- \sum_{t=0}^{T} \left(\frac{dpH}{dt}^{cell} \times \beta \right) + \sum_{t=0}^{T} \left(\frac{dpH}{dt}^{cell-free} \times \beta \right) \right) \quad (7)$$

$$C_{O2} = V \times \sum_{t=0}^{T} \left(J_{O2}{}^{cell} - P_{O2} \times \left([O_2]_{atm} - [O_2]_{well}^{cell} \right) \right) = V \times \sum_{t=0}^{T} \left(\frac{d[O_2]}{dt}^{cell} - P_{O2} \times \left([O_2]_{atm} - [O_2]_{well}^{cell} \right) \right) \quad (8)$$

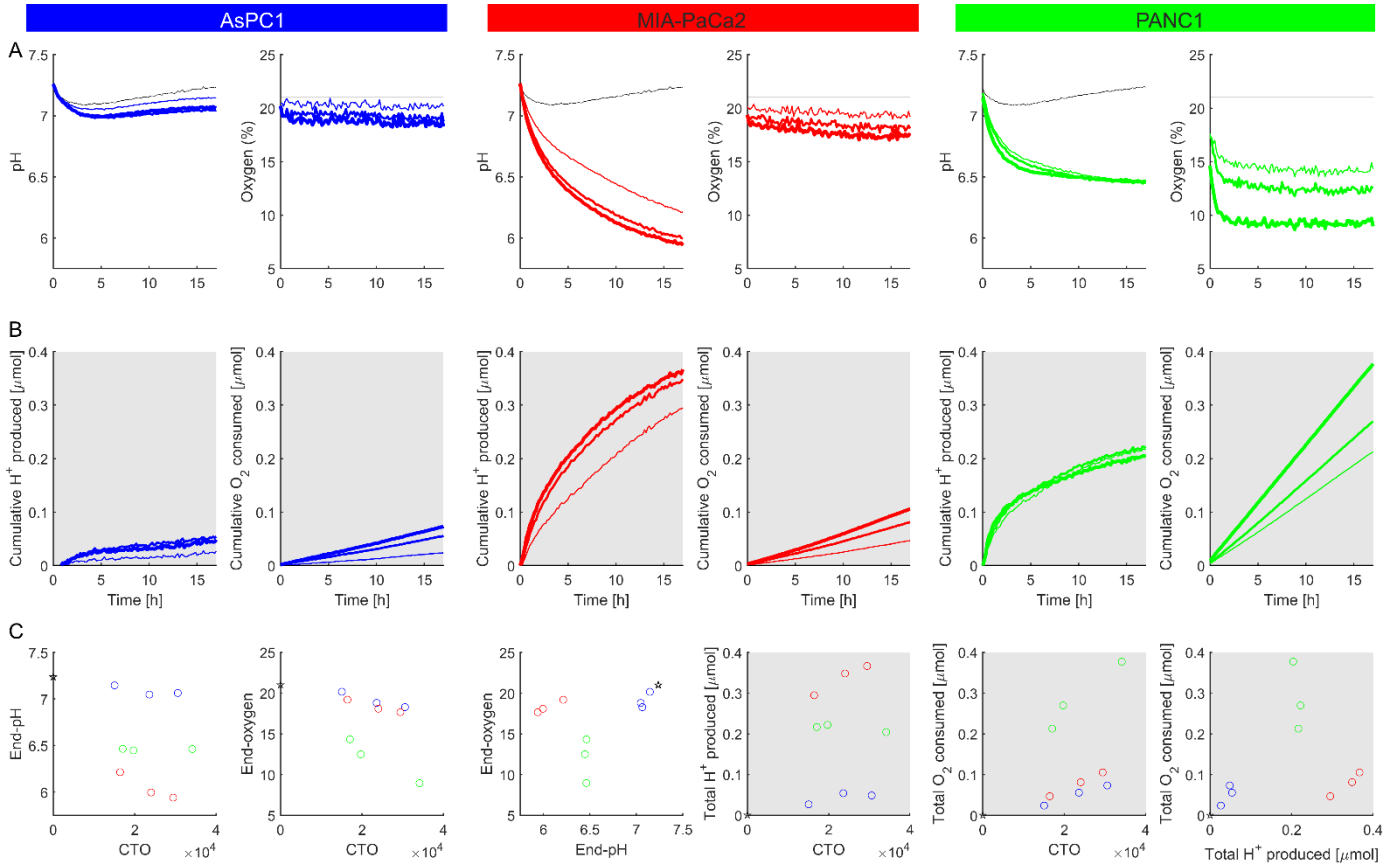


Figure 6. Metabolic profiling of PDAC cell lines. (**A**) Time courses of pH and O_2 for AsPC1 (blue), MIA-PaCa2 (red), and PANC1 (green) plated at 30, 50, or 70k cells per well. Thicker lines denote higher cell density. Blank time courses were obtained from cell-free wells. Media were prepared using DMEM 5030 and contained 2 mM HEPES and 2 mM MES, 25 mM glucose, supplemented with 10% FBS, 1% penicillin–streptomycin mixture. (**B**) Cumulative H^+ production and O_2 consumption, calculated using Equations (7) and (8). (**C**) Data from a and b replotted as a function of cell number, measured by CTO fluorescence. Plots with white background relate to end-point pH and O_2, and plots with gray background relate to cumulative H^+ production and O_2 consumption. The black star symbol denotes data from cell-free wells. Plots represent a mean of 3 biological repeats.

The time courses of C_{H+} and C_{O2} are shown in Figure 6B. The three PDAC cells presented strikingly different phenotypes: AsPC1 had low glycolytic and respiratory rates; MIA-PaCa2 had elevated glycolysis, whereas PANC1 had raised glycolysis and a very high respiratory rate. The relationship between cell number and end-point O_2 and pH, and cumulative O_2 consumption and H^+ production are shown in Figure 6C. The approach can therefore monitor glycolysis and respiration in real-time, investigate their interplay and the effect of cell density, delivering information that has hitherto been largely inaccessible to many researchers.

3.4.3. Measuring Metabolic Responses

The imaging system can be used to study the effect of changing respiratory substrate on glycolytic and respiratory fluxes. MIA-PaCa-2 and PANC1 cells were seeded at 70k per well and left to adhere overnight. Standard medium was then replaced with 100 µL of a high-buffering formulation that contained either 25 mM glucose or 25 mM galactose as a primary substrate, plus fluorescent dyes (2 µM HPTS and 50 µM RuBP). After covering each well with 150 µL of mineral oil, the plate was immediately transferred into the plate-reader for measurements. Consistent with the literature, galactose is less effective as a glycolytic substrate, which re-routes energetic flows towards respiration, as shown by the increase in O_2 consumption (Figure 7A).

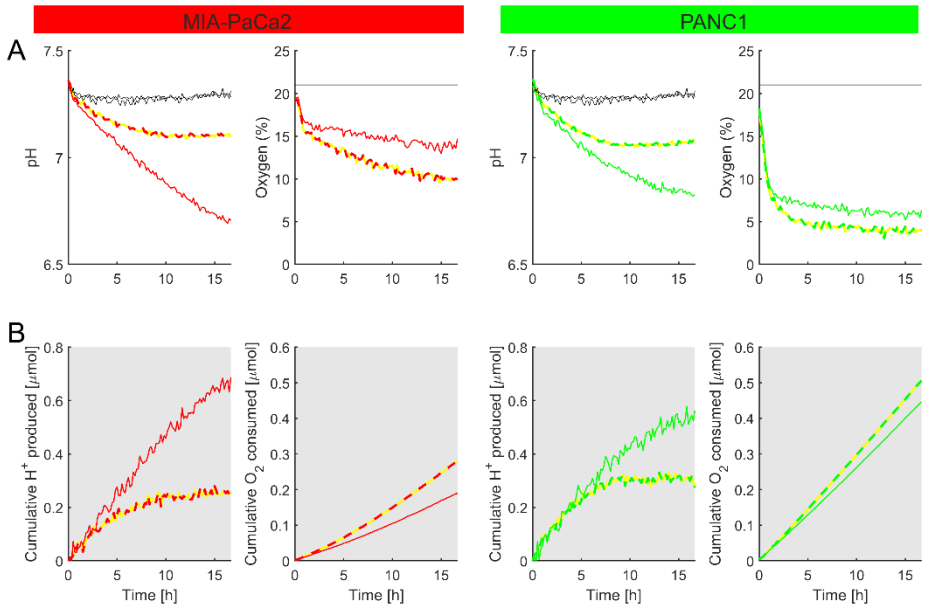


Figure 7. Using the method to study the response to a change in metabolic substrate. (**A**) Time courses of pH and O_2 measured for MIA-PaCa2 (red) and PANC1 (green) plated at 70k cells per well. Thick dashed lines denote media containing galactose (25 mM) in place of glucose. Media contained 20 mM HEPES, 25 mM glucose or galactose, 25 mM NaCl and was supplemented with 10% FBS, 1% penicillin–streptomycin mixture, 1% GlutaMAX, and 1% sodium pyruvate. (**B**) The cumulative H^+ production and O_2 consumption, calculated using Equations (7) and (8). Plots represent a mean of 3 biological repeats.

The method can also study responses to inhibitors, such as the effect of blocking mitochondrial respiration with electron transport chain inhibitors (e.g., rotenone) [44]. To measure the metabolic responses to mitochondrial inhibition in real-time, MIA-PaCa2 and PANC1 cells were plated at 70k per well and left to attach overnight. Next, the medium was replaced with 100 µL of the low-buffering formulation containing 2 µM HPTS and 50 µM RuBP, with or without 10 µM rotenone. Then, 150 µL of mineral oil was added to each well, and the plate was transferred into the plate-reader for measurements (Figure 8). As expected, pharmacological inhibition of the electron transport chain resulted in a shift from O_2 consumption towards a higher level of glycolysis, which verifies the assay's ability to report responses to metabolic inhibition.

3.5. Proof-of-Principle Measurements on Non-Adherent Cells

This plate-based assay can also measure O_2 and pH in suspensions of cells, such as non-adherent primary cells. As proof-of-principle, ventricular myocytes, freshly isolated from a mouse heart, were re-suspended in low-buffer media and aliquoted into wells of a plate for measurements according to the methods described for cancer cells. Myocytes have a high respiratory rate, as shown by the extent to which O_2 is depleted. A smaller

but significant rate of glycolysis was observed (Figure 9). Thus, the system can be used to characterize the metabolism of non-cancer cells, including primary non-adherent cells.

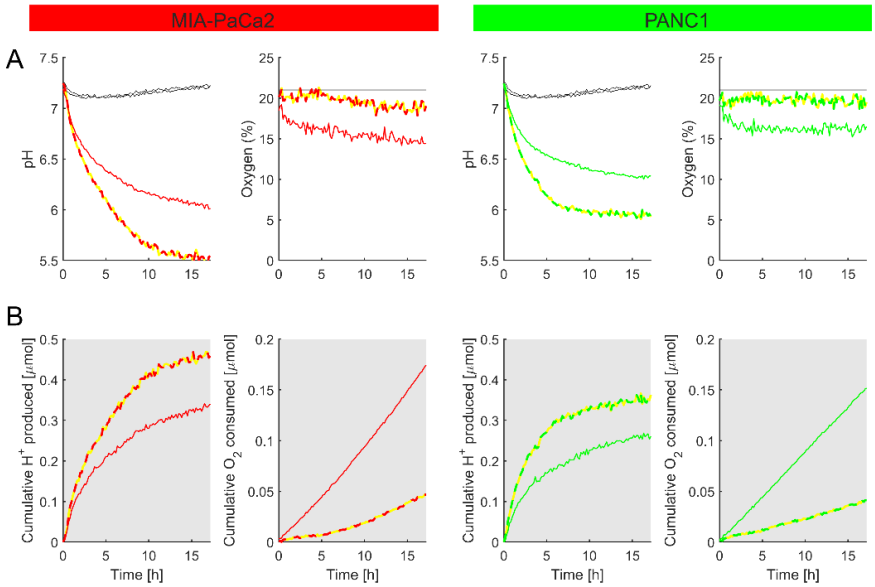


Figure 8. Using the method to study the effect of metabolic inhibitors. (**A**) Time courses of pH and O_2 for MIA-PaCa2 (red) and PANC1 (green) plated at 70k cells per well. The metabolic substrate was glucose throughout. Media contained 2 mM HEPES and 2 mM MES, 25 mM glucose, supplemented with 10% FBS, 1% penicillin–streptomycin mixture, 1% GlutaMAX, and 1% sodium pyruvate. Thick dashed lines indicate the effect of 10 μM rotenone. (**B**) The cumulative H^+ production and O_2 consumption, calculated using Equations (7) and (8). Plots represent a mean of 3 biological repeats.

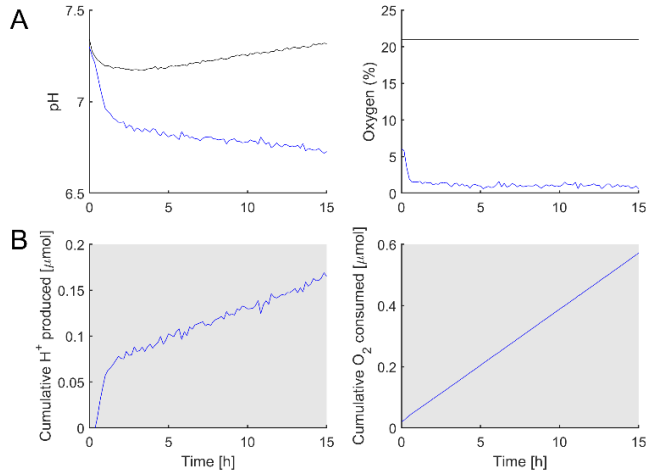


Figure 9. Using the method to study metabolism in primary myocytes freshly isolated from the mouse ventricle. (**A**) Time courses of pH and O_2. A suspension of myocytes in media was probed for O_2 and pH over a period of 15 h, shortly after enzymic isolation from a mouse heart. Media contained 2 mM HEPES and 2 mM MES, 25 mM glucose, supplemented with 10% FBS, 1% penicillin–streptomycin mixture, 1% GlutaMAX, and 1% sodium pyruvate. (**B**) The cumulative H^+ production and O_2 consumption, calculated using Equations (7) and (8). Myocytes have a high oxidative metabolism, causing the rapid depletion of O_2. Some degree of glycolytic metabolism was also noted. Mean of 3 technical repeats.

4. Discussion

This article presents a complete workflow for assaying the metabolic fluxes in cells. Most experiments were performed on cultured cancer cell lines, but the system can also be used to measure metabolic rate in primary non-adherent cells, as illustrated using ventricular myocytes. The key advantages of our method relate to its (i) low running costs and (ii) delivery of direct measurements of molar fluxes of H^+ and O_2 in real-time and under culture conditions over an extended period of time.

The protocol can be readily implemented using a suitable fluorescence plate reader, which is standard equipment in many laboratories. The running costs are very low thanks to the choice of sensors optimized for the assay. RuBPY is available for the list price of £33 for 250 mg, and the cost per plate, assuming a working concentration of 50 μM across 96 wells, is £0.05. HPTS is available at a list price of £70 for 1 g, and the equivalent cost per plate is £0.0068. Greiner plates are available at £5 per unit, which means an assay can be performed for £5.05 per plate. The cost will increase if normalization using CTO is required for specific experiments.

The protocol's workflow includes a step-by-step guide to calculating glycolytic and respiratory fluxes and normalizing these to the cell number. These calculations consider buffering for H^+ ions as well as O_2 ingress in the open system of plate wells. Molar H^+ and O_2 fluxes are the most direct readouts of the state of metabolism and we recommend that they are adopted as the reporting standard to facilitate data sharing, exchange, and comparison between studies. Fluxes normalized to cell number are less prone to measurement error than raw measurements such as pH or O_2. In principle, these values can be compared between runs and even between laboratories, as they are characteristic of cell lines under a given state and not subject to errors that arise from the lack of adequate normalization or flawed calculations.

The ability to follow metabolism in real-time and for extended periods (e.g., many hours) is a major advantage as it allows time for cells to implement more complete biological responses, e.g., to inhibitors or substrates. Critically, cells can be maintained in appropriate cell culture media as required, provided that these are characterized with respect to pH buffering and O_2 diffusivity. Importantly, longer-term follow-up can include the attainment of steady-state between pH, O_2, and metabolism, which is rarely reported in metabolic studies in vitro. Such a steady-state represents the balance of fluxes and may relate accurately to the in vivo scenario. Understanding the steady-state can explain the genesis of particular levels of pH and O_2 tension in tissues.

The ability to perform metabolic assays cheaply and on a large scale opens opportunities for high-throughput studies. Combining this with molar flux measurements and integrating the data over longer time periods can supply high-quality data for mechanistic studies on cancer and other disciplines of life science.

5. Appendix: Step-by-Step Protocol

(1) Dissolve HPTS and RuBPY in sterile, deionized water to obtain stocks of 4 and 100 mM, respectively. Mix both dyes in a 1:1 ratio, divide them into aliquots, and store them at −20 °C. Avoid multiple thaw-freeze cycles.

(2) Seed cells onto a black, fluorescence-compatible, flat-bottom 96-well plate at the desired density and leave to attach overnight. Higher densities will produce larger and more resolvable fluxes. When planning the plate, ensure that some wells are cell-free (blanks) to serve as reference points for pH and O_2. Recommendation: Add PBS to the outermost wells to help maintain humidity and prevent evaporation in the remainder of the plate.

(3) Thaw and vortex the dye mixture. Dissolve (1:1000 *v/v*) in Phenol Red-free medium of choice. Allow aliquots of 100 μL per well.

(4) Replace media that had bathed cells during the settling period with the dye-containing medium of the desired composition (e.g., pH, buffering, inhibitors etc). Whilst tilting the plate slightly, gently add 150 μL of mineral oil to each well to cover the medium

and introduce a controlled diffusion barrier to gas exchange. Volumes of medium and mineral oil should be optimized for the given oxygen consumption and acid production rate.

(5) Place the plate into the plate-reader, keeping the lid on. Start collecting the data immediately to capture the initial state.

(6) Perform calculations according to the equations described herein. Note: Media prepared for the assay must be characterized in separate experiments in terms of buffering capacity and oxygen diffusivity.

Author Contributions: Conceptualization, P.S.; methodology, W.B., Z.T. and P.S.; collecting data and analysis, W.B. and Z.T.; resources, P.S.; writing P.S., W.B. and Z.T. All authors have read and agreed to the published version of the manuscript.

Funding: This research was funded by the European Research Council, grant number SURVIVE, and the Marie Skłodowska-Curie Innovative Training Network (ITN) (grant Agreement number: 813834—*pHioniC*—H2020-MSCA-ITN-2018).

Institutional Review Board Statement: The study was conducted according to the guidelines of the Declaration of Helsinki, and approved by Oxford University ethical review board.

Informed Consent Statement: Not applicable.

Data Availability Statement: All data relevant to the work has been presented herein. Raw traces are available on request made to the corresponding author.

Acknowledgments: We thank Kyung Chan (KC) Park for isolating ventricular myocytes.

Conflicts of Interest: The authors declare no conflict of interest. The funders had no role in the design of the study; in the collection, analyses, or interpretation of data; in the writing of the manuscript, or in the decision to publish the results.

References

1. Birsoy, K.; Possemato, R.; Lorbeer, F.K.; Bayraktar, E.C.; Thiru, P.; Yucel, B.; Wang, T.; Chen, W.W.; Clish, C.B.; Sabatini, D.M. Metabolic determinants of cancer cell sensitivity to glucose limitation and biguanides. *Nature* **2014**, *508*, 108–112. [CrossRef]
2. Nowell, P.C. The clonal evolution of tumor cell populations. *Science* **1976**, *194*, 23–28. [CrossRef]
3. Hanahan, D.; Weinberg, R.A. Hallmarks of cancer: The next generation. *Cell* **2011**, *144*, 646–674. [CrossRef]
4. Li, Z.; Wang, Z.; Tang, Y.; Lu, X.; Chen, J.; Dong, Y.; Wu, B.; Wang, C.; Yang, L.; Guo, Z.; et al. Liquid biopsy-based single-cell metabolic phenotyping of lung cancer patients for informative diagnostics. *Nat. Commun.* **2019**, *10*, 3856. [CrossRef]
5. Ke, C.; Li, A.; Hou, Y.; Sun, M.; Yang, K.; Cheng, J.; Wang, J.; Ge, T.; Zhang, F.; Li, Q.; et al. Metabolic phenotyping for monitoring ovarian cancer patients. *Sci. Rep.* **2016**, *6*, 23334. [CrossRef]
6. Jain, M.; Nilsson, R.; Sharma, S.; Madhusudhan, N.; Kitami, T.; Souza, A.L.; Kafri, R.; Kirschner, M.W.; Clish, C.B.; Mootha, V.K. Metabolite profiling identifies a key role for glycine in rapid cancer cell proliferation. *Science* **2012**, *336*, 1040–1044. [CrossRef]
7. San-Millan, I.; Brooks, G.A. Reexamining cancer metabolism: Lactate production for carcinogenesis could be the purpose and explanation of the Warburg Effect. *Carcinogenesis* **2017**, *38*, 119–133. [CrossRef] [PubMed]
8. Mayer, A.; Vaupel, P. Hypoxia, lactate accumulation, and acidosis: Siblings or accomplices driving tumor progression and resistance to therapy? *Adv. Exp. Med. Biol.* **2013**, *789*, 203–209. [CrossRef]
9. Kato, Y.; Ozawa, S.; Miyamoto, C.; Maehata, Y.; Suzuki, A.; Maeda, T.; Baba, Y. Acidic extracellular microenvironment and cancer. *Cancer Cell Int.* **2013**, *13*, 89. [CrossRef]
10. Sun, C.; Liu, X.; Wang, B.; Wang, Z.; Liu, Y.; Di, C.; Si, J.; Li, H.; Wu, Q.; Xu, D.; et al. Endocytosis-mediated mitochondrial transplantation: Transferring normal human astrocytic mitochondria into glioma cells rescues aerobic respiration and enhances radiosensitivity. *Theranostics* **2019**, *9*, 3595–3607. [CrossRef]
11. O'Neill, S.; Porter, R.K.; McNamee, N.; Martinez, V.G.; O'Driscoll, L. 2-Deoxy-D-Glucose inhibits aggressive triple-negative breast cancer cells by targeting glycolysis and the cancer stem cell phenotype. *Sci. Rep.* **2019**, *9*, 3788. [CrossRef]
12. Guo, J.; Su, Y.; Zhang, M. Circ_0000140 restrains the proliferation, metastasis and glycolysis metabolism of oral squamous cell carcinoma through upregulating CDC73 via sponging miR-182-5p. *Cancer Cell Int.* **2020**, *20*, 407. [CrossRef]
13. John, G.T.; Goelling, D.; Klimant, I.; Schneider, H.; Heinzle, E. PH-sensing 96-well microtitre plates for the characterization of acid production by dairy starter cultures. *J. Dairy Res.* **2003**, *70*, 327–333. [CrossRef] [PubMed]
14. Heux, S.; Philippe, B.; Portais, J.C. High-throughput workflow for monitoring and mining bioprocess data and its application to inferring the physiological response of Escherichia coli to perturbations. *Appl. Environ. Microbiol.* **2011**, *77*, 7040–7049. [CrossRef]
15. Wu, S.; Wu, S.; Yi, Z.; Zeng, F.; Wu, W.; Qiao, Y.; Zhao, X.; Cheng, X.; Tian, Y. Hydrogel-Based Fluorescent Dual pH and Oxygen Sensors Loaded in 96-Well Plates for High-Throughput Cell Metabolism Studies. *Sensors* **2018**, *18*, 564. [CrossRef] [PubMed]

16. Kieninger, J.; Aravindalochanan, K.; Sandvik, J.A.; Pettersen, E.O.; Urban, G.A. Pericellular oxygen monitoring with integrated sensor chips for reproducible cell culture experiments. *Cell Prolif.* **2014**, *47*, 180–188. [CrossRef] [PubMed]
17. Steinegger, A.; Wolfbeis, O.S.; Borisov, S.M. Optical Sensing and Imaging of pH Values: Spectroscopies, Materials, and Applications. *Chem. Rev.* **2020**, *120*, 12357–12489. [CrossRef]
18. Wang, X.D.; Wolfbeis, O.S. Optical methods for sensing and imaging oxygen: Materials, spectroscopies and applications. *Chem. Soc. Rev.* **2014**, *43*, 3666–3761. [CrossRef]
19. Nonnenmacher, Y.; Palorini, R.; Hiller, K. Determining Compartment-Specific Metabolic Fluxes. *Methods Mol. Biol.* **2019**, *1862*, 137–149. [CrossRef]
20. Zhang, J.; Zhang, Q. Using Seahorse Machine to Measure OCR and ECAR in Cancer Cells. *Methods Mol. Biol.* **2019**, *1928*, 353–363. [CrossRef]
21. Hynes, J.; Swiss, R.L.; Will, Y. High-Throughput Analysis of Mitochondrial Oxygen Consumption. *Methods Mol. Biol.* **2018**, *1782*, 71–87. [CrossRef] [PubMed]
22. Naciri, M.; Kuystermans, D.; Al-Rubeai, M. Monitoring pH and dissolved oxygen in mammalian cell culture using optical sensors. *Cytotechnology* **2008**, *57*, 245–250. [CrossRef] [PubMed]
23. Arguello, R.J.; Combes, A.J.; Char, R.; Gigan, J.P.; Baaziz, A.I.; Bousiquot, E.; Camosseto, V.; Samad, B.; Tsui, J.; Yan, P.; et al. SCENITH: A Flow Cytometry-Based Method to Functionally Profile Energy Metabolism with Single-Cell Resolution. *Cell Metab.* **2020**, *32*, 1063–1075.e1067. [CrossRef] [PubMed]
24. Tanumihardja, E.; Slaats, R.H.; van der Meer, A.D.; Passier, R.; Olthuis, W.; van den Berg, A. Measuring Both pH and O2 with a Single On-Chip Sensor in Cultures of Human Pluripotent Stem Cell-Derived Cardiomyocytes to Track Induced Changes in Cellular Metabolism. *ACS Sens.* **2021**, *6*, 267–274. [CrossRef] [PubMed]
25. Diepart, C.; Verrax, J.; Calderon, P.B.; Feron, O.; Jordan, B.F.; Gallez, B. Comparison of methods for measuring oxygen consumption in tumor cells in vitro. *Anal. Biochem.* **2010**, *396*, 250–256. [CrossRef] [PubMed]
26. Ge, X.; Hanson, M.; Shen, H.; Kostov, Y.; Brorson, K.A.; Frey, D.D.; Moreira, A.R.; Rao, G. Validation of an optical sensor-based high-throughput bioreactor system for mammalian cell culture. *J. Biotechnol.* **2006**, *122*, 293–306. [CrossRef]
27. Alim Uysal, B.A.; Kotan, G.; Guneser, M.B.; Dincer, A.N.; Senturk, H.; Rafiqi, A.M. Investigation of the effect of different chelation solutions on penetration of resin-based and bioceramic sealers with a novel method. *Microsc. Res. Tech.* **2021**. [CrossRef]
28. Michl, J.; Park, K.C.; Swietach, P. Evidence-based guidelines for controlling pH in mammalian live-cell culture systems. *Commun. Biol.* **2019**, *2*, 144. [CrossRef]
29. Yao, J.; Czaplinska, D.; Ialchina, R.; Schnipper, J.; Liu, B.; Sandelin, A.; Pedersen, S.F. Cancer Cell Acid Adaptation Gene Expression Response Is Correlated to Tumor-Specific Tissue Expression Profiles and Patient Survival. *Cancers* **2020**, *12*, 2183. [CrossRef]
30. Forciniti, S.; Dalla Pozza, E.; Greco, M.R.; Amaral Carvalho, T.M.; Rolando, B.; Ambrosini, G.; Carmona-Carmona, C.A.; Pacchiana, R.; Di Molfetta, D.; Donadelli, M.; et al. Extracellular Matrix Composition Modulates the Responsiveness of Differentiated and Stem Pancreatic Cancer Cells to Lipophilic Derivate of Gemcitabine. *Int. J. Mol. Sci.* **2020**, *22*, 29. [CrossRef]
31. Ford, K.L.; Moorhouse, E.L.; Bortolozzi, M.; Richards, M.A.; Swietach, P.; Vaughan-Jones, R.D. Regional acidosis locally inhibits but remotely stimulates Ca2+ waves in ventricular myocytes. *Cardiovasc. Res.* **2017**, *113*, 984–995. [CrossRef]
32. Chung, Y.J.; Luo, A.; Park, K.C.; Loonat, A.A.; Lakhal-Littleton, S.; Robbins, P.A.; Swietach, P. Iron-deficiency anemia reduces cardiac contraction by downregulating RyR2 channels and suppressing SERCA pump activity. *JCI Insight* **2019**, *4*, e125618. [CrossRef]
33. Hulikova, A.; Harris, A.L.; Vaughan-Jones, R.D.; Swietach, P. Regulation of intracellular pH in cancer cell lines under normoxia and hypoxia. *J. Cell Physiol.* **2013**, *228*, 743–752. [CrossRef]
34. Jo, J.; Lee, C.H.; Kopelman, R.; Wang, X. In vivo quantitative imaging of tumor pH by nanosonophore assisted multispectral photoacoustic imaging. *Nat. Commun.* **2017**, *8*, 471. [CrossRef]
35. Contreras-Baeza, Y.; Sandoval, P.Y.; Alarcon, R.; Galaz, A.; Cortes-Molina, F.; Alegria, K.; Baeza-Lehnert, F.; Arce-Molina, R.; Guequen, A.; Flores, C.A.; et al. Monocarboxylate transporter 4 (MCT4) is a high affinity transporter capable of exporting lactate in high-lactate microenvironments. *J. Biol. Chem.* **2019**, *294*, 20135–20147. [CrossRef] [PubMed]
36. Bachmeier, C.J.; Trickler, W.J.; Miller, D.W. Drug efflux transport properties of 2′,7′-bis(2-carboxyethyl)-5(6)-carboxyfluorescein acetoxymethyl ester (BCECF-AM) and its fluorescent free acid, BCECF. *J. Pharm. Sci.* **2004**, *93*, 932–942. [CrossRef] [PubMed]
37. Lucien, F.; Harper, K.; Pelletier, P.P.; Volkov, L.; Dubois, C.M. Simultaneous pH measurement in endocytic and cytosolic compartments in living cells using confocal microscopy. *J. Vis. Exp.* **2014**, *86*, 51395. [CrossRef] [PubMed]
38. Hinton, A.; Sennoune, S.R.; Bond, S.; Fang, M.; Reuveni, M.; Sahagian, G.G.; Jay, D.; Martinez-Zaguilan, R.; Forgac, M. Function of a subunit isoforms of the V-ATPase in pH homeostasis and in vitro invasion of MDA-MB231 human breast cancer cells. *J. Biol. Chem.* **2009**, *284*, 16400–16408. [CrossRef]
39. Ray, A.; Koo Lee, Y.E.; Epstein, T.; Kim, G.; Kopelman, R. Two-photon nano-PEBBLE sensors: Subcellular pH measurements. *Analyst* **2011**, *136*, 3616–3622. [CrossRef]
40. Willoughby, D.; Schwiening, C.J. Electrically evoked dendritic pH transients in rat cerebellar Purkinje cells. *J. Physiol.* **2002**, *544*, 487–499. [CrossRef] [PubMed]
41. Lima, S.; Bonifacio, R.L.; Azzellini, G.C.; Coichev, N. Ruthenium(II) tris(bipyridyl) ion as a luminescent probe for oxygen uptake on the catalyzed oxidation of HSO3-. *Talanta* **2002**, *56*, 547–556. [CrossRef]

42. Zhou, C.; Zhao, W.X.; You, F.T.; Geng, Z.X.; Peng, H.S. Highly Stable and Luminescent Oxygen Nanosensor Based on Ruthenium-Containing Metallopolymer for Real-Time Imaging of Intracellular Oxygenation. *ACS Sens.* **2019**, *4*, 984–991. [CrossRef] [PubMed]
43. Jiang, Z.; Yu, X.; Zhai, S.; Hao, Y. Ratiometric Dissolved Oxygen Sensors Based on Ruthenium Complex Doped with Silver Nanoparticles. *Sensors* **2017**, *17*, 548. [CrossRef] [PubMed]
44. Scholler-Mann, A.; Matt, K.; Hochecker, B.; Bergemann, J. Ex vivo Assessment of Mitochondrial Function in Human Peripheral Blood Mononuclear Cells Using XF Analyzer. *Bio. Protoc.* **2021**, *11*, e3980. [CrossRef]

British Journal of Cancer www.nature.com/bjc

ARTICLE OPEN

Check for updates

Translational Therapeutics

Autoregulation of H^+/lactate efflux prevents monocarboxylate transport (MCT) inhibitors from reducing glycolytic lactic acid production

Wiktoria Blaszczak[1], Hannah Williams[1] and Pawel Swietach[1]✉

© The Author(s) 2022

BACKGROUND: Pharmacological inhibition of membrane transporters is expected to reduce the flow of solutes, unless flux is restored (i.e., autoregulated) through a compensatory increase in the transmembrane driving force. Drugs acting on monocarboxylate transporters (MCTs) have been developed to disrupt glycolytic metabolism, but autoregulation would render such interventions ineffective. We evaluated whether small-molecule MCT inhibitors reduce cellular H^+/lactate production.
METHODS: Cellular assays measured the relationship between MCT activity (expressed as membrane H^+/lactate permeability; P_{HLac}) and lactic acid production (inferred from H^+ and lactate excretion; J_{HLac}) in a panel of pancreatic ductal adenocarcinoma (PDAC) cells spanning a range of glycolytic phenotype.
RESULTS: MCT activity did not correlate with lactic acid production, indicating that it is not set by membrane permeability properties. MCT inhibitors did not proportionately reduce J_{HLac} because of a compensatory increase in the transmembrane [lactate] driving force. J_{HLac} was largely insensitive to [lactate], therefore its cytoplasmic build-up upon MCT inhibition does not hinder glycolytic production. Extracellular acidity, an MCT inhibitor, reduced J_{HLac} but this was via cytoplasmic acidification blocking glycolytic enzymes.
CONCLUSIONS: We provide mathematically verified evidence that pharmacological and physiological modulators of MCTs cannot proportionately reduce lactic acid production because of the stabilising effect of autoregulation on overall flux.

British Journal of Cancer (2022) 127:1365–1377; https://doi.org/10.1038/s41416-022-01910-7

INTRODUCTION

Cancer cells harness considerable energy from glycolytic metabolism, and in doing so, generate large quantities of lactic acid even under aerobic conditions (the Warburg effect). As the terminal step in this process, H^+-lactate export by monocarboxylate transporters (MCTs) is considered an attractive target for controlling cancer metabolism therapeutically [1–3] for at least two reasons. Firstly, MCT isoforms, notably MCT1 (*SLC16A1*) and MCT4 (*SLC16A3*), conduct the vast majority of lactic acid efflux from cells [4], and blocking these is intuitively predicted to impact glycolytic metabolism. Secondly, surface-expressed MCTs are accessible to a range of chemical modulators [5, 6]. These considerations led to the assertion that MCT blockers, by reducing membrane H^+/lactate permeability, also proportionately inhibit glycolytic lactic acid production, a key component of tumour metabolism. This presumed relationship between H^+/lactate permeability and production has underpinned the rationale for developing novel MCT inhibitors [7–10] and studying physiological MCT modulation [11–13].

To investigate the relationship between MCT inhibition and the cell's lactic acid output, it is important to consider the factors determining flux. By definition, net metabolic production of lactic acid inside cells (J_{HLac}) must be in balance with transmembrane removal through MCTs (as H^+/lactate) and the lipid bilayer (as lactic acid). As shown in the Appendix, this can be described mathematically as the product of overall membrane permeability and driving force defined in terms of the intracellular (i) and extracellular (e) concentrations:

$$J_{HLac} = P_{HLac} \times \left([H^+]_i \times [\text{lactate}]_i - [H^+]_e \times [\text{lactate}]_e \right) \quad (1)$$

Here, P_{HLac} describes the total conductance of surface-expressed MCTs to H^+ and lactate ions, after considering all relevant influences (e.g., allosteric actions and affinity) plus a lesser contribution from MCT-independent permeability across the lipid bilayer. MCT inhibitors act directly to reduce P_{HLac} by interrupting the transport cycle; however, a reduction in P_{HLac} may not necessarily decrease J_{HLac} if the driving force increases in a compensatory manner as a result of the solute build-up in the cytoplasm. This scenario is a case of autoregulation because flux remains constant irrespective of membrane permeability properties (Fig. 1a). The compensatory increase in driving force could take the form of cytoplasmic lactate and/or H^+ ions accumulation, provided this does not hinder further metabolic production. Intracellular H^+ ions are known to block

[1]Department of Physiology, Anatomy & Genetics, University of Oxford, Sherrington Building, Parks Road, OX1 3PT Oxford, UK. ✉email: pawel.swietach@dpag.ox.ac.uk

Received: 7 February 2022 Revised: 24 June 2022 Accepted: 29 June 2022
Published online: 15 July 2022

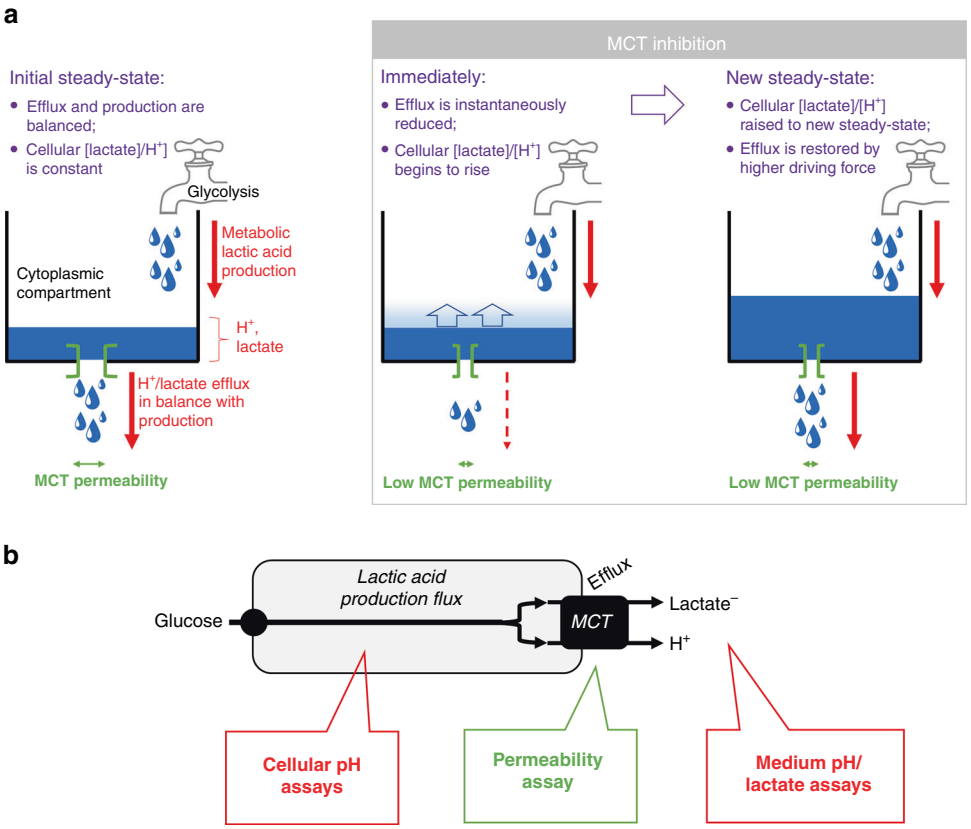


Fig. 1 In a system that auto-regulates efflux, pharmacological inhibition of a transporter does not necessarily reduce the carried flux. **a** By definition, net metabolic production of lactic acid (represented by tap) is equal to H^+/lactate efflux across the membrane, largely mediated by surface-expressed MCTs (represented by green vent). The level of H^+/lactate in the cytoplasmic compartment is set by the production flux and permeability. A drug-evoked reduction in membrane permeability will initially reduce efflux. This results in a build-up of lactate/H^+ in the cell, which increases the driving force for efflux. A new steady-state is attained, at which efflux is restored, despite the lower permeability. For this to take place, the build-up of H^+/lactate must not block production, the ultimate driver of lactic acid release from cells. **b** Schematic of the relationship between glycolytic flux and MCT-dependent H^+/lactate efflux, indicating the variables interrogated by assays. Flux (typically in units of mM per min) described the rate at which a solute is produced (e.g., by glycolysis) or transported (e.g., by MCTs). Permeability is a property of the cell membranes that measures how easily solutes can cross (e.g., aboard MCTs). Pharmacological drugs are often designed to influence flux by interrupting permeability, but this may not hold true if the system shows autoregulation of flux.

glycolytic enzymes [14] (e.g., phosphofructokinase-1 [15, 16]), thus cytoplasmic [H^+] build-up is unlikely to provide the necessary increase in driving force. However, cytoplasmic [lactate] accumulation could plausibly boost the driving force for MCT-operated efflux without blocking H^+/lactate production. Since enzyme-dependent steps in glycolysis are near-equilibrium and have spare capacity to adjust to changes in load [17], autoregulation is plausible but not yet verified. An appraisal of autoregulation is important because it defines the scope of MCT inhibitors to influence lactic acid production. Biologically, the rationale for autoregulation would be in stabilising energy flows and preventing isolated changes (e.g., in MCT activity) from disrupting metabolic flows [18]. Indeed, there are precedents where a change to permeability does not proportionately alter flux. In cardiomyocytes, for example, inhibitors (or activators) of ryanodine receptor-type calcium channels cannot change calcium release from the sarcoplasmic reticulum store because of compensatory adjustments to the driving force [19]. If H^+/lactate efflux from cells were similarly autoregulated, then MCT modulators would be ineffective in altering lactic acid production directly. An appraisal of autoregulation is therefore warranted to assess the feasibility of influencing cancer metabolism by targeting MCT pharmacologically.

To test for autoregulation, we used innovative cell-based approaches that interrogate P_{HLac} and J_{HLac} independently on the same biological material (Fig. 1b). For this, we used six pancreatic ductal adenocarcinoma (PDAC) cell lines that span a range of glycolytic phenotype. It was important that the biological responses were probed over a period long enough to engage autoregulation (i.e., several hours) because measurements of short-term responses (e.g., by Seahorse XF Analyzers) are likely to miss the autoregulatory phenomenon. Autoregulation was tested against its characteristic features, namely (i) lack of correlation between P_{HLac} and J_{HLac}, (ii) absence of a sustained effect of MCT inhibitors on lactic acid release from cells and (iii) evidence that driving force can be changed in a manner that does not hinder lactic acid production. We find that H^+/lactate efflux meets these criteria and conclude that drugs targeting MCTs are not effective in blocking lactate production over a realistic dosage range.

METHODS

Cell culture and media

Cells were cultured in RPMI (Sigma-Aldrich, R0883) supplemented with 10% FBS, 1% penicillin–streptomycin mixture, 1% GlutaMAX (35050-038, Gibco, Waltham, MA, USA), 1% sodium pyruvate (11360-039, Gibco, Waltham, MA, USA). In the case of media incubated in 5% CO_2, the appropriate [HCO_3^-] was determined empirically to equilibrate at pH 7.4. Other media were buffered with non-volatile buffers, such as HEPES or MES, and titrated to the desired pH with HCl or NaOH. Equimolar HEPES and MES provided near-constant pH buffering over the biological pH range. NaCl was added to maintain osmolarity constant [20]. For some experiments, cells were incubated in with 1 mM dimethyloxalylglycine (DMOG; 4408, Tocris) for 48 h to stabilise HIF signalling. Cell lines were

authenticated by AuthentiCell service provided by the European Collection of Authenticated Cell Cultures (a part of UK Health Security Agency).

Superfusion

Cells were seeded at 70,000 per well in 4-chamber Nunc Lab-Tek slides (734-2060, ThermoScientific). Experiments involving superfusion were performed on a Leica LCS confocal microscope to image fluorescence. Most experiments measured intracellular pH using cSNARF1 (17 μM for 10 min; C1272 ThermoFisher), excited at 514 nm and collected at 580/640 nm. The ratio was calibrated to units of pH using a calibration curve determined in separate experiments using the nigericin technique [21]. Solutions were delivered by a system of tubes operated by a peristaltic pump, with a two-level solution switcher to alternate between one of two superfusates heated to 37 °C. Excess solution was drawn by a vacuum pump to ensure laminar flow. Solutions were based on normal Tyrode containing 4.5 mM KCl, 1 mM $CaCl_2$, 1 mM $MgCl_2$, 11 mM glucose, 10 mM HEPES, 10 mM MES and 130 mM NaCl, titrated to the desired pH (5.7–7.7) using HCl or NaOH.

Rapid solution switching

cSNARF1-loaded PDAC cells seeded in Lab-Tek chambers were superfused with normal Tyrode. A dual microperfusion device was manipulated into the field of view, 100 microns from the cells of interest. Switching a system of valves alternated between the two microstreams, driven by gravity flow. The speed of solution switching is 25 ms [22]. To evoke MCT activity, the first microstream contained 30 mM L-lactate at pH 7.4 (osmotically compensated with NaCl) and the second was lactate-free titrated to a particular test pH (5.7–7.7). Cells were equilibrated with the lactate microstream for 5 min to load cytoplasm with MCT substrate. MCT activity could therefore be mapped as a function of pHe from the initial rate of pHi change [23]. This protocol keeps the thermodynamic driving force constant, whilst allowing pHe to change (note, $[H^+]_e \times [lactate]_e$ is zero under superfusion with lactate-free microstream). For measurements in the presence of the MCT1 inhibitor SR13800, the MCT1/2 inhibitor AR-C155858 (1 μM; 4960, Tocris [24]) or the MCT4/1 inhibitor syrosingopine (1 μM or 10 μM; SML1908, Merck) drug was added to both microstreams to ensure adequate access time to the inhibitory site. For the single-cell glycolytic rate assay, the first microstream contained lactate-free normal Tyrode and the second was supplemented with 2 mM α-cyano-4-hydroxycinnamate (CHC; S8612, Selleckchem) to block lactic acid efflux by MCT. Both microstreams contained 30 μM 5-*N*,*N*-dimethylamiloride to block acid extrusion by Na^+/H^+ exchanger-1, the dominant pH regulator. For assaying the rate of intracellular acidification, the first microstream contained normal Tyrode and the second was titrated to either pH 5.7 or 6.6.

Well-based fluorimetric assay of lactic acid production

The time course of medium acidification was used to gauge lactic acid production. Cells were seeded onto a 96-well plate at high density (55,000/well) and left to adhere for 24 h in standard RPMI. Cells were then washed in PBS twice. Replacing with 100 μL medium buffered with 2 mM HEPES/2 mM MES, titrated to a target pH and containing cSNARF1-dextran (0.083 mg/ml, D3304, ThermoFisher Scientific) initiated the measurement. In some experiments, media were supplemented with 10 mM or 20 mM L-lactate, or 5 mM of acetate, propionate, butyrate, phosphate or imidazole, and then re-titrated to the desired pH. The plate was placed immediately in a Biotek Cytation 5 plate reader pre-heated to 37 °C, recording fluorescence at 590 nm and 640 nm excited by 555 nm light every 30 min. The combination of low buffering and high confluency enabled the system to acidify. Control wells containing no cells were used to offset measurements. To calculate cumulative acid production, the stepwise pHe change was multiplied by medium buffering capacity and integrated.

Well-based fluorimetric assay of lactic acid production and respiratory rate

This dual-dye fluorimetric assay was based on a recently published method [25].

Biochemical lactate assay

After a period of incubation, the medium was collected and frozen at −80 °C to deactivate L-lactate dehydrogenase prior to [lactate] measurements on a YSI 2500 Biochemistry Analyzer (525000, Xylem) or ABX Pentra C400 analyzer (Horiba).

Western blotting

Samples were sonicated, denatured by BME in Laemmli buffer (1:20). Gels were prepared with 15% acrylamide. The primary antibodies were raised against MCT1 (1:500, Millipore Cat# AB3538P, RRID:AB_2189203, rabbit), MCT2 (1:4000, Proteintech Cat# 20355-1-AP, AB_2878680, rabbit) MCT4 (Millipore Cat# AB3316P, RRID:AB_2189344, rabbit), HIF1α (1:1000, BD Biosciences Cat # 610958, RRID:AB_398271, mouse), HRP-conjugated GAPDH 1:6000 (Proteintech Cat# HRP-60004, RRID:AB_2737588). The secondary antibody was HRP-goat anti-rabbit (1:4000, 6556120, Invitrogen). To detect total protein lactylation samples were collected and denatured as described previously and separated on 12.5% polyacrylamide gel. The primary antibody was raised against L-lactyl-lysine (1:1000, PTM-1401, PTM-Biolabs, rabbit), and secondary HRP-conjugated and raised against β-actin (1:5000, Proteintech, mouse).

Seahorse XF assays

Media for ECAR and OCR measurements on the Seahorse XFe96 Analyzer (Agilent) were prepared with 2 mM HEPES and 2 mM MES to provide light buffering that is constant over the biological pH range. Media were titrated to pH 7.4 but not supplemented with FBS or antibiotics. Consecutive injections of 0.5 N HCl and 0.4 M NaOH produced a decrease and then a recovery of pH. PDAC cells were seeded onto a 96-well plate 24 h prior to experiments in a standard RPMI-based medium at a density of 25k/well. Cells were washed twice with PBS before adding 100 μL of the final medium. Initial and post-injection values of ECAR and OCR were recorded, confirmed for reversibility and normalised to readings at pH 7.4.

High-throughput pH imaging

Cells were plated in 96-well plates and loaded with cSNARF1 (used to measure pHi) and Hoechst (used to identify nuclei for cell segmentation) for 10 min. Media were then replaced with formulations buffered with 10 mM HEPES and 10 mM MES, titrated to a pH between 5.5 and 7.7. After allowing 10 min for equilibration, images were taken using the Biotek Cytation 5 at 37 °C [20].

Statistical analysis

The number of observations is reported as "n/N", indicating the number of cells or wells and the number of biological repeats yielded from separate plating and passage. Additional tests used are listed in corresponding figure legends. At least three biological repeats were performed (i.e., from an independent cell passage), with at least three technical repeats each (i.e., concurrent measurements from same yield of cells, but treated separately to drugs, e.g., in a separate well). All *t* tests were two-sided. Summary statistics are shown as mean ± SEM, unless stated otherwise. Significance level for all tests was 5%.

See supplement for further methods.

RESULTS

Across different PDAC lines, MCT-facilitated H^+/lactate permeability does not correlate with lactic acid production

The relationship between MCT-facilitated membrane H^+/lactate permeability (P_{HLac}) and metabolic lactic acid production (J_{HLac}) was first studied using cellular assays performed on a panel of six PDAC cell lines. If the membrane's conductance to H^+/lactate, facilitated by surface-expressed MCTs, was rate-limiting for lactic acid release from cells, a linear P_{HLac}-J_{HLac} relationship would be expected across different cell lines. Membrane permeability was measured by manipulating the extracellular concentration of lactate to drive net efflux across MCTs. For this approach to be accurate, the solution change must be rapid, so that permeability is not underestimated because of a slow-mixing artefact. To avoid this common problem, extracellular solutions were changed by means of an ultra-rapid solution switcher [22]. This device alternately released a microstream containing 30 mM lactate to load cells with MCT substrate, and a lactate-free microstream to activate H^+-lactate efflux. Lactic acid efflux was calculated from the rate of intracellular alkalisation (measured with cSNARF fluorescence; Fig. 2a), multiplied by the intrinsic buffering capacity (Supplementary Fig. S1). Flux was then converted to P_{HLac} using known values of $[H^+]_e$, $[lactate]_e$, $[H^+]_i$ and an estimate of $[lactate]_i$

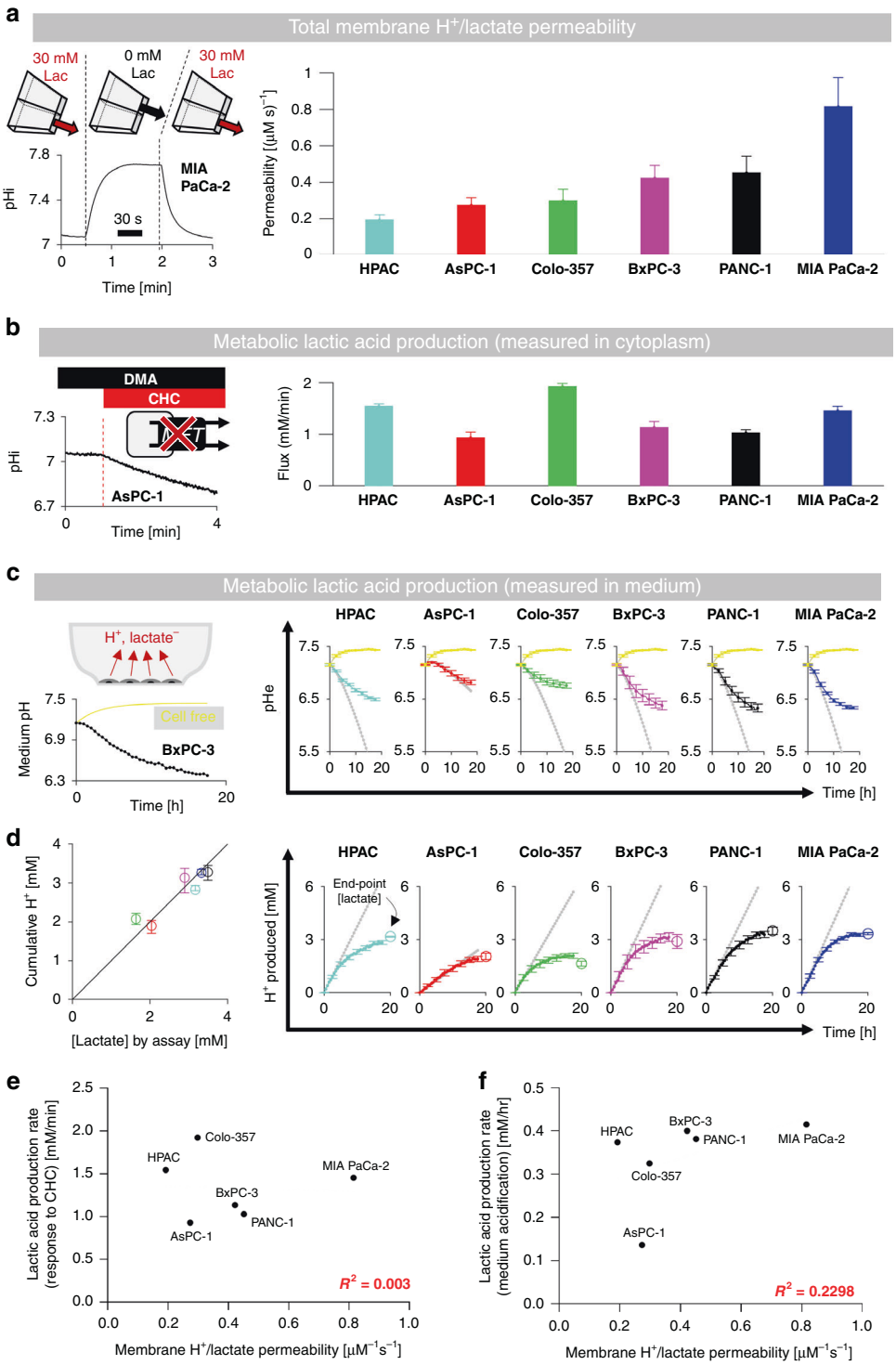


Fig. 2 Membrane H+/lactate permeability does not correlate with lactic acid production. a Measuring MCT-dependent H^+/lactate permeability (P_{HLac}) using rapid solution switcher alternately releasing 30 mM lactate-containing and lactate-free microstreams. Exemplar pHi time course (cSNARF1). P_{HLac} in six PDAC cell lines ($n = 2500–3500$ cells/$N = 4–6$ platings). **b** Lactic acid production rate inferred from the immediate effect on pHi of MCT blockade with α-cyano-4-hydroxycinnamate (CHC; 2 mM) ($n = 500/N = 2$). **c** Lactic acid production measured from medium acidification (cSNARF1-dextran) and end-point lactate by biochemical assay ($n = 9/N = 3$). Yellow traces are cell-free wells; grey lines indicate the initial rate. **d** Concordance between lactate and H^+ production in media (Pearson's $R = 0.93$; $P = 0.008$). Medium pH time courses converted to cumulative acid production, also showing endpoint [lactate] measured biochemically. **e**, **f** Lack of significant correlation between P_{HLac} and lactic acid production measured by the two assays (R^2 is the Pearson correlation coefficient).

from Eq. (1). Uniquely, this technique can exchange solutions in under 30 ms, ensuring that P_{HLac} is not underestimated by slow mixing, a concern with most conventional superfusion systems. P_{HLac} measured in the six PDAC cells is shown in Fig. 2a, ranked by magnitude; permeability was four times higher in MIA PaCa-2 cells compared to HPAC cells. In all cases, measured permeability was at least two orders of magnitude higher than MCT-independent permeability (see Appendix).

The rate of lactic acid production by cells (J_{HLac}) was measured by two independent methods. The first approach inferred J_{HLac} from the intracellular pH (pHi) response to an abrupt and broad-spectrum inhibition of MCTs with α-cyano-4-hydroxycinnamate (CHC; 2 mM) delivered by the rapid solution switcher. Abrupt blockade of MCT traps endogenously produced lactic acid in the cytoplasm, causing an immediate cytoplasmic acidification that, when multiplied by intrinsic buffering capacity, measures J_{HLac} (Fig. 2B). To inactivate H^+-handling transporters, which would normally restore pHi to normal, superfusates were CO_2/HCO_3^- free to inactivate HCO_3^--dependent pHi regulators (e.g., Na^+-HCO_3^- cotransporters) and contained 30 μM DMA to block Na^+/H^+ exchanger activity, the main residual pHi-regulator present under a HEPES-buffered regime. As a secondary effect, CHC may block monocarboxylate (e.g., pyruvate) uptake into the mitochondria, thereby diverting fluxes to glycolysis and, potentially, over-estimate of glycolytic rate. To test the extent to which this may occur, experiments were repeated under conditions where the metabolic substrate (glucose) is replaced with galactose. This switch attenuates lactic acid production [25], as well as the CHC-response by tenfold (Supplementary Fig. S2). This finding indicates that the flux response to CHC provides a fair measure of glycolytic rate.

The second approach interrogated J_{HLac} from the initial rate of medium acidification arising from lactic acid release. To initiate medium acidification, standard culture media were replaced with a lightly buffered formulation (2 mM HEPES, 2 mM MES), which ensures a resolvable pH response to glycolytic production. A limitation of this method is that it reports the ensemble rate for the population of cells and is therefore sensitive to seeding density. Medium pH was measured from cSNARF1-dextran fluorescence (Fig. 2c) and converted to a time course of acid production by integrating the product of medium pH change and its buffering capacity (Fig. 2d). This approach was verified to provide an accurate readout of lactic acid production by the excellent agreement between cumulative acid production and [lactate] at the experimental endpoint. The initial rate of acidification was measured from the slope of the acid-production time course, at which point the cell density and medium conditions were the same in all experiments.

J_{HLac} measured using either approach did not correlate with P_{HLac} (Fig. 2e, f). The absence of a linear P_{HLac}-J_{HLac} correlation is consistent with flux autoregulation and must reflect substantial differences in driving force between cells of different lines. The lack of correlation also indicates that a measurement of membrane H^+/lactate permeability (or equivalent, e.g., *SLC16* expression) cannot predict glycolytic lactic acid production.

Pharmacological MCT inhibition does not proportionately reduce lactic acid release from cells

Flux through a system that auto-regulates is not expected to decrease in proportion to a reduction in membrane permeability. To test if lactic acid production auto-regulates, its response to MCT inhibition was tested. For this, drugs used previously to block MCTs were investigated at appropriate concentrations (1 μM AR-C155858 [9], 1 μM SR13800 [26, 27], 10 μM syrosingopine [9], >1 mM CHC [28]). The pharmacological activity of the MCT1/2 inhibitor AR-C155858, MCT1 inhibitor SR13800 and MCT1/4 inhibitor syrosingopine was confirmed by the powerful inhibitory effect on ensemble P_{HLac} (Fig. 3a). SR13800 at 1 μM reduced P_{HLac} by 91% in MIA PaCa-2 cells and 85% in BxPC-3 cells. AR-C155858 (1 μM) reduced P_{HLac} by 96% in MIA PaCa-2 cells and 83% in BxPC-3 cells. In MCT4-expressing PANC-1 cells, syrosingopine reduced P_{HLac} by 51% at 1 μM and by 69% at 10 μM. It is noteworthy that the higher dose produced intracellular acidification which should be considered when interpreting the drug's action. The MCT-blocking potency of CHC is well established and confirmed earlier (Fig. 2b). Across the six PDAC cells tested, the identity of isoforms underpinning MCT activity was determined by western blotting for MCT1, MCT2 and MCT4 (Fig. 3b) and from the sensitivity of P_{HLac} to AR-C155858 (Fig. 3c). Patterns of MCT expression were consistent with previous studies [29–31]. Overall, P_{HLac} was dominated by MCT1 in MIA PaCa-2 cells whereas MCT4 dominated activity in PANC-1 cells, therefore these two highly glycolytic lines were selected for further studies.

The effect of MCT inhibitors on lactic acid release from cells was inferred from real-time measurements of medium acidification and verified by end-point biochemical lactate assays (Fig. 3d). To ensure that the pharmacological disruption to P_{HLac} had sufficient time to implement any compensatory responses (e.g., through driving force), the time course was measured over 16 h. Despite an inhibitory effect on P_{HLac}, AR-C155858 (10 μM), SR13800 (10 μM), CHC (2 mM) and syrosignopine (10 μM) did not proportionally reduce lactic acid production in MIA PaCa-2 or PANC-1 cells. There was also no significant effect of these drugs on end-point glucose levels (Supplementary Fig. S3). At the higher concentration of 10 μM, syrosingopine produced a very small (10%) decrease in lactic acid production, but this was not proportional to its effect on P_{HLac}, and may relate to its effect on acidifying cytoplasm, instead. The effect of SR13800 was studied further using a fluorimetric assay that measures acid production (glycolysis) and oxygen consumption (respiration) simultaneously (Supplementary Fig. S4). Again, this showed no substantial consequences of pharmacological MCT inhibition on glycolytic metabolism or respiratory rate.

The apparent constancy of J_{HLac}, despite P_{HLac} falling by as much as 90%, must be explained in terms of a steeper driving force, i.e., greater cytoplasmic lactate and/or H^+ accumulation. Owing to the cell's powerful pH-regulatory apparatus, substantial $[H^+]_i$ changes are unlikely; however, a cytoplasmic build-up of lactate is plausible. Evidence for stable lactate build-up in cells with pharmacologically inhibited MCT was sought by western blotting for lactylated lysines after 16 h of incubation in lightly buffered medium. This method can identify whether cells experienced a period of elevated cytoplasmic [lactate] using a biomarker that is relatively stable for sample processing. The use of lactate sensors, such as FRET probes, is less suitable for this purpose, as the protocol would require cells to be handled for imaging, during which any cytoplasmic lactate accumulation may wash away. To confirm the adequate resolving power of lactylation, experiments were performed in media where glucose was replaced with galactose (negative control) or in glucose-containing media supplemented with lactate (positive control). As expected, lactylation of proteins, particularly near 55 kDa, was reduced in galactose and increased with lactate supplementation (Fig. 3e). AR-C155858 raised protein lactylation in MCT1-dependent MIA PaCa-2, and broad-spectrum inhibition by CHC increased lactylation in both PANC-1 and MIA PaCa-2 lines (Fig. 3f). In MCT4-dependent PANC-1 cells, 10 μM syrosingopine also raised protein lactylation (Fig. 3g). In summary, MCT inhibitors at concentrations that reduce membrane H^+/lactate permeability do not proportionately reduce lactic acid production, gauged in terms of medium acidification and lactate production. This discordance supports the notion that lactic acid efflux across the surface membrane is autoregulated because it can remain constant even at reduced permeability.

Lactic acid production is relatively insensitive to [lactate] but strongly inhibited at low pH

In order for efflux to remain constant under reduced permeability, the build-up of cytoplasmic solutes cannot block production. This was tested by measuring the time course of acidification of media

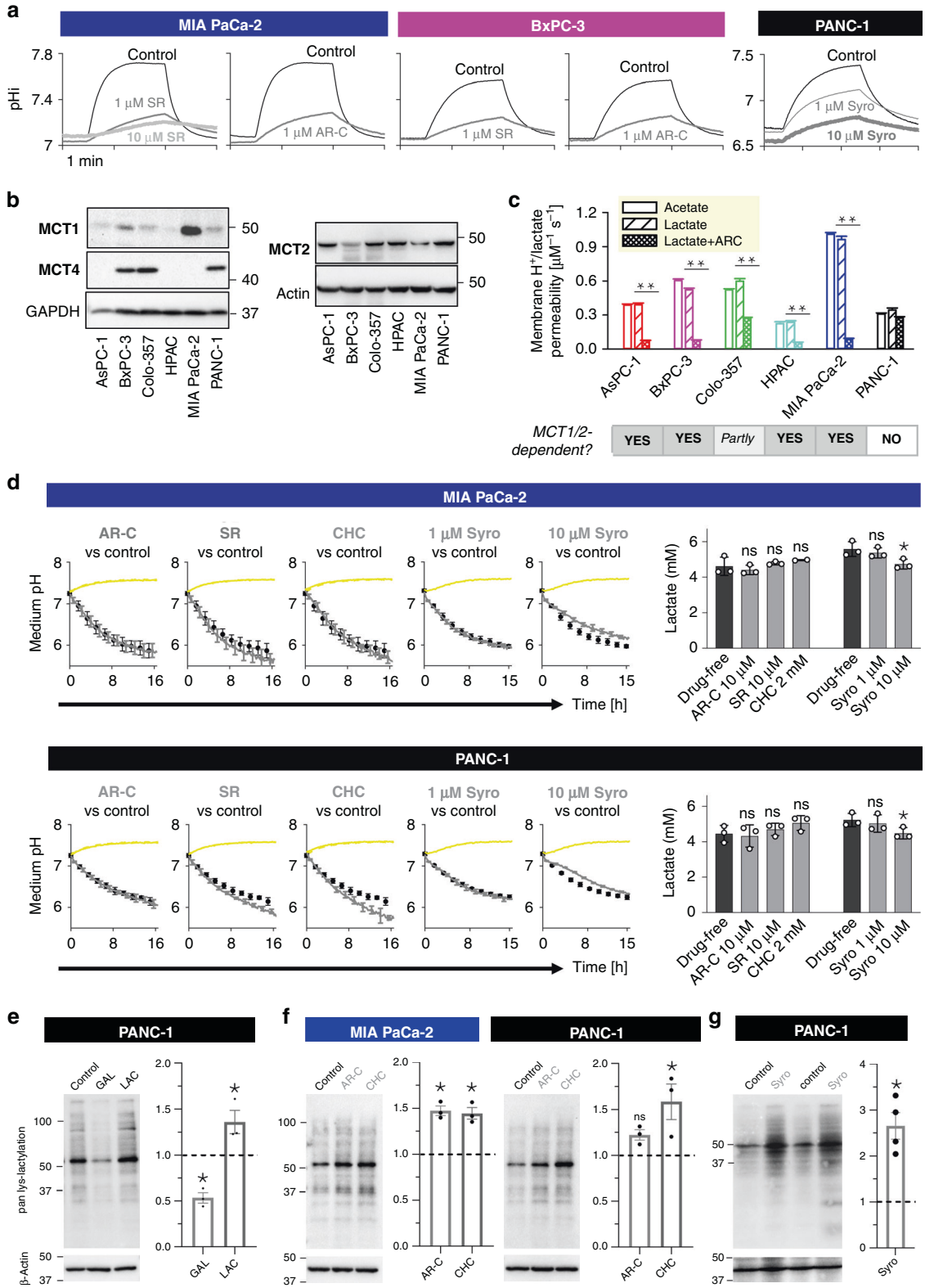


Fig. 3 Pharmacological MCT inhibitors do not block lactic acid production. a Confirmation of the inhibitory effect of SR13800 (SR), AR-C155858 (AR-C) and syrosingopine (Syro) on H^+/lactate permeability. **b** Western blot showing expression of MCT1, MCT2 and MCT4. **c** Membrane permeability measured for H^+/lactate in the presence and absence of MCT1/MCT2 inhibitor AR-C (1 µM), and compared to H^+/acetate ($n = 500–1000/N = 3$). $^{**}P < 0.01$, multiple comparisons *t* test. **d** Medium acidification (cSNARF1-dextran) in presence of AR-C (10 µM), SR (10 µM) or CHC (2 mM). Cumulative acid production and endpoint [lactate] are unaffected by MCT inhibitors ($n = 3$ repeats each; not significant; one-way ANOVA) The data are plotted as mean ± SD. **e** Western blot showing response of protein lactylation in media containing galactose instead of glucose (GAL) or media supplemented with lactate (LAC), and densitometric analysis. **f** Lactylation increases after treatment with 10 µM AR-C ($n = 3$) and 2 mM CHC ($n = 3$) and (**g**) 10 µM Syro ($n = 4$). $^{*}P < 0.05$, repeated measures ANOVA). Densitometric analyses were normalised to controls (dashed lines).

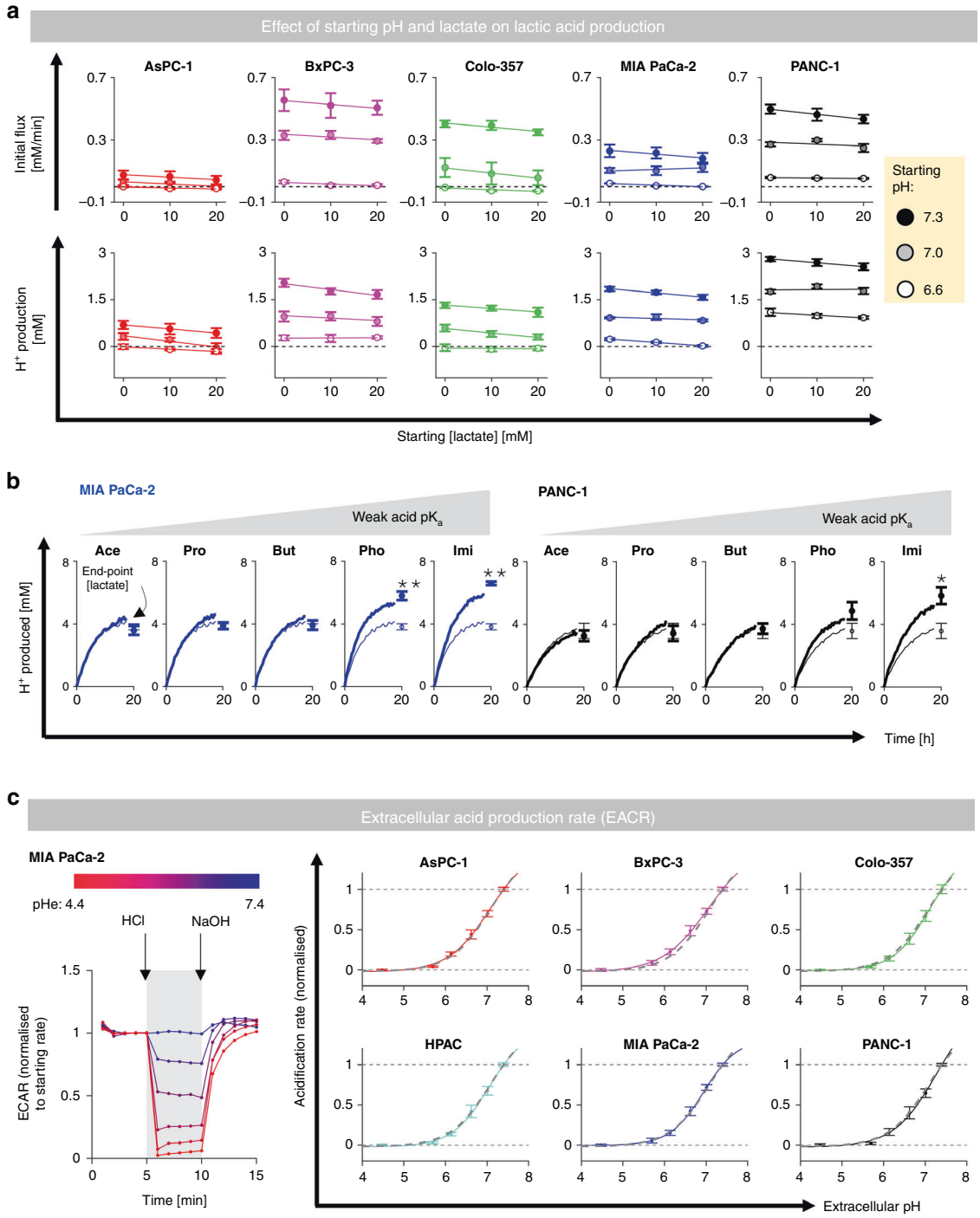


Fig. 4 Lactic acid production is strongly influenced by pH but not [lactate]. **a** Fluorimetric assay for medium acidification (cSNARF1-dextran). Starting medium pH and [lactate] were varied ($n = 12/N = 4$). Two-way ANOVA: $P < 0.001$ for effect of pH, $P > 0.05$ for effect of lactate. **b** Acid production into media supplemented with weak acids of increasing pK_a (thick line: 5 mM of Ace-acetate, Pro-propionate, But-butyrate, Pho-phosphate, Imi-imidazole), compared to controls (thin line). Error bars not shown for clarity. Endpoint [lactate] measured by biochemical assay ($n = 12/N = 4$). Significant effect of buffer tested by t test: $^*P < 0.05$; $^{**}P < 0.01$. **c** Glycolytic production of lactic acid inferred from the extracellular acidification rate (ECAR; Seahorse) in response to reducing pH from 7.4 with HCl injection, and then restoring pH to 7.4 with NaOH injection ($n = 8/N = 2$). Exemplar time course shows ECAR normalised to initial rate (i.e., prior to first pH change). Grey lines show pHe-ECAR curve averaged for all six lines.

titrated over a range of starting pH (6.6–7.3) and lactate concentration (0–20 mM). These modified initial conditions load the intra- and extracellular compartments with H^+ and/or lactate ions, revealing any inhibitory actions on glycolytic metabolism. The rate of medium acidification trended to be only mildly sensitive to starting [lactate], but decreased sharply and significantly at lower pH (Fig. 4a). Similarly, total acid output from cells was strongly sensitive to starting pH, but only weakly reduced with higher [lactate]. These findings indicate that a cytoplasmic build-up of lactate will not block glycolysis to a significant degree, at least

compared to the effect of pH. In the context of MCT inhibitors, this metabolic insensitivity to lactate would permit a steeper driving force to compensate for reduced permeability, thereby enabling autoregulation to take place.

The observation that exogenously applied [lactate] does not affect endogenous lactic acid production can be explained in terms of the transmembrane gradient. Supplementing media with lactate raises intra- and extracellular [lactate] in tandem. The inhibitory effect of reduced pH is well documented, although it is debated whether this is a consequence of MCT inhibition by extracellular H^+ ions or glycolytic inhibition by intracellular H^+ ions. This distinction is critical in the context of autoregulation because any form of direct MCT inhibition is not expected to block overall flux. Thus, establishing the mechanism for acid inhibition of lactic acid production is another test of autoregulation.

Consistent with an inhibitory action of H^+ ions, lactic acid production could be dysinhibited using pH buffers, with the strongest effect attained with substances of high pK_a (Fig. 4b). Strikingly, a high concentration of HEPES buffer accelerated glycolytic rate to a degree that reduced respiratory demand (Supplementary Fig. S5A). The linearity between medium buffering power and lactic acid production may indicate extracellular pH (pHe) as an apparent regulator of glycolytic rate (Supplementary Fig. S5B), ostensibly acting via MCT inhibition. This inference contradicts autoregulation and merited further investigation. To test if this pHe effect is apparent on a more acute timescale, the extracellular acidification rate (ECAR) was measured by Seahorse assay in response to rapid shifts to extracellular pH (pHe) attained by HCl/NaOH injections to lightly buffered media (2 mM HEPES and 2 mM MES). The injected amounts of HCl and NaOH were determined empirically to reduce pHe from 7.4 to a test level (down to pH 4.5), and then return to 7.4. Oxygen consumption rate (OCR) was measured in parallel. In all six PDAC lines, ECAR was profoundly inhibited at low pHe (Fig. 4c), whereas OCR was remarkably insensitive (Supplementary Fig. S6).

To test if the ECAR result is a manifestation of pH-sensitive glucose transport, cellular uptake of the fluorescent derivative NBDG was measured. NBDG was loaded into cells for 15 min over a range of pHe, followed by rapid washout to clear extracellular dye. NBDG uptake, imaged in cells identified by CellTracker Red signal, showed no clear pHe-sensitivity (Supplementary Fig. S7). Thus, low pHe strongly inhibits lactic acid production, but not through an effect on glucose uptake or respiration. If the pHe effect on ECAR was via MCT inhibition, it would argue against autoregulation. To investigate this, the pHe-ECAR relationship was compared to the pHe-sensitivity of MCT activity.

Low pHe reduces P_{HLac} but this does not underpin inhibition of lactic acid production

To test how MCT responds to an acute decrease in pHe, P_{HLac} measurements were performed using the rapid switcher device, with one microstream containing 30 mM lactate at pH 7.4 and the other containing lactate-free solution titrated to a pH between 5.7 and 7.4. In all six PDAC lines, P_{HLac} was inhibited at low pHe, following a non-cooperative Hill curve (Fig. 5a). As the effect on P_{HLac} was interrogated instantaneously upon a pHe change, it likely relates to a direct inhibitory effect of extracellular H^+ ions. Although the six PDAC lines express various combinations of MCT isoforms (see Fig. 3b), the pHe-P_{HLac} relationships were remarkably conserved even after activation of hypoxic signalling with 48 h DMOG treatment (Fig. 5b) which induces the MCT4 gene *SLC16A3* [32] (Supplementary Fig. S8), confirming a prior observation with these cell lines [33]. The process underpinning pHe-sensitivity was determined, using a six-state model of MCT (Fig. 5C) [34], to be rate-limiting deprotonation from an exofacial site of $pK_a = 7.26$ (Fig. 5d).

The striking resemblance between the pHe-P_{HLac} (Fig. 5a) and pHe-ECAR (Fig. 4c) relationships could be interpreted to indicate that low pHe reduces lactic acid production by reducing MCT activity. However, unlike P_{HLac} measurements reporting the immediate response to pHe, ECAR measurements are slower to acquire and during that delay, extracellular acidification could evoke intracellular responses that influence glycolysis independently of the pHe-sensitivity of P_{HLac}. Indeed, the cytoplasm of cells acidifies promptly upon exposure to acidic environments, as determined in cSNARF1-loaded cells subjected to rapid solution switching (Fig. 6a). At steady-state, the relationship between pHe and pHi was curvilinear, with a slope of 0.6, as determined using a high-throughput imaging system following 10- min equilibration period in 10 mM HEPES and 10 mM MES media titrated over a range of pHe (Fig. 6b). Thus, under these experimental conditions, a 1-unit drop in pHe will, within minutes, reduce pHi by 0.6 units and hence influence glycolytic enzymes. To demonstrate that lactic acid production is directly sensitive to pHi, rather than pHe, the fluorimetric assay was performed in low-chloride medium, which alkalinises cytoplasm by inactivating acid-loading processes [35]. This pHi-selective manoeuvre significantly accelerated lactic acid production in MIA PaCa-2 and PANC-1 cells (Fig. 6c). In light of this finding, ECAR data were re-plotted as a function of pHi, and the resulting relationship was found to be highly conserved among PDAC cell lines (Fig. 6d). Crucially, application of this pHi-ECAR relationship was sufficient to predict the trajectory of medium acidification, as well as the effect of buffer supplementation, without needing to implicate a role for H^+-sensitivity of MCT activity (Fig. 6e).

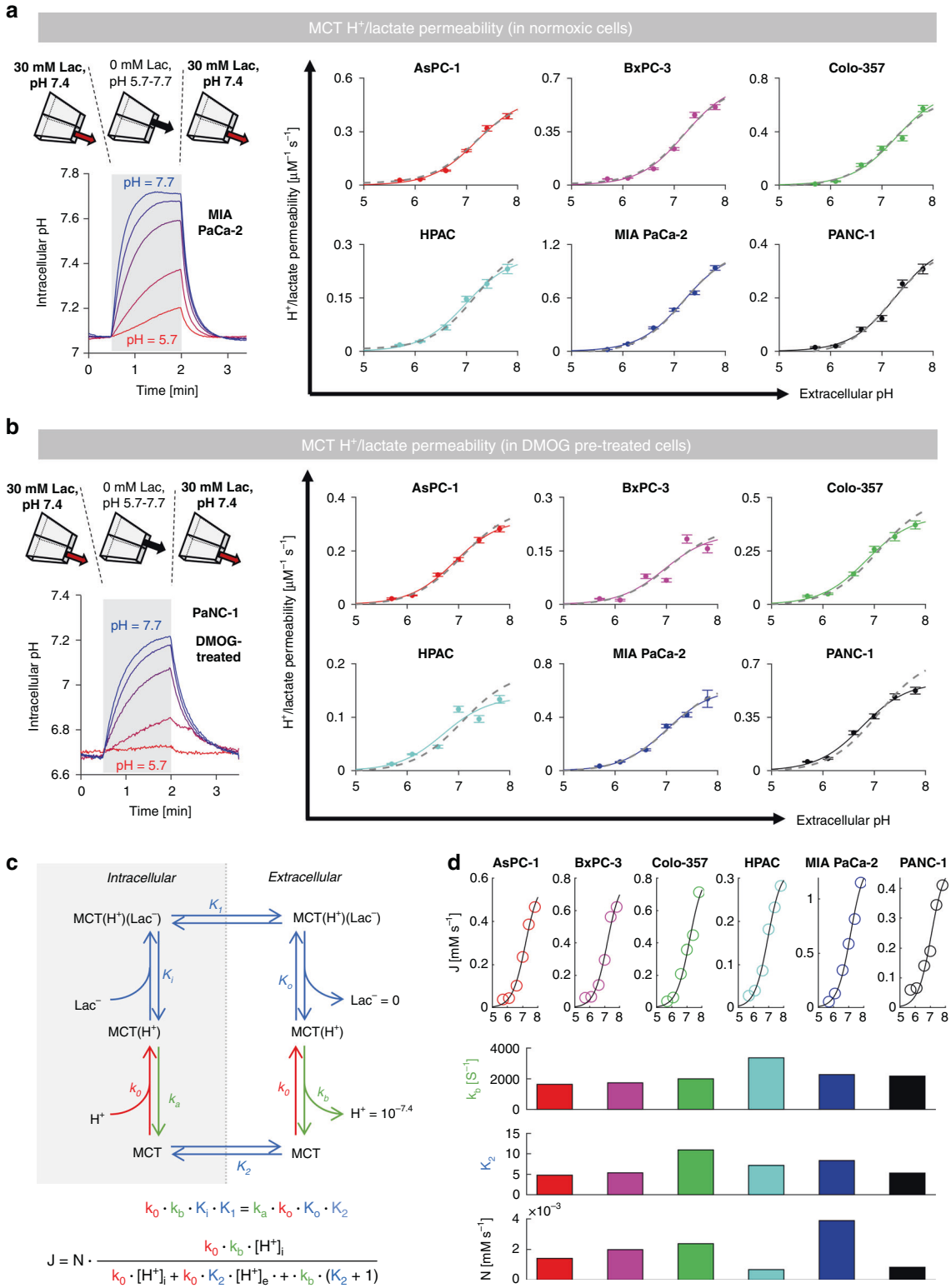
In summary, the direct inhibitory action of extracellular H^+ ions on P_{HLac} does not underpin the reduction in glycolytic rate, which is, instead, a response to the secondary cytoplasmic acidification. This mechanism is consistent with autoregulation because lactic acid production is not rate-limited by P_{HLac}.

Simulating flux autoregulation using mathematical modelling

Mathematical modelling verified the experimental finding that P_{HLac} inhibition has only a weak effect on glycolytic lactic acid production (Supplementary Fig. S9A). Various modelling scenarios were simulated, including the in silico implementation of (i) pHi regulation, (ii) pHe-sensitivity of MCT, (iii) MCT pharmacological inhibition and (iv) pHi-sensitivity of glycolysis. Lactic acid production was decreased only in scenarios where glycolysis was pHi-sensitive. When pHi-sensitivity of glycolysis was programmatically disabled, lactic acid production was unaffected by reductions in P_{HLac} by as much as 100-fold (Supplementary Fig. S9B). Autoregulation arose from compensatory changes to the transmembrane [lactate] gradient. Thus, the results of modelling are consistent with the notion that isolated changes to P_{HLac}, such as those evoked by the direct action of MCT inhibitors, do not produce a proportional effect on glycolytic output.

DISCUSSION

We present evidence that the efflux of glycolytically generated lactic acid across the surface membrane is autoregulated, which means that drugs acting on MCT-facilitated permeability cannot influence glycolytic production in a proportional manner. This phenomenon arises because a reduction in H^+/lactate permeability inadvertently increases the driving force (i.e., cytoplasmic [lactate]) and restores the original magnitude of lactic acid efflux. In other words, lactic acid release from cells is ultimately driven by glycolytic production rather than rate-limited by membrane conductance. Consequently, MCT inhibitors, especially at doses attainable in vivo, are not predicted to block cellular lactic acid production, a major component of tumour metabolism. Even with maximal drug bioavailability, it is not possible to completely ablate H^+/lactate permeability because lactic acid is able to diffuse across the lipid bilayer [36]. Our findings also caution that measurements



$$k_0 \cdot k_b \cdot K_i \cdot K_1 = k_a \cdot k_o \cdot K_o \cdot K_2$$

$$J = N \cdot \frac{k_0 \cdot k_b \cdot [H^+]_i}{k_0 \cdot [H^+]_i + k_0 \cdot K_2 \cdot [H^+]_e \cdot + \cdot k_b \cdot (K_2 + 1)}$$

Fig. 5 MCT-dependent H^+/lactate permeability is sensitive to extracellular pH. a Protocol for mapping pHe-P_{HLac} relationship by altering pH of lactate-free superfusate (shaded). pHe-P_{HLac} relationship fitted with a non-cooperative Hill curve for six PDAC cell lines; grey lines show mean for all six lines (pK = 7.19, Hill coefficient 1.26). **b** Protocol for measuring P_{HLac} in PDAC cells after 48 h treatment with DMOG (1 mM) to induce HIF signalling. pHe-dependence fitted with a non-cooperative Hill curve for six PDAC lines. All cells could be described by the same Hill coefficient and apparent pK_a. **c** Six-state model fit to pHe-P_{HLac} data. **d** Estimates of deprotonation rate constant k_b and equilibrium constant K_2 and the copy-number of MCT proteins at the membrane.

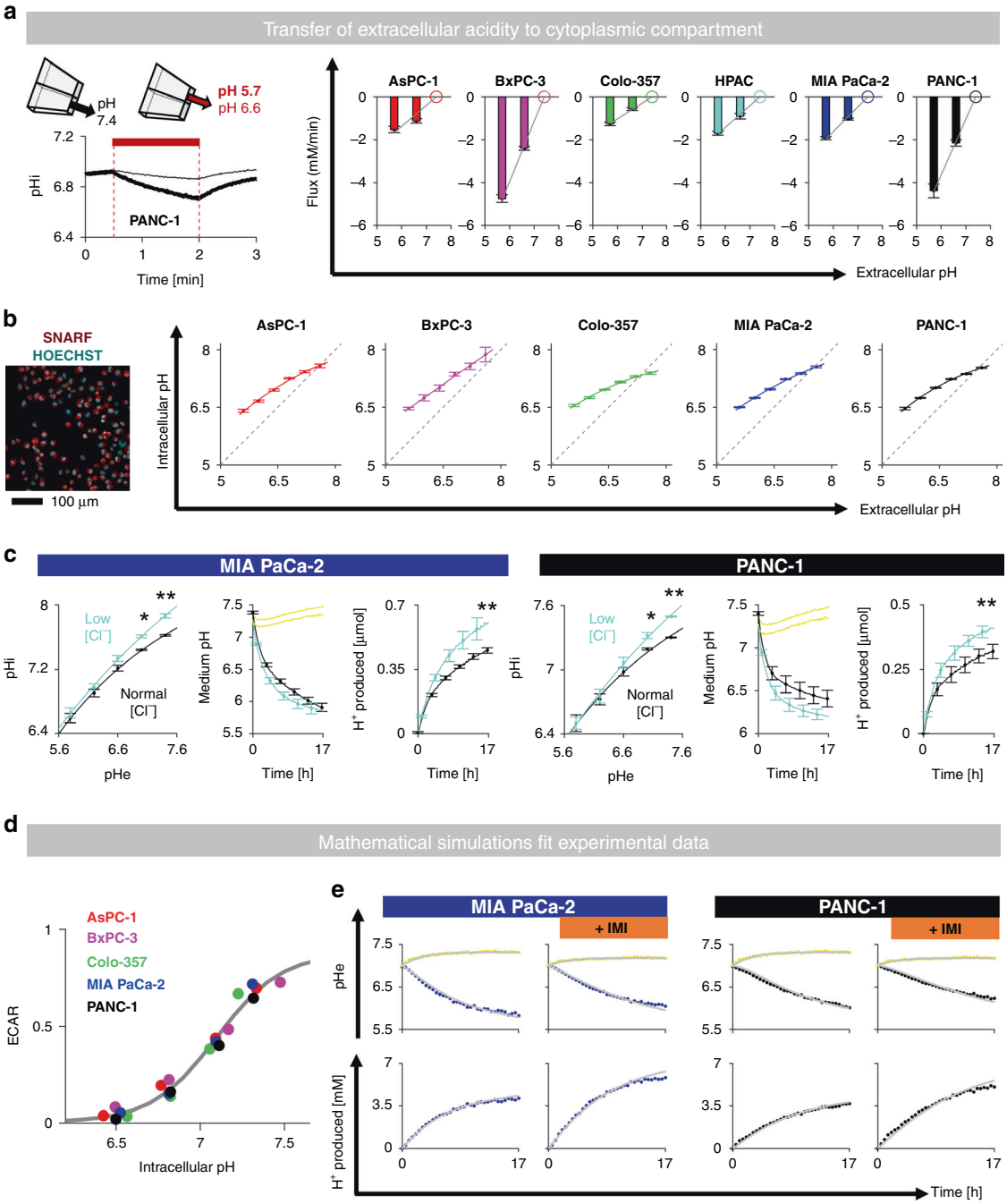


Fig. 6 Low extracellular pH reduces lactic acid production through intracellular acidification. a Response of pHi to sudden extracellular acidification to pHe 6.6 or 5.7, converted to flux ($n = 1000–3000/N = 3$). **b** Resting pHi measured after a >10 min equilibration period at test pH ($n = 1000–3000/N = 3$). **c** Incubation in low-chloride medium raises pHi at constant pHe ($n = 12/N = 4$) and accelerates glycolysis ($n = 12/N = 4$; effect of low chloride: $^{*}P < 0.05$, $^{**}P < 0.01$ by two-way ANOVA). **d** ECAR data from five PDAC lines is described by a unique function of pHi (pKa = 7.10, Hill coefficient 2.25). **e** pHi-sensitivity is sufficient to predict the time course of medium acidification and the effect of 5 mM imidazole.

of MCT activity or expression cannot accurately describe the glycolytic profile of cells. Indeed, any two cell lines can have dramatically different MCT activity, yet produce similar glycolytic rates, or vice versa.

Autoregulation may have been overlooked because of the design of measurements. The compensatory increase in driving force following acute MCT inhibition will not be immediate, as it requires the system to adjust to the lower permeability. For this reason, assays giving fast readouts (e.g., Seahorse), may not capture the autoregulatory correction, and give the impression that MCT blockers also reduce glycolysis. The methods implemented herein overcame this issue by tracking lactic acid release over hours, a timeline that is relevant to drug actions in vivo or under culture conditions. Various studies assessing the effects of MCT inhibitors have routinely focused on lactate influx [26, 37–39], a direction that is less relevant to most hypoxic tumour scenarios, where cells tend to be net lactate producers. We addressed this issue by studying lactate release driven by cellular metabolism. Several reports have taken lactate build-up, following MCT inhibition, as a measure of metabolic flux [26, 37–39]. Indeed,

autoregulation predicts that MCT inhibition shall raise cytoplasmic lactate, but this may occur without a change in metabolic flux. The methods herein inferred flux and permeability using direct methods that provide measurement in relevant units, which can then be compared between different cells and cell lines.

Autoregulation of lactic acid flux does not preclude a genuine biological effect of MCT inhibitors on other aspects of cancer biology. We speculate that reports of reduced cell proliferation or tumour growth following MCT inhibition are a product of toxic levels of cytoplasmic lactate build-up [40] or possibly off-target effects [1, 9, 10, 41], rather than glycolytic blockade per se. In contrast to lactate, which can build-up substantially in the cytoplasm, the combination of high intracellular buffering and pHi regulation restrict the extent to which pHi is able to change, but an effect of disrupted pHi cannot be excluded as a consequence of MCT inhibitors. This may explain the acidification of cells after treatment with a high concentration of syrosingopine. If pHi does change, then this will impact glycolytic rate via the direct action of intracellular H^+ ions on cytoplasmic enzymes [42, 43].

The action of extracellular H^+ ions is a peculiar example of a modulator that reduces H^+/lactate permeability and production in apparent tandem. However, inhibition of lactic acid flux is not a consequence of reduced permeability, but rather an effect of intracellular acidification on enzymes arising because of coupling between pHi and pHe. Thus, the extracellular accumulation of excreted H^+ ions inhibits glycolysis indirectly by reducing pHi, rather than through the inhibitory effect on MCTs. The glycolysis-stimulating actions of augmented buffering [44] should therefore be interpreted in terms of the increase in pHi evoked by more alkaline environment. Although MCTs are positioned strategically to monitor the release of glycolytic end-products [45, 46], autoregulation renders this feedback ineffective. In terms of control, the condition for shutting-down glycolysis is critically low pHi, rather than a threshold chemical composition of the extracellular milieu. This highlights the importance of the pHe–pHi transfer function, and is consistent with the notion that cytoplasmic enzymes are rate-limiting for glycolysis [46].

The biological rationale for autoregulation may relate to the elimination of a potential vulnerability in the Warburg effect. Without autoregulation, fermentative metabolism would be subservient to external modulators, which often vary over a wide range [2]. Furthermore, we speculate that cells control their MCT expression to regulate intracellular [lactate] (a proxy of under-perfused, hypoxic tissues [47, 48]), rather than to control glycolytic flux.

Autoregulation of H^+/lactate efflux in glycolytic cells draws an analogy to calcium signalling in the heart, a robust process that is notably insensitive to modulators of RyR-type calcium channels. The magnitude of calcium release is ultimately set by a pump (SERCA), and any imposed changes to RyR permeability are compensated by an adjustment to the calcium gradient [19]. In this analogy, glycolytic enzymes represent the pump, MCT activity defines permeability and lactate build-up is equivalent to the driving force.

In conclusion, we provide evidence that pharmacological targeting of MCTs does not reduce cancer cell glycolytic flux in a proportional manner, as long as pHi regulators maintain constancy of intracellular pH. We postulate that the reported biological actions of MCT inhibitors are more likely related to the build-up of lactate in the cytoplasm, rather than a change in metabolic fluxes per se.

DATA AVAILABILITY

All data are presented in the figures and supplements. Additional information and raw data are available upon reasonable request to the corresponding author.

REFERENCES

1. Bonglack EN, Messinger JE, Cable JM, Ch'ng J, Parnell KM, Reinoso-Vizcaino NM, et al. Monocarboxylate transporter antagonism reveals metabolic vulnerabilities of viral-driven lymphomas. Proc Natl Acad Sci USA. 2021;118:e2022495118.
2. Gatenby RA, Gawlinski ET. The glycolytic phenotype in carcinogenesis and tumor invasion: insights through mathematical models. Cancer Res. 2003;63:3847–54.
3. Renner K, Bruss C, Schnell A, Koehl G, Becker HM, Fante M, et al. Restricting glycolysis preserves T cell effector functions and augments checkpoint therapy. Cell Rep. 2019;29:135–50 e139.
4. Halestrap AP, Wilson MC. The monocarboxylate transporter family–role and regulation. IUBMB Life. 2012;64:109–19.
5. Sun X, Wang M, Wang M, Yao L, Li X, Dong H, et al. Role of proton-coupled monocarboxylate transporters in cancer: from metabolic crosstalk to therapeutic potential. Front Cell Dev Biol. 2020;8:651.
6. Kim HK, Lee I, Bang H, Kim HC, Lee WY, Yun SH, et al. MCT4 expression is a potential therapeutic target in colorectal cancer with peritoneal carcinomatosis. Mol Cancer Ther. 2018;17:838–48.
7. Wang N, Jiang X, Zhang S, Zhu A, Yuan Y, Xu H, et al. Structural basis of human monocarboxylate transporter 1 inhibition by anti-cancer drug candidates. Cell. 2021;184:370–83 e313.
8. Zhao Y, Li W, Li M, Hu Y, Zhang H, Song G, et al. Targeted inhibition of MCT4 disrupts intracellular pH homeostasis and confers self-regulated apoptosis on hepatocellular carcinoma. Exp Cell Res. 2019;384:111591.
9. Benjamin D, Robay D, Hindupur SK, Pohlmann J, Colombi M, El-Shemerly MY, et al. Dual inhibition of the lactate transporters MCT1 and MCT4 is synthetic lethal with metformin due to NAD+ depletion in cancer cells. Cell Rep. 2018; 25:3047–58 e3044.
10. Beloueche-Babari M, Casals Galobart T, Delgado-Goni T, Wantuch S, Parkes HG, Tandy D, et al. Monocarboxylate transporter 1 blockade with AZD3965 inhibits lipid biosynthesis and increases tumour immune cell infiltration. Br J Cancer. 2020;122:895–903.
11. Yamaguchi A, Futagi Y, Kobayashi M, Narumi K, Furugen A, Iseki K. Extracellular lysine 38 plays a crucial role in pH-dependent transport via human monocarboxylate transporter 1. Biochim Biophys Acta Biomembr. 2020;1862:183068.
12. Sasaki S, Kobayashi M, Futagi Y, Ogura J, Yamaguchi H, Iseki K. Involvement of histidine residue His382 in pH regulation of MCT4 activity. PLoS ONE. 2014;10: e0122738.
13. Kirk P, Wilson MC, Heddle C, Brown MH, Barclay AN, Halestrap AP. CD147 is tightly associated with lactate transporters MCT1 and MCT4 and facilitates their cell surface expression. EMBO J. 2000;19:3896–904.
14. Casey JR, Grinstein S, Orlowski J. Sensors and regulators of intracellular pH. Nat Rev Mol Cell Biol. 2010;11:50–61.
15. Webb BA, Forouhar F, Szu FE, Seetharaman J, Tong L, Barber DL. Structures of human phosphofructokinase-1 and atomic basis of cancer-associated mutations. Nature. 2015;523:111–4.
16. Trivedi B, Danforth WH. Effect of pH on the kinetics of frog muscle phosphofructokinase. J Biol Chem. 1966;241:4110–2.
17. Park JO, Tanner LB, Wei MH, Khana DB, Jacobson TB, Zhang Z, et al. Near-equilibrium glycolysis supports metabolic homeostasis and energy yield. Nat Chem Biol. 2019;15:1001–8.
18. Subramanian A, Capalbo A, Iyengar NR, Rizzo R, di Campli A, Di Martino R, et al. Auto-regulation of secretory flux by sensing and responding to the folded cargo protein load in the endoplasmic reticulum. Cell. 2019;176:1461–76 e1423.
19. Eisner DA, Trafford AW, Diaz ME, Overend CL, O'Neill SC. The control of Ca release from the cardiac sarcoplasmic reticulum: regulation versus autoregulation. Cardiovasc Res. 1998;38:589–604.
20. Michl J, Park KC, Swietach P. Evidence-based guidelines for controlling pH in mammalian live-cell culture systems. Commun Biol. 2019;2:144.
21. Dovmark TH, Hulikova A, Niederer SA, Vaughan-Jones RD, Swietach P. Normoxic cells remotely regulate the acid-base balance of cells at the hypoxic core of connexin-coupled tumor growths. FASEB J. 2018;32:83–96.
22. Richardson SL, Hulikova A, Proven M, Hipkiss R, Akanni M, Roy NBA, et al. Single-cell O2 exchange imaging shows that cytoplasmic diffusion is a dominant barrier to efficient gas transport in red blood cells. Proc Natl Acad Sci USA. 2020;117: 10067–78.
23. Jackson VN, Halestrap AP. The kinetics, substrate, and inhibitor specificity of the monocarboxylate (lactate) transporter of rat liver cells determined using the fluorescent intracellular pH indicator, 2',7'-bis(carboxyethyl)−5(6)-carboxyfluorescein. J Biol Chem. 1996;271:861–8.
24. Ovens MJ, Manoharan C, Wilson MC, Murray CM, Halestrap AP. The inhibition of monocarboxylate transporter 2 (MCT2) by AR-C155858 is modulated by the associated ancillary protein. Biochem J. 2010;431:217–25.
25. Blaszczak W, Tan ZC, Swietach P. Cost-effective real-time metabolic profiling of cancer cell lines for plate-based assays. Chemosensors. 2021;9:139.

26. Khan A, Valli E, Lam H, Scott DA, Murray J, Hanssen KM, et al. Targeting metabolic activity in high-risk neuroblastoma through monocarboxylate transporter 1 (MCT1) inhibition. Oncogene. 2020;39:3555–70.
27. Doherty JR, Yang C, Scott KE, Cameron MD, Fallahi M, Li W, et al. Blocking lactate export by inhibiting the Myc target MCT1 disables glycolysis and glutathione synthesis. Cancer Res. 2014;74:908–20.
28. Diers AR, Broniowska KA, Chang CF, Hogg N. Pyruvate fuels mitochondrial respiration and proliferation of breast cancer cells: effect of monocarboxylate transporter inhibition. Biochem J. 2012;444:561–71.
29. Kong SC, Nohr-Nielsen A, Zeeberg K, Reshkin SJ, Hoffmann EK, Novak I, et al. Monocarboxylate transporters MCT1 and MCT4 Regulate migration and invasion of pancreatic ductal adenocarcinoma cells. Pancreas. 2016;45:1036–47.
30. Baek G, Tse YF, Hu Z, Cox D, Buboltz N, McCue P, et al. MCT4 defines a glycolytic subtype of pancreatic cancer with poor prognosis and unique metabolic dependencies. Cell Rep. 2014;9:2233–49.
31. Jung DE, Kim JM, Kim C, Song SY. Embigin is overexpressed in pancreatic ductal adenocarcinoma and regulates cell motility through epithelial to mesenchymal transition via the TGF-beta pathway. Mol Carcinog. 2016;55:633–45.
32. Ullah MS, Davies AJ, Halestrap AP. The plasma membrane lactate transporter MCT4, but not MCT1, is up-regulated by hypoxia through a HIF-1alpha-dependent mechanism. J Biol Chem. 2006;281:9030–7.
33. Dovmark TH, Saccomano M, Hulikova A, Alves F, Swietach P. Connexin-43 channels are a pathway for discharging lactate from glycolytic pancreatic ductal adenocarcinoma cells. Oncogene. 2017;36:4538–50.
34. Almquist J, Lang P, Prätzel-Wolters D, Deitmer JW, Jirstrand M, Becker HM. A kinetic model of the monocarboxylate transporter MCT1 and its interaction with carbonic anhydrase II. J Computer Sci Syst Biol. 2010;3:107–16.
35. Lin PY, Ahluwalia M, Gruenstein E. An alkaline pH-activated Cl(-)-anion exchanger regulates pH homeostasis in fibroblasts. Am J Physiol. 1990;258:C132–139.
36. Cassio F, Leao C, van Uden N. Transport of lactate and other short-chain monocarboxylates in the yeast *Saccharomyces cerevisiae*. Appl Environ Microbiol. 1987;53:509–13.
37. Curtis NJ, Mooney L, Hopcroft L, Michopoulos F, Whalley N, Zhong H, et al. Pre-clinical pharmacology of AZD3965, a selective inhibitor of MCT1: DLBCL, NHL and Burkitt's lymphoma anti-tumor activity. Oncotarget. 2017;8:69219–36.
38. Guan X, Morris ME. In vitro and in vivo efficacy of AZD3965 and alpha-cyano-4-hydroxycinnamic acid in the murine 4T1 breast tumor model. AAPS J. 2020;22:84.
39. Noble RA, Bell N, Blair H, Sikka A, Thomas H, Phillips N, et al. Inhibition of monocarboxyate transporter 1 by AZD3965 as a novel therapeutic approach for diffuse large B-cell lymphoma and Burkitt lymphoma. Haematologica. 2017;102:1247–57.
40. Daw CC, Ramachandran K, Enslow BT, Maity S, Bursic B, Novello MJ, et al. Lactate elicits ER-mitochondrial Mg(2+) dynamics to integrate. Cell Metab Cell. 2020;183:474–89 e417.
41. Payen VL, Hsu MY, Radecke KS, Wyart E, Vazeille T, Bouzin C, et al. Monocarboxylate transporter MCT1 promotes tumor metastasis independently of its activity as a lactate transporter. Cancer Res. 2017;77:5591–601.
42. Oginuma M, Harima Y, Tarazona OA, Diaz-Cuadros M, Michaut A, Ishitani T, et al. Intracellular pH controls WNT downstream of glycolysis in amniote embryos. Nature. 2020;584:98–101.
43. Corbet C, Feron O. Tumour acidosis: from the passenger to the driver's seat. Nat Rev Cancer. 2017;17:577–93.
44. Ibrahim Hashim A, Cornnell HH, Coelho Ribeiro Mde L, Abrahams D, Cunningham J, Lloyd M, et al. Reduction of metastasis using a non-volatile buffer. Clin Exp Metastasis. 2011;28:841–9.
45. Hancock EJ, Ang J, Papachristodoulou A, Stan GB. The interplay between feedback and buffering in cellular homeostasis. Cell Syst. 2017;5:498–508 e423.
46. Tanner LB, Goglia AG, Wei MH, Sehgal T, Parsons LR, Park JO, et al. Four key steps control glycolytic flux in mammalian cells. Cell Syst. 2018;7:49–62 e48.
47. Green H, Halestrap A, Mockett C, O'Toole D, Grant S, Ouyang J. Increases in muscle MCT are associated with reductions in muscle lactate after a single exercise session in humans. Am J Physiol Endocrinol Metab. 2002;282:E154–160.
48. Turkcan S, Kiru L, Naczynski DJ, Sasportas LS, Pratx G. Lactic acid accumulation in the tumor microenvironment suppresses (18)F-FDG uptake. Cancer Res. 2019;79:410–9.
49. Yogurtcu ON, Johnson ME. Cytosolic proteins can exploit membrane localization to trigger functional assembly. PLoS Comput Biol. 2018;14:e1006031.
50. Walter A, Gutknecht J. Permeability of small nonelectrolytes through lipid bilayer membranes. J Membr Biol. 1986;90:207–17.

ACKNOWLEDGEMENTS

We thank Prof. Adrian Harris and Dr. Christos Zoiss (Weatherall Institute of Molecular Medicine, University of Oxford) and Prof Richard Wade Martins and Dr. Brent Ryan (DPAG) for access to their Seahorse XF Analyzer. We thank Prof. Samira Lakhal-Littleton for access to ABX Pentra C400 analyzer and Dr. Goran Mohammad for his help during measurements.

AUTHOR CONTRIBUTIONS

WB and HW performed experiments. WB and PS analysed the data. PS designed the experiments and wrote the paper.

FUNDING

European Research Council, grant SURVIVE #723997, and the Marie Skłodowska-Curie Innovative Training Network (ITN) #813834 "pHioniC" H2020-MSCA-ITN-2018.

ETHICS APPROVAL AND CONSENT TO PARTICIPATE

Not applicable to this study.

CONSENT TO PUBLISH

Not applicable to this study.

COMPETING INTERESTS

The authors declare no competing interests.

APPENDIX

The sum of lactic acid and H^+/lactate production in a cell (J_{Hlac}) must be in balance with efflux through MCTs and the lipid matrix:

$$J_{HLac} = \rho \times p_{MCT} \times \left([H^+]_i \times [lactate]_i - [H^+]_e \times [lactate]_e\right) + \rho \cdot p_{lipid} \times \left([lactic\ acid]_i - [lactic\ acid]_e\right)$$

Where ρ is the surface area/volume ratio of the cells [μm^{-1}], p_{MCT} is the MCT-dependent permeability constant to H^+/lactate ions [$\mu m\ \mu M^{-1}\ s^{-1}$], and p_{lipid} is the lipid matrix permeability constant to lactic acid [$\mu m\ s^{-1}$]. The equation can be simplified by combining ρ and permeabilities (p_{MCT}, p_{lipid}) into conductances P_{MCT} and P_{lipid}:

$$J_{HLac} = P_{MCT} \times \left([H^+]_i \times [lactate]_i - [H^+]_e \cdot [lactate]_e\right) + P_{lipid} \cdot \left([lactic\ acid]_i - [lactic\ acid]_e\right)$$

Since lactic acid, lactate and H^+ are in equilibrium defined by the acid dissociation constant K_{Hlac} ($10^{-3.86}$ M):

$$K_{HLac} = [H^+] \cdot [lactate]/[lactic\ acid]$$

The equation for J_{HLac} can be re-written:

$$\begin{aligned} J_{HLac} &= P_{MCT} \cdot \left([H^+]_i \cdot [lactate]_i - [H^+]_e \cdot [lactate]_e\right) \\ &\quad + P_{lipid} \cdot \left([H^+]_i \cdot [lactate]_i - [H^+]_e \cdot [lactate]_e\right)/K_{HLac} \\ &= \left(P_{MCT} + P_{lipid}/K_{HLac}\right) \cdot \left([H^+]_i \cdot [lactate]_i - [H^+]_e \cdot [lactate]_e\right) \\ &= P_{HLac} \cdot \left([H^+]_i \cdot [lactate]_i - [H^+]_e \cdot [lactate]_e\right) \end{aligned}$$

For a typical cells, ρ is ~1 μm^{-1} ([49]) and p_{lipid} is ~0.5 μm/s ([50]), thus in the absence of MCT facilitation, P_{HLac} is ~0.003 $\mu M^{-1}\ s^{-1}$.

ADDITIONAL INFORMATION

Supplementary information The online version contains supplementary material available at https://doi.org/10.1038/s41416-022-01910-7.

Correspondence and requests for materials should be addressed to Pawel Swietach.

Reprints and permission information is available at http://www.nature.com/reprints

Publisher's note Springer Nature remains neutral with regard to jurisdictional claims in published maps and institutional affiliations.

Open Access This article is licensed under a Creative Commons Attribution 4.0 International License, which permits use, sharing, adaptation, distribution and reproduction in any medium or format, as long as you give appropriate credit to the original author(s) and the source, provide a link to the Creative Commons license, and indicate if changes were made. The images or other third party material in this article are included in the article's Creative Commons license, unless indicated otherwise in a credit line to the material. If material is not included in the article's Creative Commons license and your intended use is not permitted by statutory regulation or exceeds the permitted use, you will need to obtain permission directly from the copyright holder. To view a copy of this license, visit http://creativecommons.org/licenses/by/4.0/.

© The Author(s) 2022